



HAL
open science

Elaboration and characterization of mechanical properties of ceramic composites with controlled architecture

Malgorzata Marcinkowska

► **To cite this version:**

Malgorzata Marcinkowska. Elaboration and characterization of mechanical properties of ceramic composites with controlled architecture. Materials. Université de Lyon, 2018. English. NNT : 2018LYSEI021 . tel-02061358

HAL Id: tel-02061358

<https://theses.hal.science/tel-02061358>

Submitted on 8 Mar 2019

HAL is a multi-disciplinary open access archive for the deposit and dissemination of scientific research documents, whether they are published or not. The documents may come from teaching and research institutions in France or abroad, or from public or private research centers.

L'archive ouverte pluridisciplinaire **HAL**, est destinée au dépôt et à la diffusion de documents scientifiques de niveau recherche, publiés ou non, émanant des établissements d'enseignement et de recherche français ou étrangers, des laboratoires publics ou privés.



INSA

N°d'ordre NNT : 2018LYSEI021

THESE de DOCTORAT DE L'UNIVERSITE DE LYON
opérée au sein de
L'Institut National des Sciences Appliquées de Lyon

Ecole Doctorale N° ED34
Matériaux de Lyon

Spécialité de doctorat : Matériaux

Soutenance prévue le 20/03/2018, par :
Malgorzata Judyta Marcinkowska

**Elaboration and characterization of
mechanical properties of ceramic
composites with controlled architecture**

Devant le jury composé de :

ROSSIGNOL Fabrice
BOUVARD Didier
LE GALLET Sophie
DEZELLUS Olivier
MEILLE Sylvain
DEVILLE Sylvain

Directeur de Recherche
Professeur des Universités
Maître de Conférences
Maître de Conférences HDR
Professeur des Universités
Directeur de Recherche

SPCTS
SIMAP
Université de Bourgogne
LMI
INSA-LYON
LSFC, CNRS/Saint-Gobain

Rapporteur
Rapporteur
Examinatrice
Examineur
Directeur de thèse
Co-directeur de thèse

Département FEDORA – INSA Lyon - Ecoles Doctorales – Quinquennal 2016-2020

SIGLE	ECOLE DOCTORALE	NOM ET COORDONNEES DU RESPONSABLE
CHIMIE	CHIMIE DE LYON http://www.edchimie-lyon.fr Sec : Renée EL MELHEM Bat Blaise Pascal 3 ^e etage secretariat@edchimie-lyon.fr Insa : R. GOURDON	M. Stéphane DANIELE Institut de Recherches sur la Catalyse et l'Environnement de Lyon IRCELYON-UMR 5256 Équipe CDFA 2 avenue Albert Einstein 69626 Villeurbanne cedex directeur@edchimie-lyon.fr
E.E.A.	ELECTRONIQUE, ELECTROTECHNIQUE, AUTOMATIQUE http://edeea.ec-lyon.fr Sec : M.C. HAVGOUDOUKIAN Ecole-Doctorale.eea@ec-lyon.fr	M. Gérard SCORLETTI Ecole Centrale de Lyon 36 avenue Guy de Collongue 69134 ECULLY Tél : 04.72.18 60.97 Fax : 04 78 43 37 17 Gerard.scorletti@ec-lyon.fr
E2M2	EVOLUTION, ECOSYSTEME, MICROBIOLOGIE, MODELISATION http://e2m2.universite-lyon.fr Sec : Sylvie ROBERJOT Bât Atrium - UCB Lyon 1 04.72.44.83.62 Insa : H. CHARLES secretariat.e2m2@univ-lyon1.fr	M. Fabrice CORDEY CNRS UMR 5276 Lab. de géologie de Lyon Université Claude Bernard Lyon 1 Bât Géode 2 rue Raphaël Dubois 69622 VILLEURBANNE Cédex Tél : 06.07.53.89.13 cordey@univ-lyon1.fr
EDISS	INTERDISCIPLINAIRE SCIENCES-SANTE http://www.ediss-lyon.fr Sec : Sylvie ROBERJOT Bât Atrium - UCB Lyon 1 04.72.44.83.62 Insa : M. LAGARDE secretariat.ediss@univ-lyon1.fr	Mme Emmanuelle CANET-SOULAS INSERM U1060, CarMeN lab, Univ. Lyon 1 Bâtiment IMBL 11 avenue Jean Capelle INSA de Lyon 696621 Villeurbanne Tél : 04.72.68.49.09 Fax :04 72 68 49 16 Emmanuelle.canet@univ-lyon1.fr
INFOMATHS	INFORMATIQUE ET MATHEMATIQUES http://infomaths.univ-lyon1.fr Sec : Renée EL MELHEM Bat Blaise Pascal, 3 ^e étage Tél : 04.72. 43. 80. 46 Fax : 04.72.43.16.87 infomaths@univ-lyon1.fr	M. Luca ZAMBONI Bâtiment Braconnier 43 Boulevard du 11 novembre 1918 69622 VILLEURBANNE Cedex Tél :04 26 23 45 52 zamboni@maths.univ-lyon1.fr
Matériaux	MATERIAUX DE LYON http://ed34.universite-lyon.fr Sec : Marion COMBE Tél:04-72-43-71-70 –Fax : 87.12 Bat. Direction ed.materiaux@insa-lyon.fr	M. Jean-Yves BUFFIERE INSA de Lyon MATEIS Bâtiment Saint Exupéry 7 avenue Jean Capelle 69621 VILLEURBANNE Cedex Tél : 04.72.43 71.70 Fax 04 72 43 85 28 Ed.materiaux@insa-lyon.fr
MEGA	MECANIQUE,ENERGETIQUE,GENIE CIVIL,ACOUSTIQUE http://mega.universite-lyon.fr Sec : Marion COMBE Tél:04-72-43-71-70 –Fax : 87.12 Bat. Direction mega@insa-lyon.fr	M. Philippe BOISSE INSA de Lyon Laboratoire LAMCOS Bâtiment Jacquard 25 bis avenue Jean Capelle 69621 VILLEURBANNE Cedex Tél : 04.72 .43.71.70 Fax : 04 72 43 72 37 Philippe.boisse@insa-lyon.fr
ScSo	ScSo* http://recherche.univ-lyon2.fr/scso/ Sec : Viviane POLSINELLI Brigitte DUBOIS Insa : J.Y. TOUSSAINT Tél : 04 78 69 72 76 viviane.polsinelli@univ-lyon2.fr	M. Christian MONTES Université Lyon 2 86 rue Pasteur 69365 LYON Cedex 07 Christian.montes@univ-lyon2.fr

*ScSo : Histoire, Géographie, Aménagement, Urbanisme, Archéologie, Science politique, Sociologie, Anthropologie

Acknowledgements

As it is customary, I begin my acknowledgements with thanking my bosses, the two Sylvains: Meille and Deville. I would like to thank you for giving me a lot of freedom in my work and offering assistance whenever I encountered difficulties. Not everyone is lucky enough to have PhD thesis directors who also happen to be great people. I'd like to also thank Éric Maire and Jérôme Chevalier, who have participated in the supervision of my doctoral work.

I have encountered many people who disinterestedly helped me in my work, among whom Thierry Douillard, Sophie Cazottes, Bérangère Lesaint, Florian Mercier and Guillaume Bonnefont, deserve a special mention. Thank you for the time you dedicated to helping me in my work. In the MATEIS laboratory one can come across many people who create a friendly atmosphere: Sandrine C., Jean-Marc P., Liliane, Corinne, Antonia are only a few of the many great people I've met here.

For a moment, I will move away from Lyon, towards Cavaillon, to thank all the LSFC members I have had the pleasure to meet and cooperate with. I'd like to thank the permanent employees: Caroline, Adam, Daniel M., Stéphane, Jérôme, as well as other students: Jordi (with whom I have also shared my office in Lyon), Amin, Corinne, Khadija, Cécile, Moreno etc.

In the MATEIS lab I met many people who have made my stay in Lyon the greatest experience of my life: Marta, Carlos, Abel, Aléthèa, Silvia, Liliana, Clément, Erik, Claire, Titi (the best co-bureau ever), Fanfan, Lucie, Marwa, Hélène, Kate, Laura, Nathalie, Guillaume, Dede, Alban, Nico G., Belynda, Juan, William, Mélanie, Seb, Thibaud, Josselin, Zeina, Eloïse, Oriane, Justine, Gwen, Julie, Kurt, Dwaipayana, Aurelien, Victor, Gabriel and Théo. If I have omitted someone's names, I'm sorry: it's because I met too many amazing people.

Nico deserves a separate paragraph in these acknowledgements. He has been of inestimable help to me. I can easily say he is the most important person I have met during my doctoral studies. Sharing life with him is like looking at the world through rose-tinted glasses. Every day he motivates me to be the best version of myself. Thank you, Króliczek! <3

I'd also like to thank Maria-Pau, Cristina, David, Anna, Sara and Judit whom I met in UPC in Barcelona. It's the experience of working with them that has motivated me to take up the challenge of doctoral studies. Gracias!

The Polish support group, namely Ola and Christophe, Alicja and Thibaut, Marcin and Dominika also deserve a big "thank you!". You have no idea how important your company and the time we spend together are for me.

I would like to dedicate the last paragraph of these acknowledgements to my family and friends. I would like to thank my parents for the self-confidence they have been instilling in me since I was a child,

saying "You can do it! If not you, who will? If not now, when?". Thanks to them I have never doubted my ability to succeed, even when I was going through difficult times. I would also like to thank my whole family, who are quite a large group: you are all very dear to me, but since our family is so big, I don't have the room to name you all individually. You know I'm talking to you! Great thanks to uncle Piotrek and auntie Irenka, though you are my surrogate family, you are very dear to my heart. I'd like to also thank my other surrogate aunt, Ewa, for her help in the domain of science, for cheering me on and being understanding. I'd also like to thank my wonderful best friend, Asia, who never allows me to wallow in self-pity and Helena who is great and helps me to stay grounded and focused. I'd like to thank Magdalenka and Dominika and friends from college, high school and even middle school. It's always great to see you when I'm in Krakow.

Ostatni akapit tych podziękowań poświęcam Rodzinie i Przyjaciołom. Dziękuję moim Rodzicom za ogromną pewność siebie, którą wpajali mi od dziecka mówiąc: „Jak nie Ty, to kto? Jak nie teraz, to kiedy?”. Dzięki nim nigdy nie wątpiłam, że sobie poradzę, nawet jak było mi bardzo trudno. Dziękuję całej Rodzinie, która jest mi tak bliska. Jest też bardzo liczna, dlatego nie jestem w stanie Was wszystkich wymienić, ale wiecie, że do Was mówię. Dziękuję też wujkowi Piotrkowi i cioci Irence, mimo że jesteście „przyszywanym” wujostwem, jesteście mi niezwykle bliscy. Dziękuję przyszywanej cioci Ewie za jej wsparcie naukowe, motywacje i zrozumienie. Dziękuję mojej najlepszej przyjaciółce, Asi, która jest cudowna i nie pozwala mi się użalać nad sobą. Dziękuję też Helenie, która jest super i pomaga mi nie być kompletnie nieogarniętą. Dziękuję Magdalence i Dominice. Dziękuję kolegom i koleżankom ze studiów, liceum i nawet gimnazjum. Zawsze mi jest bardzo miło spotkać się z Wami, kiedy jestem w Krakowie.

Contents

Introduction	xix
1 Literature review	3
1.1 Properties of natural and bioinspired materials	3
1.1.1 Natural materials	3
1.1.2 Bioinspired materials	8
1.2 Fabrication of materials with controlled micro-structure at multiple length scales	11
1.3 Field assisted sintering techniques	15
1.4 Titanium and its composites with ceramics	18
1.4.1 Characteristics of titanium	18
1.4.2 Alumina/titanium composites fabricated by FAST	23
1.5 Conclusions of the chapter	26
2 Materials and methods	27
2.1 Materials preparation	27
2.1.1 Samples obtained by freezing under flow	27
2.1.2 Composites prepared by pressing	30
2.1.3 Metal/ceramic composites prepared by pressing	31
2.1.4 Sample processing before characterization	31
2.2 Characterization techniques	34
2.2.1 Morphological characterization	34
2.2.2 Mechanical testing	36
2.2.3 <i>In situ</i> three-point bending	39
3 Simplification of material fabrication	41
3.1 Freeze-casting	42
3.2 Uniaxial pressing	45
3.3 Up-scale	48
4 Modification of the interphase between platelets	53
4.1 Incorporation of zirconia	54
4.1.1 Zirconia nanopowder	55
4.1.2 Alkoxide	58
4.2 Graphene	64
4.3 Conclusions of the chapter	71

5 Alumina/titanium composites	73
5.1 Fabrication and structural characterisation	73
5.1.1 Fabrication	73
5.1.2 Study of titanium diffusion	78
5.1.3 Changing foil chemistry	83
5.2 Mechanical properties	97
5.2.1 Preliminary study	97
5.2.2 Mechanical testing <i>in situ</i>	99
5.2.3 Influence of the foil thickness	103
5.2.4 Influence of the foil chemistry	108
5.3 General discussion	113
General conclusions	121

List of Figures

1	A schematic presentation of material constituents discussed in chapters four and five.	xx
1.1	Structure and toughening mechanisms on multiple structural levels (from nano- to macro-scale) which improve mechanical properties of natural material: bone [1]	4
1.2	Crack-resistant curves (R-curves) of human bone tested in two directions: transverse and longitudinal [2]	5
1.3	Schematic illustrations of crack-resistance curves (R-curves) [3]	5
1.4	The structure of nacre: aligned aragonite tablets (diameter approximately $8 \mu\text{m}$ and thickness $0.4 \mu\text{m}$) and thin organic interphase [4]	6
1.5	Experimental set-up for tensile test under an optical microscope [5]	6
1.6	Values of tensile strain obtained during measurements [5]	7
1.7	Fracture tests (3 point bending on notched samples) performed on natural nacre in AFM, combined with quantitative analysis of tablet sliding [6]	8
1.8	On the left: comparison of fracture toughness in alumina composites with two types of microstructure: lamellar and "brick and mortar" [7]. On the right: SEM picture of "brick and mortar" structure (a) and lamellar structure (b).	9
1.9	Scheme of a) the analysed composite and b) the single unit cell for the analysis [8]	10
1.10	Improved mechanical properties of biomimetic nacre-like alumina in comparison to conventional composites of alumina [9]	11
1.11	Microstructural composition of nacre-like alumina [9]	11
1.12	Schematic diagram of the ice-templating principles. [10]	13
1.13	Thickness of the lamellae in alumina samples as a function of the speed of the solidification front.	14
1.14	Scheme of mechanism of platelets alignment by advancing ice crystals [11]	14
1.15	Schematic of a pulsed electric current sintering apparatus. [12]	16
1.16	Comparison of percentage of open porosity in ceramics sintered by FAST and sintered naturally with HIP step at different temperatures [13]	17

LIST OF FIGURES

1.17	Chosen characteristics of titanium in comparison with other structural metallic materials based on Fe, Ni and Al [14]. Direction of the allotropic transition demonstrated in the table is from high to low temperature.	19
1.18	Unit cells of α (hcp) and β (bcc) phase of titanium [14]	19
1.19	Change of value of elastic and shear modulus in function of temperature of α Ti [15]	20
1.20	Schematic phase diagrams of titanium alloys depending on alloying elements [14]	20
1.21	Concentration of elements required to stabilise β phase at room temperature [16]	21
1.22	Chosen physical properties of titanium and its alloys in comparison with other structural metallic materials [16]	22
1.23	Industrial applications of titanium thanks to its corrosion resistance [14]	23
1.24	Sintering cycle for alumina/titanium composite processing [17]	24
1.25	Comparison of XRD patterns for titanium and alumina/titanium composites [17]	24
1.26	Material properties of alumina/titanium composites fabricated by FAST [18]	25
1.27	SEM pictures of alumina/titanium composites fabricated by FAST [17]. Content of titanium (light gray) in wt% is as follows: A) 80, B) 60, C) 40 and D) 20.	26
2.1	Alumina platelets used in this study [11]	28
2.2	A schematic view of freezing under flow set up [19]	29
2.3	A schematic view of gradients created during freezing under flow [19]	30
2.4	A scheme of alumina/titanium composite	31
2.5	A notch sharpening set up	32
2.6	A notch prepared according to the protocol	33
2.7	Titanium/alumina sample polished by Ilion II+. Inside the etched zone we can see titanium foil and diffusion zone (light colour) and alumina matrix (dark colour).	33
2.8	An example of crack observation by confocal microscopy	34
2.9	Comparison of 3D reconstructions of scans performed in EasyTomo Nano tomograph in MATEIS laboratory and in ESRF synchrotron facility	36
2.10	Bottom part of bending set up	37
2.11	Upper parts of three and four point bending set up	38
2.12	Four-point bending montage assembled	38
2.13	A set up allowing to perform 3PB in SEM	40
3.1	Differences between mechanical properties prepared by the same processing protocol by two different people (thesis of Florian Bouville [11] and this work)	42
3.2	Sintering cycle for samples prepared by freeze-casting	43

3.3	Platelets orientation and grain boundaries of sample processed by freeze casting and pressing (cross section perpendicular to sample surface)	43
3.4	Force-Deflection curve of the material processed by freeze casting . . .	44
3.5	Stress-Strain curve of the material processed by freeze casting	44
3.6	R-curves of the material processed by freeze casting	45
3.7	Platelets orientation and grain boundaries of sample processed by uniaxial pressing instead of freeze casting	46
3.8	Force-Deflection curve of the material processed by uniaxial pressing .	47
3.9	Stress-Strain curve of the material processed by uniaxial pressing . . .	47
3.10	R-curves of the material processed by uniaxial pressing. ASTM invalid area concerns crack extension surpassing 0.25 of ligament length. . . .	48
3.11	Sintering cycle for the first attempt of up-scaling material fabrication, 90 g sample	49
3.12	Optimized sintering cycle for up-scaling material fabrication	50
3.13	Sample obtained by uniaxial pressing and FAST with modified sintering cycle	50
3.14	Comparison of platelets orientation and grain size of sample processed by uniaxial pressing and up-scaled one	51
4.1	Stress-Strain curves of materials with three variants of the interphase (notched samples) [9]	54
4.2	Linear thermal expansion of a composite composed of 25% alumina platelets and 75% TM-DAR as a function of direction: in plane (xy) or out of plane (z)	55
4.3	Force-Deflection curve of the material with fine zirconia powder instead of TM-DAR	56
4.4	Stress-Strain curve of the material with fine zirconia powder instead of TM-DAR	57
4.5	R-curves of the material with zirconia powder instead of TM-DAR . . .	57
4.6	SEM images of crack in the sample with zirconia powder instead of TM-DAR	58
4.7	A comparison of stress-strain curves of the material with fine zirconia powder instead of TM-DAR with standard nacre-like alumina	59
4.8	A scheme of reaction which allows to deposit zirconia on the surface of alumina platelets	59
4.9	SEM image of alumina/zirconia composite fabricated thanks to alkoxide processing [20]	60
4.10	Zirconia grain size distribution depending on processing route [20] . .	60
4.11	Force-Deflection curve of the material with platelets processed by alkoxide reaction	62
4.12	Stress-Strain curve of the material with platelets processed by alkoxide reaction	62
4.13	R-curves of the material with platelets processed by alkoxide reaction .	63

LIST OF FIGURES

4.14 SEM images of crack in the sample with platelets processed by alkoxide reaction	63
4.15 A comparison of stress-strain curves of the material with platelets processed by alkoxide reaction with standard nacre-like alumina	64
4.16 Values of fracture toughness measured by indentation and chevron notch as a function of graphene content in dense alumina composites [21]	65
4.17 Toughening mechanisms in GPL alumina composite [22]	66
4.18 Mechanical properties measured by nanoindentation for laminates: A-alumina, AZ-alumina with 5 vol. % of 3Y-TZP and AZGO-alumina with 5 vol. % of 3Y-TZP and 2 vol. % of graphene oxide [23]	66
4.19 Force-Deflection curve of the material with graphene in the interphase	68
4.20 Stress-Strain curve of the material with graphene in the interphase . .	69
4.21 R-curves of the material with graphene in the interphase	69
4.22 SEM images of crack in the sample with graphene in the interphase . .	70
4.23 A comparison of stress-strain curves of the material with graphene in the interphase with standard nacre-like alumina	71
4.24 A comparison of stress-strain curves of all the material formulations tested in this study	71
5.1 SEM image of alumina/titanium composite (sintered at 1500°C) showing three regions (initial titanium foil thickness of 50µm, final 30-40µm). Some platelets pull out has occurred during polishing in the alumina matrix.	74
5.2 Area chosen to be analysed by EDX	75
5.3 Placement of the three elements found during EDX	75
5.4 SEM image of titanium foil sintered between alumina pellets (BSE detector)	76
5.5 Band Contrast image of the titanium foil (camera EBSD). Both samples sintered at 1500°C. Sample on the left: cooling 100°C/min, initial foil thickness 50µm, sample on the right: cooling 10°C/min, initial foil thickness 100 µm. Magnification on both images is not the same. . . .	77
5.6 Comparison of crystallographical structure of two foils (100°C/min vs 10°C/min)	77
5.7 EDX image of the observed intermetallics, sample cooling speed: 100°C/min.	78
5.8 EDX images of particular elements present in the intermetallics	78
5.9 Temperature profiles of applied sintering cycles. Holding time of 30 minutes at 1200, 1300, 1400 and 1500°C respectively, max. temp. 1500°C for all treatments.	79
5.10 A sample sintered at 1500 °C with 30 minutes holding time at 1200 °C; minor diffusion of titanium (BSE detector)	79
5.11 A sample sintered at 1500 °C with 30 minutes holding time at 1300 °C; minor diffusion of titanium (BSE detector)	80
5.12 A sample sintered at 1500 °C with 30 minutes holding time at 1400 °C; significant diffusion of titanium (BSE detector)	80

5.13	A sample sintered at 1500 °C with 30 minutes holding time at 1500 °C; significant diffusion of titanium (BSE detector)	81
5.14	One picture from volume reconstruction of the sample 30 min at 1200°C. It shows residual porosity (light) in ceramic matrix (darker). It is the zone close to the titanium film (scan perpendicular to the metal layer) but no visible diffusion was noticed.	81
5.15	3D volume reconstruction of the sample sintered during 30 min at 1500°C. Ceramic phase was removed from the reconstruction to show titanium which infiltrated porosity.	82
5.16	Close-up look on grain interconnections and residual porosity which was not infiltrated by metal. Sample sintered during 30 min at 1500°C. Ceramic phase was removed from the reconstruction to show titanium and porosity. Titanium phase is in cyan and porosity in magenta. . . .	82
5.17	Temperature differences between internal and external zone of the material [24]. Sintering dies differed in diameter and thickness. Horizontal lines: thin die, grid: thick die.	83
5.18	Intermetallic structures inside Ti6Al4V foil. Bright grey: metal, dark grey: inclusions.	84
5.19	Chemical analysis of intermetallics	84
5.20	Placement of spectra measurements	85
5.21	Analysis of ceramic matrix and metal grains composition (BSE detector)	86
5.22	Differences of composition within titanium grains in the diffusion zone (BSE detector)	87
5.23	Duality in structure of a single grain	87
5.24	Varied chemical composition of a single grain	88
5.25	Analysis of linear composition of diffusion zone	88
5.26	Linear analysis of all elements present in the composite starting from alumina to titanium layer, through the diffusion zone	89
5.27	Linear analysis of titanium along the line shown in fig. 5.25	89
5.28	Linear analysis of aluminium along the line shown in fig. 5.25	90
5.29	Linear analysis of oxygen along the line shown in fig. 5.25	90
5.30	SEM picture of metal foil and diffusion zone in the composite $Al_2O_3/TiN/Ti$. Sintering temperature: 1500°C, heating rate: 100°C, cooling rate: 10°C.	91
5.31	Difference between metal in inclusions zone and metal deeper in the foil	91
5.32	Analysis of intermetallics	92
5.33	Comparison between spectres of metal and intermetallic. Y-axis: number of X-rays received and processed by the detector [cps/eV], X-axis: energy level of those counts [keV].	93
5.34	Analysis of grain composition in the diffusion zone. Sample with Ti(N) foil, sintered at 1500°C, heating rate 100°C/min, cooling rate 10°C/min.	93
5.35	Analysis of linear composition of diffusion zone	94
5.36	Linear analysis of all elements present in the composite along the line shown in fig. 5.35	94
5.37	Linear analysis of titanium along the line shown in fig. 5.35	95

LIST OF FIGURES

5.38	Linear analysis of nitrogen along the line shown in fig. 5.35	95
5.39	Linear analysis of aluminium along the line shown in fig. 5.35	96
5.40	Linear analysis of oxygen along the line shown in fig. 5.35	96
5.41	Force-Deflection curves of the reference material (no metal foil)	97
5.42	Stress-Strain curves of the reference material	98
5.43	R-curves of the reference material	98
5.44	SEM pictures of the broken reference sample during three point bending <i>in situ</i>	100
5.45	SEM pictures of the sample with a layer of titanium foil (without glassy phase) in the moment of crack offset (at 70 N) during three point bending <i>in situ</i>	101
5.46	SEM pictures of the broken (at 73 N) sample with a layer of titanium foil (without glassy phase) during three point bending <i>in situ</i>	102
5.47	Force-Deflection curves of the material with 20 μ m foil. Sintered at 1500°C, heating rate: 100°/min, cooling rate: 10°/min.	103
5.48	Stress-Strain curves of the material with 20 μ m foil	104
5.49	R-curves of the material with 20 μ m foil. For samples B and C an ASTM invalid zone begins earlier, before 0.4 mm crack extension.	104
5.50	Force-Deflection curves of the material with 100 μ m foil	105
5.51	Stress-Strain curves of the material with 100 μ m foil	105
5.52	R-curves of the material with 100 μ m foil	106
5.53	Force-Deflection curves of the material with 500 μ m foil	106
5.54	Stress-Strain curves of the material with 500 μ m foil	107
5.55	R-curves of the material with 500 μ m foil	107
5.56	Comparison of Stress-Strain curves of materials with different foil thickness	108
5.57	Force-Deflection curves of the material with Ti6Al4V foil (around 500 μ m thick)	109
5.58	Stress-Strain curves of the material with Ti6Al4V foil (around 500 μ m thick)	109
5.59	R-curves of the material with Ti6Al4V foil (around 500 μ m thick)	110
5.60	Force-Deflection curves of the material with Ti foil with TiN layer (around 500 μ m thick)	111
5.61	Stress-Strain curves of the material with Ti foil with TiN layer (around 500 μ m thick)	111
5.62	R-curves of the material with Ti foil with TiN layer (around 500 μ m thick)	112
5.63	Comparison of Stress-Strain curves of materials with different foil chemistry (500 μ m thick metal layers)	113
5.64	Ellingham-Richardson diagram of common oxides (free energy in function of temperature). It shows that thermodynamically alumina is more stable than titanium oxide (TiO_2) in our temperature range.	115
5.65	Microstructural difference between the zone which was solid and the zone that was probably liquid during sintering	115
5.66	IPFZ maps for the titanium foil	116

5.67 Orientation relationships between cubic and hexagonal phase found
in the first domain 116

5.68 Comparison of Stress-Strain curves of materials with different foil thick-
ness with reference material 119

5.69 Comparison of Stress-Strain curves of materials with different foil chem-
istry with reference material 119

List of Tables

1.1	Selected commercial titanium alloys from [14]. CP-Ti: commercially pure titanium	21
1.2	Mechanical properties of commercially pure titanium from [14]	21
2.1	Standard composition of the slurry for freeze casting	29
2.2	Details of the polishing protocol	32
3.1	Size distribution of alumina platelets in sample processed by freeze casting	44
3.2	Size distribution of alumina platelets in sample processed by uniaxial pressing instead of freeze casting	46
4.1	Components of the slurry WS_56	55
4.2	Components of the slurry WS_57	61
4.3	Concentrations of Isobam 104	67
4.4	Components of the slurry GO_11	67
4.5	Components of the slurry GO_11	68
5.1	Values of stress merging from the difference of CTE of alumina and titanium ($\Delta=1500^{\circ}\text{C}$). Alumina thickness was always 2 mm (in four layers). There were always three titanium layers so values of thickness given in the table are triple of single titanium foil thickness.	76
5.2	Comparison of composition of the metal matrix and inclusions	85
5.3	Composition of diffused grains and ceramic matrix	86
5.4	Differences in composition of diffused grains, average of spectra as indicated	86
5.5	Differences in composition of metal closer and further away from the inclusions	92
5.6	Differences in composition of titanium grains diffused into alumina matrix	94

Abstract

The goal of this thesis was to develop and characterize (microstructurally and mechanically) bioinspired ceramic composites. Nacre-like alumina fabricated by freeze-casting and developed during the PhD of Florian Bouville was chosen as a reference material. The simplification and up-scale of material fabrication was intended. Architectural levels were added to the microstructure to further improve mechanical properties of the material.

Sophisticated processing by freeze-casting technique was substituted by a simple and well-known technique: uniaxial pressing. Electron backscatter diffraction (EBSD) observations confirmed the good alignment of alumina platelets used to prepare the material. The field assisted sintering (FAST) cycle was adapted to greater quantities of ceramic powder and organic additives.

The second part of the project was dedicated to the modification of the interphase between alumina platelets. Various possibilities were explored: adding fine zirconia powder, depositing zirconia on the surface of platelets by sol-gel reaction or substituting the glassy phase by graphene. All obtained materials were characterized microstructurally by scanning electron microscopy (SEM) and mechanically by four point bending (4PB).

The third part of this study was focused on the development of metal/ceramic composites. The composites were obtained by simultaneous sintering of ceramic powder mixture layers alternating with titanium foil. The titanium layer thickness was varied (between 20 and 500 μm) as its composition (pure titanium, Ti6Al4V alloy and pure titanium with layers of TiN deposited on both sides). The composites were characterized by SEM, EBSD, energy dispersive X-ray spectroscopy (EDX) and synchrotron X-ray tomography. Detailed microstructural and chemical characterization was performed to understand mechanisms of titanium diffusion into ceramic matrix.

Simplified material fabrication allows to prepare larger samples. Processing needs to be improved. Grain growth should be limited to maintain good mechanical properties of architected alumina composites. Modification of the interphase between alumina platelets did not improve mechanical properties of the materials as compared to nacre-like alumina fabricated by freeze-casting. On the other hand, depositing nano-zirconia on platelets surface seems promising and it should be further investigated. In case of alumina/titanium composites, a multiscale architecture composite was obtained in a rather simple way. However, avoiding metal foil cracking is crucial to improve mechanical properties.

Introduction

In the recent years, in order to improve properties of ceramic materials, scientists paid a lot of attention to their microstructure. Materials inspired by natural materials (e.g., nacre and bone) can exhibit improved mechanical response thanks to their architecture. Ceramics are fragile so often they are combined with small quantities of polymers to improve their ductility. The properties of bioinspired ceramic structures are better than those expected from the rule of mixtures. Often, microstructure is controlled on multiple length scales to combine benefits from different orders of magnitude.

This thesis is part of the project funded by European Research Council called "FreeCo". Its acronym comes from words "freezing colloids", as the main focus was to obtain sophisticated microstructures thanks to freezing processing. Fabricating materials by freezing allows obtaining well-ordered microstructure on a significant scale, up to a few centimetres.

A previous PhD student, Florian Bouville ¹, has developed a kind of freeze-casting called freezing under flow. In this method slurry is frozen when it flows on a copper plate which is tilted by a few degrees. Thanks to freezing under flow he developed a material called "nacre-like alumina" because its microstructural features mimic those of nacre from abalone shells. The drawback of this freezing method is its sophistication and difficulty in up-scaling it. Freeze casting followed by freeze drying and sintering by field assisted sintering technique (FAST) is complex and time consuming. One of our goals was to simplify fabrication method without compromising ordered microstructure. In case of the successful simplification of the fabrication, next step was to prepare samples of greater dimensions than obtained up to now (pellets of 20 mm diameter and couple of millimetres thick). In addition, we planned to modify interphase between ceramic platelets and/or add another architectural level to further improve mechanical properties.

The first chapter of the manuscript is focused on the state of the art in the field of architected ceramics. Fabrication techniques and characterisation methods are described along some most known obtained materials with their microstructure characteristics and mechanical properties. Some natural materials are described as well, to explain how some microstructural features improve mechanical behaviour of those materials. It leads to the concept of biomimicry and its recent popularity. We describe FAST, as the choice of sintering technique is crucial for obtaining satisfactory microstructure.

¹Florian Bouville. *Self-assembly of anisotropic particles driven by ice growth: Mechanisms, applications and bioinspiration*. PhD thesis, 2013

In the second chapter, all technical details of elaboration and characterisation of materials are given. There is a comprehensive description of each step of sample fabrication, preparation for testing (both microstructural and mechanical) and testing methods with all necessary calculations.

The third chapter is dedicated to the two of our goals: simplifying and up-scaling fabrication of nacre-like alumina developed by Florian Bouville during his thesis. In this part of the manuscript we compare freeze casting method with simpler uniaxial pressing. We check if alignment is satisfactory when material is not processed by freezing method. We adjust sintering cycle to greater quantity of ceramic powder.

In the fourth chapter, three modifications of the interphase between alumina platelets are proposed: the addition of zirconia nano-powder, the deposition of zirconia directly on platelets and the modification of the glassy phase by the addition of graphene. All composites were characterised by scanning electron microscopy (SEM) and four point bending (4PB) on notched bars and compared with reference material.

In the last chapter alumina/titanium composites are described. First part is focused on the description of the fabrication and of the multilevel structure of the composites. Different types of titanium foils were used. The chapter provides detailed analysis of structure, chemistry, crystallography and metal diffusion. Second part resumes mechanical testing *ex situ* and *in situ*. It not only provides the information on the values of mechanical properties but also toughening mechanisms in both ceramic reference material and alumina/titanium composite.

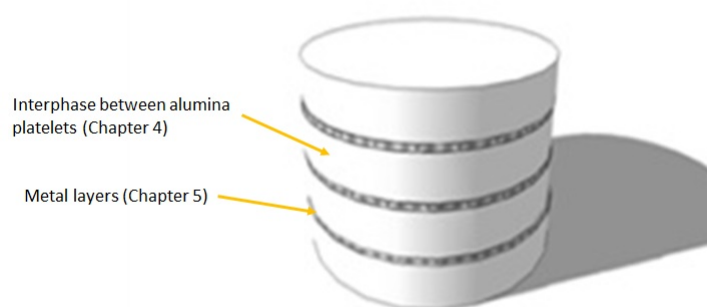


Figure 1: A schematic presentation of material constituents discussed in chapters four and five.

At the end of the thesis general conclusions are given to summarise different parts of the project and their outcomes.

Quidquid latine dictum sit,
altum videtur

Anonym

Chapter 1

Literature review

1.1 Properties of natural and bioinspired materials

1.1.1 Natural materials

As it has been known for a long time, numerous natural materials, such as abalone nacre, crab exoskeleton, turtle shell and armadillo shell to mention the most studied, present extraordinary properties in terms of mechanical performance, extending significantly values predicted from a rule of mixtures of the properties of their compounds [25].

They owe it to multiple structural levels and sophisticated architectures which are unfortunately exceptionally difficult to replicate in synthetic materials.

One of the natural materials which exhibits a very sophisticated structure and toughening mechanisms is human bone (fig. 1.1). Hierarchy of bone contains seven levels. At macro-scale it is arrangement of bone tissue: compact (at the surface) and spongy (inner part). Lamellar osteons build the compact bone and protect blood vessels. Lamellae are composed of fibers arranged in various patterns. Fibril arrays create those fibers. Mineralized collagen fibrils are elementary constituents of human bone. Three chains of amino acids create tropocollagen which is a segment of collagen fibril.

As visible in the figure 1.1 even the smallest building blocks of bone contribute to its toughening mechanisms. In collagen elongation of the structure occurs and then rupture of hydrogen bonds. Between molecules of tropocollagen sliding and rupture of bonds happen. In mineralized collagen micro-cracking occurs. At larger scales one observes breakage of sacrificial bonds, more collagen fibril and uncracked-ligament bridging and in the end crack deflection by osteons. Those numerous toughening mechanisms provoke increase of fracture resistance after crack offset, as it propagates. This phenomena is called R-curve behaviour. Fig. 1.2 illustrates crack-resistant curve of hydrated human cortical bone. It is immediately visible that it is highly anisotropic material. ESEM marks samples tested *in situ* in environmental scanning

1.1. PROPERTIES OF NATURAL AND BIOINSPIRED MATERIALS

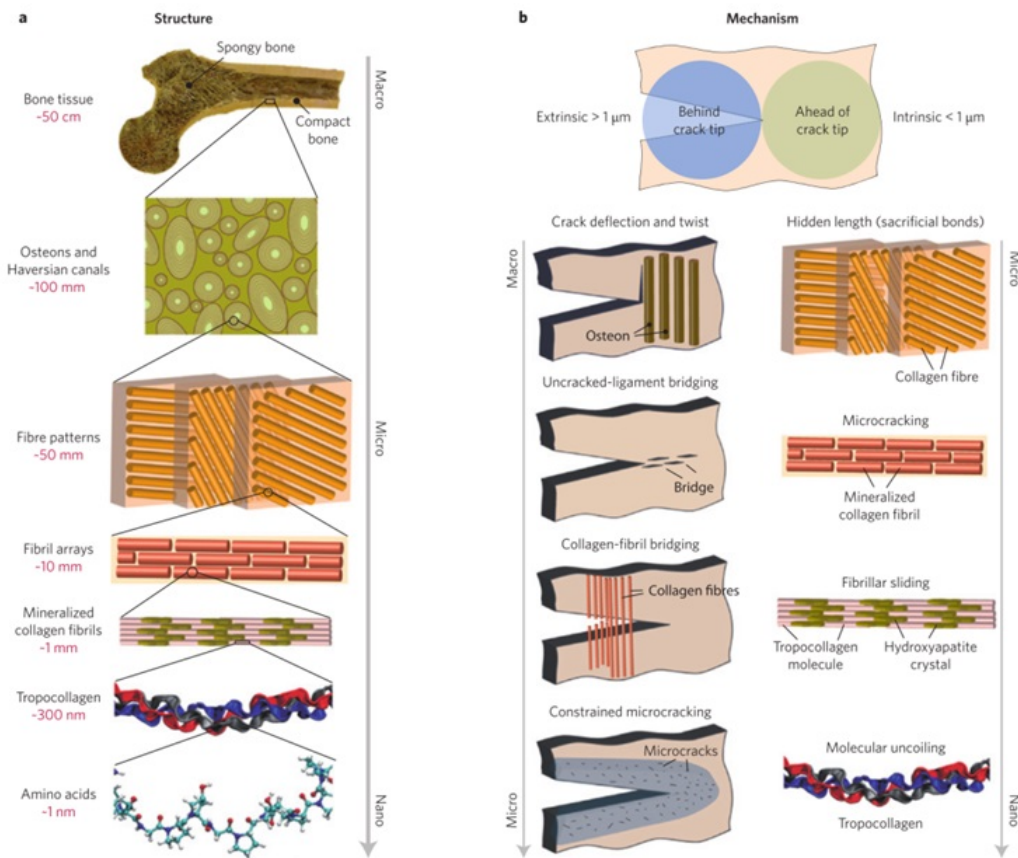


Figure 1.1: Structure and toughening mechanisms on multiple structural levels (from nano to macro-scale) which improve mechanical properties of natural material: bone [1]

electron microscope, HBSS samples tested *ex situ* immersed in Hank's Balanced Salt Solution, for each samples loading displacement rates are given.

For transverse samples failure occurred through breaking of bone structure while for longitudinal samples it happened through splitting. Main toughening mechanisms for first orientation were crack deflection and twist while for the second one it was crack bridging [1][2]. In fig. 1.3 a schematic of two types of R-curves (flat and rising) is presented.

In case of materials with flat R-curve there is one value of fracture toughness and initial crack size is equal to critical crack size; stable crack propagation does not occur. Material with rising R-curve is not characterized by one value of fracture toughness but it evolves as crack advances. Critical crack size is greater than initial crack size [3].

Another natural material which exhibits remarkable mechanical properties is nacre. Nacre also called mother of pearl is produced by some molluscs as an inner shell layer. It has a hierarchical structure and a high ceramic (aragonite $CaCO_3$) content: over 95% [5]. It became one of the model materials for material scientists. In order to understand toughening mechanisms of nacre, Espinosa et al. performed a tensile test under optical microscope[5]. Fig. 1.4 shows nacre and elements of its

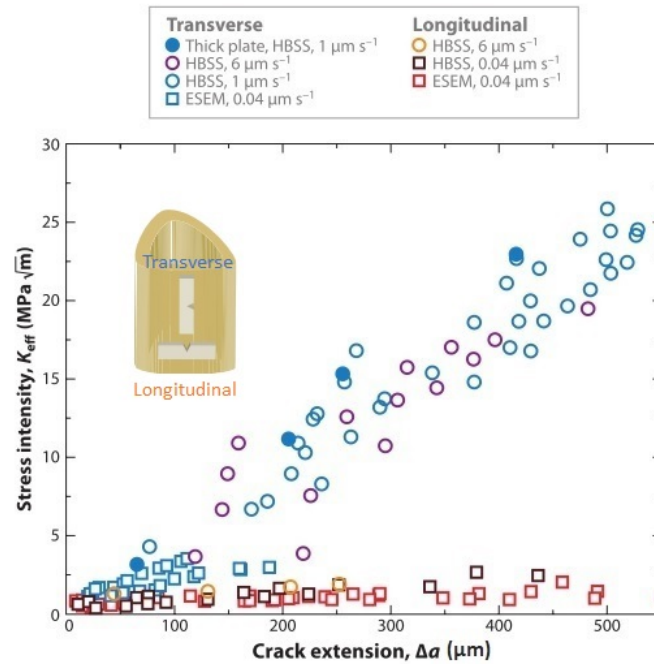


Figure 1.2: Crack-resistant curves (R-curves) of human bone tested in two directions: transverse and longitudinal [2]

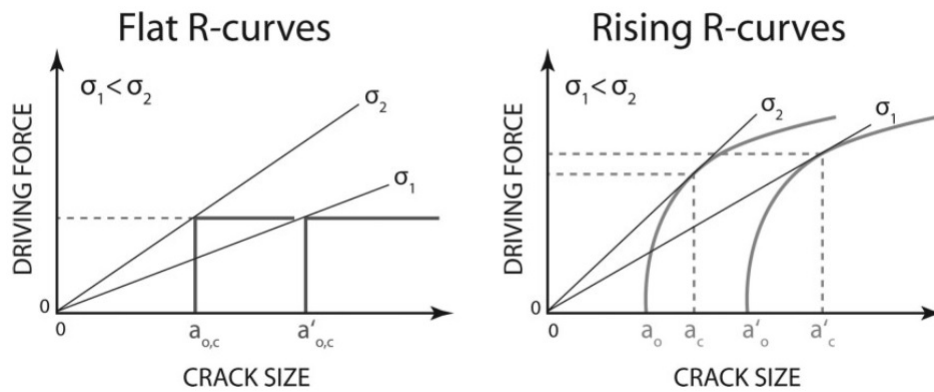


Figure 1.3: Schematic illustrations of crack-resistance curves (R-curves) [3]

micro-structure which are responsible for nacre’s toughening mechanisms.

Pictures of progressing crack can be taken at every stage of the test until failure. The specimen was 20 mm long, 0.6 mm thick and around 1.5 mm wide. Although the thickness might seem small, it contained about 3000 layers of platelets. Some specimens were tested in hydrated state, the rest was dried before the measurement. 400 N cell was used and samples were loaded at 0.001 s^{-1} strain rate, up to failure. The experimental set-up used for those measurements is presented in the fig. 1.5.

Fig. 1.6 presents values obtained in this study. Dry nacre behaves like a monolithic ceramic with a linear elastic behaviour and a failure in a brittle manner. It resembles pure aragonite, also plotted in the figure.

1.1. PROPERTIES OF NATURAL AND BIOINSPIRED MATERIALS

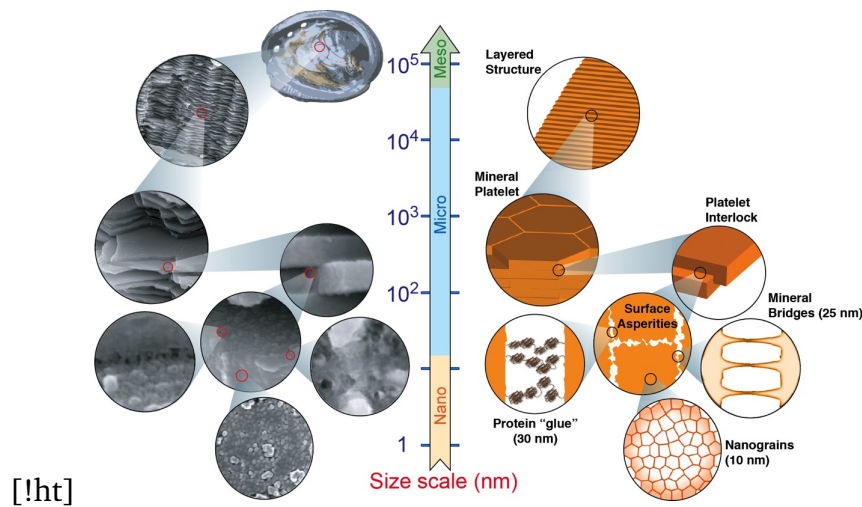


Figure 1.4: The structure of nacre: aligned aragonite tablets (diameter approximately $8 \mu\text{m}$ and thickness $0.4 \mu\text{m}$) and thin organic interphase [4]

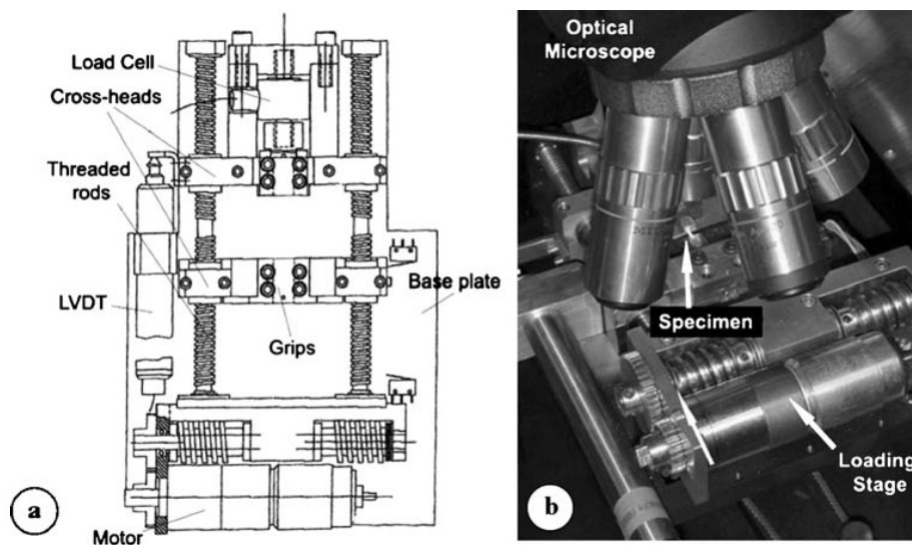


Figure 1.5: Experimental set-up for tensile test under an optical microscope [5]

Failure stress for dry samples was between 95 and 135 MPa. Young's modulus has a value of approximately 90 GPa. Hydrated samples responded differently. In the beginning they behaved in a linear elastic way, but at 70 MPa large strain began to be visible and strain at failure was significantly higher for hydrated material than for the dry one. Young's modulus was about 80 GPa. It was observed that the Young's modulus decreases when tablets start to slide. It is probably caused by less efficient transfer of load between platelets [5].

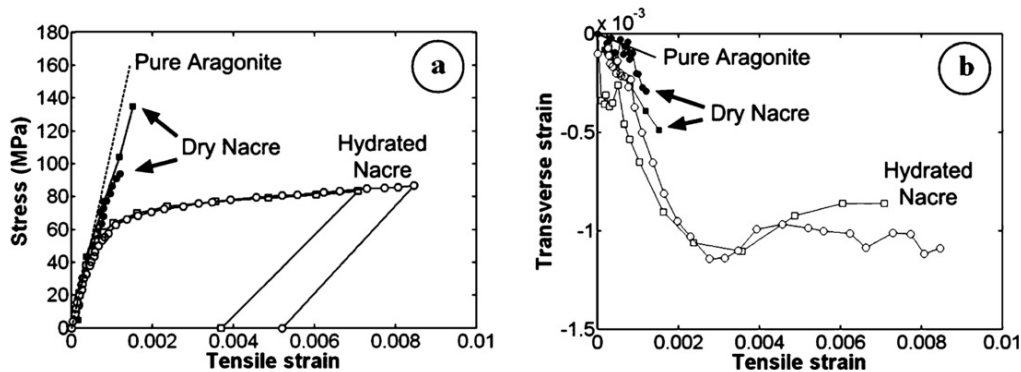


Figure 1.6: Values of tensile strain obtained during measurements [5]

Specific mechanisms stand behind relatively large deformations of nacre. At first, tensile stresses are transferred from one column of platelets to another via shear stress in the regions of overlapping. Once the shear strength of the interphase is reached, the sliding between tablets begin, leading to non-linearity in the stress-strain curve.

In another publication, bending tests are performed at an even smaller scale [6]. Authors quantified tablet sliding with nanometer precision by carrying out *in situ* fracture experiments with atomic force microscopy (AFM), combined with digital image correlation (DIC) to analyze the kinematic displacement field. Results for one representative sample are shown in Fig. 1.7.

In fig. 1.7, the first line represents the location of the scanned area (marked as SA) below the tip of the notch (scale bar is $100\mu\text{m}$). In the second line there are AFM pictures of the SA before (*e*), during loading (*f,g*) and after failure (*h*). Arrows show direction of platelets sliding and scale bar is 500 nm . The third row of figure combines AFM pictures and DIC analysis. Colours indicate longitudinal displacements fields of platelets (colour code on the left). When the color is more intense it means that sliding was progressing. After crack passing some reversal of the sliding was observed. Fig. 1.7*m* is a relative longitudinal tablet displacement along the purple line from the figure 1.7*i*, three coloured lines correspond to loading states from figure *j-l*. In fig. 1.7*n* transverse displacement at loading state from picture 1.7*k* is plotted (along dashed yellow line from picture 1.7*l*). Figure above illustrates the phenomena of platelets sliding during bending test which helps to understand this toughening mechanism in natural material.

Test in AFM allowed to quantify the sliding between platelets and identify toughening mechanisms like crack bridging and deflection (present in bone as well). Waviness and some roughness of platelet's surface hinder the sliding. Described tests can be used as a reference for any further testing of architected, hierarchical and biomimetic materials.

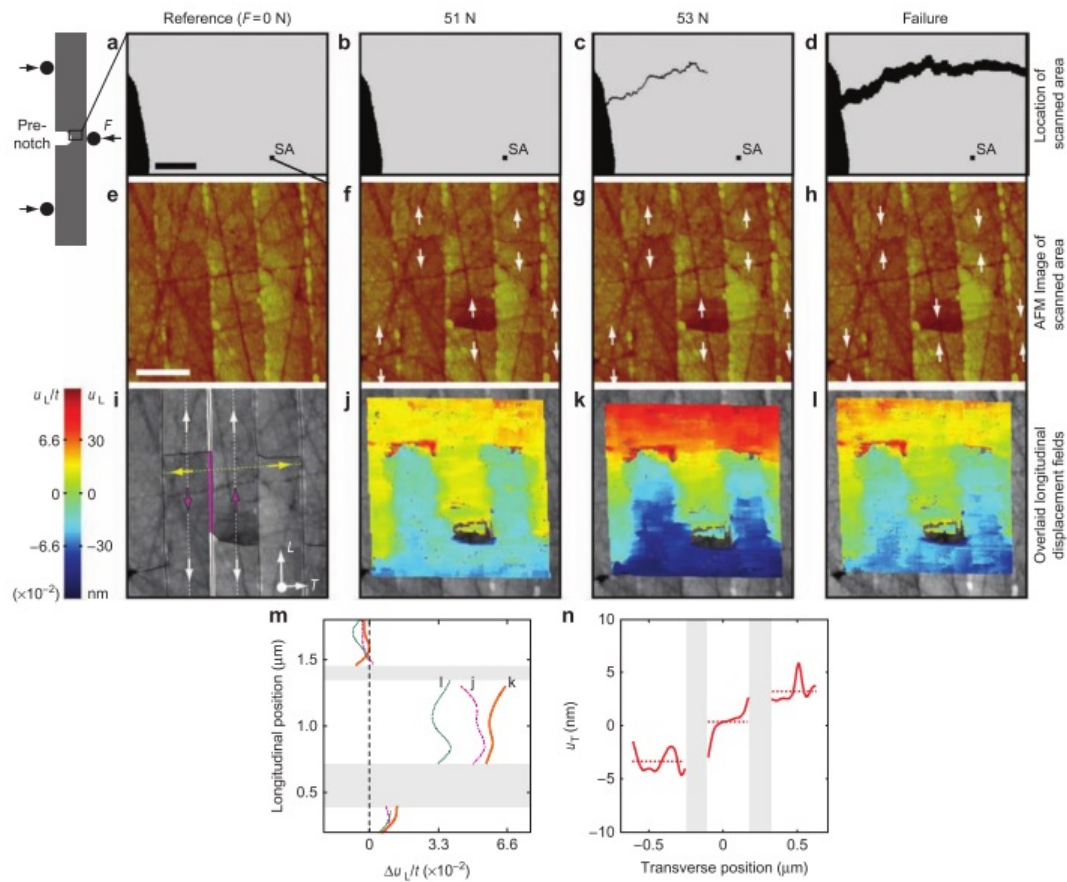


Figure 1.7: Fracture tests (3 point bending on notched samples) performed on natural nacre in AFM, combined with quantitative analysis of tablet sliding [6]

1.1.2 Bioinspired materials

Many researchers focus on mimicking natural structures to obtain materials that combine properties which until now were believed to be mutually exclusive, such as strength and toughness.

Deville et al. have developed biomimetic materials which can serve as scaffolds for bone regeneration [26]. They have chosen a two-step approach: ice-templating followed by infiltration. Porous hydroxyapatite scaffolds (obtained during the first processing step by ice-templating) were infiltrated with biodegradable organic phase to allow bone ingrowth. This way they have fabricated scaffolds with mechanical properties matching those of compact bone: stiffness 10 GPa, strength 150 MPa and work of fracture 220 J/m^2 [26].

Launey et al. have mimicked some of nacre natural features by creating a composite from aluminum oxide and polymethyl methacrylate by ice-templating. Obtained bulk materials reveal yield strength around 200 MPa and fracture toughness about $30 \text{ MPa} \cdot \text{m}^{1/2}$. As in natural materials, their microstructure is anisotropic [27]. In the direction perpendicular to the lamellae flexural strength reaches 120 MPa for lamellae and up to 210 MPa for brick and mortar structure in the composite consist-

ing of 80% alumina. Fracture toughness (K_{Ic}) value is almost doubled with respect to the prediction from the rule of mixtures for Al_2O_3 and PMMA [7]. For lamellae it is equal to $15 MPa \cdot m^{1/2}$ and for brick and mortar $30 MPa \cdot m^{1/2}$. Those materials represent characteristic R-curve behavior: their fracture resistance increases as the crack propagates. Additional test in-situ in electron microscope revealed that toughening mechanisms are present at several architectural levels [28]. Fig. 1.8 illustrates the difference in fracture toughness values for two types of micro-structure of bioinspired material: lamellar and "brick and mortar". Fig. 1.8a presents "brick and mortar" structure and fig. 1.8b lamellar structure. Lamellar structure is aligned over several centimetres, between lamellae (bright grey) polymer (PMMA, dark grey) was infiltrated. In "brick and mortar" structure alumina building blocks are separated by thin (less than a micrometer) layers of polymer. If high content of ceramic is required, "brick and mortar" structure seems suitable.

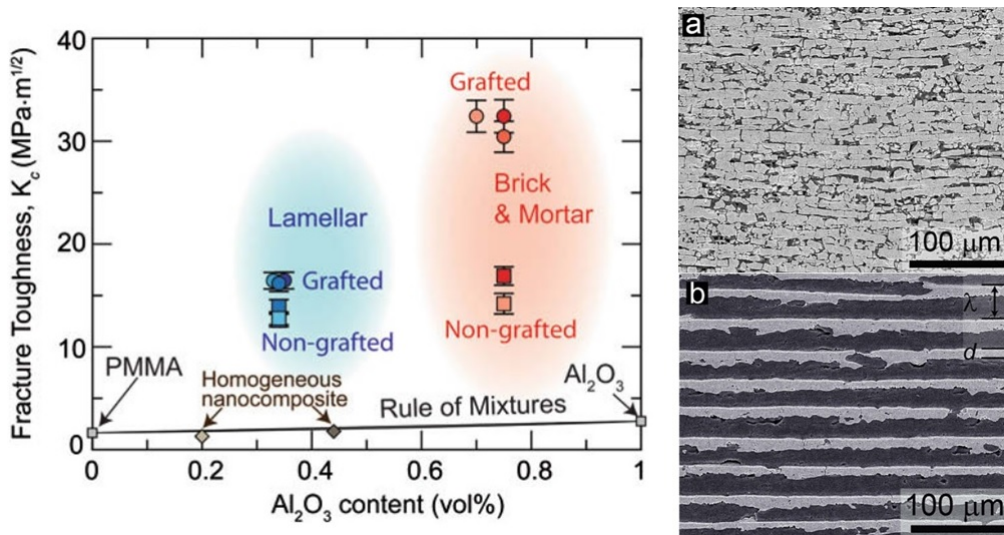


Figure 1.8: On the left: comparison of fracture toughness in alumina composites with two types of microstructure: lamellar and "brick and mortar" [7]. On the right: SEM picture of "brick and mortar" structure (a) and lamellar structure (b).

Begley et al. explained well the underlying concept of brick and mortar composites [29]. Maintaining low volume fraction (several percent) of the compliant ductile phase permits to keep high stiffness of a composite. Using ceramic bricks of small volume combined with thin layers of mortar helps to achieve high strength of a material. Loads can be concentrated onto interlocking bricks via shear transfer. Brick pull out and microcracking promote ductility [29]. Brick and mortar composites exhibit high strength thanks to the ceramic phase. Increased toughness is due to some limited sliding between the bricks which helps to dissipate local stress concentrations. In case of synthetic materials the problem lays in finding a way to raise toughness without significantly lowering their strength. Wilbrink et al. developed and uniaxial model to associate scaling relationships between component properties with global strength and work of failure in the composite [8]. Fig. 1.9 illustrates analysed composite and unit cell used for analysis.

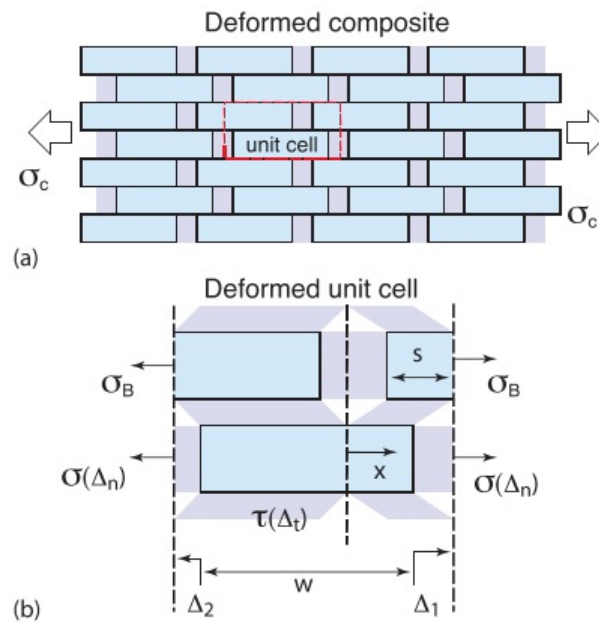


Figure 1.9: Scheme of a) the analysed composite and b) the single unit cell for the analysis [8]

Results obtained by Wilbrink et al. [8] suggest that an optimal mortar thickness exists. It should be big enough to provide effective load transfer. On the other hand it cannot be too large because it would lead to brick failure because of the additive effect of shear and normal stresses [8].

Materials presented above apart from ceramics contained ductile organic phase. Florian Bouville et al. developed a bioinspired material composed entirely of ceramic called nacre-like alumina [9]. Its advantage in comparison with other materials is that it can be used at elevated temperatures, up to 600°C or more. Fig. 1.10 presents mechanical properties (flexural strength and fracture toughness) of nacre-like alumina developed by Florian Bouville compared to conventional composites [9]. In case of traditional materials the conflict of properties is clearly visible but new bioinspired material overcomes this limitation.

Fig. 1.11 shows details of the composition of the microstructure of nacre-like alumina. This complicated architecture of the material allowed to obtain improved mechanical properties. Alumina platelets mimic building blocks of nacre. Alumina nano-particles allow better sintering of the material and imitate roughness present in natural material. A glassy phase creates an interphase between the platelets.

Work presented in this thesis was built upon material developed by Florian Bouville and focused on introducing new architectural levels and new toughening mechanisms.

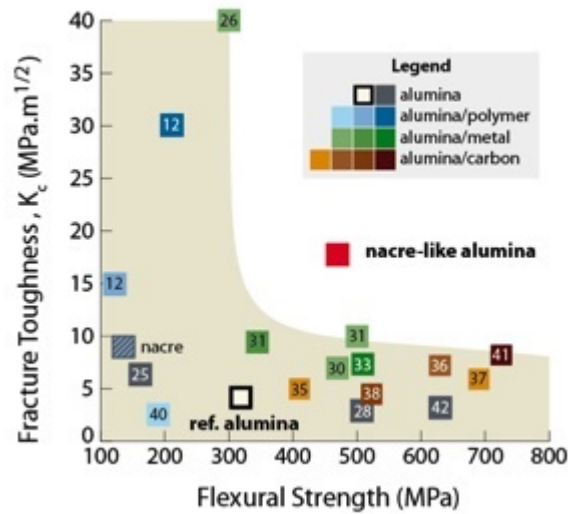


Figure 1.10: Improved mechanical properties of biomimetic nacre-like alumina in comparison to conventional composites of alumina [9]

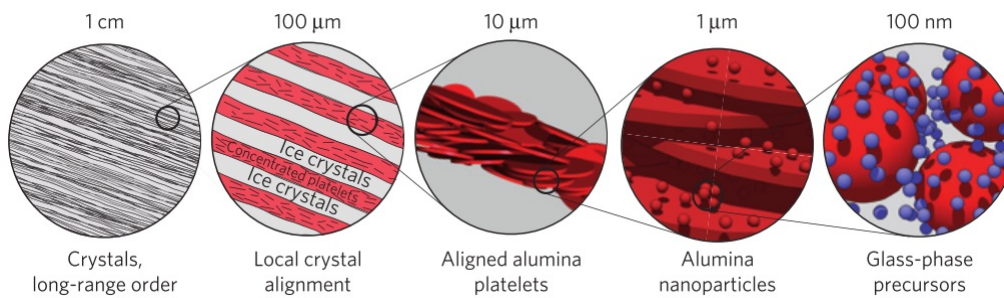


Figure 1.11: Microstructural composition of nacre-like alumina [9]

1.2 Fabrication of materials with controlled micro-structure at multiple length scales

A deep control over the material architecture at multiple levels is required in order to produce a bioinspired material. The process should permit to control layer thickness, roughness, adhesion between components, it should enable to change constituents and be relatively simple at the same time. It should also be possible to upscale it [26]. There are two possible approaches to control the arrangement at micro- and nano- scale: bottom-up and top-down. First of those occurs in nature and scientists try to mimic it through sequential deposition methods [30] which unfortunately are limited to creating thin films at the laboratory scale and not a bulk material. Biomineralization was also recognized as a technique which could provide a material with microstructure controlled on multiple scales but it proved to be extremely complicated to transfer it to the material processing domain [31] [32]. Second approach (top-down) brings difficulties in controlling multiple hierarchical

1.2. FABRICATION OF MATERIALS WITH CONTROLLED MICRO-STRUCTURE AT MULTIPLE LENGTH SCALES

levels. Several groups have obtained ceramic/polymer composites which reproduce some of nacre characteristics. They used techniques such as magnetic particle alignment [33] or gluing ceramic layers together [34] obtaining relatively good results in terms of controlled microstructure [28]. In the process which uses magnetic fields to align platelets, polyurethane is used as a matrix [35]. To obtain the highest toughness values it is required to use about 20 vol.% of organic ductile phase which limits application of the material to temperatures in range of 200°C.

Presently there are no satisfying processing techniques which would make it possible to fabricate multilayered, hierarchical architectures at industrial scale, processing those materials is restricted to small amounts. A design of those bone-like and nacre-like materials is focused on incorporating numerous toughening mechanisms present at all scales (from nanometers to millimeters)[3]. Creating processing route on an at least centimeter scale for bioinspired structures is a significant challenge for engineers in material science [3]. The development of ice-templating technique has brought a significant progress to this field [26]. Various structures with high ceramic content can be obtained using the common phenomenon of freezing of colloids. They consist of hard ceramic lamellae (bricks) and thin (thickness in range of microns) polymeric layers (mortar) which add ductility to the final material [28].

Freezing of water is a phenomenon which drawn attention of scientists long time ago. They mainly focused on pure water and diluted suspensions [36] [37]. This physical process commonly occurring in nature plays significant role in industry (like elimination of pollutants [38]) and medicine (for example cryopreservation of biological material [39]) as well.

Freezing turned out to be useful as ceramic material processing technique known as freeze casting or ice templating.

Fig. 1.12 shows the main processing steps in this method: unidirectional freezing of ceramic slurry (ceramic particles are being repelled by advancing solidification front and thus concentrated between crystals of ice, fig. 1.12b), sublimation of the solidified phase (fig. 1.12c) and densification of lamellae through sintering (fig. 1.12d) [10]. Considering that freeze casting technique allows using diverse materials it might be concluded that physical interactions, not chemical ones, play the major role on suspension stability [40].

Studies have provided some crucial pieces of information. One of them is that particles of size greater than a critical value will get entrapped by the progressing ice front. The other fact is that ice does not always grow in all directions with the same speed, if conditions are under control it is possible to obtain ice with lamellar microstructure and in result a material with anisotropical properties. Wall thickness is strongly dependent on speed of ice front or temperature gradient [26].

The first step of material processing by freeze casting is preparation of ceramic slurry. Dispersants are frequently used as a good dispersion of particles in solvent is intended. The amount of porosity in the final materials can be adjusted by the solid loading, usually in 10-40 vol.% range. To avoid segregation of particles, which might

1.2. FABRICATION OF MATERIALS WITH CONTROLLED MICRO-STRUCTURE AT MULTIPLE LENGTH SCALES

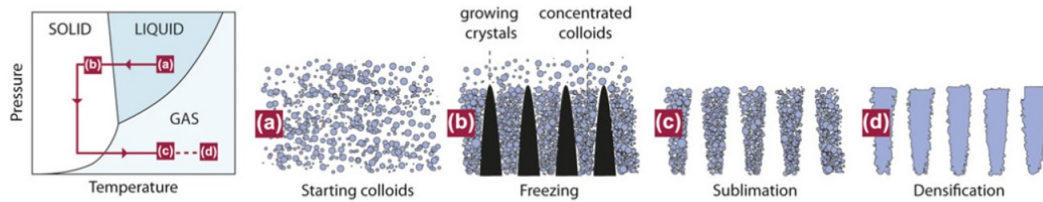


Figure 1.12: Schematic diagram of the ice-templating principles. [10]

cause gradient in density and properties of final materials, appropriate stability of the suspension should be provided. When water is used as a solvent the slurry might be prepared in room temperature. For other solvents, like camphene or tert-butyl alcohol, temperature must be adjusted to the range of temperatures where they are liquid. An organic binder is also needed, otherwise after sublimation of solvent the green body collapses [40].

Freezing is the core of the process and a stage that determines pore characteristics of the green body. The freezing solvent creates continuous crystals. Simultaneously ceramic particles are rejected by advancing ice fronts and compressed together between the crystals. The direction of solidification can be controlled by placing slurry in a mould, subsequently placed on a freezing plate, cold finger, or directly in a freezing media. The choice of the solvent determines the range of temperatures required for solidification, for water below 0°C and for camphene about $44\text{--}48^{\circ}\text{C}$ for instance. During freezing, the solvent changes its volume: water expands, while camphene shrinks. This phenomenon should be taken into account during preparing moulds and determining the amount of slurry poured into them [40].

Some of the processing parameters can be tuned in order to modify properties of obtained material. Placing ceramic slurry on cooling plate or cold finger with controlled cooling rate provides control of the speed of ice front which affects the thickness of ceramic walls. The structure obtained after sintering is porous and pores have the same shape as ice crystals [40]. Fig. 1.13 illustrates the impact of ice front velocity on lamellae thickness. Samples were prepared from powders with grain size of about $0,3\ \mu\text{m}$ [26].

If platelets are used instead of spherical particles, they can be aligned by advancing ice front as demonstrated in the fig. 1.14 [11].

The next step after the solidification of the slurry is the removal of the solvent through sublimation. For water, it is needed to stay below triple point of the solvent: low temperature of approximately -80°C and low pressure are required. Depending on physical properties of solvent, sublimation conditions might be different. For water, a standard freeze dryer is sufficient. For camphene, room temperature and a pressure of $1,3\ \text{kPa}$ is enough to provoke sublimation. After the solvent is transformed into gas we obtain a green body with pores being replicas of crystals [40].

After sublimation of the solvent, the last processing step is needed: densification of ceramic walls. Green body has a low strength, the use of pressure during sintering is not compulsory. Binder burnout is usually not required as slurries usually contain less than 5% of the organic component. The aim of sintering is to consolidate the structure [40]. Obtain material is porous but sometimes it is desired to eliminate

1.2. FABRICATION OF MATERIALS WITH CONTROLLED MICRO-STRUCTURE AT MULTIPLE LENGTH SCALES

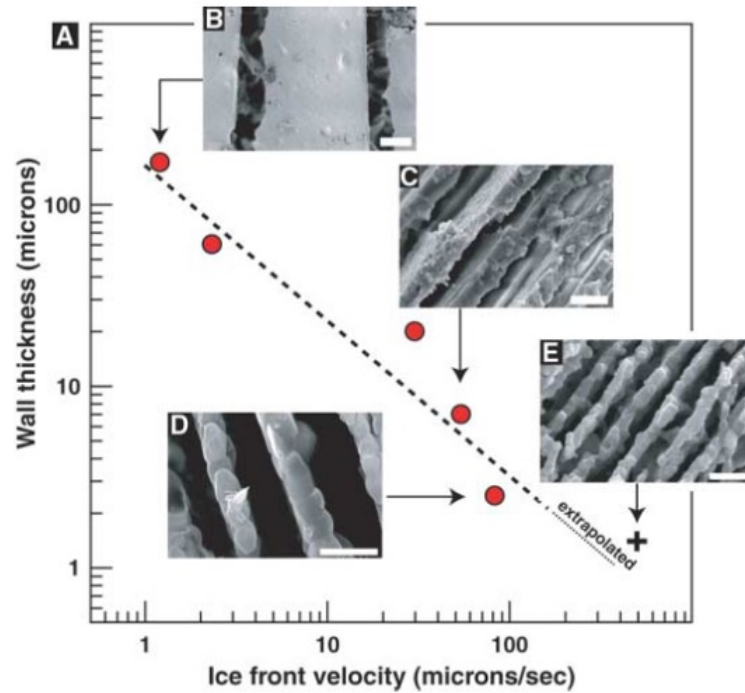


Figure 1.13: (A) Thickness of the lamellae in alumina samples as a function of the speed of the solidification front. The scanning electron micrographs shown in the graph correspond to cross sections parallel to the direction of movement of the ice front. Sample (E) was obtained with ultrafast freezing to gauge the thickness limit achievable by this technique. Scale bars indicate (B) 50 mm, (C) 10 mm, (D) 5 mm, (E) 5 mm. [26]

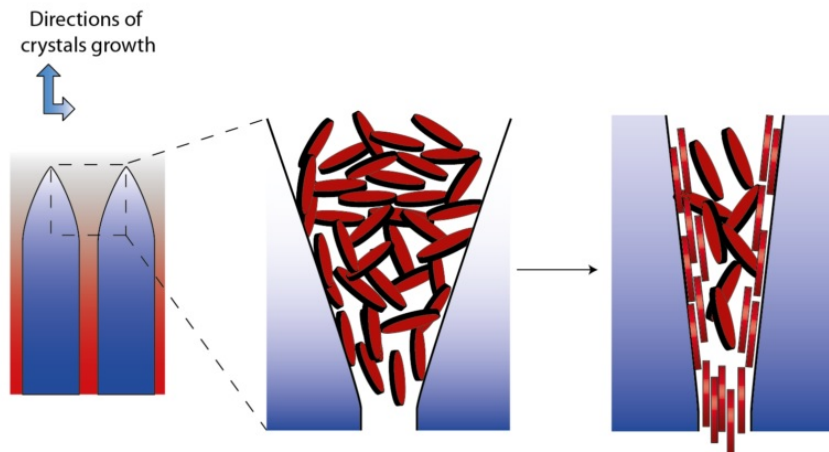


Figure 1.14: Scheme of mechanism of platelets alignment by advancing ice crystals [11]

the porosity to obtain a fully dense material. In such case sintering techniques with pressure, like field assisted sintering technique (FAST), might be applied [12].

The final structure of the material is influenced by all the processing stages mentioned above, but concerning the final porosity, solidification is the most critical one. To form the intended porosity during freezing, some requirements must be fulfilled:

rejection of particles by the advancing ice front, particles redistribution and trapping of particles between crystals of solidified solvent. This will determine the architecture of pores [40].

Preparing material by freeze casting permits to modify some processing parameters. It gives possibility to investigate influence of particular agents (amount or kind of interphase between ceramic particles for instance) on final properties. The main limitation is assessing, how difficult scale-up will be.

Obtaining porous materials by freeze-casting gives possibility of infiltrating the ceramic matrix by another phase, metal for example. Launey et al. [41] have fabricated alumina matrix by freeze-casting and after sintering infiltrated it by molten Al/Si eutectic alloy. The choice of metal was dictated by its relatively low melting point and its viscosity enabling easier infiltration. Infiltration was conducted at 900°C and pressure introduced by argon reaching 70 kPa [41]. Roy et al. [42],[43] have also chosen Al/Si alloy to infiltrate the ceramic preforms. They applied a temperature of 800°C before performing squeeze-casting of metal phase [42],[43].

Based on a literature, it seems that the choice of metal possible to infiltrate is limited by melting temperature and viscosity. In case of metal with elevated melting points it would be necessary to adapt all the elements of the set-up which are subjected to high temperatures. What is more, the fabrication itself is quite long and sophisticated as it requires fabrication of ceramic preforms, sintering them and then infiltrating by metal. As one of the goals of this thesis is to simplify materials preparation, this method is not appropriate.

1.3 Field assisted sintering techniques

Sintering is a common method of material consolidation through a thermal treatment. It is accomplished at high temperatures, without reaching a melting point. Natural sintering uses high temperature to consolidate material particles but leaves macro-porosity. In order to improve this process other means of activation have been explored. As a result new sintering techniques which use pressure and electric current were developed. They allow to consolidate materials at lower temperatures and in significantly shorter time. There are several terms which refer to those techniques: spark plasma sintering (SPS), pulsed electric current sintering (PECS), field-activated sintering technique (FAST), or current-activated pressure-assisted densification [12].

Essentially powders consolidated by FAST simultaneously undergo elevated temperatures, an electric current, and a uniaxial pressure. Thanks to the combination of those actions the processing time is significantly shorter.

The main difference between hot pressing (application of elevated temperature and pressure) and FAST is the presence of the current. It provides the heat and extreme rise of heating rate. A Fig. 1.15 below represents schematic view of PECS device.

One of the terms used to describe sintering using electric current is spark plasma sintering. Many have claimed that pulsing of current can create plasma which can

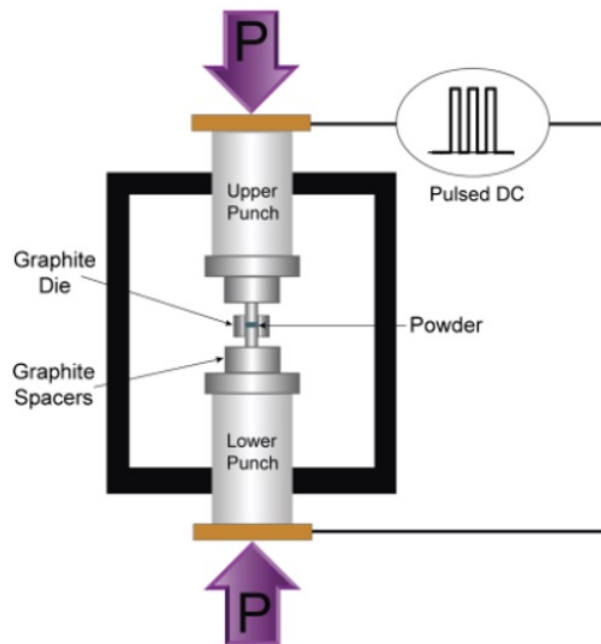


Figure 1.15: Schematic of a pulsed electric current sintering apparatus. [12]

activate particle surface of sintered powder through removing surface layers, like for example oxides. It has been a source of controversy as researchers could not prove the presence of a plasma. Contrary points of view were present in publications [44] [45]. Presently most researchers agree that evidence pointing to the lack of plasma during FAST is more convincing [12].

In recent years there has been visible a significant increase in using PECS to consolidate powders. There are two main reasons for such a tendency. First, in comparison with conventional sintering techniques, materials sintered under action of electric current represent intrinsic advantages such as limited grain growth [12], lack of undesirable phase transformation. Second, it was observed that in case of PECS, materials are characterized by better mechanical performance because of smaller grain size and limited amount of impurities [12].

Apart from better properties, a processing step is significantly shorter than for instance hot pressing. According to Perera et al. to obtain fully dense Si_3N_4 with conventional sintering and hot isostatic pressing (HIP) an over 100 minutes long dwell time was required while for FAST it was only 5 minutes [13]. Fig. 1.16 illustrates differences in values of porosity in function of temperature.

Sintering at lower temperatures and for shorter times brings other benefits:

- limited loss of material through vaporization [46] [47] [48] [49] [50],
- less frequent undesirable phase transformation [51].

Sintering material by PECS leads to finer micro-structure, lower porosity and removal of impurities from particles surface. Thanks to those characteristics numerous properties are improved:

- smaller amount of impurities and limited their segregation in grain boundaries [52] [53],

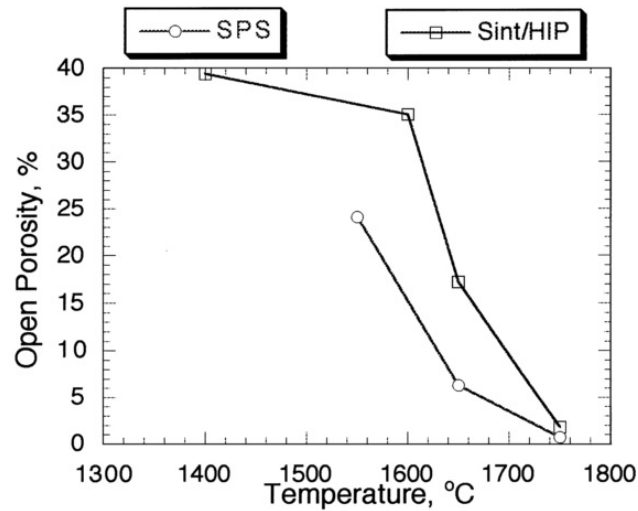


Figure 1.16: Comparison of percentage of open porosity in ceramics sintered by FAST and sintered naturally with HIP step at different temperatures [13]

- significantly increased superplasticity of ceramic materials [53] [54],
- in case of ferroelectrics, higher permittivity [55],
- better magnetic properties [56],
- increased chemical stability [57],
- in BCC metallic solutions better hydrogen storage capacity [58],
- improvement of thermoelectric properties [59] [60],
- better mechanical performance [61],
- better optical properties [12] [62].

The three parameters most commonly related with FAST process are current, applied pressure and heating rate. The sintering temperature and current are related due to the occurrence of the Joule effect, which provokes thermal activation. Usually, to apply a DC pulsed current a low voltage of approximately 10V is used. A sequence of pulses with and without current creates a pulsing pattern. One pulse typically takes 3,3 ms [12]. Although current is mostly associated with Joule heating it plays also a role in mass transport [12].

According to Nagae et al. there is a difference of electrical resistivity of samples prepared from aluminum powder prepared by FAST and hot pressing. In the first case, the materials were less resistant, probably because the DC current destroyed a layer of oxide at the contact points of the particles surface [63].

Another difference between FAST and hot pressing is the **heating rate**. Due to the different natures of heating processes in FAST we can achieve heating rates as high as 2000°C/min. Increase in heating rate helps to limit nondensifying (grain coarsening) sintering mechanisms, like surface diffusion. In case of nonelectrically conducting materials, thermal gradients might be present and create additional driving force for sintering [12] [64] [65].

There are some doubts and controversies regarding the influence of heating rate on the final materials. Experimental observations do not always correspond to theo-

retical expectations or simulations [66]. When analyzing the case of alumina, different studies provide different conclusions. In one case it was stated that variation in heating rate between 50 and 700°C/min did not affect the final density [67] while another study reported a negative effect, density decreases with increase of the heating rate to over 350°C/min [68]. In both studies, higher heating rates led to smaller grains. Recent studies provided similar conclusions for alumina [69] and cubic zirconia [59].

The final main factor, playing a crucial role in sintering materials, especially nanopowders, is the applied **uniaxial pressure**. Up until recently it was limited by mechanical properties of the graphite die, which gave an upper limit of approximately 140 MPa, or less. Due to recent development in area of FAST, some modifications were incorporated which allow to apply pressure up to 1 GPa [12] [70].

To sum up, sintering techniques which use a current are a powerful group of methods of consolidating powders. They permit to obtain nanostructured materials which presently are in the spotlight of material science world. In the near future we can expect even more improvements of not only the equipment, but also simulation methods, which allow to better understand and control the mechanisms that occur during sintering.

1.4 Titanium and its composites with ceramics

As mentioned in the introduction, our objective is to further increase the toughness of bioinspired ceramics. Architected ceramics can exhibit increased strain at failure (not true ductility) but more direct way to enhance toughness is to add some metal. To avoid complicating the fabrication process, it is suitable to chose an element with melting point high enough to sinter it with alumina during single processing step.

1.4.1 Characteristics of titanium

As shown in fig. 1.17 melting temperature of titanium equal to 1670°C makes it a suitable candidate to incorporate into ceramic matrix.

Pure titanium undergoes a phase change from hexagonal to body centered cubic at 882°C. Its two basic unit cells are shown in fig. 1.18. It also illustrates lattice planes which are most densely packed [14].

The α -phase with hexagonal structure has intrinsically anisotropic character. It means that its elastic properties change depending on the stress axis related to c-axis of the cristal [71]. When stress is parallel to c-axis modulus of elasticity E reaches 145 GPa and it decreases to 100 GPa for angle of 90°. Shear modulus G changes with angle as well; from 46 GPa to 34 GPa, respectively [71].

Correlation between mechanical properties of titanium and temperature has been recorded: both E and G decrease when temperature increases [15]. Fig. 1.19 shows that correlation is close to linear. At absolute zero elastic modulus reaches 130 GPa

1.4. TITANIUM AND ITS COMPOSITES WITH CERAMICS

	Ti	Fe	Ni	Al
Melting Temperature (°C)	1670	1538	1455	660
Allotropic Transformation (°C)	β $\xrightarrow{882}$ α	γ $\xrightarrow{912}$ α	-	-
Crystal Structure	bcc \rightarrow hex	fcc \rightarrow bcc	fcc	fcc
Room Temperature E (GPa)	115	215	200	72
Yield Stress Level (MPa)	1000	1000	1000	500
Density (g/cm ³)	4.5	7.9	8.9	2.7
Comparative Corrosion Resistance	Very High	Low	Medium	High
Comparative Reactivity with Oxygen	Very High	Low	Low	High
Comparative Price of Metal	Very High	Low	High	Medium

Figure 1.17: Chosen characteristics of titanium in comparison with other structural metallic materials based on Fe, Ni and Al [14]. Direction of the allotropic transition demonstrated in the table is from high to low temperature.

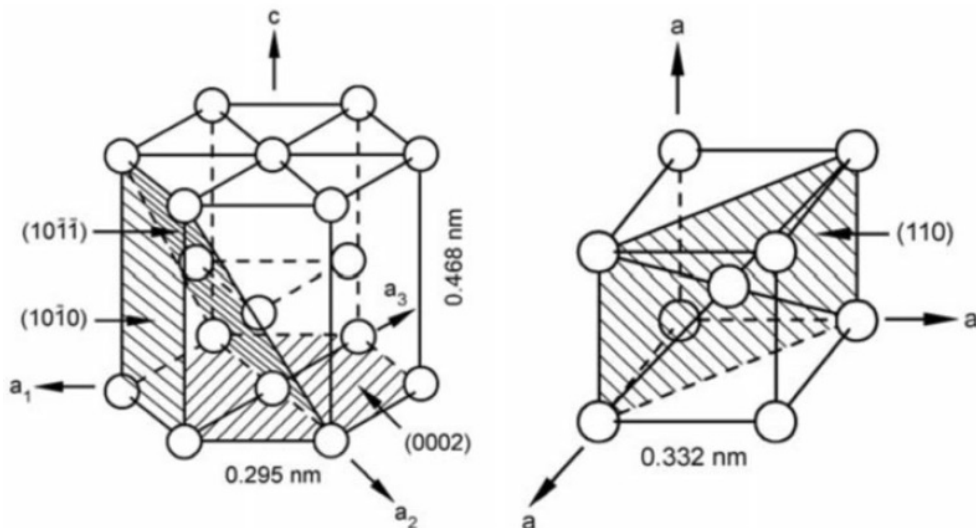


Figure 1.18: Unit cells of α (hcp) and β (bcc) phase of titanium [14]

and shear modulus almost 50 GPa to drop to around 58 GPa and 20 GPa at transition temperature (hcp \rightarrow bcc at 882°C), respectively [15].

Hexagonal titanium owes his ductility not only to slip by dislocations but also to twinning deformation, especially at low temperatures. Most of alloying components of titanium are classified either as α stabilizers or β stabilizers. First ones increase and second ones decrease $\alpha \rightarrow \beta$ transition temperature (882°C for pure Ti). Al, O, N and C fall into the first category. First image in fig. 1.20 illustrates a constant increase of transformation temperature with increase of added element content. Aluminium is an α stabilizer and has a high solubility in both hexagonal and cubic phases. It is thus a commonly used alloying element [14].

In β alloys twinning is limited to single phase state. In β alloys hardened by α particles twinning does not occur. In $\alpha + \beta$ alloys twinning is almost fully suppressed but they are quite ductile thanks to the presence of Ti_3Al precipitates [14].

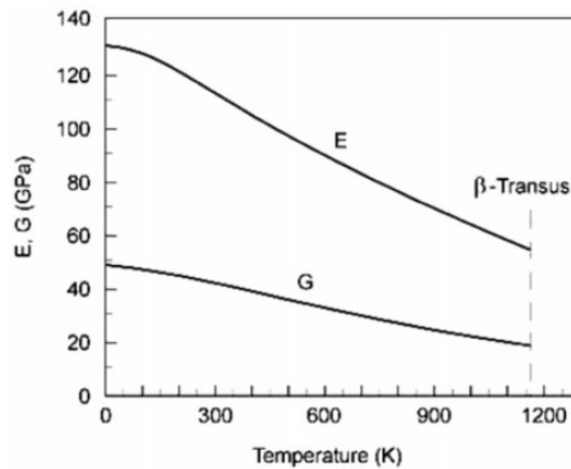


Figure 1.19: Change of value of elastic and shear modulus in function of temperature of α Ti [15]

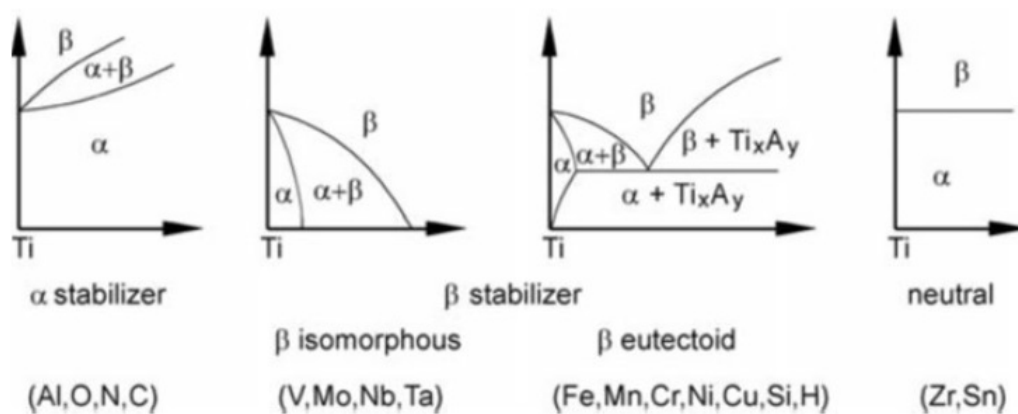


Figure 1.20: Schematic phase diagrams of titanium alloys depending on alloying elements [14]

β stabilizers can be divided into two categories: isomorphous and eutectoid forming. Difference between the phase diagrams for those two categories is illustrated in fig. 1.20. Some widely used β isomorphous elements are V, Mo, Nb or Ta. Right amount of those allows stabilising bcc phase at room temperature. Fe, Cr and Si are commonly used β eutectoid forming elements, others applications are very limited [14]. Fig. 1.21 lists concentration of elements needed to stabilise β phase at RT.

The neutral group (do not change temperature of phase transition) includes elements like zirconium or tin. Zirconium is chemically similar to titanium, isomorphous with it: have same $\alpha \rightarrow \beta$ transition (but not affecting significantly its temperature) and completely soluble in both phases of Ti. It is often used in commercial multi-component alloys. Tin is able to replace aluminum in Ti_3Al (hexagonal phase α_2) [14].

Commercially available titanium alloys can be divided into three groups: α , $\alpha + \beta$ and β (it depends on phase ratio). Table 1.1 shows a table with the most common

1.4. TITANIUM AND ITS COMPOSITES WITH CERAMICS

	V	Nb	Ta	Cr	Mo	W	Mn	Fe	Co	Ni
Wt%	15	36	50	8	10	25	6	4	6	8
At%	14.2	22.5	20.9	7.4	5.2	8	5.3	3.4	4.9	6.6

Figure 1.21: Concentration of elements required to stabilise β phase at room temperature [16]

alloys from each of three categories with their exact compositions and transition temperatures.

Common name	Alloy composition (wt%)	T(°C)
α alloys and CP titanium		
Grade 1	CP-Ti (0.2Fe, 0.18O)	890
Grade 2	CP-Ti (0.3Fe, 0.25O)	915
Grade 3	CP-Ti (0.3Fe, 0.35O)	920
Grade 4	CP-Ti (0.5Fe, 0.40O)	950
Ti-5-2.5	Ti-5Al-2.5Sn	1040
Ti-3-2.5	Ti-3Al-2.5V	935
$\alpha + \beta$ alloys		
Ti-6-4	Ti-6Al-4V (0.20O)	995
Ti-6-4 ELI	Ti-6Al-4V (0.13O)	975
β alloys		
Ti-10-2-3	Ti-10V-2Fe-3Al	800
B120VCA	Ti-13V-11Cr-3Al	700

Table 1.1: Selected commercial titanium alloys from [14]. CP-Ti: commercially pure titanium

Four grades of commercially pure titanium contain some iron to stabilize low amounts of bcc phase and different concentrations of oxygen (0.18% for grade 1 to 0.40% for grade 4) to increase yield stress. Their mechanical properties are listed in table 1.2. With increase of oxygen content in CP titanium, yield and tensile strength increase while elongation decreases [14]. Properties of $\alpha + \beta$ alloys are not listed here as they are strongly dependant on their structure: fully lamellar, fully equiaxed or bi-modal. They do not have one single value for each property but rather its evolution in function of obtained structure [14].

Material	E (GPa)	σ (MPa)	UTS (MPa)	Elong. (%)
Grade 1	105	170	240	24
Grade 2	105	275	345	20
Grade 3	105	380	445	18
Grade 4	105	480	550	15

Table 1.2: Mechanical properties of commercially pure titanium from [14]

A common characteristic of $\alpha + \beta$ alloys is their martensitic transformation from β phase during fast cooling to room temperature. The most well known alloy from this category is Ti6Al4V; its mechanical properties are extremely well balanced (fracture toughness: 65-90 MPa · m^{1/2}, fatigue strength at 10⁷ cycles: 620-725 MPa and

1.4. TITANIUM AND ITS COMPOSITES WITH CERAMICS

modulus of elasticity: 110-114 GPa [72]). The version extra low interstitials of oxygen (ELI) has remarkable damage tolerance and highly elevated fracture toughness (values listed as in Ti6Al4V: 91-92 MPa · m^{1/2}, 598-816 MPa and 101-110 GPa [72]) [14].

Among numerous known alloys of titanium Ti6Al4V is the most commonly used one. It is essential to aerospace industry due to its high specific properties and also widely used in biomedical area because of its biological compatibility [16].

This alloy covers a range of compositions. It can contain between 0.08 wt.% and 0.2 wt.% of oxygen, up to 0.05 wt.% of nitrogen, even 6.75 wt.% of aluminium and up to 4.5 wt.% of vanadium. O and N increase the strength of material. ELI grade is characterised by exceptionally high damage tolerance, in particular at cryogenic range of temperatures [16].

In case of β group alloys, commercially used ones are metastable. They do not exhibit martensitic transformation when cooled rapidly. β alloys after fast cooling and aging at temperature range 500°C-600°C reach yield stress of 1200 MPa and even more. In comparison with previous groups of alloys, ones of type β are not used as often as the others [14].

Titanium's mechanical properties are particularly important for most of applications, but some physical ones are of special interest as well, namely density, corrosion behaviour and oxidation. Some physical properties are listed in fig. 1.22 and compared with other selected metallic materials.

	Linear Thermal Expansion Coefficient (10 ⁻⁶ K ⁻¹)	Thermal Conductivity (W m ⁻¹ K ⁻¹)	Specific Heat Capacity (J kg ⁻¹ K ⁻¹)	Electrical Resistivity ($\mu\Omega$ m)
α Titanium	8.4	20	523	0.42
Ti-6Al-4V	9.0	7	530	1.67
Ti-15-3	8.5	8	500	1.4
Fe	11.8	80	450	0.09
Ni	13.4	90	440	0.07
Al	23.1	237	900	0.03

Figure 1.22: Chosen physical properties of titanium and its alloys in comparison with other structural metallic materials [16]

Linear thermal expansion coefficient does not differ much between different commercial titanium materials but is significantly lower than other metals (for comparison CTE of alumina = $7.2 \times 10^{-6} K^{-1}$). It is worth highlighting that for hexagonal structure of titanium there is a difference of around 20% in values of CTE depending on the crystallographical direction. Electrical resistivity is notably higher than that of Fe, Ni and Al. Electrical resistivity of α Ti is much lower than that of $\alpha + \beta$ alloy (Ti6Al4V) and β one (Ti-15-3) [14].

Titanium with its potential equal to -1.63 V is not intrinsically noble. However it is strongly resistant to corrosion in majority of environments. It owes it to covering of TiO_2 layer; as long as oxide coating is not broken it protects metal from corrosion in oxidizing environments, like chlorides, hypochlorites, sulfates, and sulfites, or in

nitric and chromic acid solutions. Unfortunately, under reducing conditions titaniums corrosion resistance is compromised. Protecting oxide layer is broken down in sulfuric, hydrochloric, and phosphoric acids [73].

To improve titanium's resistance to corrosion in reducing environment, low quantities (up to 0.2%) of platinumium group metals are incorporated, palladium most frequently. It is an expensive element so it is limited to applications where low price is not a priority. Ruthenium is a lower cost alternative to palladium, even though higher amounts are required to obtain the same effect. Very likely materials owe their superior corrosion resistance to presence of intermetallics like Ti_2Pd or $TiRu$ [14]. Fig. 1.23 lists various applications of titanium, where combination of its mechanical and corrosion properties are highly important. One notices directly that spectrum of industrial use of Ti is extremely wide, from paper production to biomedicine and spacecraft.

Industry	Equipment	Environment
Power generation	Condensers, heat exchangers, flue gas scrubbers	Aqueous solutions of various purity, SO ₂ containing gases
Water plants	Desalinization heat exchangers	Sea water
Petrochemical industry	Heat exchangers, well heads, pipe and down hole hardware	H ₂ S containing brines
Pulp and paper	Diffusion washers in bleaching section of process	Chlorides containing liquids
Chemical industry	Dimensionally stable electrodes	Cl ₂ and Cl ₂ compounds
Metal production	Cathodes for electrowinning Cu, Au, and Zn	Various aggressive aqueous solutions
Mineral dressing	Pressure vessels at high T and P	Various aggressive aqueous solutions
Biomedical devices	Orthopedic implants, surgical implants, surgical implements	Human body and autoclave sterilizers
Spacecraft	Cryogenic tanks	N ₂ O ₄ , liquid O ₂ , liquid H ₂

Figure 1.23: Industrial applications of titanium thanks to its corrosion resistance [14]

1.4.2 Alumina/titanium composites fabricated by FAST

Advantage of using titanium as reinforcement for alumina is its elevated melting point which allows those two components to be sintered in one processing step, without necessity of sintering alumina first.

Meir et al. have fabricated alumina/titanium composites using titanium hydride (TiH_2) as a starting powder [17]. It was chosen to avoid formation of undesired phases from oxide layer present on the surface of Ti powder. During thermal treatment TiH_2 decomposed [17]. Powders with different Al_2O_3 and TiH_2 (Ti precursor) ratios were sintered by FAST. Fig. 1.24 shows conditions of thermal treatment of the material. A temperature of 1300°C was reached with heating rate of 25°C/min and

1.4. TITANIUM AND ITS COMPOSITES WITH CERAMICS

held during 30 minutes. Simultaneously a uniaxial pressure of 64 MPa was applied [17].

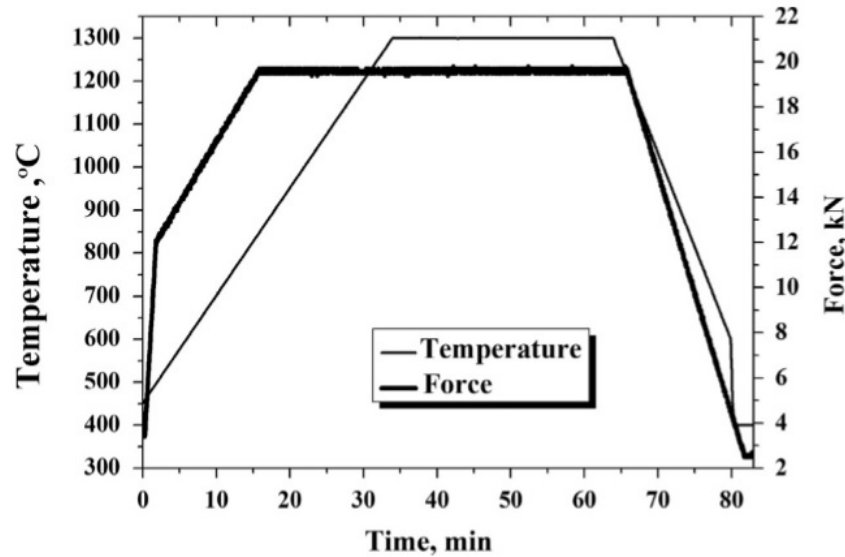


Figure 1.24: Sintering cycle for alumina/titanium composite processing [17]

Phase composition of obtained composite was examined by XRD. Fig. 1.25 shows patterns for titanium and four composites which differ by titanium content. TiH_2 was not detected after sintering. Identified peaks were attributed to alumina and α titanium. Peak for α titanium is a bit shifted, further analysis revealed that it was caused by a presence of $Ti[Al,O]$ solid solution [17].

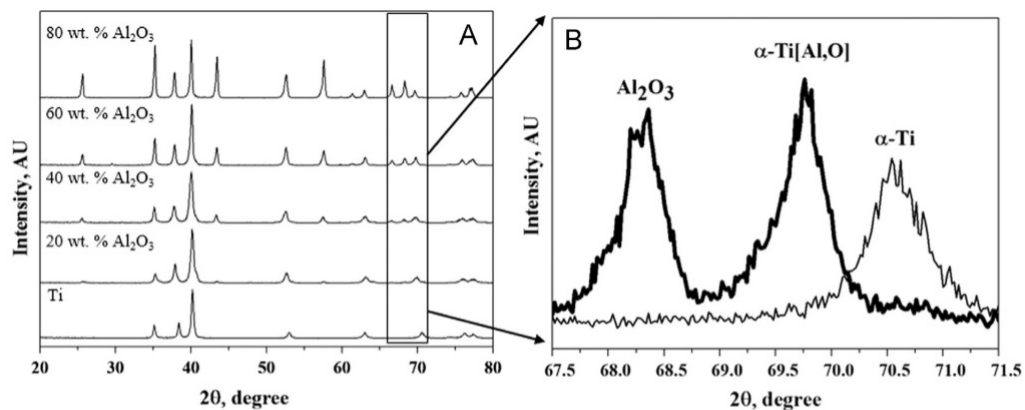


Figure 1.25: Comparison of XRD patterns for titanium and alumina/titanium composites [17]

Mechanical properties of obtained composites were measured: Vickers hardness and fracture toughness, K_{Ic} was determined based on cracks present at corners of indents (Vickers indentation fracture test) and bending strength was measured during bending tests of bars with size 1.5 mm \times 2 mm \times 10 mm. Fig. 1.26 summarizes

results for all materials tested. Uncertainties are given in parentheses, ND not determined properties due to the lack of cracks after indentation [18].

Initial Ti mass fraction	ρ , g/cm ³	E , GPa	G , GPa	Poisson's ratio ν	Fracture toughness, MPa \sqrt{m}	Bending strength, MPa	Vickers hardness, GPa
0	3.95 (2)	420 (1)	172 (1)	0.18 (1)	6.5 (2)	693 (30)	21.1 (5)
0.2	4.11 (2)	362 (1)	148 (1)	0.21 (1)	4.7 (2)	767 (21)	19.7 (5)
0.25	4.10 (2)	338 (1)	138 (1)	0.22 (1)	4.6 (2)	722 (14)	17.9 (5)
0.40	4.18 (2)	306 (1)	123 (1)	0.25 (1)	4.0 (2)	601 (6)	15.0 (5)
0.50	4.24 (2)	281 (2)	113 (1)	0.24 (1)	3.6 (2)	479 (11)	13.2 (5)
0.60	4.39 (2)	246 (1)	98 (1)	0.26 (1)	3.1 (2)	359 (15)	13.0 (4)
0.75	4.38 (2)	214 (1)	85 (1)	0.26 (1)	2.7 (2)	236 (5)	8.6 (5)
0.80	4.48 (2)	187 (1)	73 (1)	0.28 (1)	2.6 (2)	157 (4)	9.9 (3)
0.85	4.51 (2)	172 (1)	67 (1)	0.29 (1)	2.4 (2)	139 (6)	6.8 (4)
0.90	4.46 (2)	161 (1)	62 (1)	0.29 (1)	11.8 (10)	122 (13)	5.5 (3)
0.95	4.49 (2)	138 (1)	52 (1)	0.31 (1)	ND [†]	194 (5)	4.4 (3)
1.00	4.52 (2)	122 (1)	46 (1)	0.32 (1)	ND [†]	1045 (51)	3.0 (5)

Figure 1.26: Material properties of alumina/titanium composites fabricated by FAST [18]

Young's modulus, shear modulus and Vickers hardness evolve approximately with agreement with the rule of mixtures. Nevertheless, it seems that improvement of mechanical properties with incorporation of titanium was not reached. 100% ceramic material had fracture toughness of $6.5 \text{ MPa} \cdot \text{m}^{1/2}$ and bending strength of 693 MPa. Fracture toughness decreased with titanium content to $2.4 \text{ MPa} \cdot \text{m}^{1/2}$ for 85% wt. Ti. For composite 90 wt. % Ti it increased drastically to $11.8 \text{ MPa} \cdot \text{m}^{1/2}$. Bending strength values were increased in the beginning (767 MPa for 20 wt. % Ti and 722 MPa for 25 wt. % Ti) but afterwards they were dropping to 122 MPa for 90 wt. % Ti and 194 MPa for 95 wt. % Ti. Bending strength for pure titanium was given as 1045 MPa. It rises a question if tensile test should not have been performed instead of bending. Some values of mechanical properties increased with increased titanium content. Unfortunately they were not balanced. In other words, when fracture toughness was higher ($11.8 \cdot \text{m}^{1/2}$ for 0.9 of Ti) the bending strength had lower values (122 MPa) and vice versa, when bending strength had its higher values (767 MPa for 0.2 of Ti), fracture toughness was reduced $4.7 \cdot \text{m}^{1/2}$). On the other hand, reliability and validity of fracture toughness obtained by Vickers indentation is controversial even for pure ceramic materials. Applying this method for ceramic/metal composites raises even more questions. Fig. 1.27 shows micro-structure of materials with various titanium content. It is quite clear that in each case Palmqvist mode cracks could have significantly different lengths within the same sample, depending on the region when indent was made. For composites with titanium content above 0.9 there are only some isolated grains of alumina in the metal matrix. It allows to think that calculating fracture toughness from Palmqvist mode cracks of composite with very high metal content is not an optimal method.

Fabricating alumina/titanium composites with not interconnected titanium located isotropically at random places in ceramics does not seem to improve ceramic properties. However, incorporating titanium into architected alumina composites might help to improve its ductility. Unfortunately, because of explosive character of very fine powders it does not seem feasible to include it directly into the interphase between alumina platelets. On the other hand, fabricating layered materials with titanium foil between ceramic pellets would add another microstructural level into composite.

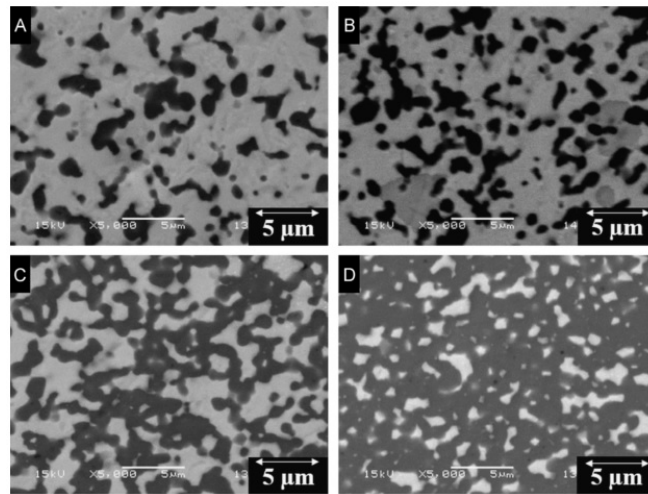


Figure 1.27: SEM pictures of alumina/titanium composites fabricated by FAST [17]. Content of titanium (light gray) in wt% is as follows: A) 80, B) 60, C) 40 and D) 20.

1.5 Conclusions of the chapter

Bioinspired materials with high alignment of their microstructural elements (like alumina platelets) exhibit improved mechanical performance thanks to their architecture. Freeze casting is a technique which allows obtaining materials with controlled microstructure at various levels.

This chapter and bibliographic sections of some result chapters provide the state of the art on exceptional properties of natural materials, benefits of taking bioinspired approach and possibilities of improving present solutions.

In the chapter "Materials and methods" all techniques of material preparation and characterisation (microscopic and mechanic) are described. More details (like sintering parameters) are given in the results chapters.

As mentioned, freeze casting is a complex technique that does not allow preparing large samples. One of the goals of this thesis was to simplify fabrication method and enable making larger quantities of the material (chapter "Simplifying material fabrication").

During this thesis, we investigated how to further improve mechanical properties of nacre-like alumina. Two approaches were chosen: modifying interphase between alumina platelets (chapter "Modification of the interphase between platelets) and adding new level of the architecture by incorporation of titanium foil (chapter "Alumina/titanium composites").

Chapter 2

Materials and methods

The work presented in this chapter is divided into two main parts: description of the materials processing and of the characterization techniques used.

First part was built around the concept of designing new bioinspired composites based on nacre-like alumina (F. Bouville et al. [9]) and exploring the possibility of introducing more complexity into their microstructure to improve their mechanical behaviour. In other words, it was intended to add architectural levels and modify already existing elements. Different compositions of the interphase between platelets were proposed: adding zirconia nano powder, depositing zirconia on the surface of alumina nano platelets and substituting glassy interphase by graphene. Furthermore, adding layers of metal was planned as a way of increasing material complexity and introducing ductility.

Second part of this manuscript was focused on detailed characterisation of obtained materials: their microstructure (SEM, EDX, EBSD, synchrotron) and mechanical properties (three and four points bending). Significant effort was made to assess the influence of each component on global properties (*in situ* three points bending).

In this chapter, fabrication methods and testing protocols are described and explained.

2.1 Materials preparation

Two different processing routes were explored in this work to generate microstructure with aligned alumina platelets. The first one, freezing under flow, was developed by Florian Bouville [19] and which allows to use ice crystals growth to align alumina platelets (see the "Literature review" chapter). The second one, uniaxial pressing, was chosen to simplify the materials' fabrication.

2.1.1 Samples obtained by freezing under flow

Freezing under flow is a type of freeze casting where a slurry flows on the surface of a cooling plate. The first step of the procedure is the preparation of the slurry. The slurry consists of alumina platelets, alumina nanoparticles, glassy phase precursors

2.1. MATERIALS PREPARATION

and rheology modifiers. Afterwards, the suspension is frozen and freeze-dried to remove ice. The final step is sintering by field assisted sintering technique (FAST). As our materials are supposed to mimic a natural structure of nacre, each constituent plays a well-defined role. The main component of the slurry are alumina platelets (Rona Flair White Sapphire, Merck) which are the main building blocks of the final ceramic composite (see Fig. 2.1). They are 500 nm thick and around 8 μm in diameter.

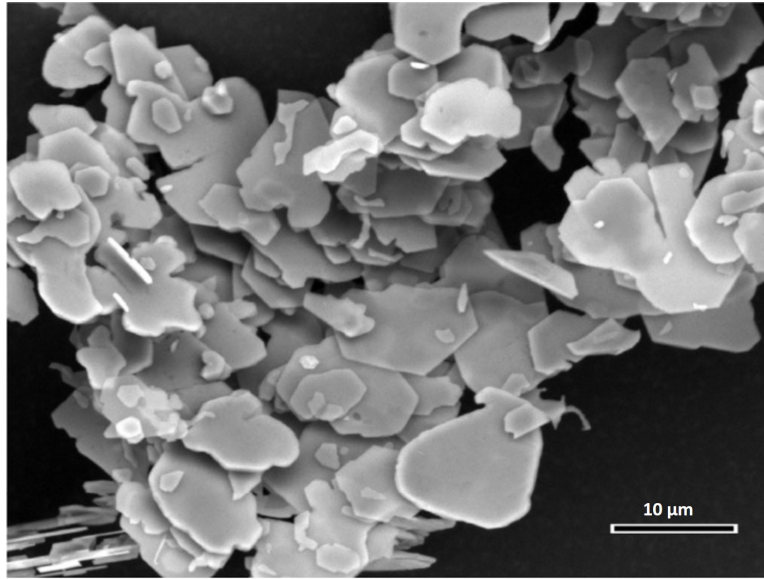


Figure 2.1: Alumina platelets used in this study [11]

Nanoalumina (100 nm diameter, TM-DAR, Taimei Chemicals Co., Ltd.) is added to the slurry to serve as ceramic bridges between platelets and improve their sintering. Calcium carbonate (20 nm diameter, Sigma-Aldrich) and colloidal silica (20 nm diameter, Nexsil 20K, Nyacol) are incorporated. During thermal treatment of the material they create a glassy interphase which binds the platelets together. Carbopol and Darvan are added to improve dispersion and rheological properties of the slurry. In the table 2.1, a detailed composition is presented. For Carbopol, percentage of water mass is given because it serves as a rheology modifier. Value for Darvan is in respect to total powder content. Nexsil 20K and Calcium Carbonate during the sintering form 1,5 vol.% of glassy phase in the final material.

A special care during elaboration is required as, apart from the composition, the microstructure plays an important role in resulting properties. Obtaining satisfactory level of alignment of the platelets is crucial because it allows to obtain material with superior mechanical properties. Freeze casting has been proven to be able to align alumina platelets and create lamellar porosity (see the "Literature review" chapter). However, if one desires to prepare dense material, after pressing and consolidation by field assisted sintering techniques (FAST), the direction of porosity is critical: crystals are vertically aligned but domains of lamellar orientation can be present due to occurrence of nucleation at different locations [74]. Freezing under flow allows to induce long-range order. In this case, the slurry is not frozen in cylindrical molds but

Component	Mass [g]	Percentage massive [%]
Water	80.0	60 (of entire slurry)
Carbopol	0.243	0.3 (of water)
Darvan 7NS	0.516	1.0 (of ceramic powder)
TM-DAR (alumina nano-powder)	1.548	2.9 (of ceramic powder)
White sapphire (alumina platelets)	50.042	37 (of entire slurry)
Nexsil 20K (colloidal silica)	1.288	2.4 (of ceramic powder)
Calcium carbonate	0.129	0.24 (of ceramic powder)

Table 2.1: Standard composition of the slurry for freeze casting

flows on the freezing plate (see fig. 2.2). Copper plate is tilted by 10° ; on its surface a silicon rectangular mold is attached. It has an opening gate at the end of the plate; it enables a slurry to leak out. Just outside there is a recipient for the slurry which is pumped back by peristaltic pump. Flow is controlled by the tap. This way flow continues until a layer of thickness of a few millimeters is frozen. In that moment the slope is removed, the gate closed and the closed silicon mold filled with the remaining slurry. Ice crystals continue to grow until all slurry is completely frozen. The Fig. 2.2 illustrates described set up developed by Bouville et al. [19].

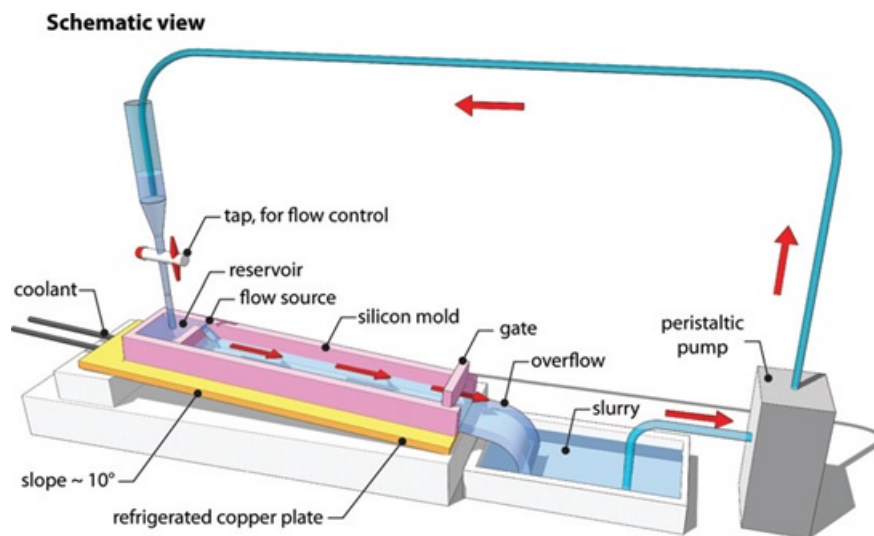


Figure 2.2: A schematic view of freezing under flow set up [19]

Ice crystals, after sublimation – pores, created during freezing under flow are very well aligned thanks to two gradients: fluid's velocity and temperature. The freezing rate is $1\text{ }^\circ\text{C}/\text{min}$ [75]. The slurry flows faster at one border of the silicon mold and, as a consequence, temperature decreases slower there [19]. In the Fig. 2.3 is presented a schematic view of those phenomena.

The frozen material is then placed in freeze dryer at $-83\text{ }^\circ\text{C}$ and around 50 mbar for at least 48 hours to ensure a complete elimination of the ice. After freeze drying the prepared porous (80% average) bar is cut into smaller pieces that fit into sintering

2.1. MATERIALS PREPARATION

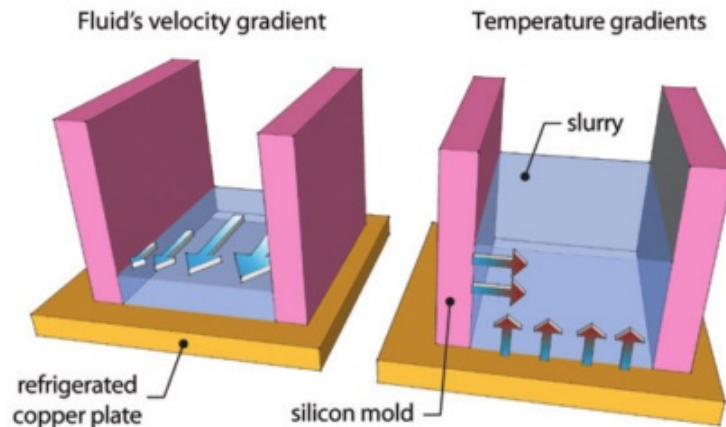


Figure 2.3: A schematic view of gradients created during freezing under flow [19]

matrix (7 cylinders of 2 cm height and 2 cm in diameter). After sintering by FAST at 1600 °C with heating and cooling rate set at 100°C/min. (HP D25 from FCT, equipment of MATEIS laboratory) we obtain dense materials with highly aligned microstructure.

Apart from standard samples, modified formulations were also prepared to investigate the possibility of improving mechanical properties through the modification of the interphase. Details are given in the chapter "Modification of the interphase between platelets".

2.1.2 Composites prepared by pressing

Freeze casting is a technique to fabricate materials with aligned microstructure. However it has some significant limitations; it is time consuming and difficult to scale-up. Uniaxial pressing was proposed as a simple alternative to align alumina platelets in a dense, bulk sample. It is simple and well-known in industry. It was expected that manufacturing layered composites by pressing should be easier and faster.

First trials were conducted to check the validity of this hypothesis. A slurry with reference composition (Table 2.1) was prepared and frozen in liquid nitrogen. It was placed in freeze dryer for 48 hours. 0.7 g of obtained powder were placed directly in the graphite sintering matrix (20 mm diameter) and pressed at approximately 100 MPa for 20 seconds. It was repeated four times so that the entire sample consisted of 2.8 g of powder. This quantity was necessary to obtain a sample of the similar thickness as those prepared by freezing under flow which is approximately 2 mm. Samples were sintered by FAST at 1600 °C. Heating and cooling rate were set at 100 °C/min. No dwell time was applied.

2.1.3 Metal/ceramic composites prepared by pressing

Simplifying material fabrication thanks to uniaxial pressing was chosen in order to introduce additional microstructural level through addition of metal foil between pressed layers (foils from GoodFellow).

Titanium was chosen because of its high melting point of 1660 °C; it permits to sinter both materials (alumina and titanium) in one step. Powder was prepared as in previous section. The only difference was that between each ceramic layer a titanium foil was placed. Final disc consisted of four ceramic layers separated by three titanium layers (Fig. 2.4). Sintering temperature was decreased to 1500°C, with heating and cooling rates remaining at 100°C/min.

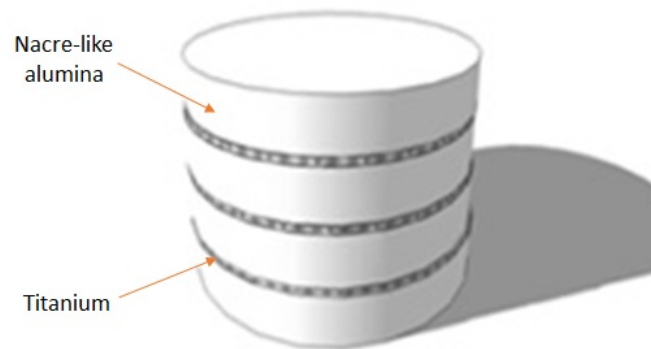


Figure 2.4: A scheme of alumina/titanium composite

A prepared pellet was cut into pieces and polished (see 2.1.4) to verify the platelets alignment by SEM. Results of tests performed on both types of composites (ceramic only and ceramic/titanium) are described in chapters: "Simplifying material fabrication" and "Alumina/titanium composites".

2.1.4 Sample processing before characterization

As the size of samples is limited due to a preparation protocol by freeze-casting (discs of 20 mm in diameter and 2-3 mm high), size of bars for mechanical testing in bending was adapted (see section 2.2.2). Selected length (l) is equal to 14 mm, height and width (h and b respectively) are approximately 2 mm.

Cutting and polishing

A high quality of specimen's surface, obtained thanks to proper polishing, plays a crucial role in obtaining reliable results for both microstructural and mechanical characterisation. For anisotropic materials like those with high platelets alignment,

2.1. MATERIALS PREPARATION

determining a suitable protocol is not straightforward. For multimaterials like alumina/titanium layered composites it gets even more complicated. Ceramic grains might be pulled out and cause damages to the Ti foil. After dedicating time and patience to this problem, an optimal polishing protocol was established. Cutting sintered material by wire saw enables to begin polishing directly by disc with fine grain size of $30\ \mu\text{m}$ (polishing materials supplied from Presi). It not only saves time but most of all prevents from damaging surface. A detailed polishing protocol is presented in the Table 2.2.

Polishing disc	Suspension	Force [N]	Plate Speed [rpm]	Head Speed [rpm]	Direction	Time [min]
P500 diamond	none	20	100	30	coincident	3
P500 diamond	none	30	150	60	coincident	3
P1200 diamond	none	30	150	60	coincident	4
Fabric NWF+	$6\ \mu\text{m}$ diamond	30	150	60	opposed	5
Fabric NWF+	$3\ \mu\text{m}$ diamond	30	150	60	opposed	5
Fabric NWF+	$1\ \mu\text{m}$ diamond	30	150	60	opposed	6

Table 2.2: Details of the polishing protocol

Bending tests were conducted on notched samples: first by a diamond disc (0.3 mm thick, Struers) and then sharpened by razor blade with diamond paste of $3\ \mu\text{m}$ in a home-made apparatus (fig. 2.5). Sharpening of the notch was conducted for about 15 minutes for each sample. Obtained notch is shown in fig. 2.6.

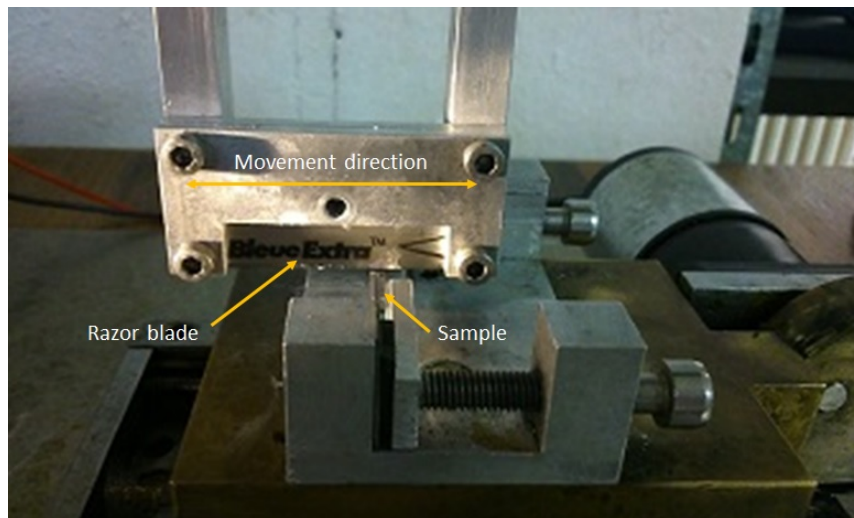


Figure 2.5: A notch sharpening set up

Ion polishing

Some characterisation techniques (EBSD or EDX analysis) require flawless surface, extremely difficult to obtain by mechanical polishing, especially in multimaterials. In that case ion polishing can be helpful. In our laboratory Ilion II+ from Gatan is used. The maximal size of sample fitting into the device is $10\ \text{mm} \times 10\ \text{mm} \times 4\ \text{mm}$. The specimen is glued by silver paint to the titanium blade, which partially blocks the ion

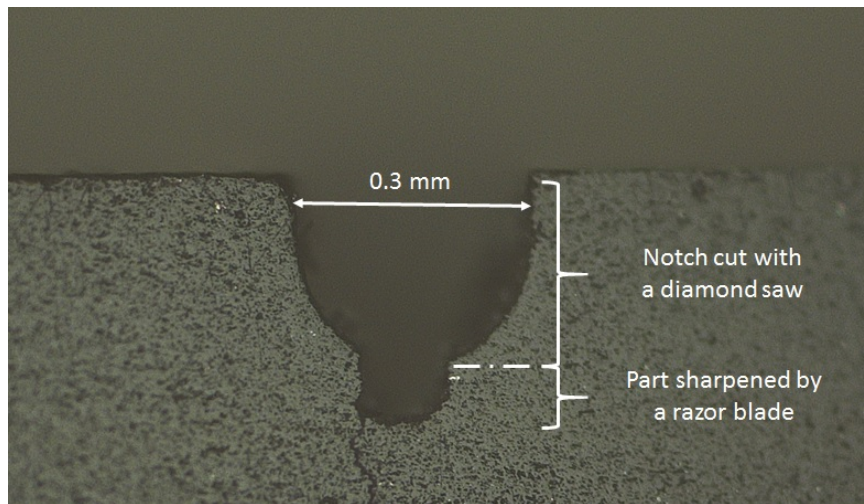


Figure 2.6: A notch prepared according to the protocol

beam, resulting in a flat and horizontal propagation of milling area. Parameters used in this study are as follows:

- sector milling angle: 90°
- rotation speed: 1 rpm
- energy: 6kV
- gun tilt: 0°
- time: 2-4 h

The main limitation of this technique is the size of the etched zone, with a maximum width of $200\ \mu\text{m}$. It is only appropriate for analysing microstructure but not enough to observe crack propagation. Fig. 2.7 shows the top view of an etched sample attached to the titanium mask.

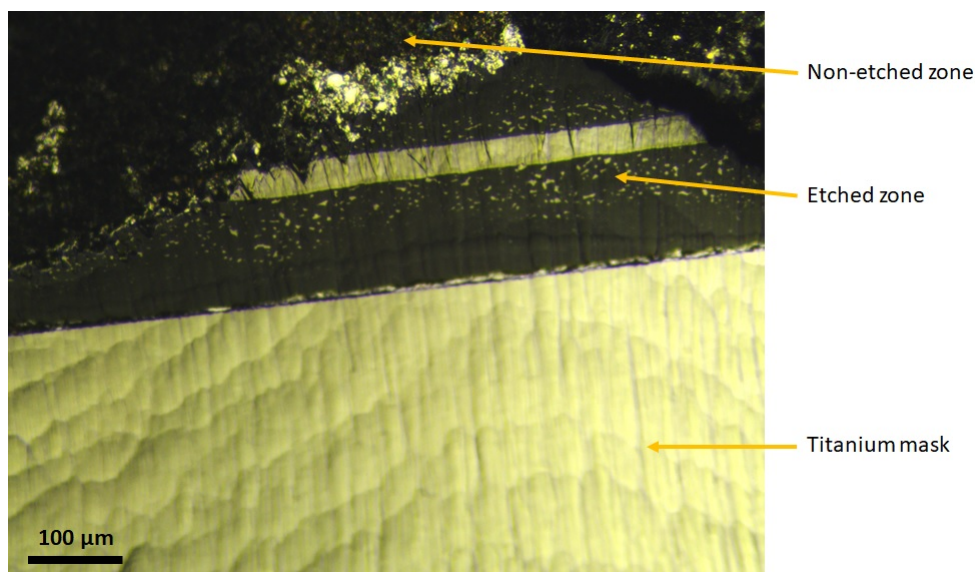


Figure 2.7: Titanium/alumina sample polished by Ilion II+. Inside the etched zone we can see titanium foil and diffusion zone (light colour) and alumina matrix (dark colour).

2.2 Characterization techniques

2.2.1 Morphological characterization

Optical microscopy

An optical microscope (Zeiss Axiophot with camera AxioCam MRC) was used to measure the size of the notch. It helped to more accurately determine the crack propagation and length and improved the precision of the calculation of mechanical properties. It was also used for general observations (surface quality, presence of visible defects) before techniques with better spatial resolution were used.

Confocal microscopy

A confocal microscope (Leica TCS SP8 in LSFC laboratory in Cavaillon) was used to image the crack path. Multiple pictures of one sample were taken, each at a different depth of view. Afterwards using programmes LAS AF (Leica Microsystems) and Fiji (based on ImageJ, developed at National Institutes of Health, Bethesda, Maryland, USA) all pictures were combined into one with an extended depth of view. The crack can clearly be observed. A good contrast between the ceramic and the metal is obtained, because of different reflection properties.

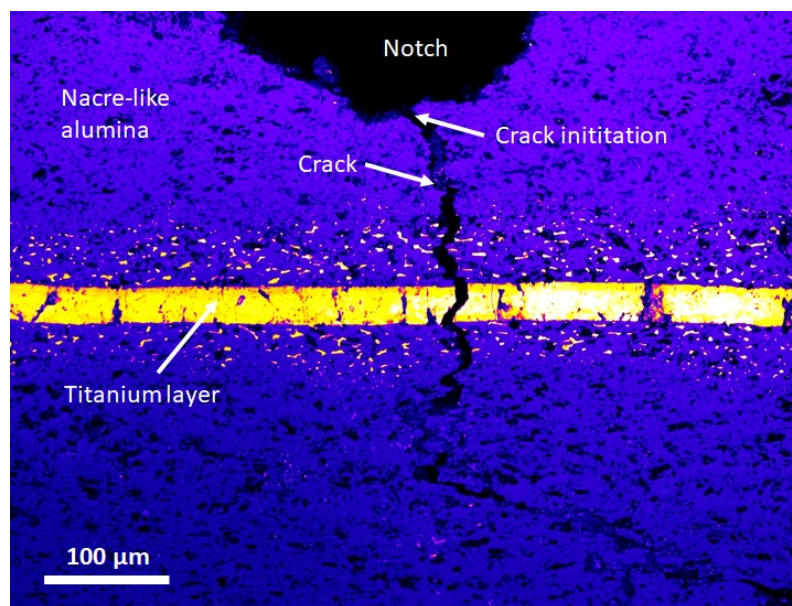


Figure 2.8: An example of crack observation by confocal microscopy

Scanning Electron Microscopy (SEM)

SEM was used for microstructural characterisation. A Supra 55 (Zeiss) allows observations at low acceleration voltage (between 1 and 2 kV), on uncoated samples, which otherwise would not be possible as alumina charges rapidly. Several detectors

were used. Secondary electrons InLens detector was used to observe intermetallics created on the Ti/ Al_2O_3 interphase. For more detailed observations of the titanium layer (intermetallics, cracks, grains), a Backscattered Electrons detector (BSE) was used.

Electron Backscattered Diffraction (EBSD)

The development of alumina/titanium composites raised some complex questions concerning crystallography of metallic phases. One of studied aspects was to determine influence of sintering parameters (heating and cooling speed for example) on the diffusion of titanium into ceramic matrix. Changing of cooling speed might have affected the crystallography of titanium layer. To study titanium crystallography, EBSD (integrated with SEM) was used. The same technique was used to observe and characterize the alumina platelets alignment. AZtec program (Oxford Instruments) was used for result analysis.

Energy Dispersive X-ray Spectroscopy (EDX)

In some metal/ceramic samples it was necessary to perform local chemical analysis to determine their composition. EDX provides information on chemical elements present in the studied area. Electron beam induces X-ray emission from the material. Each element is characterised by a unique set of peaks in the electromagnetic emission spectrum. The same software as for EBSD was used.

X-ray Microtomography

X-ray microtomography is a non-destructive imaging technique which allows to create 3D reconstruction of a sample. In the laboratory we have two microtomographs with the possibility of installing equipment for in-situ tests. The first one is a v|tome|x s from GE Sensing & Inspection Technologies Phoenix X|ray. Its detector, Varian Paxscan, has an active surface of 250×200 mm and matrix of 1920×1536 pixels (pixel size equal to $127 \mu\text{m}$). A second one, EasyTom Nano from RX Solutions, can perform scans with a higher resolution than the first one. It operates with two types of filaments: tungsten and LaB6. It has two sorts of detectors, a very high resolution camera CCD and a plane sensor (2400×2400 pixels of $50 \mu\text{m}$) for high resolution acquisitions at high energy (up to 160 kV). We used both devices to characterize the materials. The second microtomograph was specially useful during preparations for experiments in synchrotron facility (ID16 beam line) to verify the quality of the chosen samples and decide which zones should be scanned. Fig. 2.9 on the left shows one of those reconstructions.

Synchrotron

Experiments at the European Synchrotron Radiation Facility in Grenoble were conducted on titanium/alumina samples. ESRF is a world-class research center, where thanks to high brightness X-rays, we were able to obtain high-quality scans of the

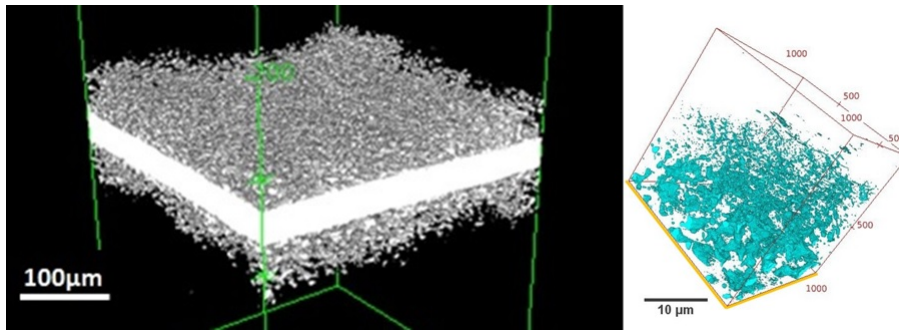


Figure 2.9: Comparison of 3D reconstructions of scans performed in EasyTomo Nano tomograph in MATEIS laboratory (on the left) and in ESRF synchrotron facility (on the right). Samples were composed of layers of alumina and titanium with significant diffusion of metal into ceramic matrix. Resolution on the left: 700 nm, on the right: 50 nm. In the right picture titanium foil is not visible because of the noise in the scan, yellow lines indicate where titanium was placed.

materials microstructure. The major goal of those observations was to image the distribution of the metal phase in the ceramic matrix to better understand the mechanisms of titanium diffusion into the ceramic matrix. Scans in phase contrast were conducted in ID16 beam line with help of Julie Villanova. Samples were cut by wire saw into bars of 2 mm height and 500 μm width and thickness. The chosen resolution was 50 nm. Each scan took around 3 hours. Images were reconstructed by Victor Vanpeene (MATEIS). Image analysis was performed using Fiji. The most important step was to clearly separate all present phases using filters: 3D Gaussian Blur and 3D Median. Throughout entire process brightness and contrast were repetitively adjusted. To differentiate all phases Image Calculator tool was used, it permits to separate image of ceramic matrix from metal grains for example. The analysis allowed to obtain 3D reconstruction of titanium infiltrated into pores between alumina platelets (fig. 2.9 on the right). Those reconstructions help to better understand the process of titanium diffusion during sintering.

2.2.2 Mechanical testing

As one of the major goals of this project was to obtain materials with high mechanical performance, choosing the right measurement method was crucial. Single edge notch bending test was selected to characterize crack propagation resistance (toughness). It does not require a large number of samples to get reliable results. Notch is the most significant defect of the same size for all the samples so results are less scattered. In the part focused on interphase modification, four point bending was used as a tool to compare diverse compositions. In the further steps three point bending was chosen, mainly for comparison purposes with data from the literature.

Commonly used bars for SENB tests on ceramic materials are 40 mm long. Due to limitations of the fabrication process (freeze casting, FAST) the length of samples is only 14 mm. Modified testing set ups had to be designed and fabricated.

Four- and three-point bending

An original set up was designed using Solid Edge ST3 (Siemens PLM Software). It is a program for CAD solid modelling in 3D which allow executing technical sketches for manufacturing as well.

The specimen size plays an important role in mechanical testing of ceramic materials. It is not advised to reduce the dimensions of a setup too much (see the "Literature review" chapter and publication by Lube et al. [76]). As sample length is 14 mm, we decided that the maximum distance between outer rollers should be 12 mm and 3 mm between the inner ones. Otherwise it could be too difficult to position samples properly. Initially rollers had 1 mm diameter but based on test results it was increased to 2 mm in order to limit its indentation into samples surface (see below eq. 2.9). Given that it is intended to perform bending in elevated temperatures as well, bottom rollers can be changed in case of creep deformation and entire montage is made of alumina. Manufacturing was delegated to Sceram Ceramics (Champagne au Mont d'Or, France).

Fig. 2.10 and 2.11 present details of design. The bottom part was made to fit into the measurement machine (INSTRON electromechanical system 8800). A hole is machined on the bottom part to allow using a linear variable differential transformer (LVDTTM), necessary for accurate displacement measurement. A hole in front side permits to observe a specimen during the test. Grooves in the front and back help to place upper part in the right position.

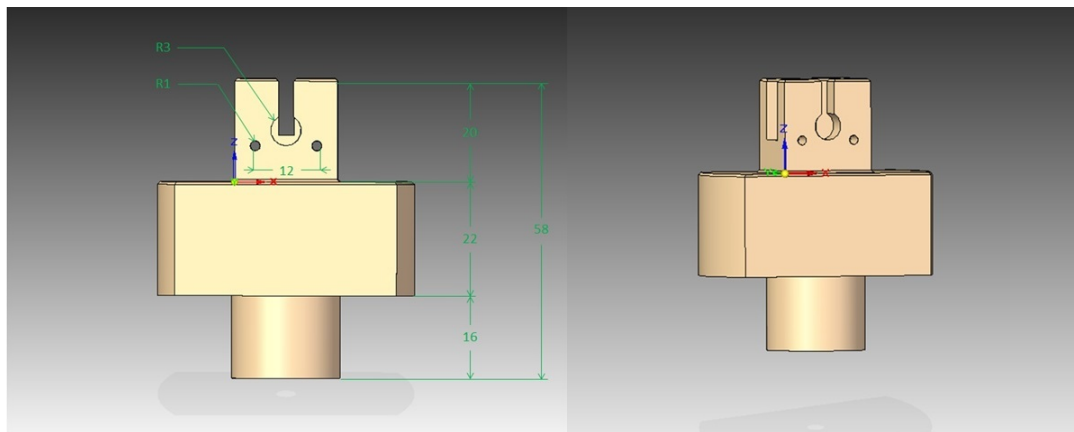


Figure 2.10: Bottom part of bending set up

A semi-cylinder on the top of the four point bending upper part allows the testing of samples with non-perfectly parallel upper and lower surfaces. It was glued after manufacturing so it is not presented in the design. The bottom part of the testing set up is versatile so the set up can be easily adapted to perform 3PB. A specific upper parts for both tests (3PB and 4PB) were machined.

Fig. 2.12 shows an assembled set up, and how the sample should be placed.

Four-and three-point bending was performed with 5 kN load cell and controlled with a 0.5 mm LVDT at a speed of 5 $\mu\text{m}/\text{min}$. Based on those measurements we calculated (according to an ASTM norm E1820-08 2008) J – non-linear strain-energy

2.2. CHARACTERIZATION TECHNIQUES

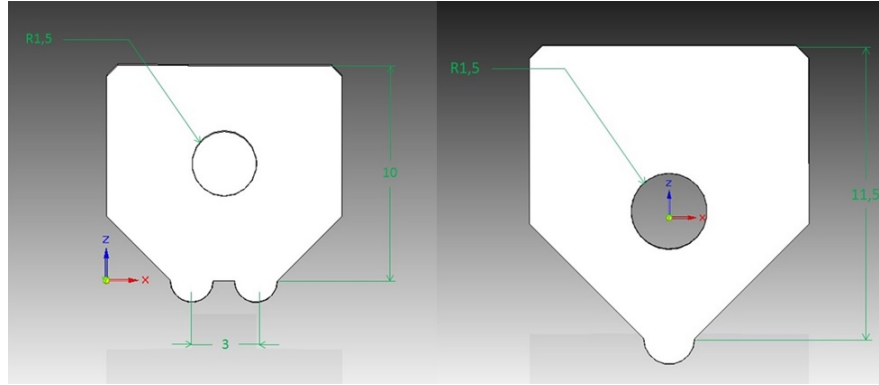


Figure 2.11: Upper parts of three and four point bending set up

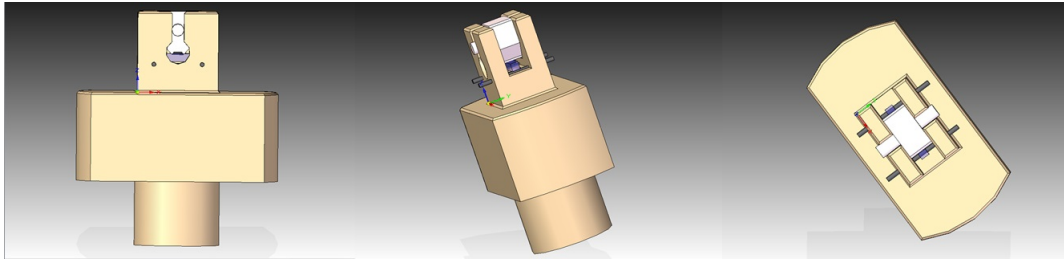


Figure 2.12: Four-point bending montage assembled

release rate, divided into elastic and plastic contribution (J_{el} and J_{pl} respectively):

$$J = J_{el} + J_{pl} \quad (2.1)$$

where based on linear-elastic mechanics J_{el} is defined as:

$$J_{el} = \frac{K_I^2}{E'} \quad (2.2)$$

where K_I is the stress-intensity factor I, $E' = E/(1 - \nu^2)$ in plane stress, E is Young's modulus and ν is a Poisson's ratio. For notched samples K_I is calculated based on applied load P :

$$K_I = \frac{PS}{BW^{3/2}} f(a/W) \quad (2.3)$$

where f is a non-dimensional function of the crack length a :

$$f(a/W) = \frac{3(a/W)^{1/2}[1.99 - (a/W)(1 - a/W)(2.15 - 3.93(a/W) + 2.7(a/W)^2)]}{2(1 + 2a/W)(1 - a/W)^{3/2}} \quad (2.4)$$

Plastic component J_{pl} for a crack in bending is calculated as follows:

$$J_{pl} = \frac{1.9A_{pl}}{Bb} \quad (2.5)$$

where A_{pl} is a plastic area under force/displacement curve, b is a uncracked ligament length ($W-a$). It can not be ignored that as crack advances, ligament b decreases. An incremental version of Eq. (2.5) should be applied:

$$J_{pl(i)} = \left[J_{pl(i-1)} + \left(\frac{1.9}{b_{(i-1)}} \right) \left(\frac{A_{pl(i)} - A_{pl(i-1)}}{B} \right) \right] \left[1 - \frac{a_{(i)} - a_{(i-1)}}{b_{(i-1)}} \right] \quad (2.6)$$

Calculations are limited for crack length equal to 0.25 of height of the ligament of the specimen (around 0.5 mm).

When samples are relatively small some phenomena, often are not taken into consideration, become crucial for obtaining reliable results. In this case we corrected values of displacement by taking into account shear modulus and contact between rollers and surface of samples.

$$\Delta l_s = P \frac{(L - L')}{4GBH} \quad (2.7)$$

where Δl_s is a displacement due to shear stress G , P is a force applied, L is distance between outer roller and L' between inner rollers, B is sample width and H sample height. For three-point bending analogical equations is used without subtraction of L' . G was calculated as follows:

$$G = \frac{E_{sp}}{2(1 + \nu_{sp})} \quad (2.8)$$

where E_{sp} is sample's Young's modulus and ν_{sp} its Poisson's ratio (0.25).

Displacement due to contact between rollers and specimen's surface, Δl_c was calculated as well:

$$\Delta l_c = 4 \left(\frac{P}{2B\pi E_r} \right) \quad (2.9)$$

where E_r is reduced modulus:

$$E_r = \frac{1}{\frac{1 - \nu_{al}^2}{E_{al}} + \frac{1 - \nu_{sp}^2}{E_{sp}}} \quad (2.10)$$

where E_{al} is Young's modulus of alumina and ν_{al} its Poisson's ratio.

Both values were added to displacement measured by LVDT.

2.2.3 *In situ* three-point bending

In case of nacre-like alumina, extrinsic toughening mechanisms are present during crack. Performing bending *in situ* in SEM allows to observe with high precision the crack propagation in the material and identify those mechanisms. Experiments were conducted with the help of Sophie Cazottes and Thierry Douillard (MATEIS).

2.2. CHARACTERIZATION TECHNIQUES

Fig. 2.13 shows a montage from Deben (Suffolk IP30 9QS, UK) adjusted for this type of experiments. Its size does not correspond to that of the *ex situ* set-up; velocity of bending is higher so this experiment serves for exploring crack path and not for the exact calculations of mechanical properties.



Figure 2.13: A set up allowing to perform 3PB in SEM

The first tests were performed with 0,1 mm/min speed but it was significantly higher than the value used in *ex situ* testing. For further experiments we applied a minimal speed: 0,033 mm/min. Bending was stopped each time when crack visibly progressed to enable detailed observations and to take pictures. Results of experiments *in situ* are presented in the chapter "Alumina/titanium composites".

Chapter 3

Simplification of material fabrication

Freeze-casting is a method which allows to fabricate materials with high alumina platelets alignment. Unfortunately, it is limited for now to laboratory scale and not yet proper for the production of large quantities of material. Up to now, the largest samples prepared by this method are 20 mm in diameter. Freezing under flow of large quantities of slurry and maintaining platelets alignment does not seem feasible because increasing thickness of slurry limits control of the cooling rate. It is an obstacle for industrialization of the process. In order to transfer production to industry other method should be employed. It needs to be rather simple and, most importantly, possible to up-scale.

Furthermore, in order to compare results with other studies it is convenient to perform mechanical testing according to ASTM standards which recommend rollers outer span of 40 mm [77]. Smaller dimensions are possible but they should not be lower than 16 mm outer span.

In this chapter we investigate if uniaxial pressing of alumina platelets (with additives from standard formula) is a reasonable and efficient alternative to freeze-casting. To verify that this technique can be used to manufacture architected material at larger scale, microstructural and mechanical testing is required. EBSD analysis (with T. Douillard and N. Vache, MATEIS laboratory) helped determine level of alumina platelets alignment and three points bending of notched samples allowed to compare mechanical properties with samples prepared by freeze-casting.

First step of the study was to characterize reference material: samples prepared by freeze-casting. Results of the mechanical testing (fig. 3.1) revealed significant differences between properties of materials prepared by the same processing protocol (all parameters were identical) by two different operators. It is one of the drawbacks of the freezing under flow: although one person is capable of preparing samples with very consistent mechanical behaviour, there is variance between materials prepared by different people. It might be caused by some small differences in manipulation, like changing position of cooling plate (from tilted to allow flow of the slurry to horizontal) at slightly different moment.

Later, uniaxial pressing process was introduced on the small scale and its results compared with reference. Powder used for fabrication of samples by pressing technique had the same composition as for freezing under flow. First, it was ball-milled

3.1. FREEZE-CASTING

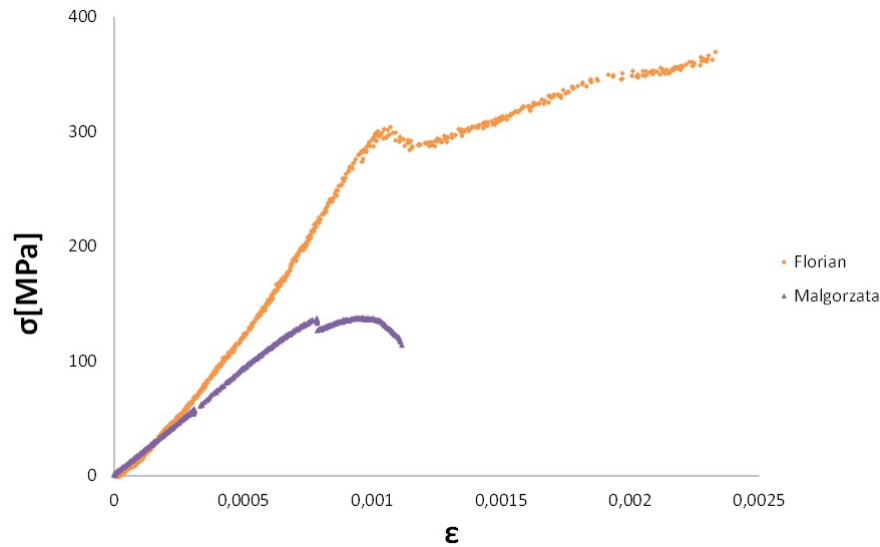


Figure 3.1: Differences between mechanical properties prepared by the same processing protocol by two different people (thesis of Florian Bouville [11] and this work)

and then frozen in liquid nitrogen and freeze-dried. The last part was focused on up-scaling new fabrication protocol.

3.1 Freeze-casting

Freeze-casting is a starting point for fabrication of materials with aligned microstructure. It should be replaced by significantly simpler process. Details of "freezing under flow" are described in "Materials and methods" chapter. Sintering cycle is shown in fig. 3.2.

Heating and cooling rates are set to $100^\circ/\text{min}$. There is no holding time at 1500° . Pressure of 75 MPa is applied at the beginning and removed immediately after cooling.

As a result, a material composed of well-aligned alumina platelets is obtained, as illustrated in fig. 3.3. On the right side of the figure, colour codes for texture mapping are presented. Intense red/fuchsia colours correspond to platelets orientation close to 001 plane. Those colours were visibly dominant in the picture. EBSD analysis shown that platelets orientation is consistent and it allowed to calculate platelets size distribution.

Table 3.1 lists platelets area and its percentage. 24.48% of platelets has area inferior to $1 \mu\text{m}^2$. 5.84 % of grains have surface superior to $10 \mu\text{m}^2$. It means that some grain growth during sintering occurred (average initial size of a platelet: $0.5 \mu\text{m}$ thickness and $5\text{-}7 \mu\text{m}$ diameter).

This data will serve as a reference for assessment of influence of material fabrication on microstructure parameters.

For mechanical properties evaluation three points bending (3PB) of notched samples was done. Force-Deflection curves show raw results (fig. 3.4). Orange arrows

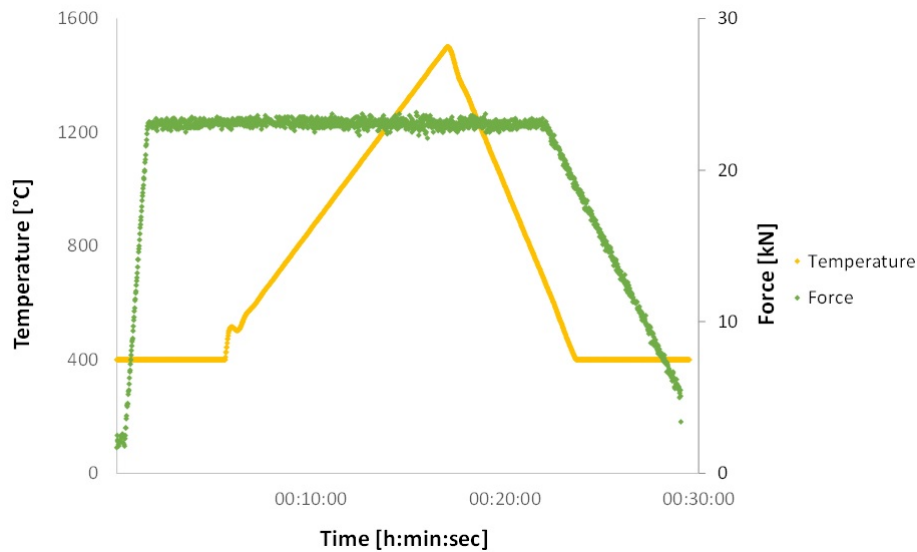


Figure 3.2: Sintering cycle for samples prepared by freeze-casting

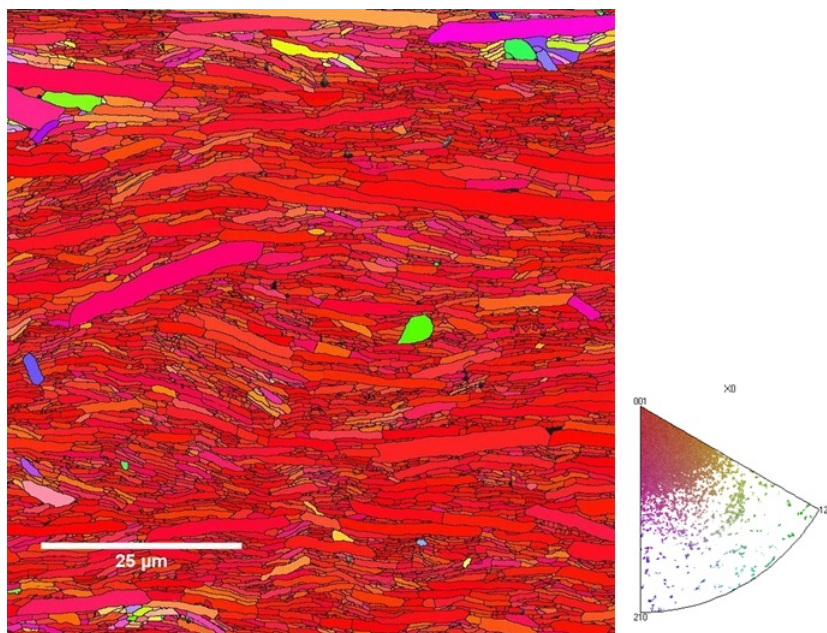


Figure 3.3: Platelets orientation and grain boundaries of sample processed by freeze casting and pressing (cross section perpendicular to sample surface)

point to the onset of crack propagation.

It is worth noting that just after crack initiation value of force drops slightly only to grow next. This phenomena is representative of crack propagation resistance, known as R-curve behaviour. Although individual values differ between samples, shapes of plots are similar.

Fig. 3.5 shows strain/stress curves of tested samples. Stress-strain values were calculated on the basis of sample height with subtracted notch depth and assuming a purely elastic behaviour. Two of them (A and B) are comparable while the third

3.1. FREEZE-CASTING

area [μm^2]	grains no	percentage [%]
<1	554	24.48
1-2	748	33.05
2.0032-10	829	36.63
10.003-50	123	5.44
50<	9	0.4
Total	2263	100

Table 3.1: Size distribution of alumina platelets in sample processed by freeze casting

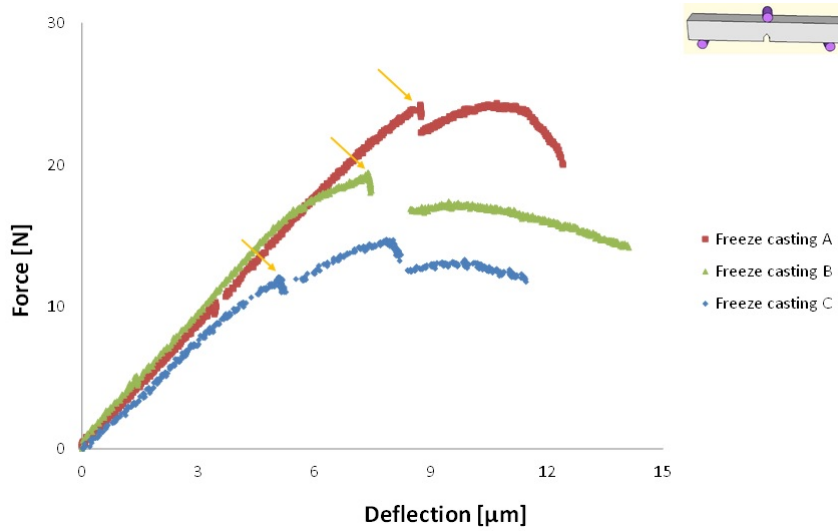


Figure 3.4: Force-Deflection curve of the material processed by freeze casting

one (C) is clearly weaker. For A and B crack starts to propagate at calculated stress higher than 125 MPa whereas for C it is just around 80 MPa.

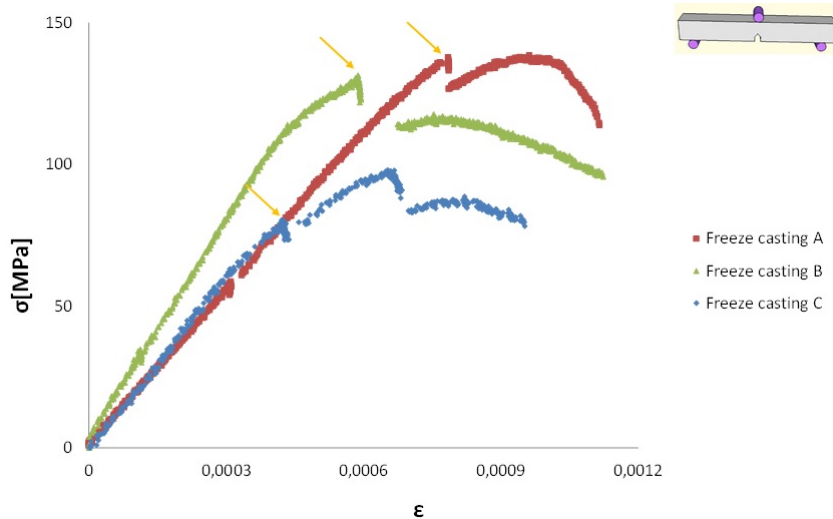


Figure 3.5: Stress-Strain curve of the material processed by freeze casting

Based on the 3PB results, the evolution of fracture toughness as a function of

crack extension was calculated and results presented in fig. 3.6 (see "Materials and methods" chapter for details of the method). Samples A and B have K_j increasing from 3 to around 5 $\text{MPa} \cdot \text{m}^{1/2}$, when C changes value from 2 to 4 $\text{MPa} \cdot \text{m}^{1/2}$. Values of ΔK_j are close for three of them.

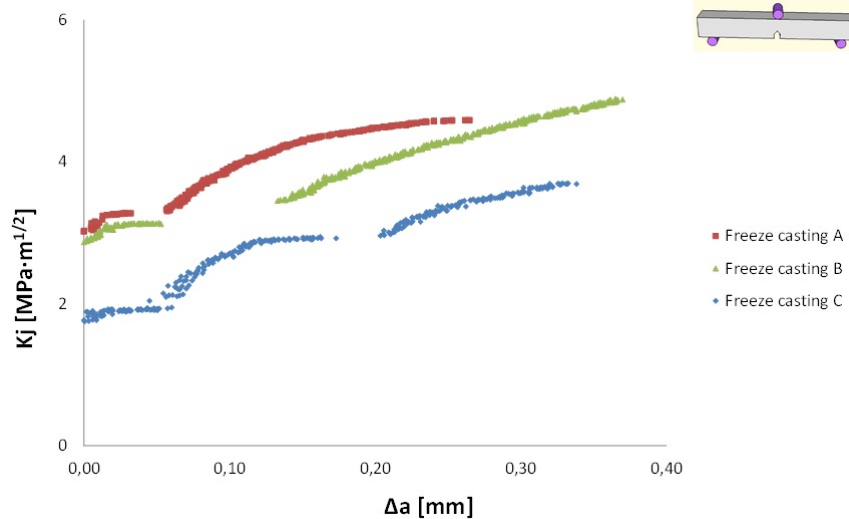


Figure 3.6: R-curves of the material processed by freeze casting

Plots confirm the crack propagation resistance for those samples. Some variations in materials properties are present.

3.2 Uniaxial pressing

Uniaxial pressing was proposed as an alternative to freeze-casting. It is simple and straightforward method, frequently used for pieces of large dimensions in industry. Pellets can also be pressed directly in the sintering die, without a risk of damage during demolding.

To begin, samples of 20 mm diameter (same as in freeze-casting) were prepared by pressing in hydraulic press four layers of 0.7 g of powder of the same composition as for freezing under flow, each with pressure of about 150 MPa, maintained during around 20 sec at room temperature. Sintering cycle was the same as previously (fig. 3.2).

First step of sample characterization was SEM and EBSD analysis to check alumina platelets alignment. Fig.3.7 shows the results indicating very similar platelets orientation as in case of sample prepared by freezing under flow. Alignment of alumina platelets.

In table 3.2 the grain size distribution is listed. For this sample 40.25 % of grains have area inferior to 1 μm^2 in comparison to 24.48 from the sample prepared by freeze casting. Only 0.51 % of grains has surface higher than 10 μm^2 , and there are non over 50 μm^2 . It is visible that in sample prepared by uniaxial pressing platelets are smaller although it is not clear why.

3.2. UNIAXIAL PRESSING

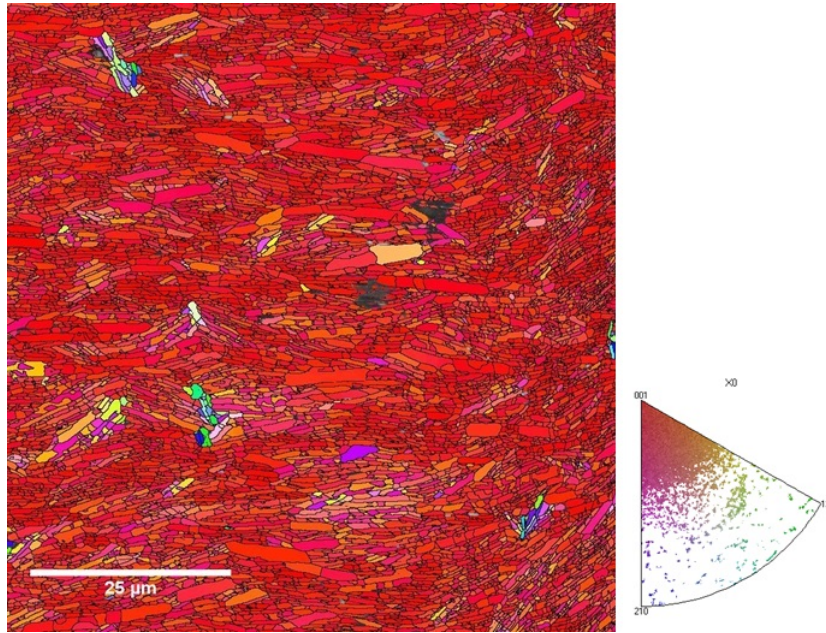


Figure 3.7: Platelets orientation and grain boundaries of sample processed by uniaxial pressing instead of freeze casting

area [μm^2]	grains no	percentage [%]
<1	1587	40.25
1-2	1508	38.24
2.0032-10	828	21
10<	20	0.51
Total	3943	100

Table 3.2: Size distribution of alumina platelets in sample processed by uniaxial pressing instead of freeze casting

EBSD indicates that pressing and sintering protocols lead to materials with good platelets alignment. It is justified to perform mechanical testing. It is needed to specify that all samples were notched. Stress-strain values were calculated on the basis of sample height with subtracted notch depth. In fig.3.8 raw results from 3PB are presented because to calculate stress-strain curves notched samples were used instead of unnotched. Orange arrows indicate onset of crack propagation.

For all three samples crack starts to propagate at stress between 175 and 200 MPa and strain between 0.0015 and 0.002.

Values of fracture toughness as a function of crack extension are presented in fig. 3.10. For all samples initial value is close to $5 \text{ MPa} \cdot \text{m}^{1/2}$. At 0.5 mm of Δa sample A has K_j of $8 \text{ MPa} \cdot \text{m}^{1/2}$, sample B close to $9 \text{ MPa} \cdot \text{m}^{1/2}$ and sample C over $10 \text{ MPa} \cdot \text{m}^{1/2}$.

In comparison with samples prepared by freeze-casting, those fabricated by uniaxial pressing reveal good mechanical properties. Crack begins to propagate at values of stress 50 MPa higher than in case of the previous material. Strain at fracture initiation is between 2 and 4 times higher. Samples survive longer crack extensions

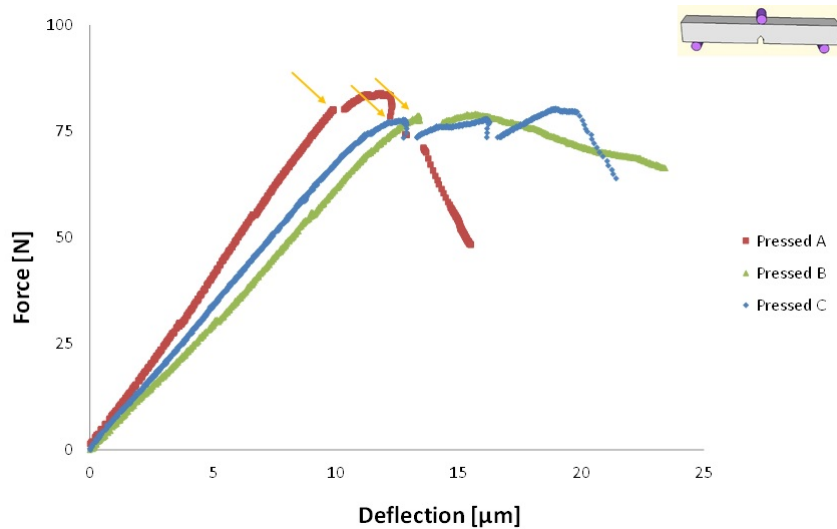


Figure 3.8: Force-Deflection curve of the material processed by uniaxial pressing

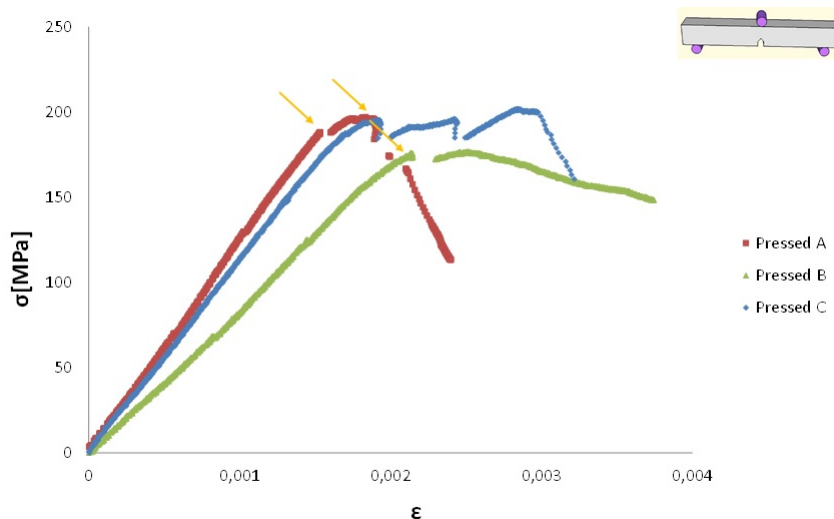


Figure 3.9: Stress-Strain curve of the material processed by uniaxial pressing

with ΔK_j (for crack extension of 0.5 mm) is between 3 and 5 $\text{MPa} \cdot \text{m}^{1/2}$, while for frozen samples it is only 2 $\text{MPa} \cdot \text{m}^{1/2}$. Those properties are inferior to those of material prepared by Florian Bouville using freezing under flow but significantly better than those prepared by freezing in this work. As uniaxial pressing is a straightforward method of fabrication hopefully there would be less inconsistencies in material properties of samples prepared by different operators.

To sum up, uniaxial pressing proves to be useful for preparation of aligned alumina with satisfactory mechanical properties.

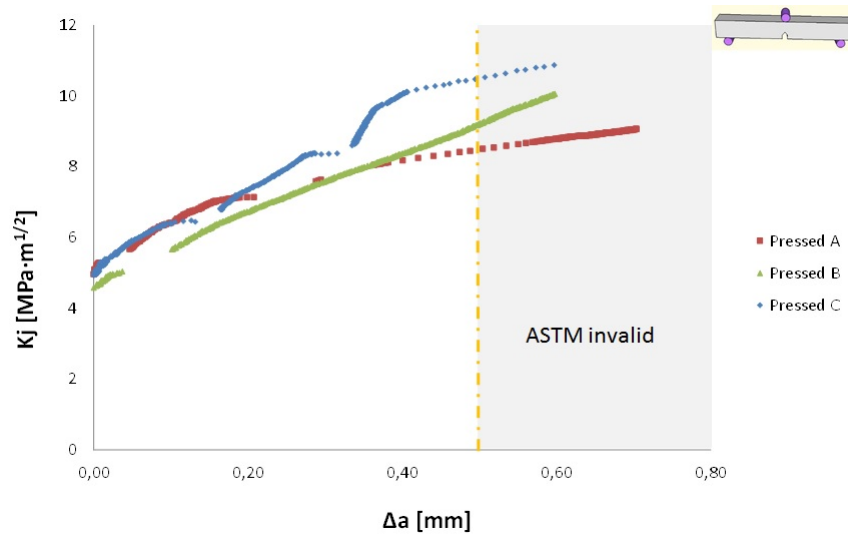


Figure 3.10: R-curves of the material processed by uniaxial pressing. ASTM invalid area concerns crack extension surpassing 0.25 of ligament length.

3.3 Up-scale

One important purpose of studying the effect of changing of material processing from freeze-casting to uniaxial pressing was to determine if this method could allow up-scale production. It was confirmed that pressing is a suitable alternative to freezing which permits to obtain architected material. Consequently the next step was an attempt to fabricate significantly larger sample. The goal was to prepare disc of 50 mm diameter. It is a considerable in size which could determine if larger samples could achieve the same mechanical properties. This disc diameter allows cutting bars suitable for three point bending with rollers' outer span of 35 mm, as recommended by ASTM standards [77] [78].

Approximately 90 g of powder (alumina nanoplatelets, alumina nanopowder and glassy phase precursors) is needed to prepare a sintered pellet of 50 mm diameter and around 10 mm height. Powder was placed inside a sintering die in 20 portions, each of 4.5 g (0.5 mm height after sintering). Each layer was subjected to pressure of 25 MPa. It was lower than in case of smaller samples because at higher pressure values graphite sintering die was cracking and some pieces of it were contaminating powder. When whole powder was pressed, the sintering die was placed in FAST device. During the first trial the previous thermal treatment protocol was applied. Unfortunately, during the initial increase of pressure, before the temperature rise (fig.3.2), the sintering die exploded. In fig.3.11 moment of the explosion on the thermal treatment scheme is marked by red "X". Internal pressure induced by organic phase burn out must have been too high. When only 2.8 g of powder was sintered (20 mm of diameter and 2 mm height) pressure from binder burn out was low enough not to give negative effects on the thermal treatment cycle. Dashed line indicates the temperature which was intended for sintering. Previously less than 3 g of powder was sintered at a time so burn out of organic components did not affect

sintering considerably. In comparison with 90 g sample, burn out of organics became most likely too violent and combined with application of external force resulted in cracking of the matrix. To avoid this issue for the next trials, modification of sintering cycle was crucial.

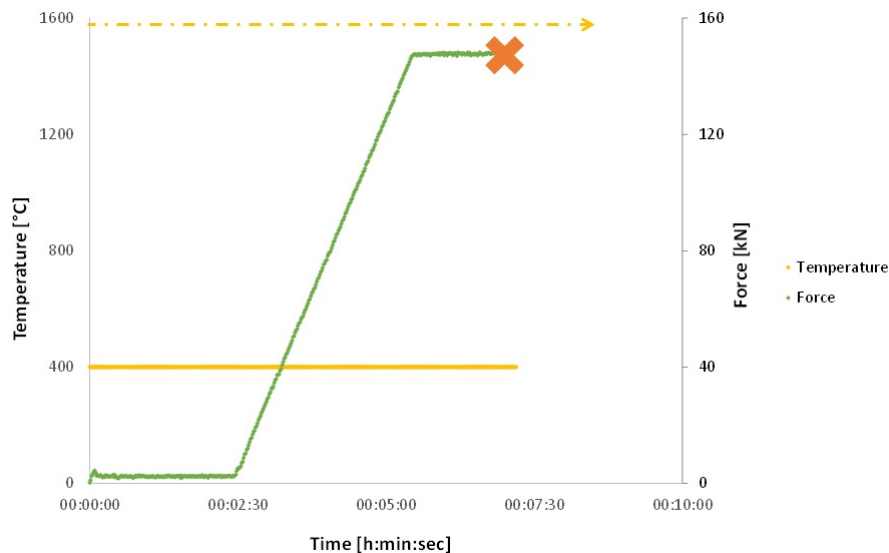


Figure 3.11: Sintering cycle for the first attempt of up-scaling material fabrication, 90 g sample

It was decided to change two aspects. Firstly, holding time of about 3.5 hours at 490°C was applied in order to let organics burn out completely. Secondly, pressure was not applied as usually at the beginning of the sintering, but at the end of the stage of bonder burning to allow gas release. Afterwards pressure was introduced and then temperature increased during 1 hour up to 1600°C (heating rate of 20°C/min). Unfortunately cooling rate was extremely high (around 600°C/min) and sample was very cracked although it held in one piece.

Later, cooling rate was set to 10°C/min to avoid cracking. Final sintering protocol is shown in fig.3.12.

It allowed the fabrication of a pellet of 50 mm diameter and 8.5 mm height (fig. 3.13). Sample was superficially damaged but it held in one piece due to lack of deep cracks.

To verify alumina platelets alignment in up-scaled material processed by uniaxial pressing EBSD analysis of first sample (heating 20°C/min, cooling 600°C/min) was performed. In the fig. 3.14 results are presented in comparison with sample processed by freeze casting. Platelets alignment is satisfactory. It is also visible that grain size has significantly increased in comparison to previous samples. Size distribution was not calculated as there is not enough grains in the analysed area. Decrease of heating speed from 100°C/min to 20°C/min increased time of thermal treatment, resulting thus in grain growth.

Samples sintered according to final protocol were cooled slower (10°/min) so it is possible that grain growth was even more pronounced. It is highly probable that con-

3.3. UP-SCALE

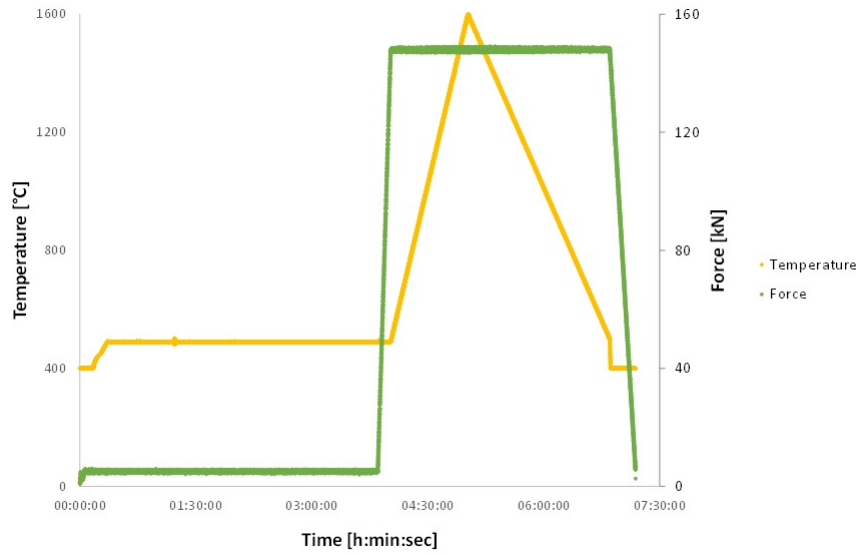


Figure 3.12: Optimized sintering cycle for up-scaling material fabrication

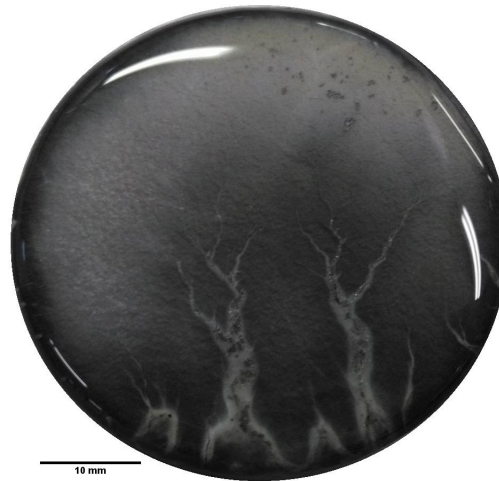


Figure 3.13: Sample obtained by uniaxial pressing and FAST with modified sintering cycle

siderable increase in grain size will have negative effects on mechanical properties of the material. It is crucial to find a way to modify thermal treatment to limit grain growth. It is probable that as slurry stability is less important in case when there is no freezing under flow required, some organic components could be excluded from the composition or at least their quantities limited. That could shorten burn out step. On the other hand presence of polymers might induce platelets sliding which allows their alignment. It should be also possible to perform some powder pre-treatment to eliminate organics before sintering. However, it is most important to limit time when sample's temperature is over 1400°C. Maybe slightly faster heating and cooling would not result in material cracking. There is no doubt that uniaxial pressing simplifies fabrication of materials with aligned alumina platelets and that there is still room for improvement.

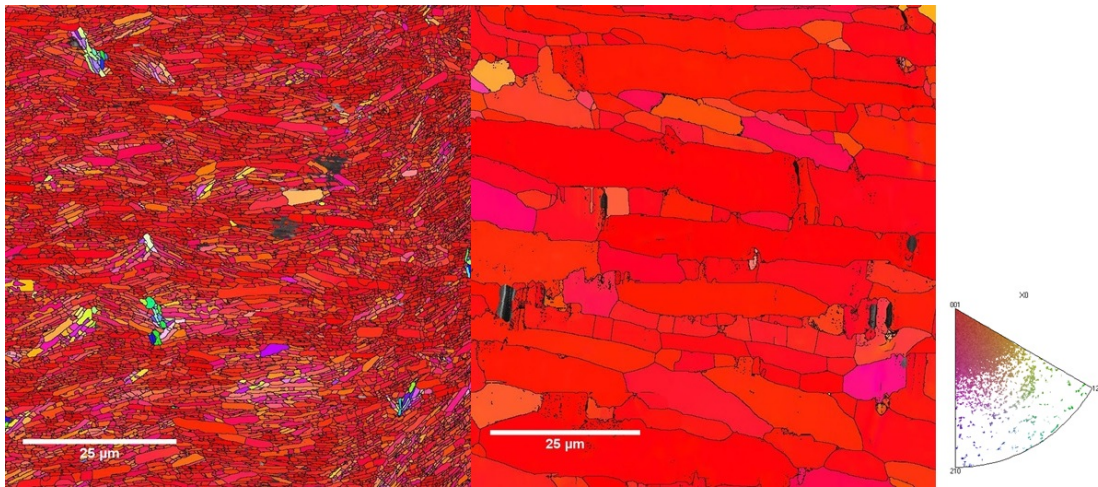


Figure 3.14: Comparison of platelets orientation and grain size of sample processed by uniaxial pressing and up-scaled one

Unquestionably, replacement of freeze-casting by uniaxial pressing and adapting sintering cycle to greater quantities of a powder is a step towards industrializing of architected alumina. There are some aspects that should be improved before moving towards mass production. Grain growth problem should definitely be solved. Eliminating of freezing under flow step permits to change some components of the slurry, like reducing organics content. After optimising of fabrication mechanical testing must be performed to determine whether mechanical properties of the material are close to material prepared at the laboratory scale.

Chapter 4

Modification of the interphase between platelets

Nacre-like alumina, elaborated by Florian Bouville during his thesis, turned out to be a superior material. Its excellent mechanical properties proved that if we manage to mimic natural microstructures, we can obtain materials with mechanical performance that surpasses what we could have expected from the rule of mixtures. It leads to a conclusion that good arrangement of components of composite is also crucial. Satisfactory alumina platelets alignment leads to improvement of mechanical properties. It gives us the opportunity to work on novel materials combining properties which were believed to be mutually exclusive.

To reveal the potential of bioinspired materials various modifications were introduced into primary formulation. In this chapter, we focus on modifications of the interphase between platelets. Firstly, alumina nanopowder was replaced by zirconia nanopowder to check if it would allow to improve the interphase properties. Zirconia is frequently added to alumina to improve its mechanical performances. The fracture resistance of alumina can be improved thanks to residual stresses arising from difference in thermal expansion coefficients of those materials. Using graphene oxide as a mortar for 'bricks' of alumina was another option explored to improve first hierarchical level.

This chapter summarises the outcome of mentioned experiments and compares them to each other. Four point bending was used to measure the mechanical properties of the diverse composites. Crack propagation helps assess if a particular interphase composition improves the properties of a material. Fig. 4.1 illustrates this dependency.

The figure above shows stress-strain curves of three composites made of alumina nanoplatelets, with different interphases: nanoparticles of alumina, glassy phase and nanoparticles with glassy phase. Material containing nanoparticles has increased value of strain but material with glassy phase has significantly higher stress at failure. There is also a visible difference in materials' failure: nanoparticles allow cracks to propagate in a more stable way before complete failure while material with glassy phase is rapidly broken in a brittle mode. The third curve illustrates that mixture of two elements of the interphase provides the optimal mechanical response.

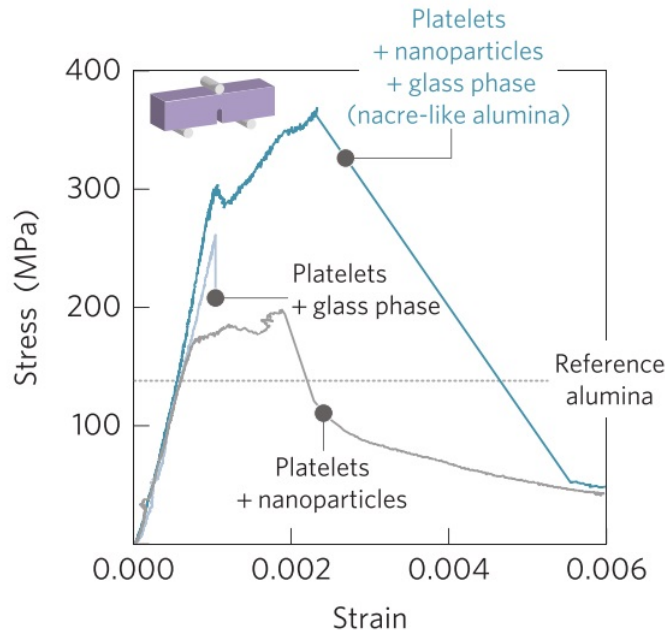


Figure 4.1: Stress-Strain curves of materials with three variants of the interphase (notched samples) [9]

4.1 Incorporation of zirconia

Alumina is commonly used in industrial applications due to its satisfying mechanical behaviour. On the other hand increasing its fracture toughness is a desired modification. One way to improve the mechanical response of alumina is to add stabilised zirconia and thus develop a transformation-toughened ceramic [79] [80]. As it is commonly stated in the literature improvement of fracture resistance can also be obtained by introducing residual stresses [81] [82].

These residual stresses are the result of a difference between values of coefficient of thermal expansion of both materials: $10.5 \times 10^{-6} K^{-1}$ for ZrO_2 and $7.2 \times 10^{-6} K^{-1}$ for Al_2O_3 .

The difference is probably even higher in the case of alumina platelets which are highly anisotropic. As illustrated in fig. 4.2, thermal expansion occurs mainly along the thickness direction and value of difference in size for length and width is significantly lower. The most desired microstructure of such composite is small (nanoscale) grain size of zirconia and narrow particle size distribution of both components [20] [83].

Several techniques to incorporate ZrO_2 into Al_2O_3 matrix are known: mechanical mixing of powders [80], attrition milling of zirconia grinding media [80] or various sol-gel syntheses [79] [20].

In this study we considered two approaches to develop alumina/zirconia composites with architected microstructure and investigated their properties in com-

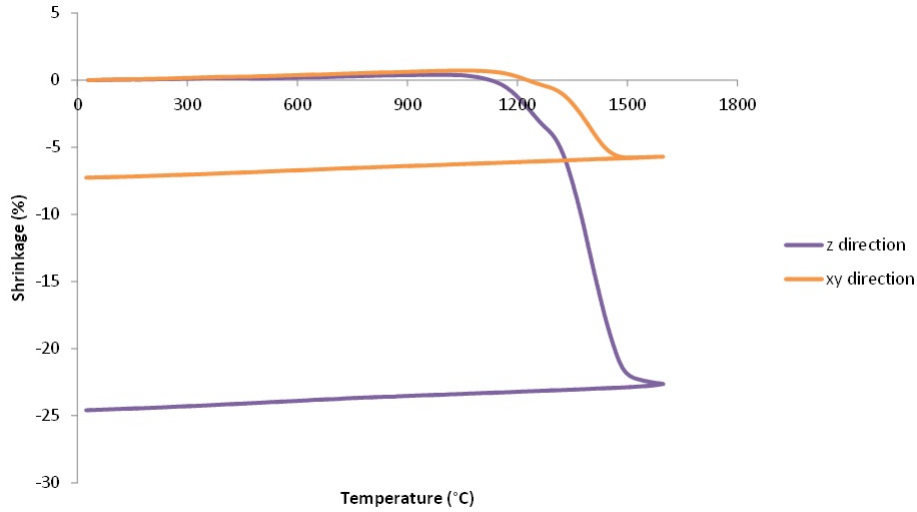


Figure 4.2: Linear thermal expansion of a composite composed of 25% alumina platelets and 75% TM-DAR (alumina nano-powder) as a function of direction: in plane (xy) or out of plane (z)

parison to the reference nacre-like alumina. In both cases, ZrO_2 replaces Al_2O_3 nanopowder which creates bridges between platelets and surface roughness. In the first approach, TM-DAR was simply exchanged by the same amount of fine stabilised zirconia powder to benefit from both: transformation toughening and residual stresses. The second approach consisted of sol-gel processing of alumina platelets and, as a result, the deposition of zirconia at their surface.

4.1.1 Zirconia nanopowder

To prepare Al_2O_3 / ZrO_2 composite, TM-DAR from the standard formula (see chapter "Materials and methods") was replaced by the same weight of TZ-3Y-E fine powder (TOSOH) in the slurry (composition no. WS_56). As the density of zirconia and alumina are different, we ended up with different vol. % (2.1 vol. % instead of 3 vol. %). In the table no. 4.1 all constituents are listed.

Component	Mass [g]	Percentage massive [%]
Water	80.0	60 (of entire slurry)
Carbopol	0.243	0.3 (of water)
Darvan 7-NS	0.516	1.0 (of ceramic powder)
Fine zirconia powder	1.548	2.9 (of ceramic powder)
White sapphire (alumina platelets)	50.042	37 (of entire slurry)
Nexsil 20K	1.288	2.4 (of ceramic powder)
Calcium carbonate	0.129	0.24 (of ceramic powder)

Table 4.1: Components of the slurry WS_56

Later the mixture was frozen under flow with a cooling rate of $1^\circ\text{C} / \text{minute}$ in the range 0 to -60°C . Its rheology was not studied; it was only required that it flows

4.1. INCORPORATION OF ZIRCONIA

through tubes of the freezing setup and at the surface of the freezing plate. Afterwards a sample was placed in a freeze dryer for about 48h. The obtained material had lamellar porosity. It has been cut into cylinders of 20 mm diameter and 20 mm height. It was sintered by FAST (heating rate: 100°/minute, max. temperature: 1600° and pressure: 75 MPa). The addition of zirconia did not affect negatively sintering: the obtained material had 96.1% density (in comparison to 95.3% of reference formula).

Samples were cut into small bars and notched (see chapter "Materials and Methods"). Four-point bending was chosen to the evaluation of material properties and comparing them with others. As samples had notches it was decided that two samples were enough for the purpose of initial screening which was conducted in order to choose the most promising formulations which would be tested further. The results are presented in figures 4.3, 4.4 and 4.5.

Unnotched samples should be used to calculate stress-strain curves. As notched samples were used here, we present force-deflection curves as well. For stress-strain curves calculations from sample height, the notch depth was subtracted.

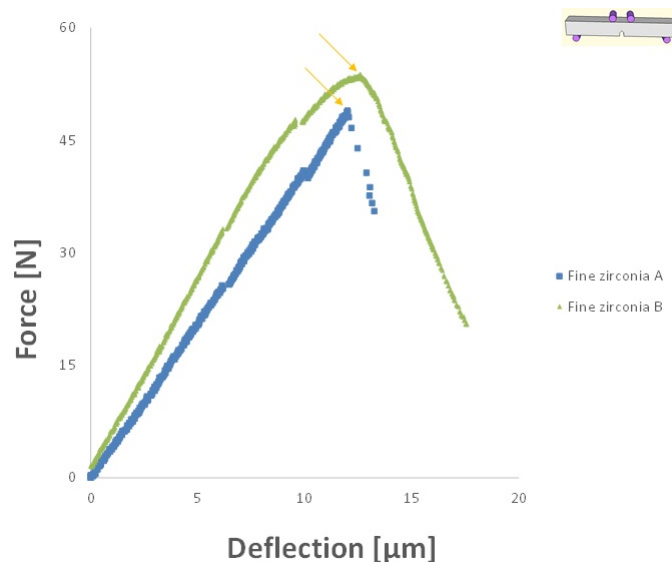


Figure 4.3: Force-Deflection curve of the material with fine zirconia powder instead of TM-DAR

Stress values surpassed 125 MPa. For both sample strain at maximum stress was over 0.0005. For one sample failure with good control of the crack propagation was observed and for the other one not. It is visible that there is no plateau value of stress; when crack propagates, the resistance of a material is quite poor. A very limited R-curve behaviour was observed (fig. 4.5).

The fracture toughness increases slightly (from 4 to 5 $\text{MPa} \cdot \text{m}^{1/2}$ for crack propagation from 0 to 0.4 mm) during bending of the sample. For crack extension of 0.4 mm it reaches value of approximately 5 $\text{MPa} \cdot \text{m}^{1/2}$.

Fig. 4.6 illustrates crack propagation in the material with zirconia powder instead of TM-DAR.

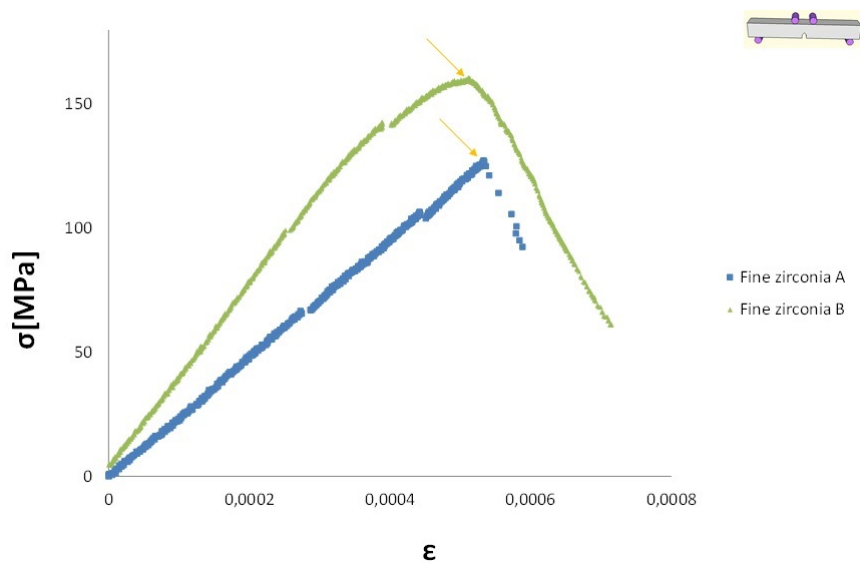


Figure 4.4: Stress-Strain curve of the material with fine zirconia powder instead of TM-DAR

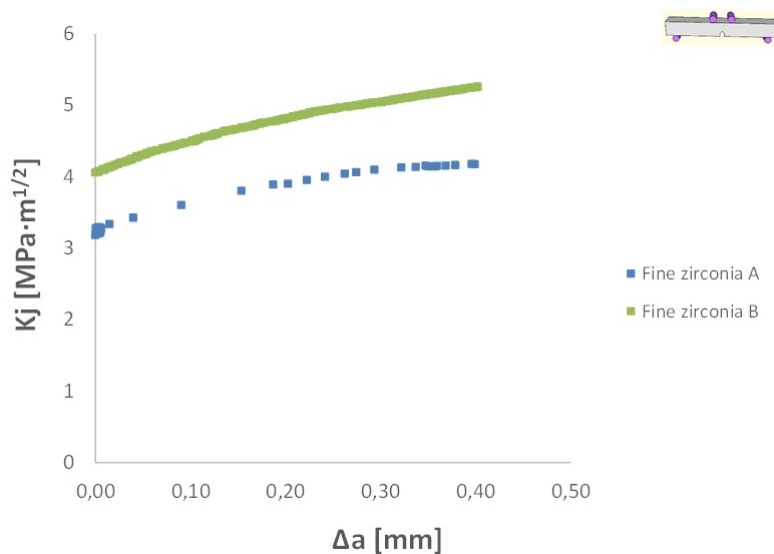


Figure 4.5: R-curves of the material with zirconia powder instead of TM-DAR

Image A represents beginning of the crack propagation at notch tip (indicated by a white arrow). It starts to advance directly on the side as in case of samples prepared by Florian Bouville [9]. The high platelets alignment impedes crack from passing straight through the sample. Image B shows the crack onset with a higher magnification. It allows to notice some crack branching. Images C and D show more details of crack branching.

4.1. INCORPORATION OF ZIRCONIA

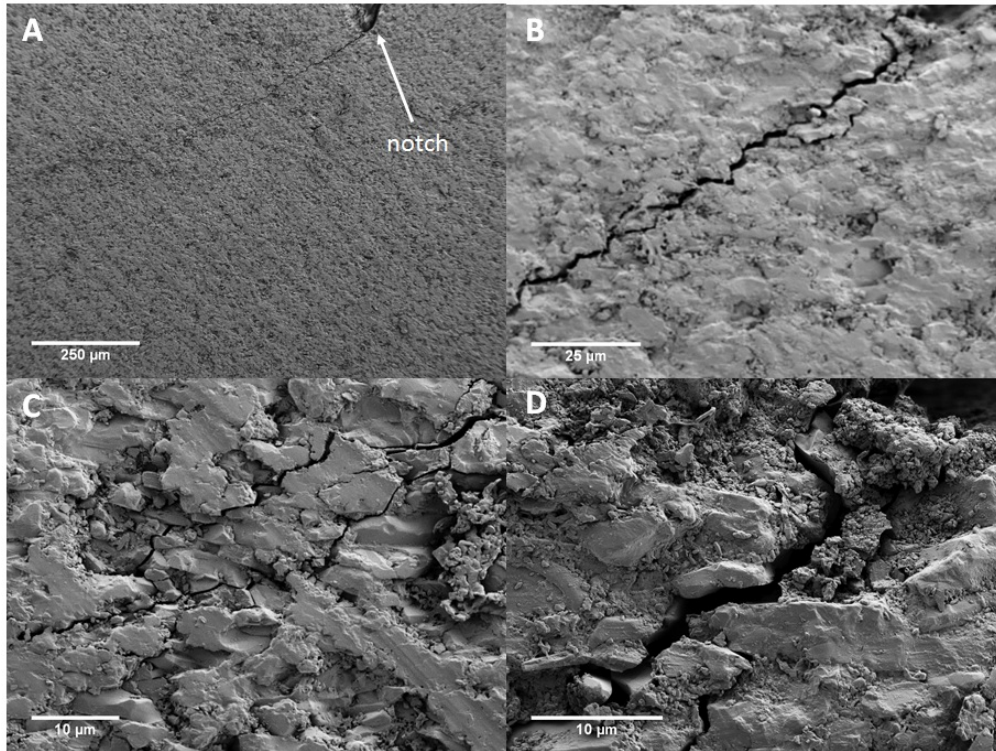


Figure 4.6: SEM images of crack in the sample with zirconia powder instead of TM-DAR. A) A white arrow indicates the tip of the notch and beginning of crack which propagates visibly on one side; B) Same zone of the sample with higher magnification; C and D) Crack branching

Conclusions

The modification of interphase between alumina platelets was performed in order to improve mechanical properties. Results of mechanical testing were thus compared to our reference material: nacre-like alumina prepared by freeze-casting and tested by four points bending as well. Fig. 4.7 shows stress-strain curves of compared materials.

Adding fine zirconia powder does not seem to improve material properties. Although values of stress are similar to that of the reference material, its strain at failure is significantly lower. It seems that proposed composition is not as efficient as expected. It is possible that the vol. % of nanoparticles should be increased.

On the other hand, adding ZrO_2 might give better results if processing route is changed. Depositing fine zirconia particles by sol-gel processing can result in different microstructure and improve mechanical properties of the material.

4.1.2 Alkoxide

As it was already mentioned, there are several techniques to incorporate ZrO_2 into Al_2O_3 matrix: mechanical mixing of powders [80], attrition milling of zirconia grinding media [80] or various sol-gel syntheses [79] [20].

Hydrolysis of zirconium alkoxide on alumina particles meets requirements in terms

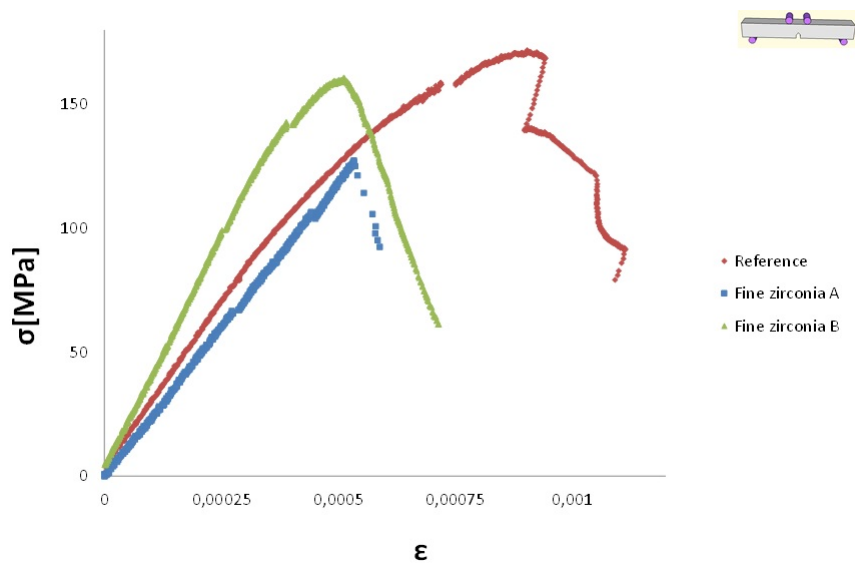


Figure 4.7: A comparison of stress-strain curves of the material with fine zirconia powder instead of TM-DAR with standard nacre-like alumina

of microstructure (homogenous repartition of zirconia) and consequently seems an appropriate powder processing route [79]. Scheme below (Fig. 4.8) illustrates the principle of alkoxide reaction technique.

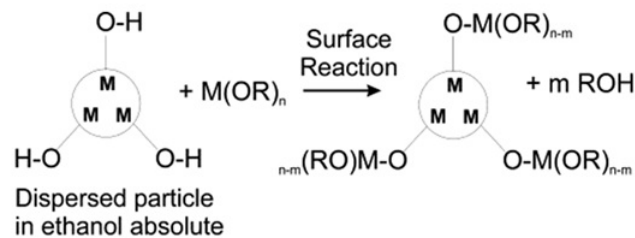


Figure 4.8: A scheme of reaction which allows to deposit zirconia on the surface of alumina platelets

Schehl et al. described a few procedures to prepare of alumina based composites by alkoxide processing; one of them leads directly to alumina/zirconia material with controlled zirconia percentage [20]. The composite obtained after sintering contained 5% of ZrO_2 , fig. 4.9 shows that fine zirconia particles are well distributed at alumina grain boundaries.

The mean grain size of alumina shown above is $1.63 \mu\text{m}$, and zirconia 200 nm. Zirconia is located in 50% of triple points [20]. The density of this material is 98.99%, Young's modulus 381 GPa, bending strength 343 MPa and fracture toughness $7.5 \text{ MPa} \cdot \text{m}^{1/2}$ (in comparison with alumina without additives: Young's modulus 400 GPa, bending strength 326 MPa and fracture toughness $4.5 \text{ MPa} \cdot \text{m}^{1/2}$). Mechanical properties were measured by four point bending technique, fracture toughness

4.1. INCORPORATION OF ZIRCONIA

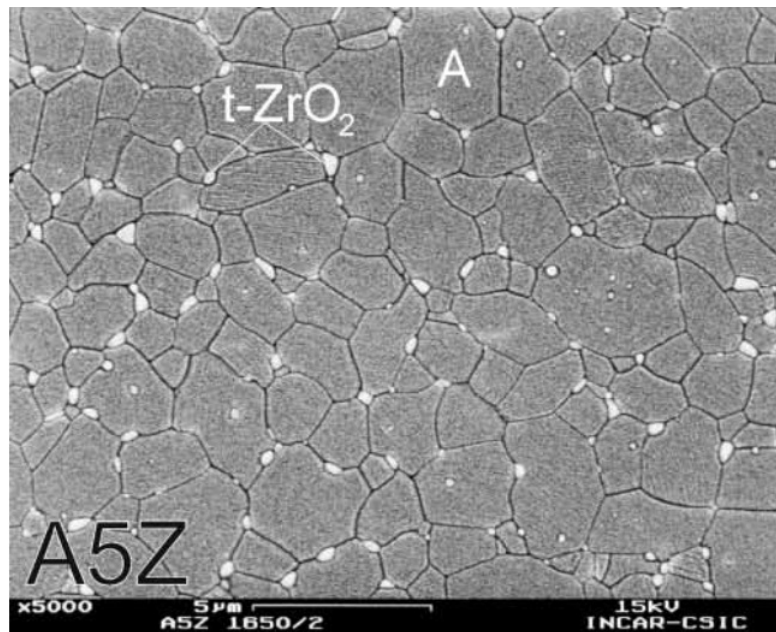


Figure 4.9: SEM image of alumina/zirconia composite fabricated thanks to alkoxide processing [20]

was measured on single edge notched samples ($a/w=0.4$) [20].

Improvement of some mechanical characteristics might be explained by alkoxide processing.

Fig. 4.10 illustrates zirconia grain distribution in two composites, prepared by different processing routes: conventional powder mixing and sol-gel technique.

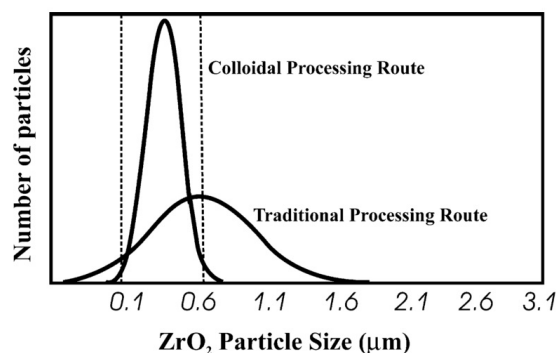


Figure 4.10: Zirconia grain size distribution depending on processing route [20]

Materials prepared by alkoxide technique show good mechanical properties and it seems that sol-gel processing could help to improve mechanical performance of nacre-like alumina and other alumina platelets based composites.

The processing protocol described by Schehl et al. was followed in this study

[20].

To obtain an amount of powder necessary for freezing under flow, 55g of White Sapphire were mixed into 500ml of ethanol absolute 99.9% (any trace of water is undesired during this processing). The slurry was stirred with a magnetic stirrer at room temperature. 6.46g of Zirconium IV-propoxide, 70% solution in 1-propanol (Sigma-Aldrich) was placed in measuring cylinder. Its volume was around 6 ml. 3 ml of ethanol absolute were added; the solution was stirred for a couple of minutes. Alkoxide solution was being added drop-wise to stirred slurry during approximately 15 minutes. Quantities of those components were chosen to obtain 2 vol. % of zirconia in solid phase. In order to evaporate ethanol the mixture was left on the stirrer at 40° overnight. In the morning it was removed from the hot plate and placed in a rotary evaporator. The powder was left in a furnace at 80°. After 3 hours it was used to prepare a slurry no. WS_57. Its components are listed in the table below.

Component	Mass [g]	Percentage massive [%]
Water	80.0	60 (of entire slurry)
Carbopol	0.243	0.3 (of water)
Darvan 7-NS	0.516	1.0 (of ceramic powder)
WS alkoxide modified	51.59	38.5 (of entire slurry)
Nexsil 20K	1.288	2.4 (of ceramic powder)
Calcium carbonate	0.129	0.24 (of ceramic powder)

Table 4.2: Components of the slurry WS_57

Like previous compositions, the slurry WS_57 was frozen under flow and freeze-dried for 48 hours. After sintering (heating rate: 100°/minute, max. temperature: 1600° and pressure: 75 MPa), the material density (93.9%) was slightly lower in comparison with reference formula and the one with fine zirconia powder instead of TM-DAR. A protocol of preparation of samples for mechanical testing was exactly the same. Results of 4PB are presented in figures 4.11, 4.12 and 4.13.

Value of stress (almost 170 MPa) are higher than in case of using fine zirconia powder (close to 160 MPa). However, values of strain are very different for two samples. One sample failed at value only slightly surpassing 0,0005 while the other reached value almost five times higher.

While both have value of fracture toughness only slightly over 5 MPa · m^{1/2} at the onset of crack propagation, the first one breaks at crack extension of 0.38 mm and fracture toughness of 6.86 MPa · m^{1/2}; the second one reaches value of 8.29 MPa · m^{1/2} at crack extension of 0.4 mm without breaking.

Fig. 4.14 illustrates crack propagation in the material with platelets processed by alkoxide reaction.

As in case of previously tested material crack beginning is located at notch tip (indicated by a white arrow) and parting directly to the side (images A and B). In the image C crack branching is visible. In the image D the are pulled out platelets.

4.1. INCORPORATION OF ZIRCONIA

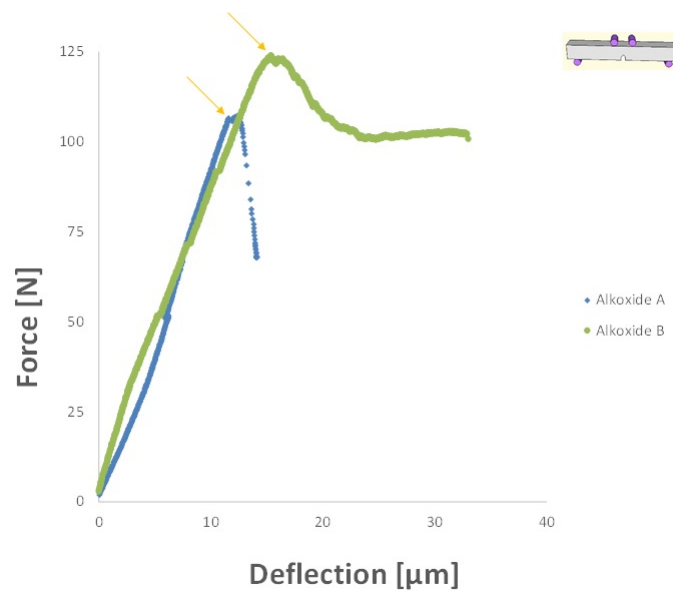


Figure 4.11: Force-Deflection curve of the material with platelets processed by alkoxide reaction

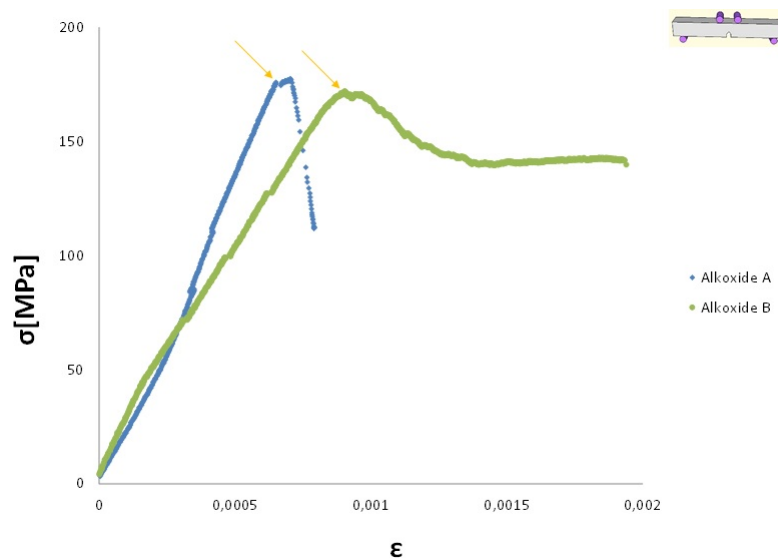


Figure 4.12: Stress-Strain curve of the material with platelets processed by alkoxide reaction

Conclusions

Stress-strain curves of the material in comparison with reference formulation are presented in the fig. 4.15.

Assessing material elaborated by sol-gel chemistry is more difficult. Stress is comparable with reference but strain does not provide clear information if it is favourable modification: one sample is significantly better than the other. Homogeneity of deposit should be assessed by TEM to determine if processing should be improved. It is possible that thanks to some adjustments in the processing, the results could be

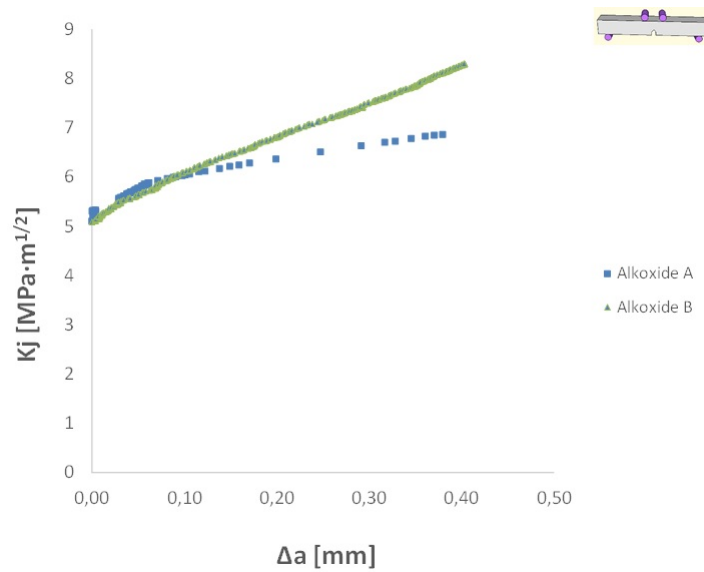


Figure 4.13: R-curves of the material with platelets processed by alkoxide reaction

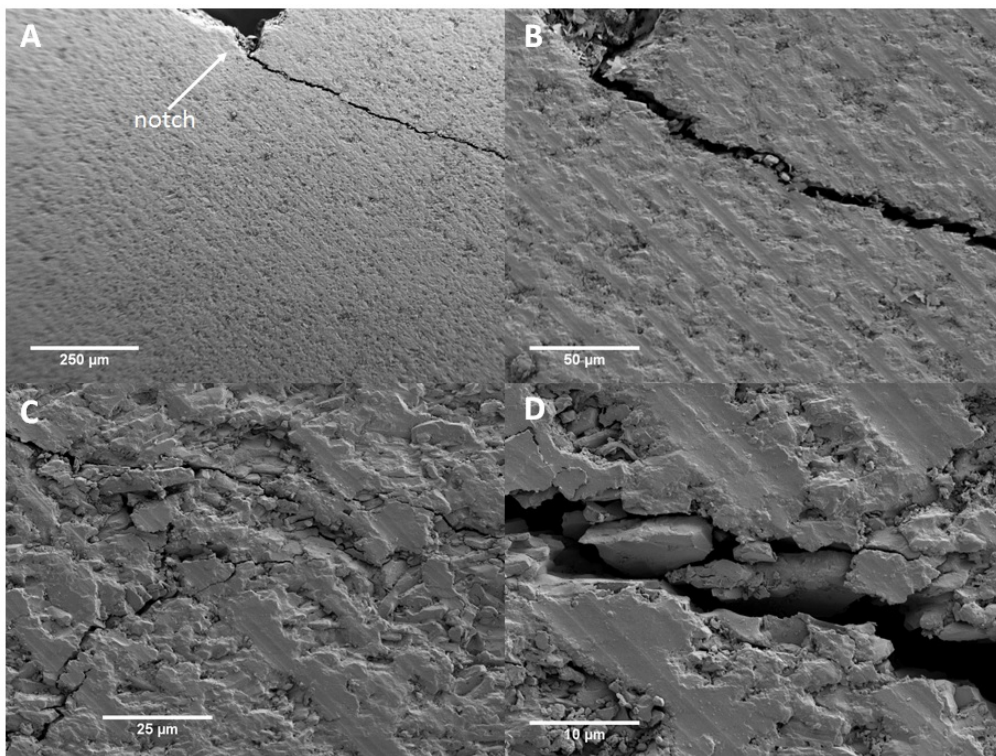


Figure 4.14: SEM images of crack in the sample with platelets processed by alkoxide reaction. A) A white arrow indicates the tip of the notch and beginning of crack which propagates visibly on one side; B) Same zone of the sample with higher magnification; C) Crack branching; D) Zone where some platelets probably have been pulled out, it looks like crack had passed from their both sides

better. Sample B had a really promising mechanical response so it deserves more exploration in the future. On the other hand, apart from mechanical properties, in

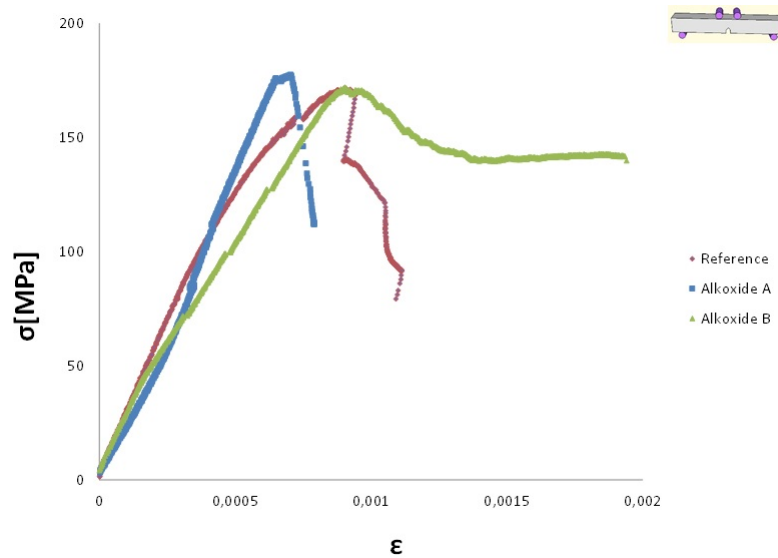


Figure 4.15: A comparison of stress-strain curves of the material with platelets processed by alkoxide reaction with standard nacre-like alumina

this work we also took into account optimisation of material preparation and its potential to be upscaled. Conducting alkoxide reaction is quite complicated and time consuming. Seeing that potential improvement of mechanical properties is not that significant regarding level of complexity needed to obtain it, it was decided that a more efficient solution should be found.

4.2 Graphene

Adding various forms of zirconia into alumina composite was not the only way to modify the interphase between alumina platelets. Another approach was to add graphene to the material.

Since its discovery in 2004 by A.K. Geim (although its existence has been theoretically predicted in 1947 by P. R. Wallace [84]) graphene has attracted a lot of attention [85]. Graphene exhibits exceptional electrical [86], mechanical [87] and thermal properties [88]. It seems like a good candidate to improve properties of materials applied in lithium ion batteries [89], bio-sensors [90], transparent conductors [91] or supercapacitors [92].

Graphene exists in several forms: nanosheets (GNs), carbon nanofibers (CNFs), single-walled carbon nanotubes (SWCNTs), multi-walled carbon nanotubes (MWCNTs) or graphene platelets (GPLs) [23]. Adding GPLs seems to be particularly interesting in case of this study as it could form desired flat interphase between the alumina platelets. As one of the steps of freeze casting processing is slurry preparation, it would be advantageous to choose a form of graphene that could be easily dispersed in water.

Graphene oxide has functional groups on its surface so obtaining stable suspension seems feasible. Its polar character provokes electrostatic repulsion so it is easily dispersed in polar solvents like water [93] [94].

A. Centeno et al. obtained graphene/alumina composites using GO as a graphene precursor and sintering their powders by FAST [94]. They have confirmed by Raman spectroscopy that thermal reduction of GO has occurred.

H. Porwal et al. [21] studied the effect of graphene content in alumina matrix on material fracture toughness. They used powder processing route and spark plasma sintering to obtain dense composites with various amounts of graphene. In Fig. 4.16 an optimal amount of graphene in terms of mechanical performance exists around 0.8 vol.%. Increasing concentration above 1 vol.% did not further increase K_{IC} but significantly reduced it. According to the authors the addition of 0.8 vol.% of graphene improved K_{IC} by around 40% when measured by Vickers indentation fracture test and by approximately 25% when measured by chevron notch method.

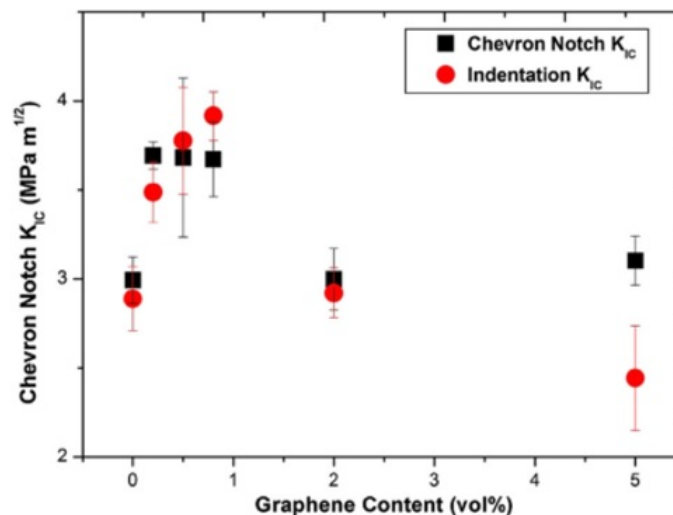


Figure 4.16: Values of fracture toughness measured by indentation and chevron notch as a function of graphene content in dense alumina composites [21]

The addition of graphene changes the mechanisms of crack propagation in alumina from inter-granular to trans-granular. Graphene anchored between the grains of alumina induces various toughening mechanisms (Fig. 4.17) like graphene pull out, crack bridging, crack deflection, and crack branching [21].

As there are publications which report positive effect of addition of graphene on mechanical properties of ceramics, there are also ones that claim no effect or even a

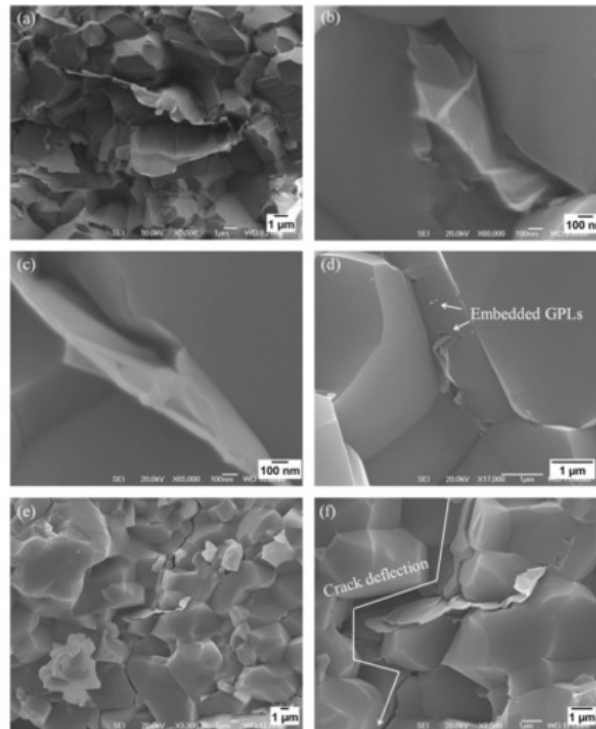


Figure 4.17: Toughening mechanisms in GPL alumina composite [22]

negative one.

A. Rincon et al. prepared three groups of samples to compare material properties and estimate the influence of graphene addition. Those groups were: pure alumina (A), alumina reinforced with zirconia (AZ), and alumina reinforced with zirconia and graphene (AZGO). In Fig. 4.18 it is shown that in comparison with pure α -alumina the addition of ZrO_2 and graphene reduces values of hardness and modulus [23].

Layer	H_{IT} (GPa)	Std. dev	E (GPa)	Std. dev.	E_r (GPa)	HV_{2kg}
A	27.0	0.3	409.8	2.9	395.8	2145
AZ	25.8	0.4	400.0	3.7	317.8	2020
AZGO	23.5	0.3	373.9	3.1	298.0	1856

Figure 4.18: Mechanical properties measured by nanoindentation for laminates: A-alumina, AZ-alumina with 5 vol. % of 3Y-TZP and AZGO-alumina with 5 vol. % of 3Y-TZP and 2 vol. % of graphene oxide [23]

Even though it has not been clearly determined if the addition of graphene to ceramic leads to improvement of mechanical behaviour, we decided to study if the addition of graphene into the interphase of nacre-like alumina could promote extrinsic reinforcement mechanisms and as a consequence an increase its strength and toughness.

Presently on the market there are numerous graphene products available. Making our own synthesis was not required as a first stage. Graphene Oxide is known for being a proper precursor of graphene if the material is sintered by FAST. This technique provides the reducing atmosphere necessary to obtain ceramic/graphene composite [95]. In order to avoid sophisticated dispersing process of the compound, ready-made suspension was used to prepare a slurry. Its concentration (4mg/mL) was appropriate for using it directly instead of distilled water. This way the quantity of GO in respect to alumina platelets was equal to 1.6%. It is an adequate proportion, similar to that of organic phase to aragonite in natural nacre [96].

Substituting interphase composed of calcia and silica by graphene is not straightforward. It requires adapting quantities of additives like dispersant or binder. From the broad spectrum of currently available binders, Isobam 104 was chosen as the most promising. It is not only water soluble but also improves strength of a green body making it easier to handle. Apart from functioning as a binder it is also a dispersing agent. In order to determine how much of Isobam 104 was needed to obtain a green body easy to handle, various formulations were considered. As typically low dosages are required we studied three values: 1%, 3% and 5% of the mass of alumina platelets. In table 4.3 detailed compositions of tested slurries are given.

Slurry	Water [g]	Graphene Oxide [g]	Alumina platelets [g]	Isobam 104 [g]; [%]
GO_1	20.0	0.08	8.80	0; 0
GO_3	20.0	0.08	8.80	0.088; 1
GO_4	20.0	0.08	8.80	0.264; 3
GO_5	20.0	0.08	8.80	0.44; 5

Table 4.3: Concentrations of Isobam 104

Prepared mixtures were sonicated at 30% amplitude during approximately 8 minutes. Afterwards they were poured into moulds placed on the copper freezing plate and frozen at 1°C/minute. Once completely frozen (at -65°) they were placed in the freeze-dryer for 48h. When samples were completely dry we assessed if their handling was satisfactory. All concentrations of the binder seem to work well and provide materials with adequate green strength. A binder concentration of 1% was chosen for further works, because it makes it easier to eliminate organics during sintering.

Slurry number GO_11 was prepared to perform first trial with alumina/graphene composite. Its composition is shown in the table below.

Component	Mass [g]
Water	80.0
Graphene Oxide	0.32 (within liquid phase)
WS	50.5
Isobam	0.505

Table 4.4: Components of the slurry GO_11

For comparison with composition mentioned above a slurry of standard composition was prepared as well. Isobam 104 was replaced by Carbopol and Darvan; TM-DAR powder was also added.

4.2. GRAPHENE

Component	Mass [g]
Water	80.0
Graphene Oxide	0.32 (within liquid phase)
WS	49.5
TM-DAR	1.531
Carbopol	0.241
Darvan 7-NS	0.510

Table 4.5: Components of the slurry GO_11

Unfortunately this slurry was extremely viscous and it was not possible to freeze it under flow. It is not sure why viscosity was so high. It might have been due to interactions between nanoparticles of alumina and liquid phase precursors and graphene oxide. It was frozen in the cylindrical moulds instead but those samples were not appropriate for comparison of mechanical properties because their porosity was oriented in another direction. During sintering by FAST it was observed that the maximal densification occurred at lower temperature than for material without addition of graphene (decrease of maximal temperature from 1600 to 1500°C). Samples made from slurry GO_11 were tested according to the same protocol as Al_2O_3 / ZrO_2 composites. Results of 4PB are presented in figures 4.19, 4.20 and 4.21.

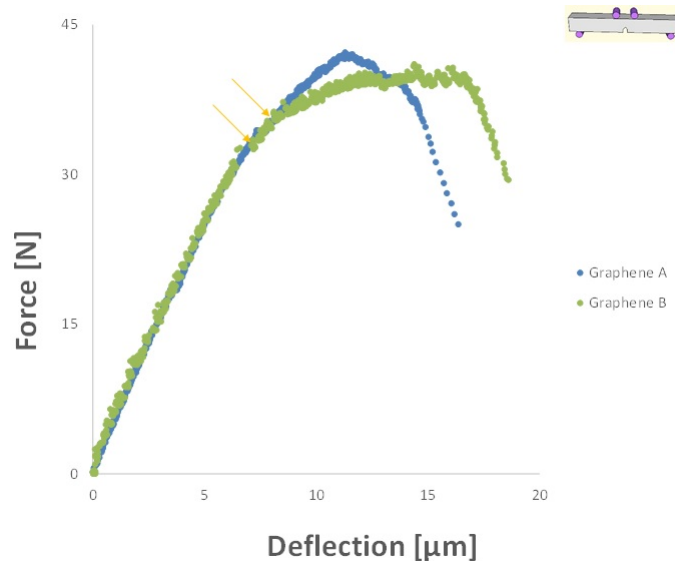


Figure 4.19: Force-Deflection curve of the material with graphene in the interphase

It is immediately visible that values of stress are lower than in case of addition of zirconia, they do not reach 100 MPa. Strain at failure for both samples surpasses 0.0008. Graphene favours crack deflection giving larger capacity of deflection in bending.

A proper estimation of the evolution of fracture toughness value was difficult, as the determination of the onset of crack propagation is not obvious. Yellow arrows in figs. 4.19 and 4.20 mark the probable onset of crack propagation. Fracture toughness, even though increasing with crack propagation, is not satisfactory as stronger

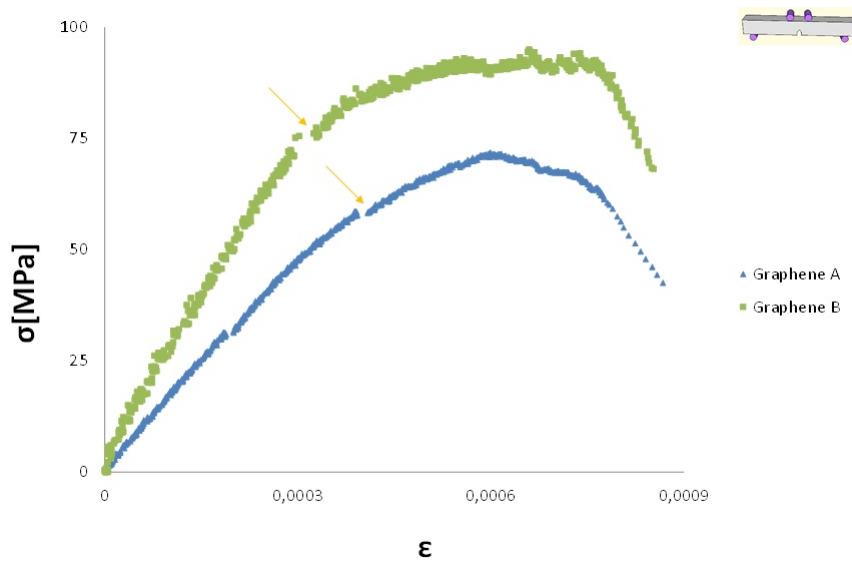


Figure 4.20: Stress-Strain curve of the material with graphene in the interphase

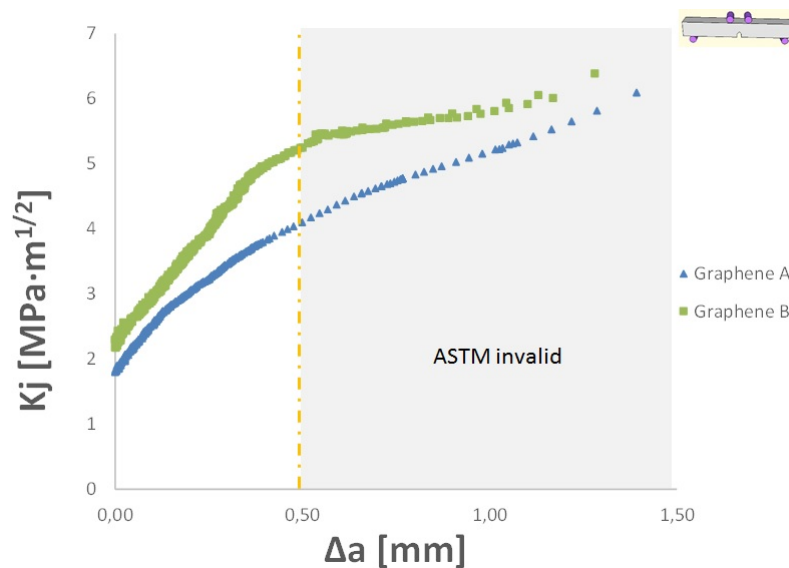


Figure 4.21: R-curves of the material with graphene in the interphase

sample reached a value of only $5 \text{ MPa} \cdot \text{m}^{1/2}$ within zone valid by standard ASTM (0.25h; h-sample height [78]). Values for crack extension surpassing 0.5 mm are not valid for ASTM norms.

Fig. 4.22 illustrates crack propagation in the material with graphene in the interphase. There seems to be an extreme crack deflection here.

As in case of previously tested material crack onset is located at notch tip (indicated by a white arrow) and moving directly to the side (images A and B). Image C illustrates a zone where crack sharply changed its direction from horizontal to vertical. In the picture D higher magnification of fracture zone is presented. There are some flaky structures visible. They could be stacks of graphene platelets but it is not

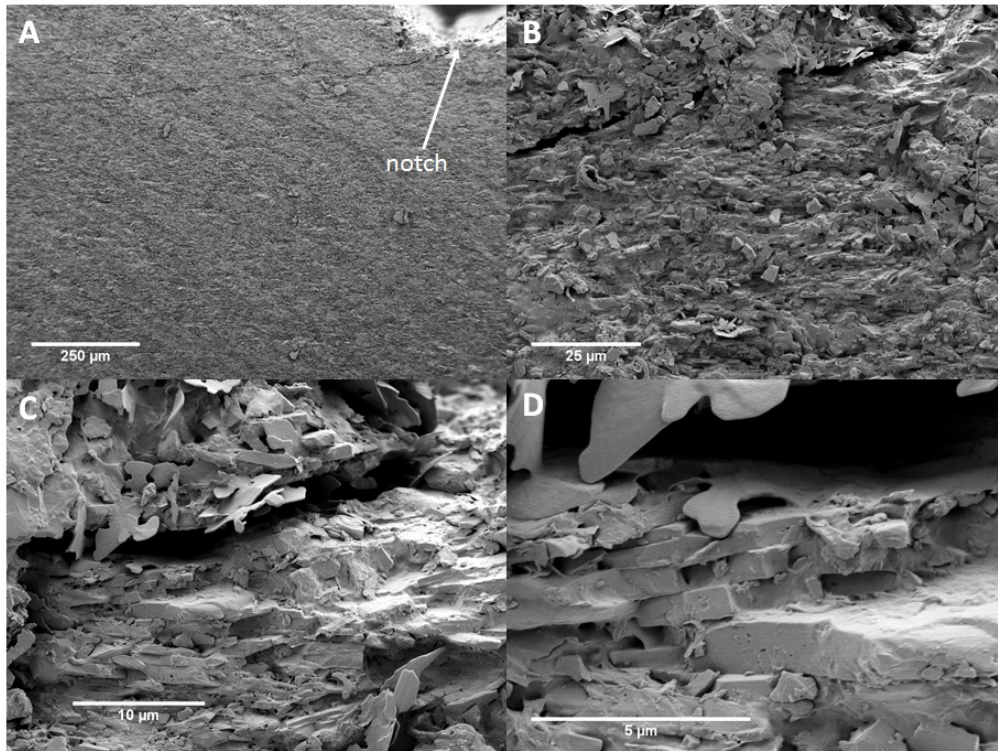


Figure 4.22: SEM images of crack in the sample with graphene in the interphase. A) A white arrow indicates the tip of the notch and beginning of crack which propagates visibly on one side; B) Same zone of the sample with higher magnification; C) A zone where crack has changed its path (from horizontal in the middle of the image to vertical on the left); D) Zone where some flaky structures are visible on the surface of some alumina platelets

sure. More accurate analysis should be conducted to determine character of those forms.

Conclusions

Stress-strain curves of the material in comparison with reference formulation are presented in the fig. 4.23.

In case of samples where graphene substituted glassy phase and nanoparticles of alumina it is clearly seen that mechanical properties are strongly reduced. Then again, because of rheological requirements, that slurry had to flow through the freezing setup, adding graphene to standard composition without eliminating some components was impossible. In case when mechanical properties are the most important, the addition of graphene does not seem to be useful. Maybe, if priority is developing electrically or thermally conductive ceramics (like self-monitoring materials [97]), some compromises in terms of material strength can be made.

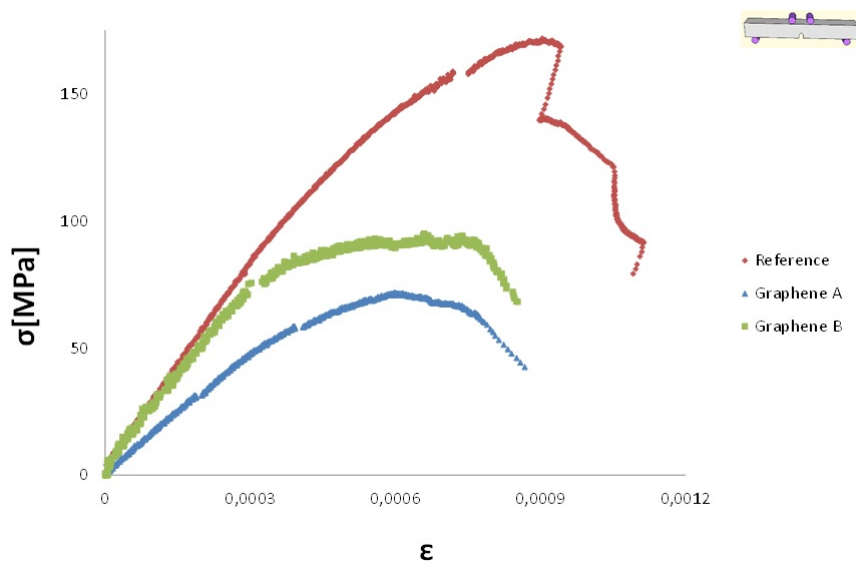


Figure 4.23: A comparison of stress-strain curves of the material with graphene in the interphase with standard nacre-like alumina

4.3 Conclusions of the chapter

In this chapter we proposed three modifications of the material interphase to improve the mechanical behaviour of biomimetic alumina material. In the plots below (fig. 4.24), the comparison of properties of materials with tested formulations is presented, one selected sample for each formulation.

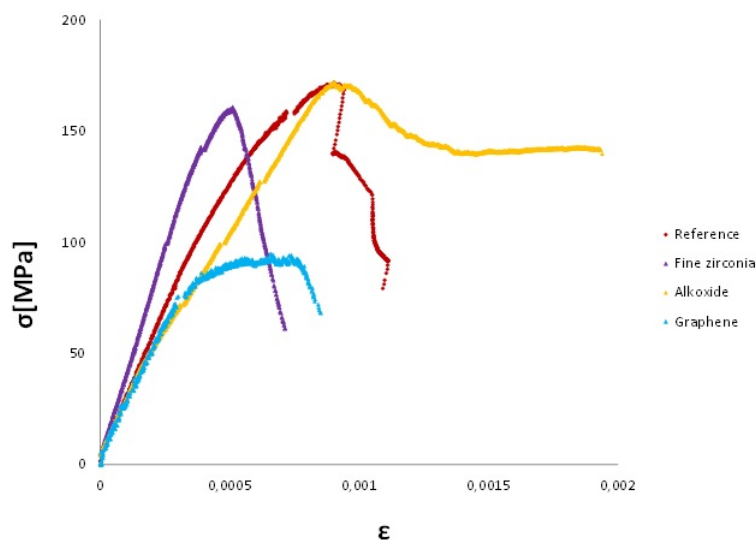


Figure 4.24: A comparison of stress-strain curves of all the material formulations tested in this study

Material with platelets processed by sol-gel chemistry seems the most promising. On the other hand two tested samples gave significantly different results (fig. 4.12).

4.3. CONCLUSIONS OF THE CHAPTER

While maximal stress values are close, strains reached by two samples are completely different: one did not reach value 0.001 and the second was close to 0.002. It seems clear that more tests should be performed to optimize this processing.

Samples with fine zirconia powder instead of TM-DAR (nano alumina) reached values of stress slightly lower than reference material but strain was importantly lower, not reaching 0.0008. It is difficult to say, why residual stresses did not improve mechanical properties of the material. It is possible that influence of TM-DAR on the quality of alumina platelets sintering is so important that excluding it from the formulation has a negative effect difficult to compensate by another additives. Plots in the fig. 4.1 suggest that the presence of nanopowder of alumina ameliorate failure strain of the material with aligned alumina nanoplatelets. Maybe combining optimal quantities of two types of fine powders could improve mechanical properties.

Replacing the reference interphase with graphene gave the least impressive properties. As for previous formulations it was probably lack of alumina nanopowder which provoked decrease in mechanical properties. In addition, in case of formulation containing graphene, it was impossible to freeze under flow slurry with liquid phase precursors, so formulation tested by 4PB was lacking not only TM-DAR but also glassy phase precursors. It is understandable that graphene alone could not substitute alumina nanopowder and glassy phase at once. Those two components contribute significantly to increase of stress and strain and excluding them from the composition gives negative effects. Maybe using another, non polar form of graphene could decrease its interactions with nanoparticles in the slurry and thus enable freezing under flow composition with graphene and TM-DAR in the interphase.

To sum up, tested modifications did not meet our expectations. We decided that adding another hierarchical level to material's architecture should be more efficient than modifying interphase which already seems well optimised.

Chapter 5

Alumina/titanium composites

Adding some metal is a direct way of inducing ductility in ceramic materials. To avoid complicated fabrication process it is suitable to choose metal with high melting point, which would allow to sinter it simultaneously with alumina. Titanium melting temperature equal to 1670°C [14] makes it a proper element to incorporate into aligned alumina matrix. In the chapter "Literature review" there is a section dedicated to mechanical and physical properties of titanium which further justifies the choice of this metal (Young's modulus 105 GPa, stress 170-480 MPa, tensile strength 240-550 MPa and elongation 15-24 % for commercially pure titanium of grades 1-4 [14]).

This choice is a bit unusual as alumina is commonly paired with aluminium. With some additives, aluminium creates strong interphase with alumina [98]. In this case its low melting point (660°C) would complicate already sophisticated fabrication technique.

5.1 Fabrication and structural characterisation

5.1.1 Fabrication

To fabricate titanium/alumina composites, a powder of the reference composition (alumina platelets, nano-alumina powder and glassy phase precursors) and titanium foil of various thickness (20-500 μ m, 99.6 % purity, GoodFellow) were used. Alternating layers of ceramic and metal (four ceramic layers and three metal layers) were pressed directly in the sintering die (around 150 MPa). Field assisted sintering technique (FAST) protocol was simple: heating at 100°C/min up to 1500°C and immediate cooling with the same speed, applied pressure of 75 MPa (fig. 3.2). After sintering each ceramic layer was approximately 500 μ m thick. More details can be found in the chapter "Materials and methods".

Obtained material was cut into bars and polished (as in "Materials and methods"). Microscopic observations were conducted first. Scanning electron microscope (SEM) picture (fig. 5.1) illustrates the obtained microstructure. It can be divided into three parts: titanium foil, diffusion zone of metal into ceramic matrix and alumina part. Thanks to diffusion, metal is incorporated between platelets. This interphase mod-

5.1. FABRICATION AND STRUCTURAL CHARACTERISATION

ification otherwise is very difficult, if not impossible, to achieve. Infiltrating metal into so small pores can be difficult and it would add one more processing step (first sintering of ceramic matrix and then infiltration). Furthermore, elements of a set-up for liquid metal infiltration are made of alumina so melting point of titanium is too elevated for this processing [99]. Adding titanium nano-powder directly into powder mixture would also not be feasible due to its high explosivity.

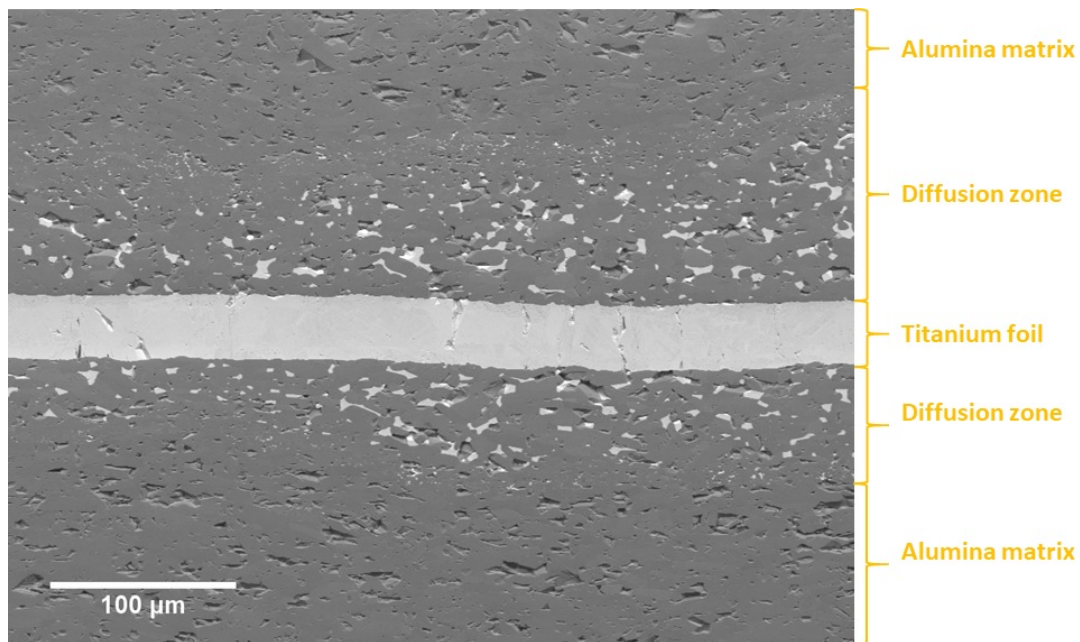


Figure 5.1: SEM image of alumina/titanium composite (sintered at 1500°C) showing three regions (initial titanium foil thickness of 50 μm , final 30-40 μm). Some platelets pull out has occurred during polishing in the alumina matrix.

Thanks to one simple processing step we have obtained a composite with a sophisticated hierarchical structure. Firstly alumina platelets are aligned thanks to uniaxial pressing (see the chapter "Simplification material fabrication"). Abnormal grain growth was not noticed. Interphase between the platelets is composed of nano particles of alumina and glassy phase. Pores are infiltrated by titanium and remaining porosity is low (less than 5%). Finally, ceramic pellets alternate with titanium foil. To our knowledge nobody has achieved ceramic/metal composites with three hierarchical levels in one processing step.

Energy Dispersive X-ray Spectroscopy (EDX) allowed us to analyse the obtained composite. Entire foil thickness and an area close to it were chosen (see fig. 5.2).

EDX revealed that in the Ti foil there was some oxygen in the entire cross-section and some traces of aluminium close to the interphase (fig. 5.3).

As during SEM observations numerous cracks in the metal were noticed, closer look at them was taken. Backscattered Electron (BSE) detector allowed us to see foil topography in more detail (fig. 5.4). Some cracks seem to be superficial but it is visible that there are cracks passing through the foil. Any cracking was not noticed in alumina layers.

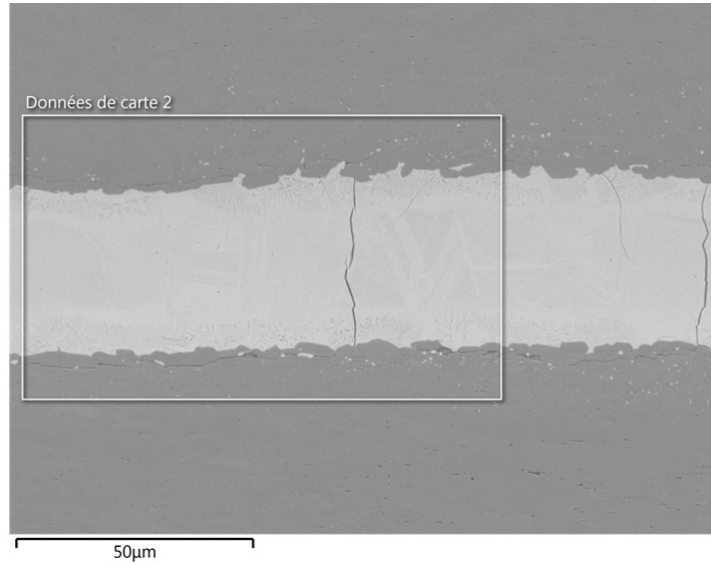


Figure 5.2: Area chosen to be analysed by EDX

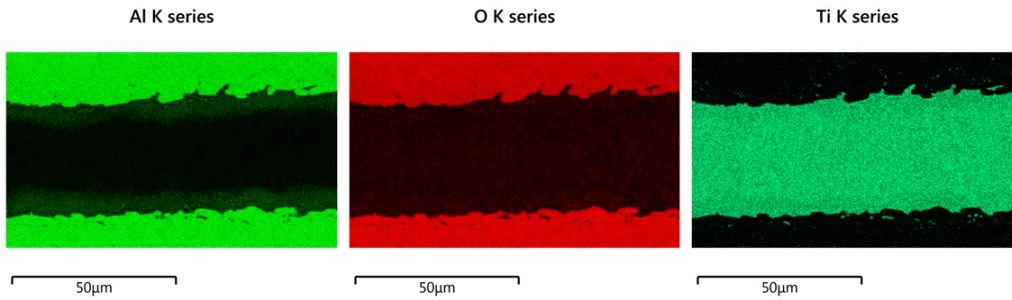


Figure 5.3: Placement of the three elements found during EDX

Given that cracks are perpendicularly oriented to the titanium film, it is probable that they are caused by stresses from the difference in linear coefficients of thermal expansion between Ti and Al_2O_3 . For $\alpha_{Ti} = 8.6 \times 10^{-6} \times ^\circ C^{-1}$ and $\alpha_{Al_2O_3} = 7.1 \times 10^{-6} \times ^\circ C^{-1}$ and $\Delta T = 1500^\circ C$ stress reaches 360 MPa. Values of stress for different titanium thickness were calculated from the equation (supposed perfect interphase):

$$\sigma_{Ti} = \frac{h_{Al_2O_3} E_{Al_2O_3} E_{Ti} (\alpha_{Al_2O_3} - \alpha_{Ti}) \Delta T}{(1 - \nu_{Ti}) E_{Al_2O_3} h_{Al_2O_3} + h_{Ti} E_{Ti} (1 - \nu_{Ti})} \quad (5.1)$$

where: h layer thickness, E Young's modulus and ν Poisson's ratio.

Table 5.1 shows values of stress merging from the difference in CTE values for both materials: titanium and alumina. Calculated stress does not surpass titanium tensile strength of 430 MPa.

In fact, stress stemming from the difference of CTE might be significantly higher. In the chapter "Modification of the interphase between platelets" fig. 4.2 there is a graph showing the difference between CTE in plane (xy) and out of plane (z) of alumina platelets. In plane shrinkage during the cooling is significantly smaller than

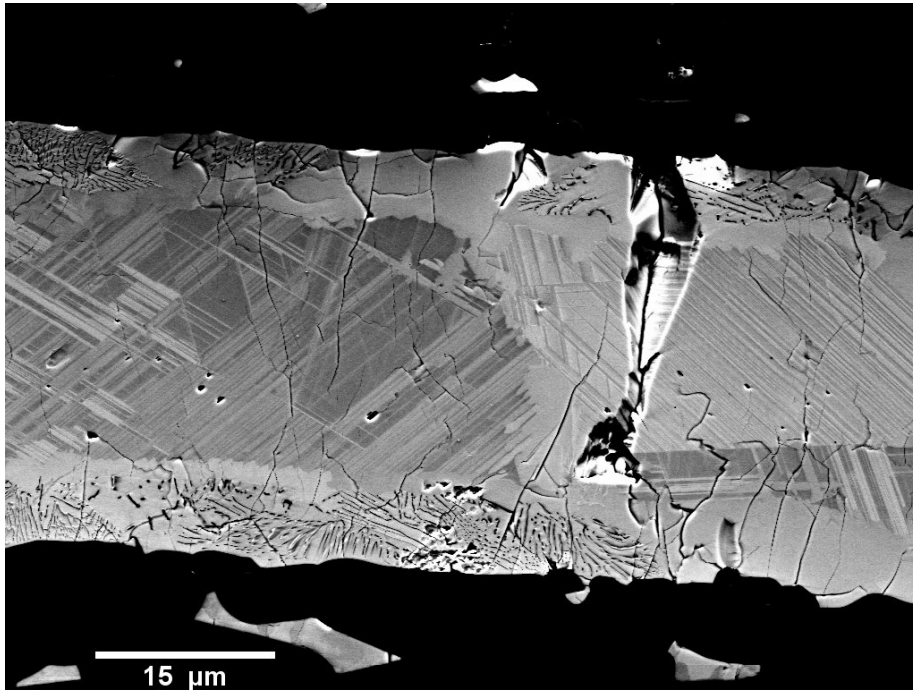


Figure 5.4: SEM image of titanium foil sintered between alumina pellets (BSE detector)

Thickness of Ti foil [mm]	Stress in Ti from CTE difference [MPa]	Stress in Al_2O_3 from CTE difference [MPa]
0.06	360.6	-10.8
0.15	355.6	-26.7
0.3	347.5	-52.1
1.5	294.3	-220.8

Table 5.1: Values of stress merging from the difference of CTE of alumina and titanium ($\Delta=1500^\circ\text{C}$). Alumina thickness was always 2 mm (in four layers). There were always three titanium layers so values of thickness given in the table are triple of single titanium foil thickness.

out of plane.

Ozer et al. performed measurements of the shrinkage during sintering of different alumina samples [100]. They compared sintering behaviours between material containing 100% spherical nano-powder and materials containing 10% and 20% of oriented alumina platelets. In samples without addition of platelets the shrinkage was isotropic in all directions, while in samples with platelets significant differences between xy direction and z direction were observed [100]. It further confirms anisotropy of thermal expansion in alumina platelets that may lead to significantly higher stress values than indicated in table 5.1.

It was decided that cooling speed should be lower, it was changed from $100^\circ\text{C}/\text{min}$ to $10^\circ\text{C}/\text{min}$ (possible stress relaxation at high temperature). Unfortunately it did not permit to completely eliminate cracking.

Changing cooling speed could significantly affect crystallography of metal component. Electron Backscattered Diffraction (EBSD, with help of Thierry Douillard

and Nicolas Vache, MATEIS laboratory) was done to confirm it. On the left there is image of sample cooled 100°C/min and on the right the one cooled 10°C/min. Band contrast image (fig. 5.5) allows to see the intensity of diffracted signal.

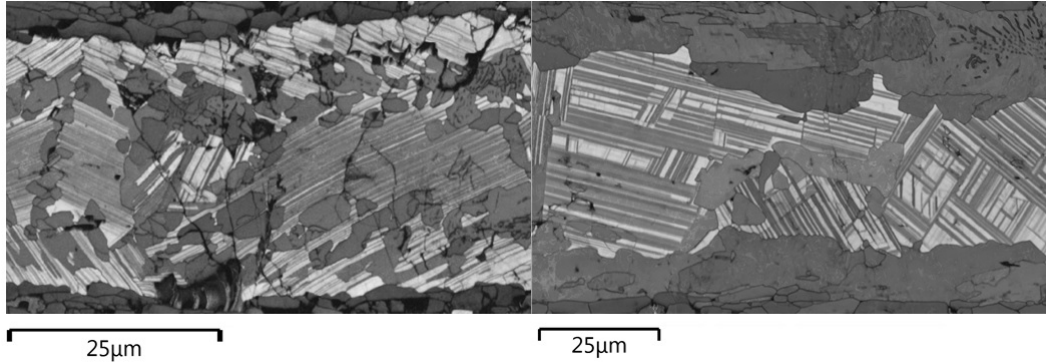


Figure 5.5: Band Contrast image of the titanium foil (camera EBSD). Both samples sintered at 1500°C. Sample on the left: cooling 100°C/min, initial foil thickness 50µm, sample on the right: cooling 10°C/min, initial foil thickness 100 µm. Magnification on both images is not the same.

The second image (fig. 5.6) shows the crystallography of the titanium foil. Both phases of titanium (hexagonal α and cubic β) are present but in different proportions. In the first sample, cubic phase is present mostly on the outside of the foil while hexagonal is more concentrated closer to the middle. In the second sample is it contrary. In addition, in the sample on the left there is approximately 70% of hexagonal phase and 30% of cubic phase while in the second sample proportion is 82% and 18% respectively.

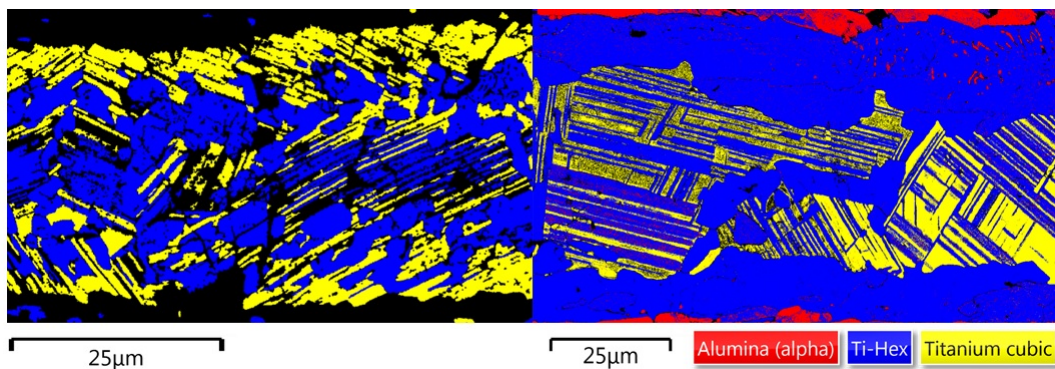


Figure 5.6: Comparison of crystallographical structure of two foils (100°C/min vs 10°C/min)

On the edges of the foil some "brain-like" structures are noticeable (see fig. 5.7). Consequently EDX analysis of the zone of interest was performed (fig. 5.7).

O, Al, and Ti were detected. When those elements were observed separately (fig. 5.8) it became clear that those intermetallic structures did not contain titanium, only aluminium and oxygen. It seems that these are ceramic inclusions in the titanium foil. In further paragraph more detailed analysis is presented (see table 5.2 and 5.5).

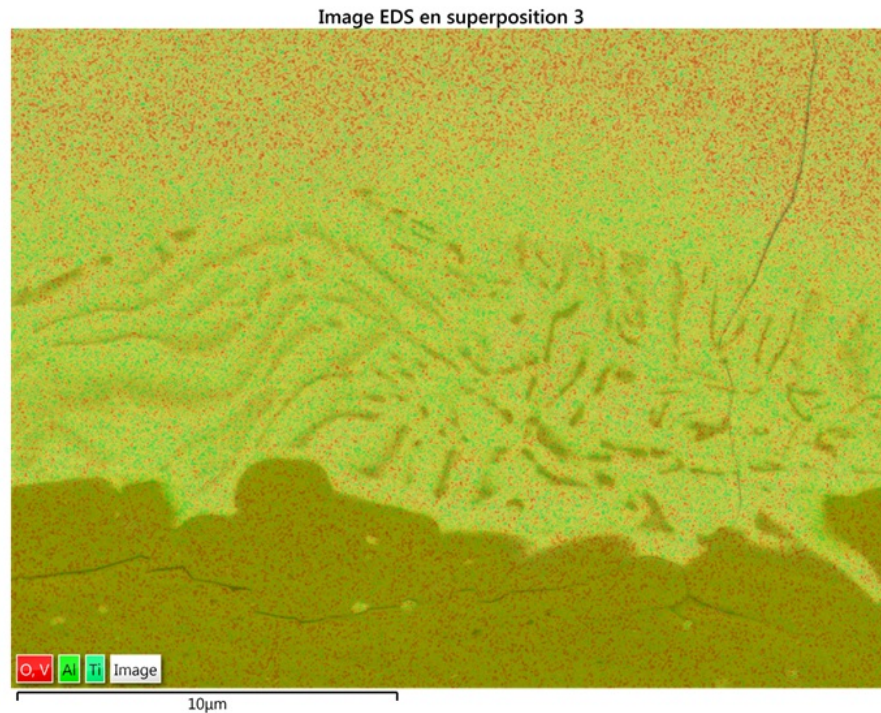


Figure 5.7: EDX image of the observed intermetallics, sample cooling speed: 100°C/min.

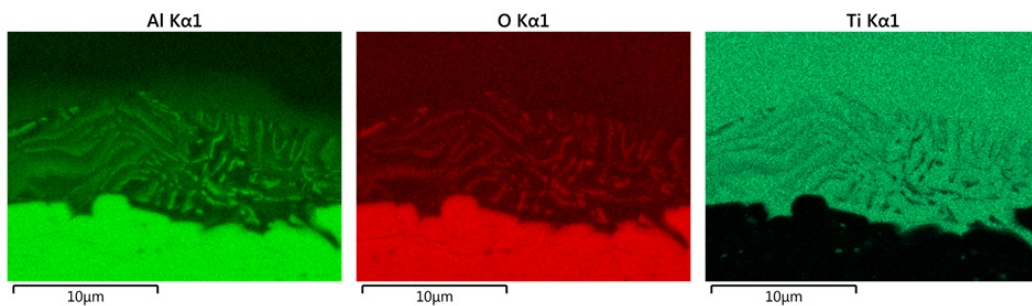


Figure 5.8: EDX images of particular elements present in the intermetallics

5.1.2 Study of titanium diffusion

Diffusion of titanium is a phenomenon which called for attention. Being able to control it could lead to development of metal/ceramic composites with sophisticated microstructure, gradient materials for example. To better understand diffusion mechanisms, various thermal treatments in FAST were conducted. Holding times of 30 minutes at different temperatures (1200°C, 1300°C, 1400°C and 1500°C, heating and cooling rate: 100°C/min.) were applied. The idea was to give time for diffusion of titanium into the porosity before sintering alumina. Graphs below present temperature profiles for those four sintering cycles.

After sintering the samples were cut, polished and observed by SEM. There is a clear difference in diffusion between them. In the fig. 5.10 images of a specimen with holding time at 1200°C are presented. Picture on the right was taken with

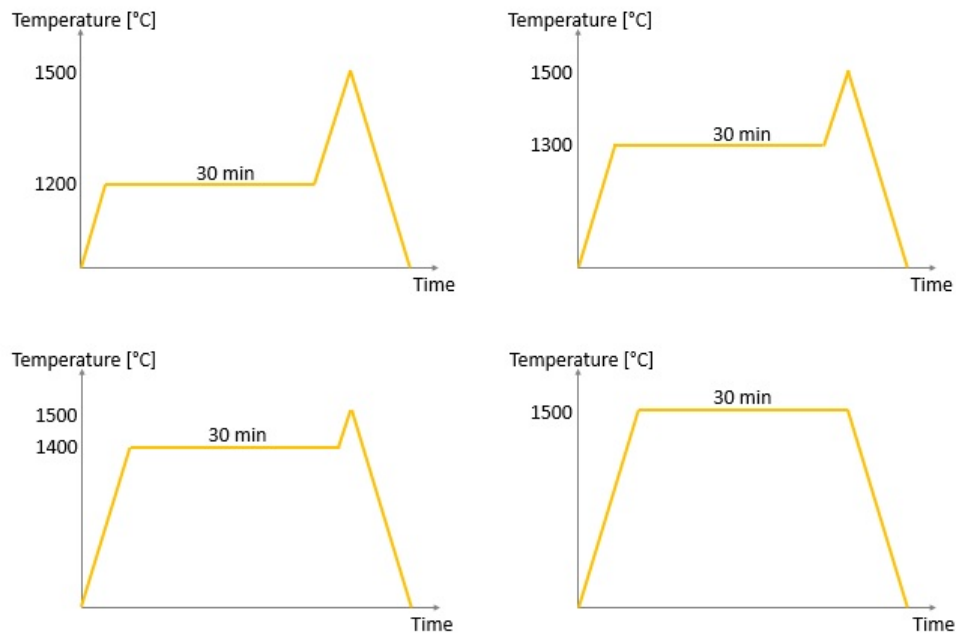


Figure 5.9: Temperature profiles of applied sintering cycles. Holding time of 30 minutes at 1200, 1300, 1400 and 1500°C respectively, max. temp. 1500°C for all treatments.

higher magnification to show that even in close proximity to the foil there are only few small Ti grains in the ceramic matrix.

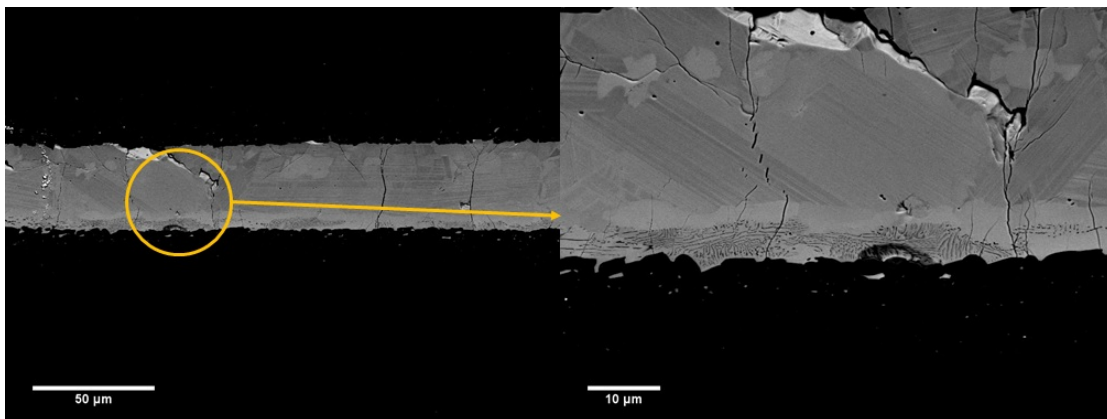


Figure 5.10: A sample sintered at 1500 °C with 30 minutes holding time at 1200 °C; minor diffusion of titanium (BSE detector)

Fig. 5.11 shows SEM image of a sample with holding time at 1300 °C. As in case of the previous sample (holding time at 1200 °C) diffusion is minor, only a few small titanium grains are visible in the close proximity of the foil.

In fig. 5.12 there is a SEM image of a sample with holding time at 1400 °C. The difference in the intensity of diffusion is immediately visible. It is not homogeneous along the foil. There are some regions (from the left to the center of the image) where distance of diffused grains from the foil reaches 50 μm.

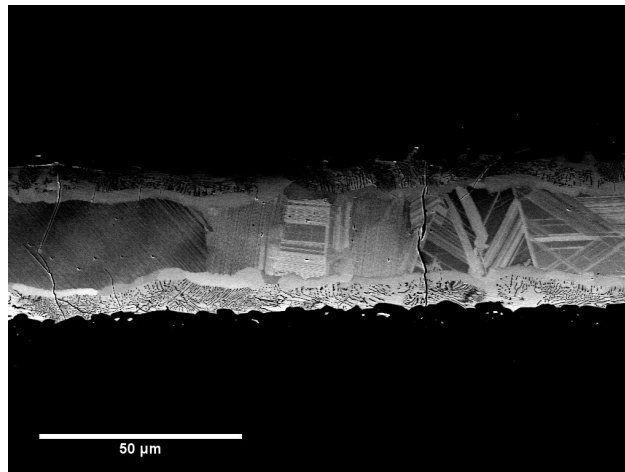


Figure 5.11: A sample sintered at 1500 °C with 30 minutes holding time at 1300 °C; minor diffusion of titanium (BSE detector)

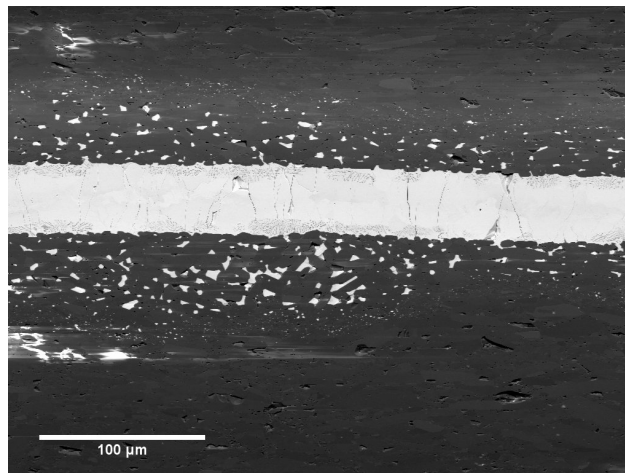


Figure 5.12: A sample sintered at 1500 °C with 30 minutes holding time at 1400 °C; significant diffusion of titanium (BSE detector)

In fig. 5.13 picture of sample with applied holding time at 1500 °C is presented. Diffusion resembles the diffusion in the previous specimen.

Pictures in figures 5.10 and 5.11 were taken with higher magnifications than 5.12 and 5.13 to demonstrate that even close to the foil diffusion was minor and grains smaller than in samples where holding time was applied at temperature 1400 °C and 1500 °C. There seems to exist an activation temperature for titanium diffusion between 1300 °C and 1400 °C.

X-ray tomography observations could improve understanding of titanium diffusion into alumina matrix giving 3D information instead of 2D by SEM. It was decided to perform some experiments in synchrotron (European Synchrotron Radiation Facility in Grenoble, ID16, with help of Julie Villanova and Victor Vanpeene). Chosen scan resolution was 50 nm. More details available in corresponding section in the chapter "Materials and Methods".

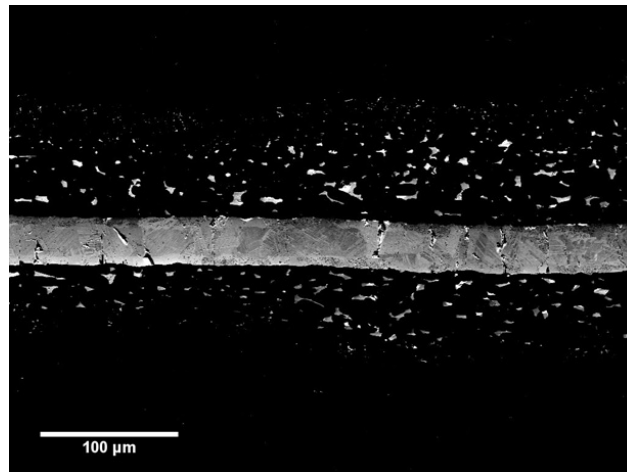


Figure 5.13: A sample sintered at 1500 °C with 30 minutes holding time at 1500 °C; significant diffusion of titanium (BSE detector)

The scan of the specimen with 30 min holding time at 1200°C confirmed that in the entire volume, diffusion was minimal in comparison with samples where holding time was applied at 1400°C and 1500°C. Fig. 5.14 shows one image from the volume reconstruction, perpendicular to the Ti film. Dark grey colour is the ceramic phase, while light part is the residual porosity in the samples. There is no visible titanium diffused into the alumina matrix.

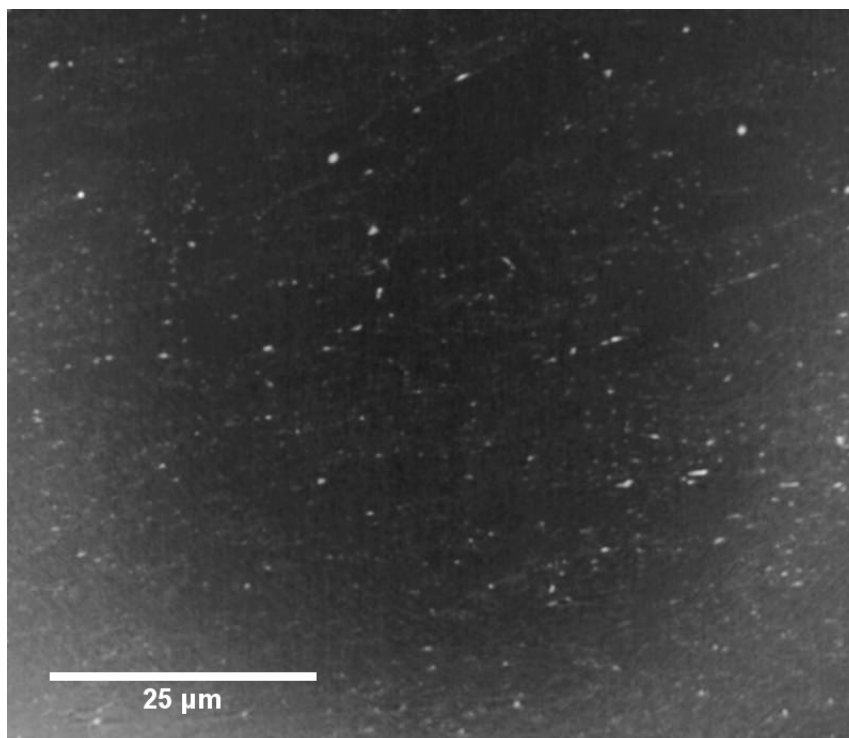


Figure 5.14: One picture from volume reconstruction of the sample 30 min at 1200°C. It shows residual porosity (light) in ceramic matrix (darker). It is the zone close to the titanium film (scan perpendicular to the metal layer) but no visible diffusion was noticed.

5.1. FABRICATION AND STRUCTURAL CHARACTERISATION

On the other hand, the scan of the sintered sample with a 30 min holding time at 1500°C showed significant diffusion all around the titanium foil. Fig. 5.15 presents 3D reconstructions of titanium diffused into ceramic in this sample. Foil was removed from the analysed volume because there was too much noise in the interphase between metal and ceramic. Yellow lines mark plane, where the titanium foil is placed.

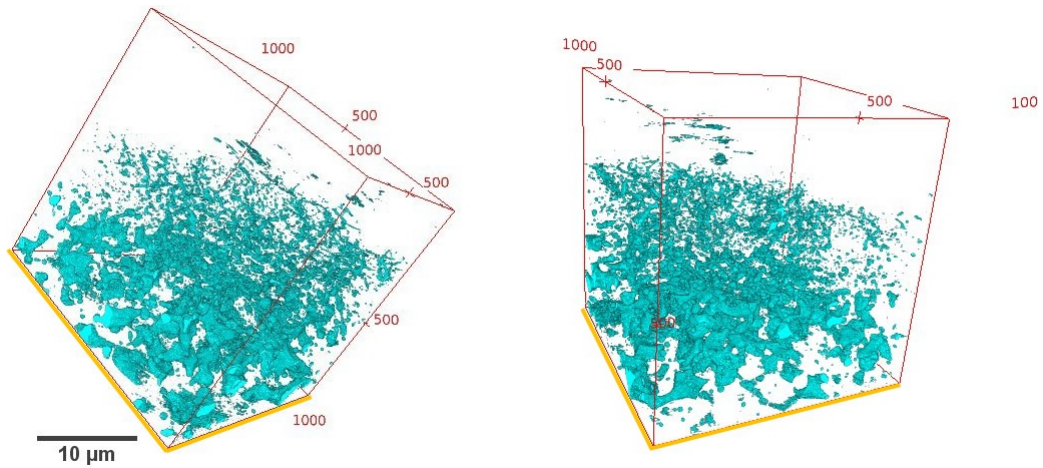


Figure 5.15: 3D volume reconstruction of the sample sintered during 30 min at 1500°C. Ceramic phase was removed from the reconstruction to show titanium which infiltrated porosity.

Careful observations allowed to see that many grains of diffused titanium are interconnected. In fig. 5.16 a close-up look on the interconnected grains and some residual porosity is presented.

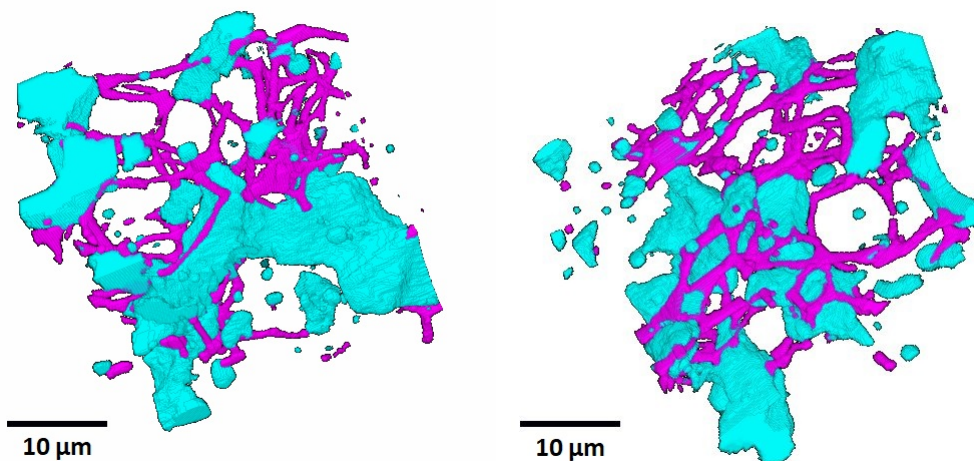


Figure 5.16: Close-up look on grain interconnections and residual porosity which was not infiltrated by metal. Sample sintered during 30 min at 1500°C. Ceramic phase was removed from the reconstruction to show titanium and porosity. Titanium phase is in cyan and porosity in magenta.

Interconnections between diffused grains suggests that titanium was liquid while infiltrating porosity. Even if during sintering programmed temperature was supposed to reach only 1500°C it is possible that conductive titanium was heated much faster than not conductive alumina. Rathel et al. performed experimental and finite elements analysis of heat distribution during FAST sintering of two materials: electrically conductive (tungsten carbide) and non-conductive (96 wt.% silicon nitride with addition of alumina and yttria) [24]. Results confirm that heating and heat distribution depend on properties of sintered materials. Non-conductive ones tend to have elevated temperature in the outside part while conductive on the inside [24]. Fig.5.17 illustrates differences in material temperature measured by internal and external pyrometer.

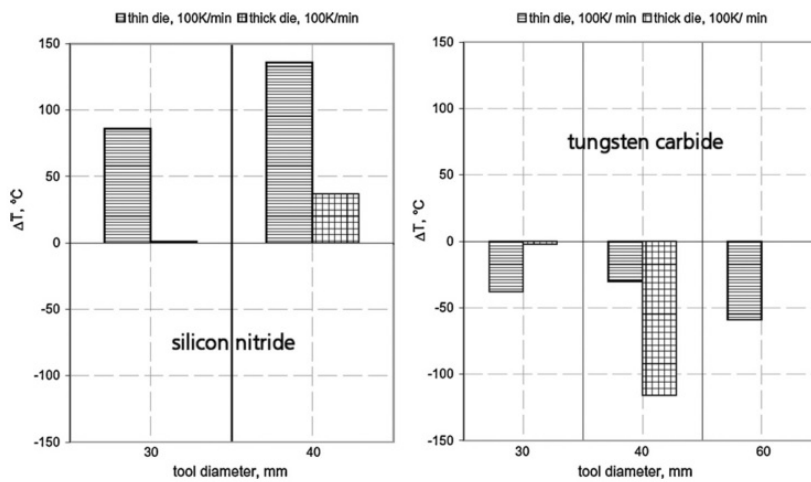


Figure 5.17: Temperature differences between internal and external zone of the material [24]. Sintering dies differed in diameter and thickness. Horizontal lines: thin die, grid: thick die.

In addition, it is visible that titanium grain size decreases with distance from the foil. Possibly, during thermal treatment porosity closes simultaneously with diffusion. In consequence some pores are already partially closed when titanium reaches them.

In summary, it is probable that during thermal treatment titanium is liquid. Titanium grain size decreases with distance from the foil. Cooling rate during sintering affects crystallographic structure of metal. Holding time applied at 1200 and 1300 °C impede diffusion. During sintering, sophisticated chemical and physical phenomena occur.

5.1.3 Changing foil chemistry

One of considered possibilities of solving the problem of titanium foil cracking was to change its chemical composition. Changing chemical composition should not drastically change CTE but can modify mechanical properties. Two alternatives were tested: Ti6Al4V and Ti foil with thin layer (around 2-3 μm, coated by physical vapour deposition technique) of TiN on both sides.

Sample with layer of Ti6Al4V

Titanium alloy's Ti6Al4V ultimate tensile strength indicated by supplier is significantly higher than that of pure titanium (896 MPa in comparison with 430 MPa). It raised hopes that during cooling the foil would not crack.

As in case for pure titanium composites, diffusion was noticed. Unfortunately, metal foil was cracked as well. "Brain-like" intermetallic structures were found during SEM observations (Fig. 5.18).

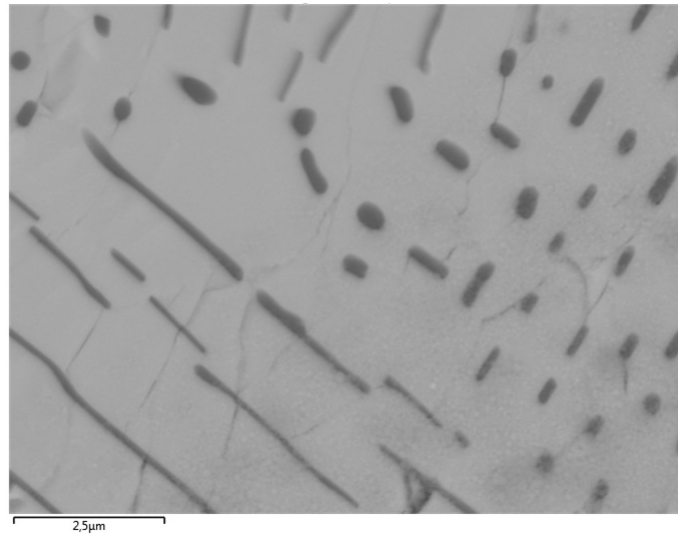


Figure 5.18: Intermetallic structures inside Ti6Al4V foil. Bright grey: metal, dark grey: inclusions.

Chemical analysis of those structures revealed presence of three elements: aluminium and oxygen embedded in titanium matrix (Fig. 5.19).

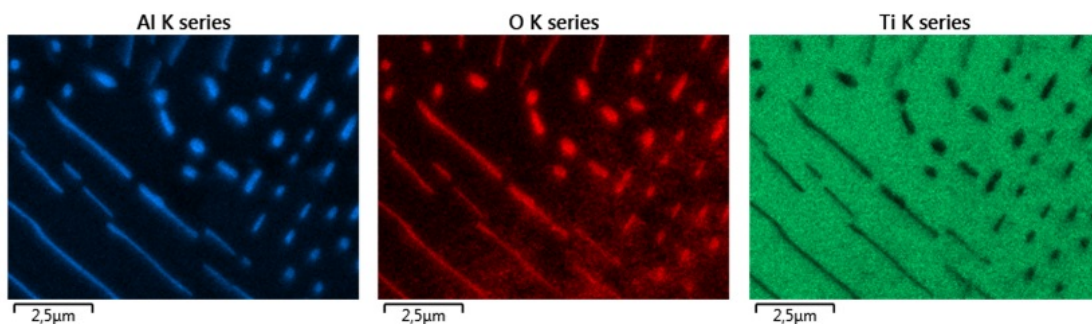


Figure 5.19: Chemical analysis of intermetallics

To calculate quantity of elements, three punctual spectra measurements were done in metal around structures (1-3) and five inside those forms themselves (4-8) (Fig. 5.20).

Metallic matrix contained in average 90.3 at% of titanium, 7.5 at% of aluminium and 2.2 at% of vanadium. Inclusions are composed of 51.1 at% of oxygen, 31 at%

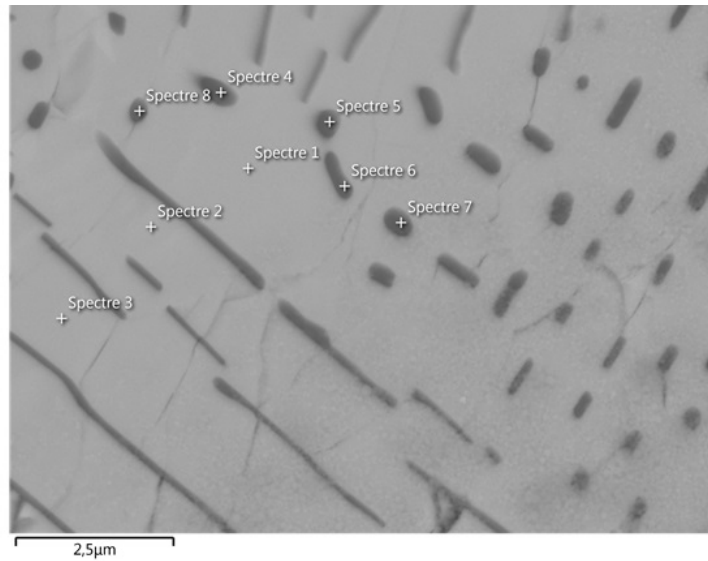


Figure 5.20: Placement of spectra measurements

of aluminium, 17.4 at% of titanium and 0.4 at% of vanadium. Table 5.2 lists those elements.

Elements [at%]:	Ti	Al	V	O
Metallic matrix (spectra 1-3)	90.3	7.5	2.2	-
Inclusions (spectra 4-8)	17.4	31	0.4	51.1

Table 5.2: Comparison of composition of the metal matrix and inclusions

In case of measurement of quantity of elements inside inclusions there is a risk of having some signal coming from matrix as inclusions are quite thin (maximum 300 nm).

Spectra 12-20 were analysed to determine compounds and their quantities in metal grains diffused into nacre-like alumina matrix and the matrix itself (Fig. 5.21).

Grain 20 contains 15.7 at% of oxygen which is unusual so average values were calculated from spectra 13, 14, 15 and 18 which do not include oxygen. Ratio of titanium is 60.2 at%, of aluminium 33.5 at%, vanadium 2.2 at% and silicon 0.6 at%. Spectres of alumina in proximity to metal (12, 16, 17, 19) gave values of 56 at% for oxygen, 43.3 at% for aluminium and small amounts of yttrium (0.5 at%) and zinc (0.2 at%). Table 5.3 summarizes those measurements.

During observations differences of colour within same grain were noticed. It was noticed for multiple grains in the diffusion zone. Differences of shade seen by BSE detector correspond to differences in chemical composition of observed material. Spectra 21-27 address the question of chemical composition of diffused grains (Fig. 5.22). Odd numbers correspond to lighter parts and even numbers to darker parts.

Average atomic percentages for lighter grain parts are as follow: 53.3 for tita-

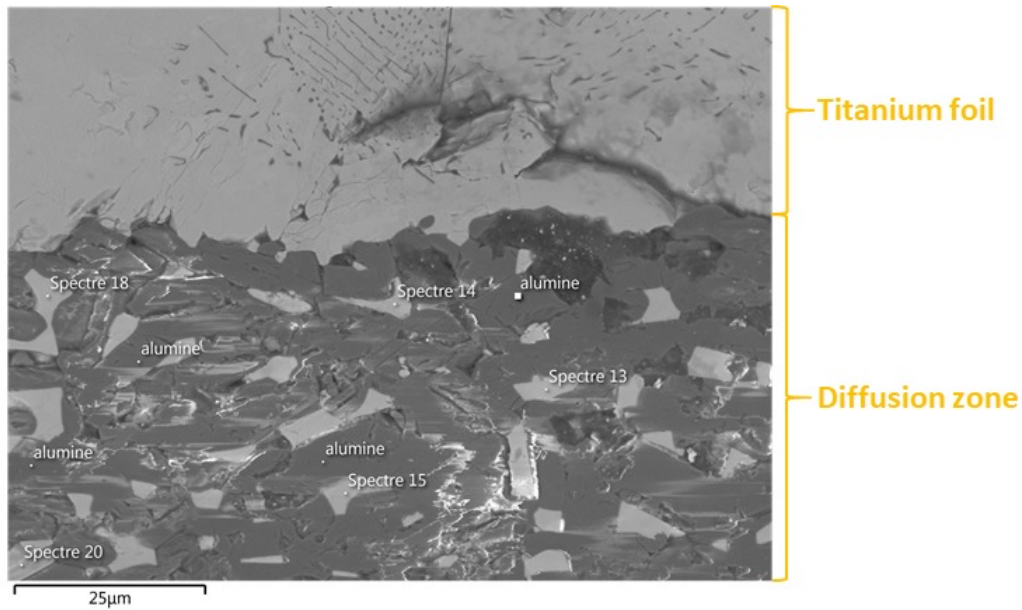


Figure 5.21: Analysis of ceramic matrix and metal grains composition (BSE detector)

Elements [at%]:	Ti	Al	V	Si	O	Y	Zn
Spectra 13-15, 18 (titanium grains)	60.2	33.5	2.2	0.6	-	-	-
Spectra 12, 16, 17, 19 (alumina)	-	43.3	-	-	56	0.5	0.2

Table 5.3: Composition of diffused grains and ceramic matrix

niun, 39.6 for silicon, 5.6 for aluminium and 1.5 for vanadium. In darker areas silicon has not been detected. They contain high amount of aluminium (72.5 at%), some titanium (26.9 at%) and traces of vanadium (0.2 at%). Based on this measurement we can differentiate two types of areas in diffused grains: rich in aluminium and rich in silicon and titanium. Table 5.4 lists all the elements and their quantities.

Elements [at%]:	Ti	Si	Al	V
Lighter parts (spectra 21, 23, 25, 27)	53.3	39.6	5.6	1.5
Darker parts (spectra 22, 24, 26)	26.9	-	72.5	0.2

Table 5.4: Differences in composition of diffused grains, average of spectra as indicated

SEM picture below (Fig. 5.23) presents one of these "dual" grains. It was analysed to determine chemical composition of lighter and darker part.

K series (X-ray photon emission corresponding with $L \rightarrow K$ electronic transition) analysis shows three heterogeneously dispersed elements in the grain (Fig. 5.24). Outer part is significantly different from the inner one. In the inner part of the grain there is titanium and no oxygen. Closer to ceramic, matrix concentration of aluminium is higher and it decreases significantly towards the center part. On the

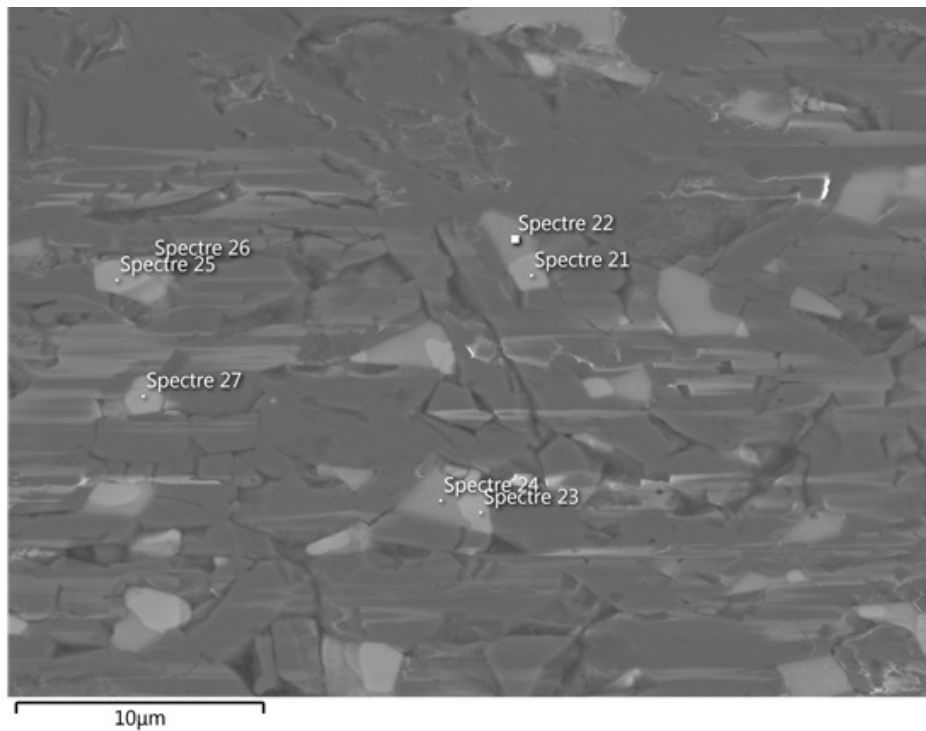


Figure 5.22: Differences of composition within titanium grains in the diffusion zone (BSE detector)

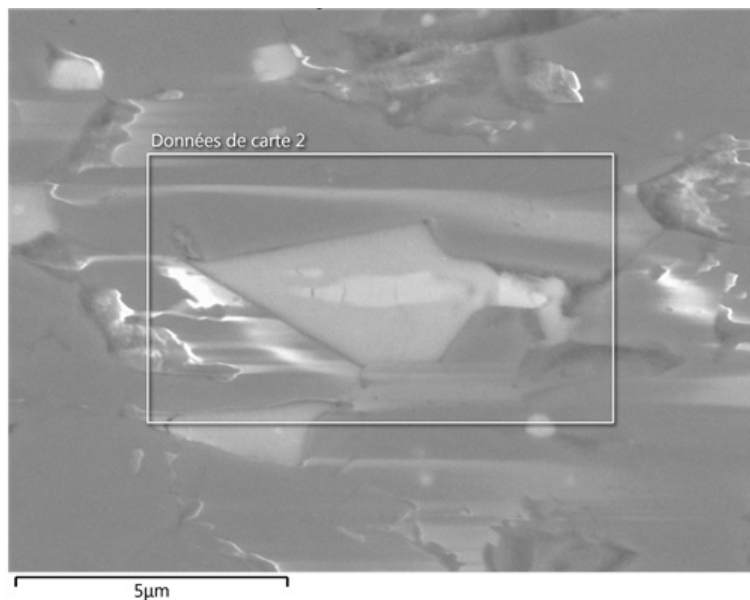


Figure 5.23: Duality in structure of a single grain

other hand, center is rich in silicon which is not present in the outer part. Silicon probably comes from the glassy phase which acts as a mortar in nacre-like alumina.

A profil line was traced from the Ti6Al4V foil trough ceramic matrix and two diffused grains (Fig. 5.25). This way of analysing chemical composition allows to follow

5.1. FABRICATION AND STRUCTURAL CHARACTERISATION

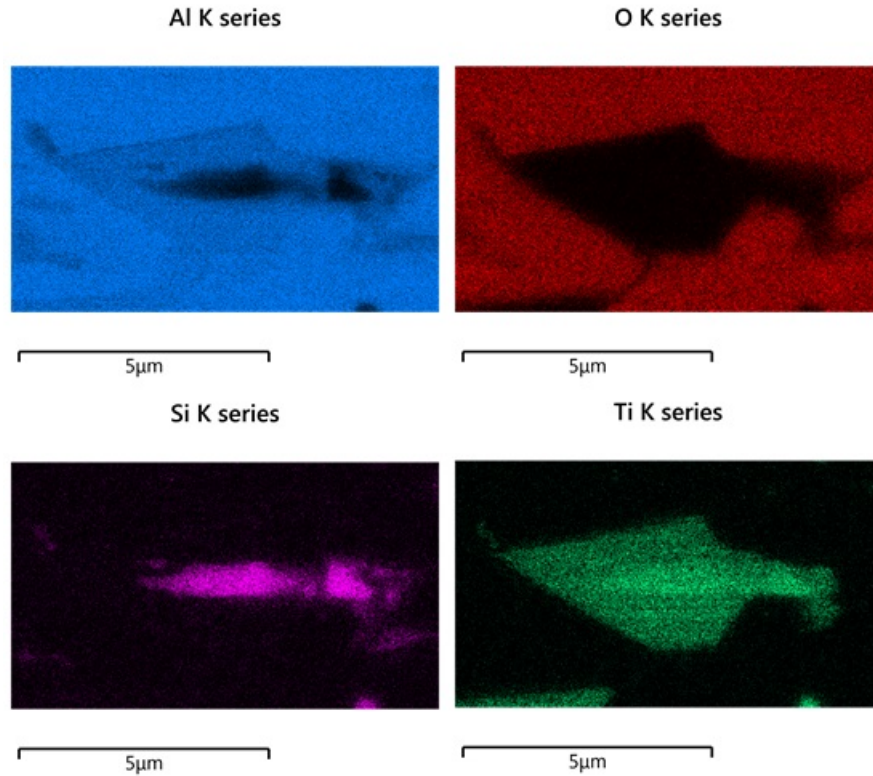


Figure 5.24: Varied chemical composition of a single grain

evolution of elements ratios (and maybe to better understand diffusion mechanisms).

As in previous analysis there were five elements detected: Ti, O, Al, V, Si (Fig. 5.26). Thanks to lines corresponding to each element, boundaries between ceramic matrix and metallic grains are clearly visible.

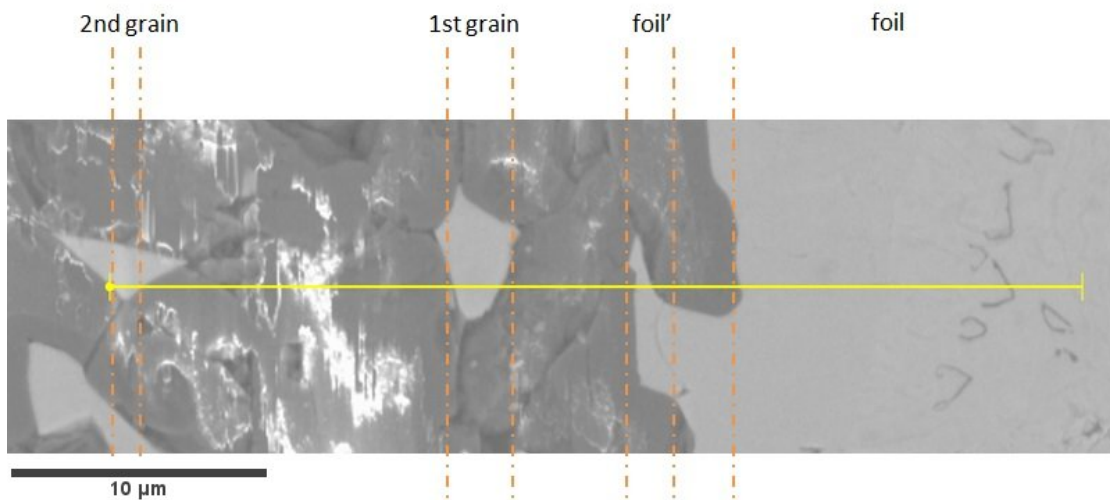


Figure 5.25: Analysis of linear composition of diffusion zone

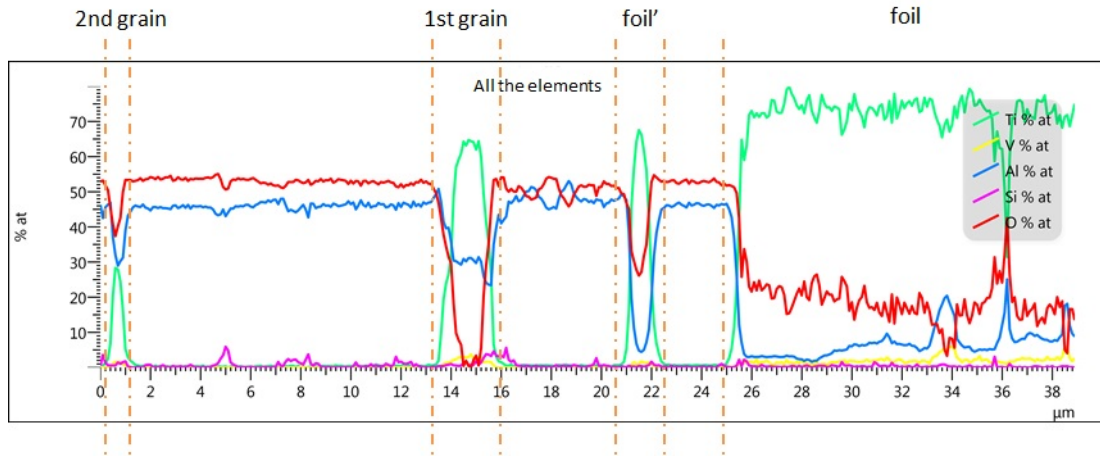


Figure 5.26: Linear analysis of all elements present in the composite starting from alumina to titanium layer, through the diffusion zone

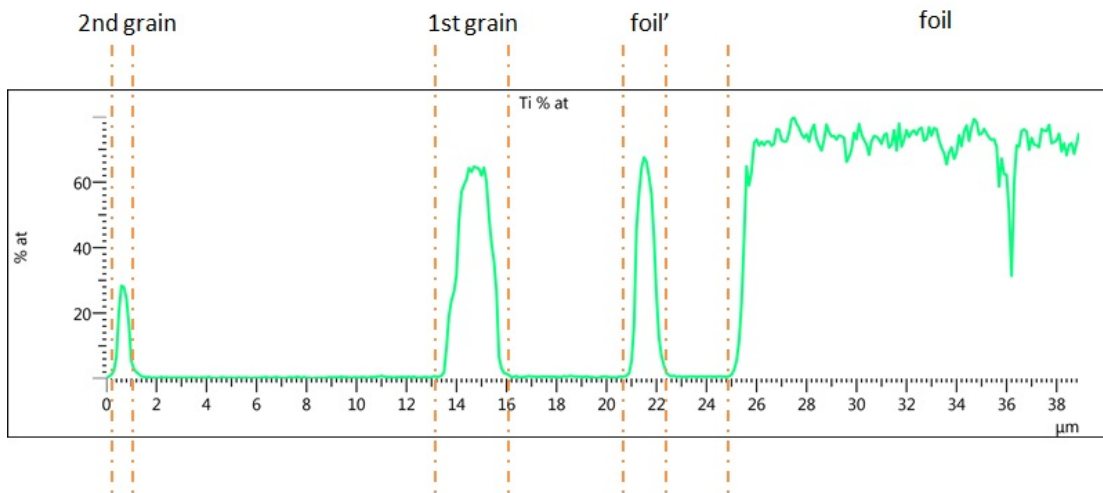


Figure 5.27: Linear analysis of titanium along the line shown in fig. 5.25

Evolution of the quantity of titanium as a function of distance from the foil is detailed in fig. 5.27. In the first grain (10 μm from the foil) ratio of titanium is above 60 at% while in the second grain (25 μm) it is below 30 at%. In the second grain detected quantity of titanium might be affected by the surrounding alumina matrix.

In contrast, the quantity of aluminium logically increases with distance (Fig. 5.28). Inside the metal foil it is almost not present, then it increases from around 25 at% (in the first grain) to a bit over 30 at% (in the second one). Increased amount of detected aluminium might come from the surrounding ceramic phase as well.

In case of oxygen relationship between distance and quantity is not so clear (Fig. 5.29). While foil in direct proximity of ceramic contains oxygen (up to 25 at%), in the first grain it is almost completely absent and in the second one it exceeds a value of 35 at%

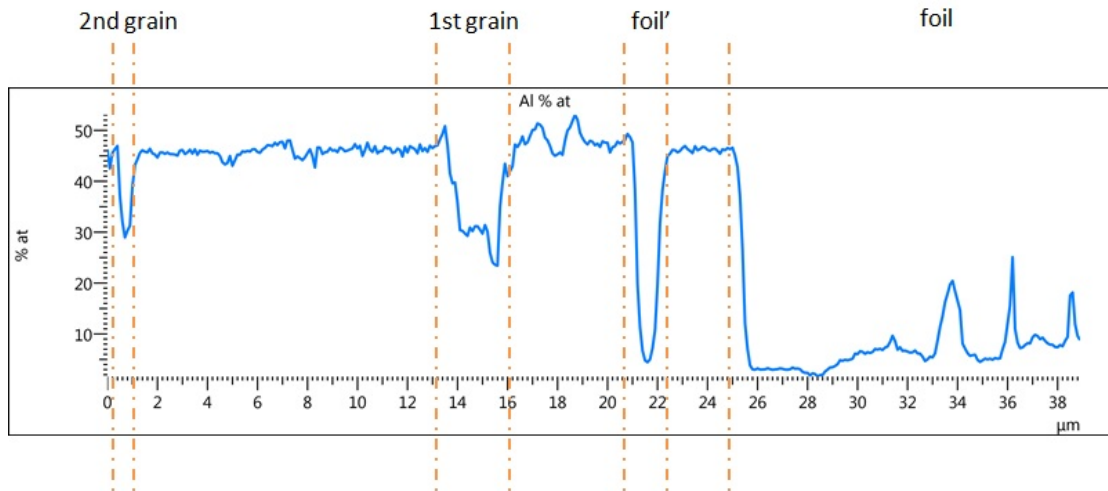


Figure 5.28: Linear analysis of aluminium along the line shown in fig. 5.25

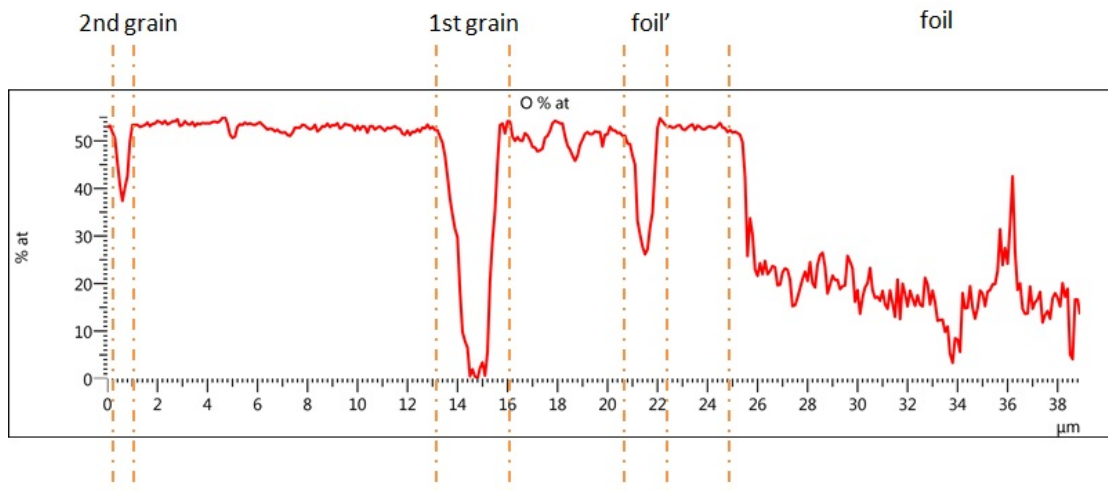


Figure 5.29: Linear analysis of oxygen along the line shown in fig. 5.25

Sample with Ti coated by TiN layer

Another proposed way of improving composite was to use a pure titanium foil with a layer of titanium nitride (thickness around 2-3 μm). TiN is commonly used as a coating for turbines and engines for instance. It significantly increases superficial hardness (up to 2400 HV). According to supplier its Young's modulus reaches 600 GPa. It was tested to check if a layer of TiN could protect Ti from cracking or change diffusion mechanism.

As in case of pure titanium and Ti6Al4V alloy, in composite there are grains diffused into alumina and "brain-like" inclusions present in the foil (Fig. 5.30).

Looking at the picture shown in fig. 5.31 it seems that there is a difference of shades between metal in direct contact with inclusions and metal deeper in the foil. Spectra from 28-34 were analysed to determine if slight difference in shade is related to material chemistry.

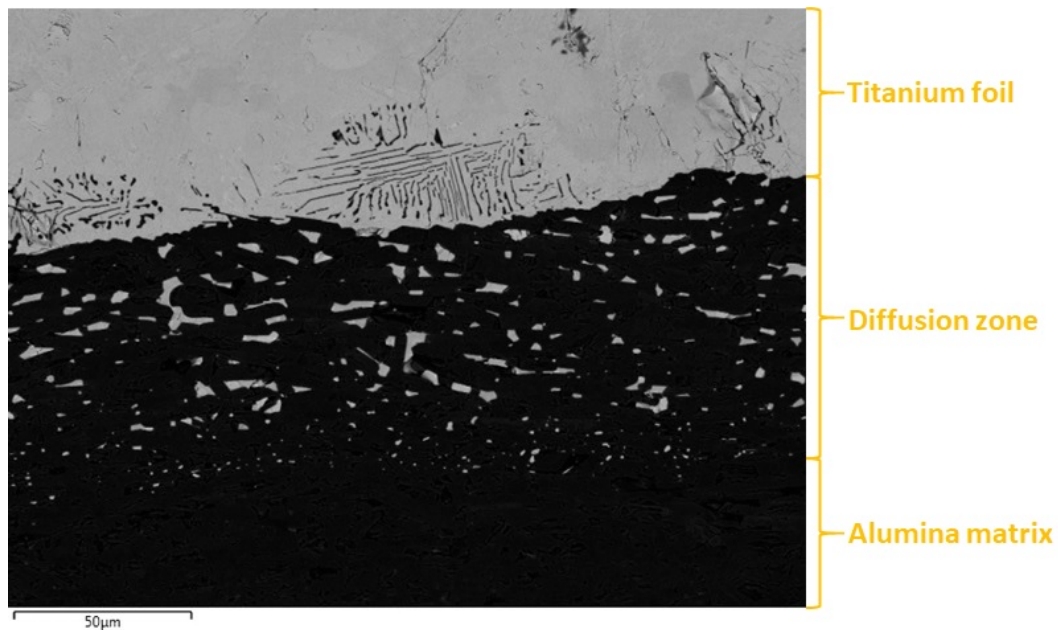


Figure 5.30: SEM picture of metal foil and diffusion zone in the composite $Al_2O_3/TiN/Ti$. Sintering temperature: 1500°C, heating rate: 100°C, cooling rate: 10°C.

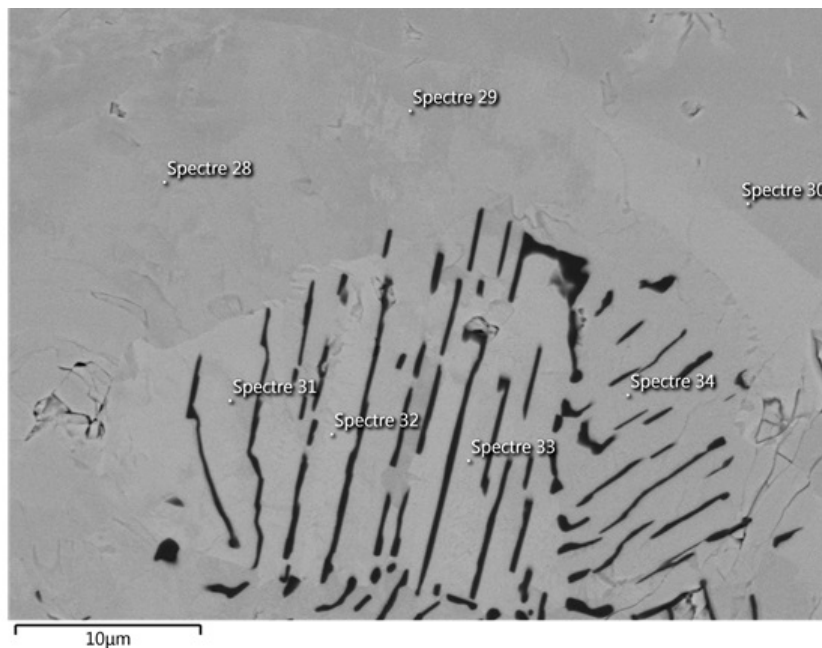


Figure 5.31: Difference between metal in inclusions zone and metal deeper in the foil

Spectra 28-30 are placed outside of inclusions zone. Their average composition is as follows: titanium 96.4 at%, aluminium 3.4 at% and silicon 0.2 at% Spectra 31-34 localized between inclusions differ from previous ones. Titanium ratio drops to 83.9 at% while aluminium ration increases to 15.4 at% and silicon to 0.7 at% It suggests that some elements diffuse to the foil.

5.1. FABRICATION AND STRUCTURAL CHARACTERISATION

Elements [at%]:	Ti	Al	Si
Outside of inclusions zone (spectra 28-30)	96.4	3.4	0.2
Inside inclusions zone (spectra 31-34)	83.9	15.4	0.7

Table 5.5: Differences in composition of metal closer and further away from the inclusions

Spectra 35-43 were analysed similarly as in case of composite with Ti6Al4V alloy to check the composition of inclusions (Fig. 5.32).

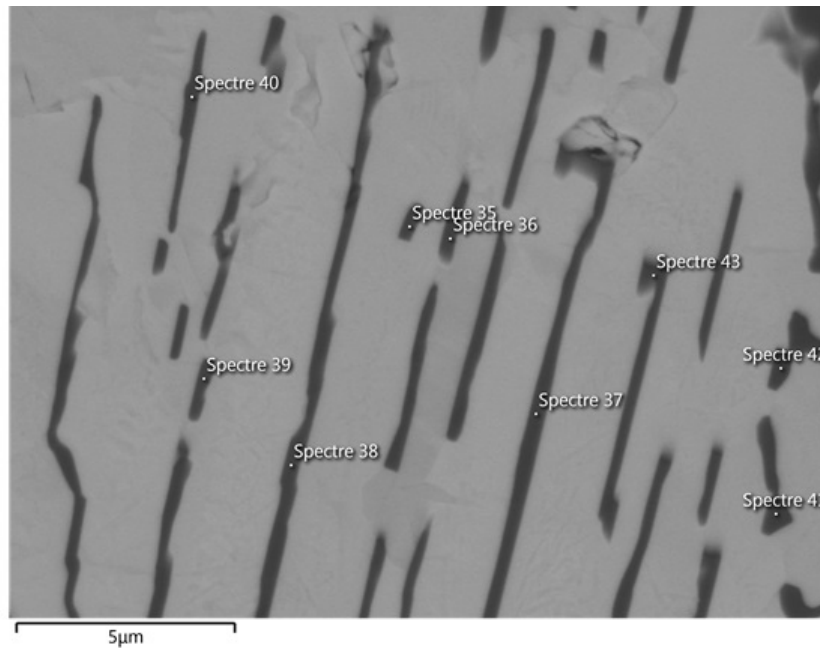


Figure 5.32: Analysis of intermetallics

There is more oxygen 56.7 at% (in comparison with 51.1 at%), more aluminium 34.3 at% (as opposed to 31 at%) and less titanium 9 at% (17.4 at% in case of Ti6Al4V).

To determine the nature of intermetallic two spectra were compared. Spectre 29 from metal and 38 from inclusion were plotted together (Fig. 5.33).

First peak of spectre 38 at 0.5 [keV] proves that inclusions contain oxygen. Titanium detected in spectre 38 (4.1 % at.) probably comes from the surrounding titanium matrix due to the size of interaction volume ($0.5-1.0 \mu m^3$). It leads to the conclusion that intermetallics are actually oxides, possibly Al_2O_3 (see fig. 5.19 where titanium was not detected inside the inclusions). One can apply same reasoning to composite with Ti6Al4V alloy.

Metal grains in the diffusion zone were analysed to detect potential differences between them (Fig. 5.34).

Based on spectra analysis they were divided in three "subgroups": rich in Al and Ti (44, 45, 47, 48), rich in Ti and Si (49-51) and one grain "transitive" (46). Averages

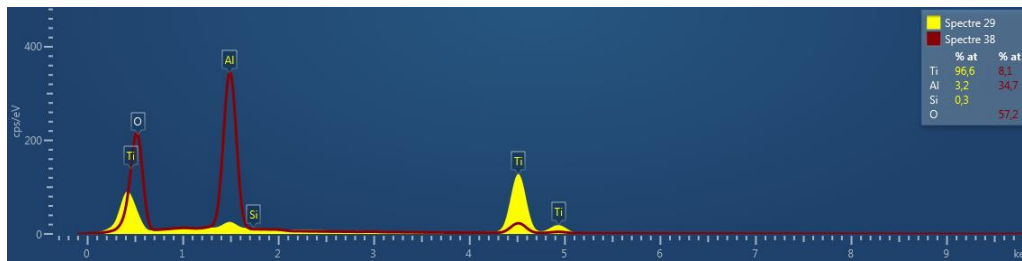


Figure 5.33: Comparison between spectres of metal and intermetallic. Y-axis: number of X-rays received and processed by the detector [cps/eV], X-axis: energy level of those counts [keV].

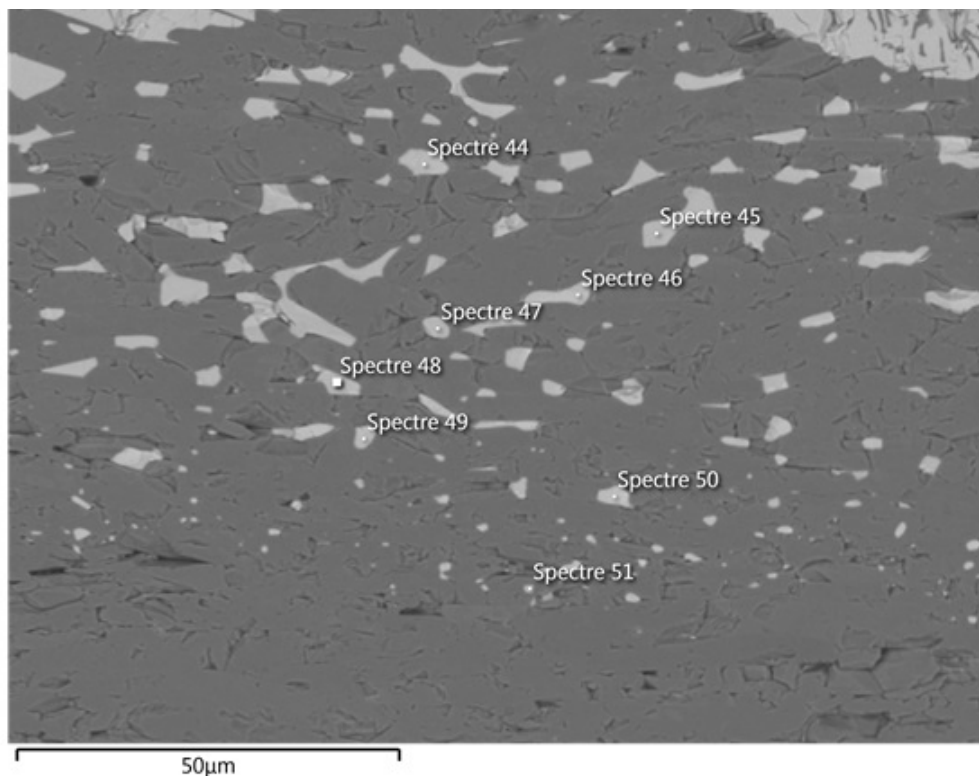


Figure 5.34: Analysis of grain composition in the diffusion zone. Sample with Ti(N) foil, sintered at 1500°C, heating rate 100°C/min, cooling rate 10°C/min.

of elements in spectra 44, 45, 47, 48 are 56.9 at% for titanium and 43.1 at% for aluminium. In grains with numbers 49-51 ratios of elements are as follows: 55.9 at% Ti, 33.7 at% Si and 10.3 at% Al. Transitive grain contains mainly titanium (60.5 at%), with addition of aluminium (23.7 at%) and silicon (15.8 at%). Again, silicon probably comes from the glassy phase from the reference formula of ceramic phase. First subgroup of grains (rich in Al and Ti) is visibly placed closer to the metal foil, while the second subgroup (rich in Ti and Si) is much further. "Transitive grain" is localised between those subgroups.

For composite with titanium foil covered with layer of titanium nitride chemical linear analysis was performed (Fig. 5.35). Line was traced through a fragment of

5.1. FABRICATION AND STRUCTURAL CHARACTERISATION

Elements [at%]:	Ti	Al	Si
Spectra 44, 45, 47, 48	56.9	43.1	-
Spectra 49-51	55.9	10.3	33.7
Spectre 46	60.5	23.7	15.8

Table 5.6: Differences in composition of titanium grains diffused into alumina matrix foil (with small inclusion) and two diffused grains in ceramic matrix.

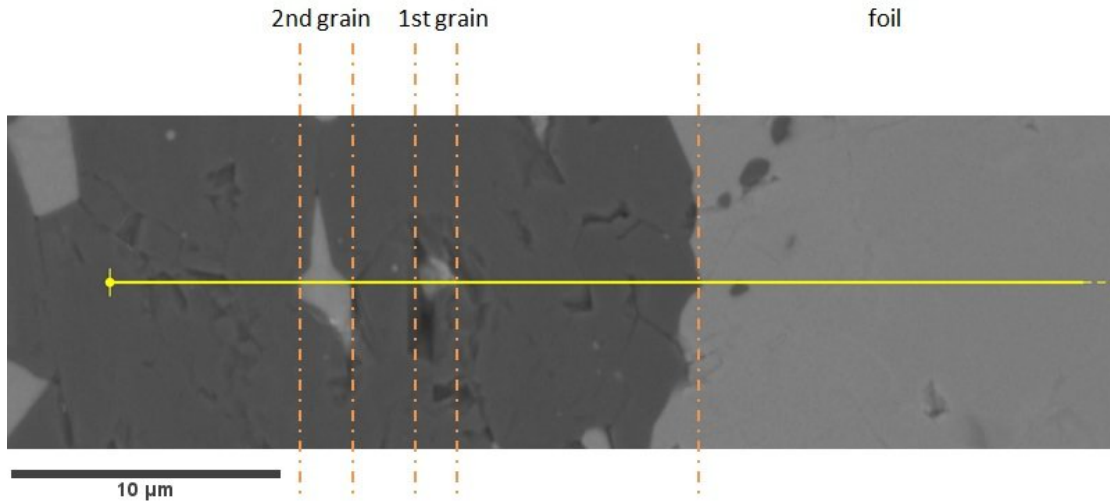


Figure 5.35: Analysis of linear composition of diffusion zone

Similarly five elements were detected: Ti, Al, Si, O and in this case N instead of V (Fig. 5.36). Boundaries between metal and ceramic areas are clearly visible as well.

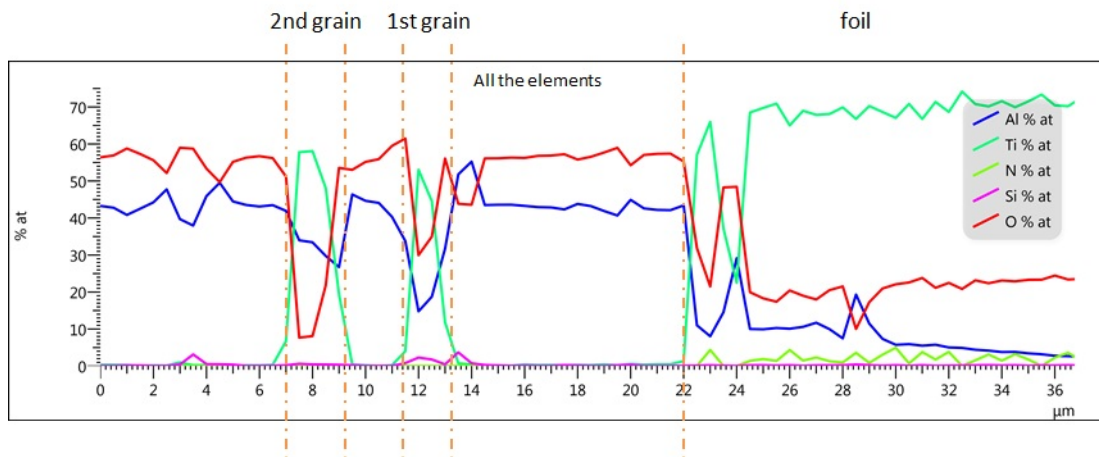


Figure 5.36: Linear analysis of all elements present in the composite along the line shown in fig. 5.35

Variation in quantity of titanium (Fig. 5.37) is not as significant as in previous composite (with Ti6Al4V foil). In both grains titanium ratio is slightly below 60 at% while in the foil this value reaches 70 at%.

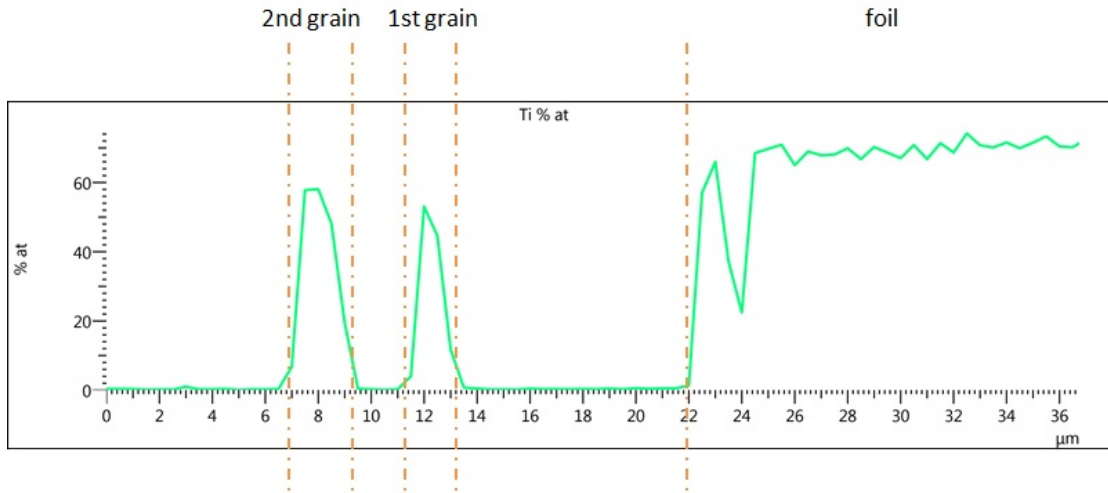


Figure 5.37: Linear analysis of titanium along the line shown in fig. 5.35

Distribution of nitrogen is quite interesting (Fig. 5.38). It does not diffuse to ceramic but it seems that it penetrates foil. Initial layer of TiN has around 2-3 μm thickness (information provided by supplier). In the curve it is clearly visible that N is present even 14 μm into the foil but only at ratio around 4 at%. Presently it is unclear what is the origin of this heterogeneous distribution of nitrogen.

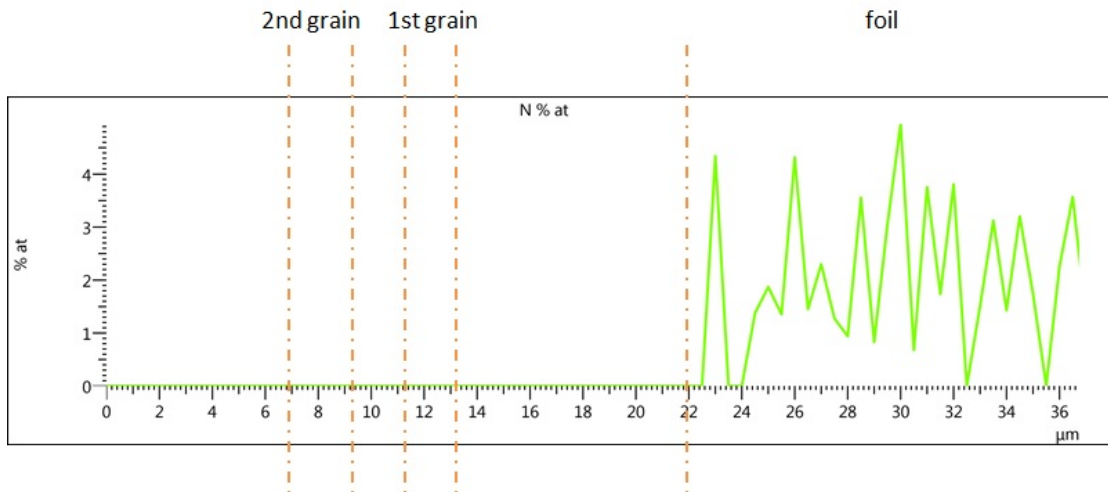


Figure 5.38: Linear analysis of nitrogen along the line shown in fig. 5.35

Tendency in aluminium distribution (Fig. 5.39) seems to be similar to the one in $\text{Al}_2\text{O}_3/\text{Ti6Al4V}$ composite (fig. 5.28). In grain closest to the foil there is around 15 at% of Al while in the second one it is already over 25 at%.

Observation of oxygen ratio in alumina/surface treated titanium composite (Fig. 5.40) is coherent with observation from the previous section (Ti6Al4V). There is some oxygen present in the foil, in the first grain its atomic percentage is slightly over 30 and in the second grain there is below 10 at% of oxygen.

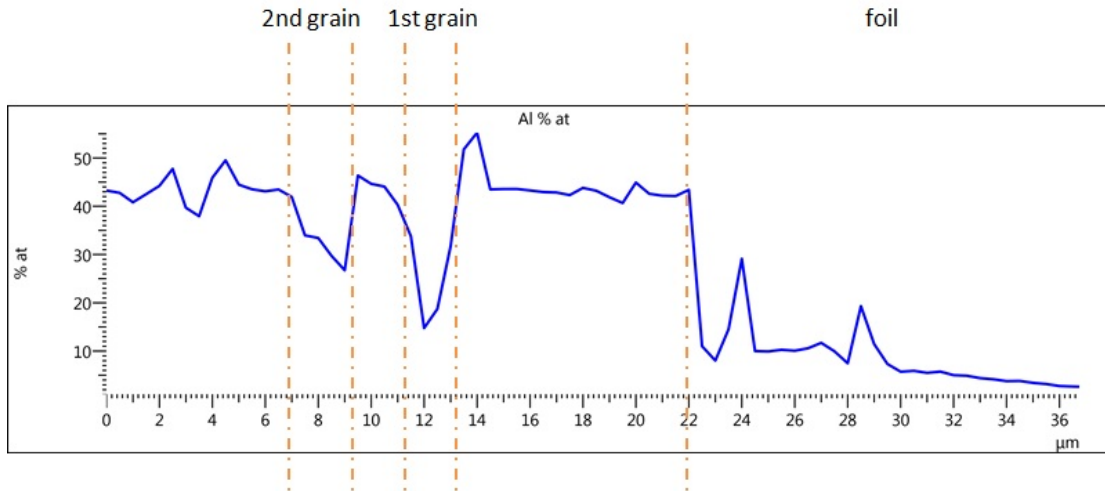


Figure 5.39: Linear analysis of aluminium along the line shown in fig. 5.35

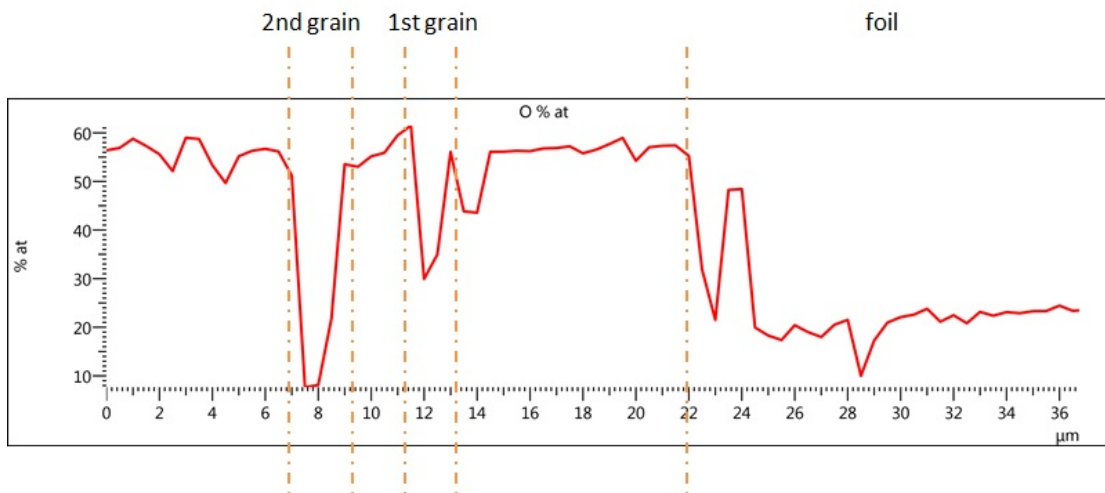


Figure 5.40: Linear analysis of oxygen along the line shown in fig. 5.35

Thanks to simultaneous sintering of alumina and titanium by FAST, ceramic/metal composites can be fabricated. In one processing step multiple hierarchical levels are obtained. Diffusion probably occurs when titanium is liquid. Decreasing cooling rate from 100°C/min to 10°C/min does not prevent cracking of metal foil. After sintering, two crystallographic phases of titanium are present; hexagonal and body centred cubic. Depending on cooling rate their proportion change. Inside the titanium foil some "brain-like" inclusions are present, further testing suggested that in fact, it is alumina. Composition of metal grains in the diffusion zone varies. Further microscopic tests are required to further understand physical and chemical phenomena occurring during the thermal treatment.

5.2 Mechanical properties

The main objective of fabricating titanium/alumina composites was to improve ductility without compromising strength. Three point bending (3PB) on notched samples was conducted to measure mechanical response: stress-strain and R-curves.

5.2.1 Preliminary study

Those materials were formed by uniaxial pressing so for the reference, samples from pressed powder without metal foil were prepared. 3.8g of powder was divided into four portions and pressed one after another in order to maintain platelets alignment (each layer was around $500\ \mu\text{m}$ thick after sintering). They were sintered at $1500\ ^\circ\text{C}$. Afterwards they were cut into bars (2 mm height and width, 14 mm length).

All samples were tested according to the same protocol (deflection speed equal to $5\ \mu\text{m}/\text{min}$). More details in the chapter "Materials and Methods". The results are presented in figures below 5.41, 5.42 and 5.43.

In the chapter "Modification of the interphase between platelets" it was stated that unnotched samples should be used to calculate stress-strain curves. As notched samples were used in this case, we present force-deflection curves as well. For stress-strain calculations from sample height, the notch depth was subtracted. Calculations were conducted as described in "Materials and methods". Yellow arrows mark onset of the crack propagation.

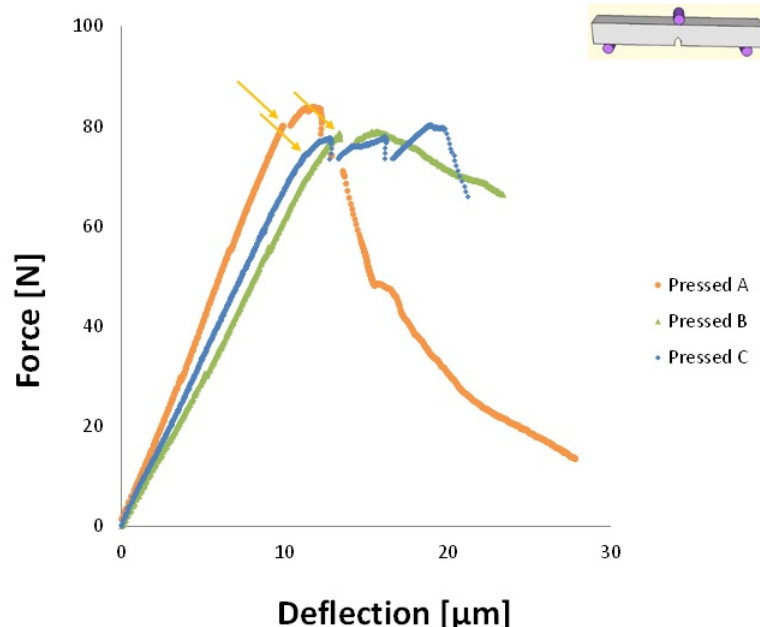


Figure 5.41: Force-Deflection curves of the reference material (no metal foil)

All three samples have maximum stress values close to 200 MPa with strain below 0.002. After reaching maximal value of stress it drops significantly in sample A.

5.2. MECHANICAL PROPERTIES

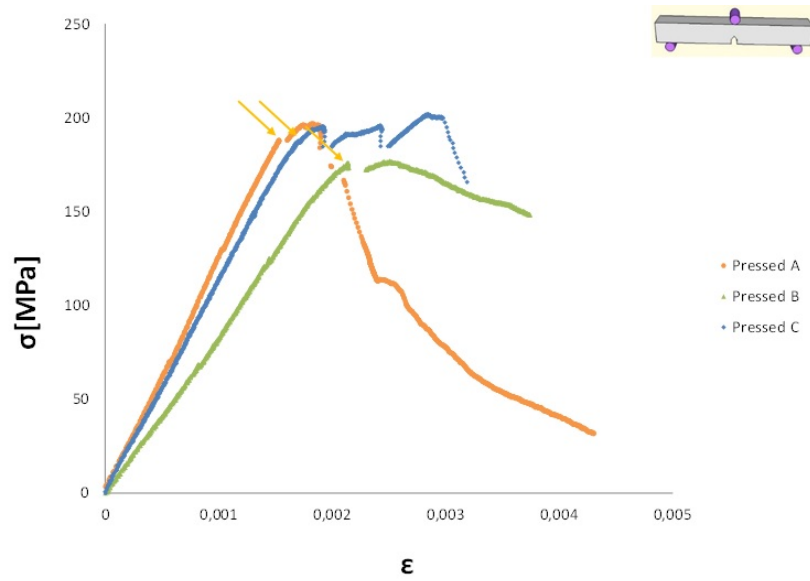


Figure 5.42: Stress-Strain curves of the reference material

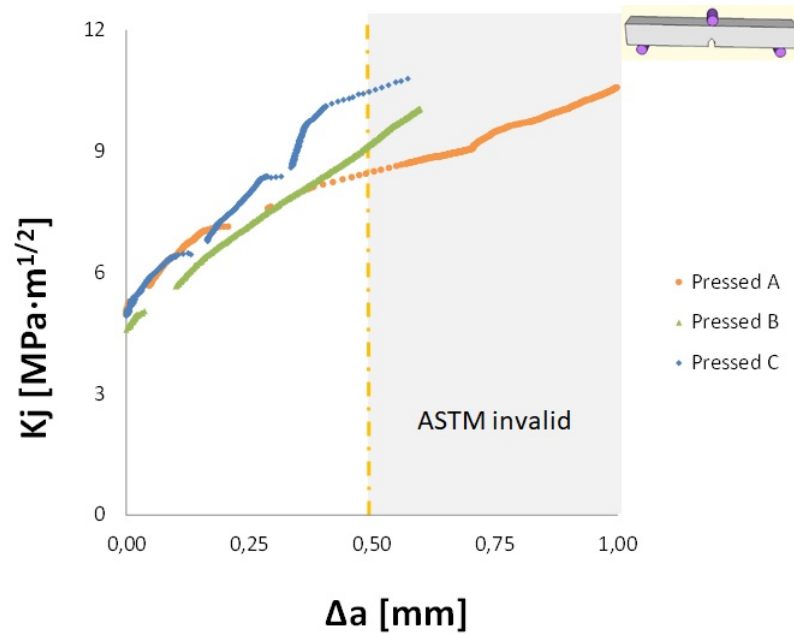


Figure 5.43: R-curves of the reference material

Within validity of ASTM norm fracture toughness increases notably from around $5 \text{ MPa}\cdot\text{m}^{1/2}$ to around $8 \text{ MPa}\cdot\text{m}^{1/2}$ for sample A and close to $10 \text{ MPa}\cdot\text{m}^{1/2}$ for B and C.

5.2.2 Mechanical testing *in situ*

Three point bending *in situ* was conducted in SEM to identify toughening mechanisms of fabricated materials (Thierry Douillard, Sophie Cazottes, MATEIS laboratory). Two samples were chosen for comparison: reference nacre-like alumina and a sample with titanium layer and without glassy phase.

First 3PB was performed at 0.1 mm/min speed. Pre-load of 6N was applied. Test was paused for observations at force of: 37, 67 and 90 N. Fatal failure with multiple signs of reinforcement occurred at 120 N. Fig. 5.44 shows a broken reference sample.

Fig. 5.44A shows an entire path of the crack from the tip of the notch (in the right upper corner). Crack deviated from the beginning and changed its direction multiple times. In the fig. 5.44B there is a close-up on the first part of the crack propagation. Fig. 5.44C presents a thin crack branch which deviated from the main path. Fig. 5.44D and E show zoom on the zone, where crack branch first deviated and then notably changed its direction to return to the main crack. In the picture D some platelets pull-out is also visible.

Second test was conducted on the sample with titanium foil and without glassy phase. Fig. 5.45 and 5.46 present pictures taken during this test. Fig. 5.45 shows the sample during the crack offset (at 70 N) from the tip of the notch.

As in case of 100 % ceramic sample, crack deviates directly at the beginning. Close-ups are in figures 5.45B and C.

Fig. 5.46 shows the same sample but after its failure (at 73 N).

After the off-set of the crack it propagated rapidly. As in full ceramic sample, presence of crack branching and deviation is visible. Unfortunately crack passes easily through cracked titanium foil. Presence of metal layer does not seem to improve mechanical properties by enhancing ductility. On the other hand, it seems that propagating crack is "searching" for a deep crack, already present in the foil, making it easier for crack do deviate. Nevertheless, avoiding cracking of the titanium foil would then improve mechanical behaviour of the composite.

5.2. MECHANICAL PROPERTIES

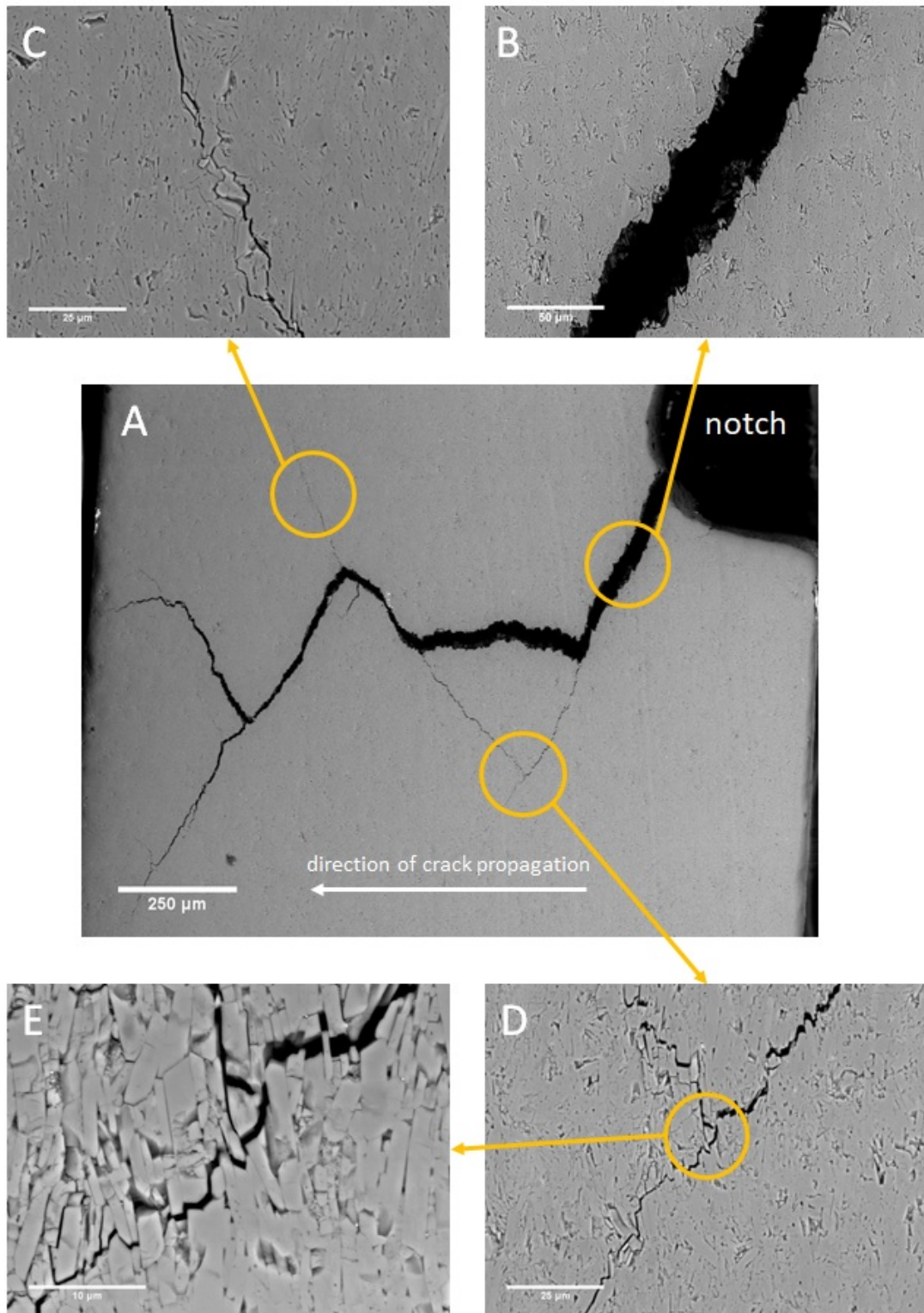


Figure 5.44: SEM pictures of the broken reference sample during three point bending *in situ*

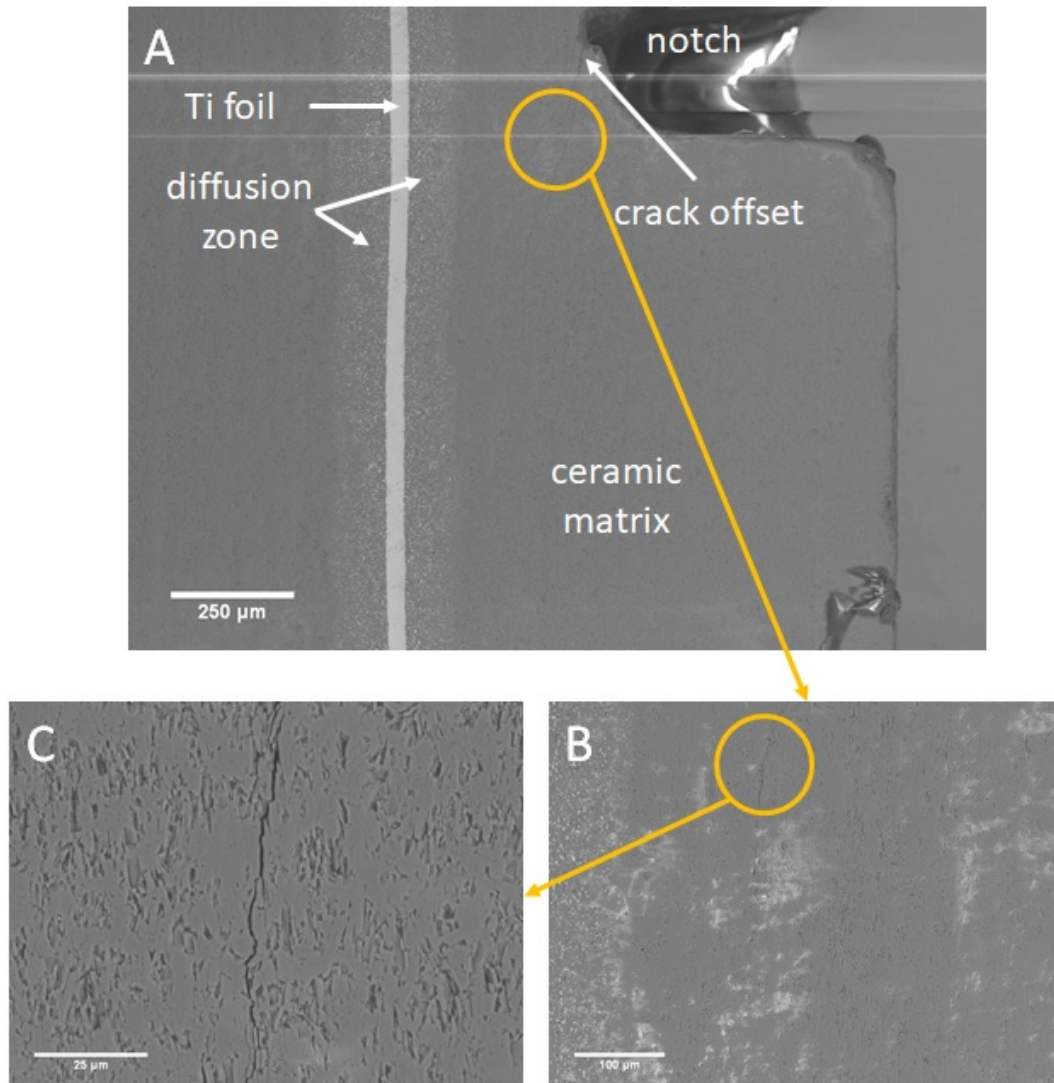


Figure 5.45: SEM pictures of the sample with a layer of titanium foil (without glassy phase) in the moment of crack offset (at 70 N) during three point bending *in situ*

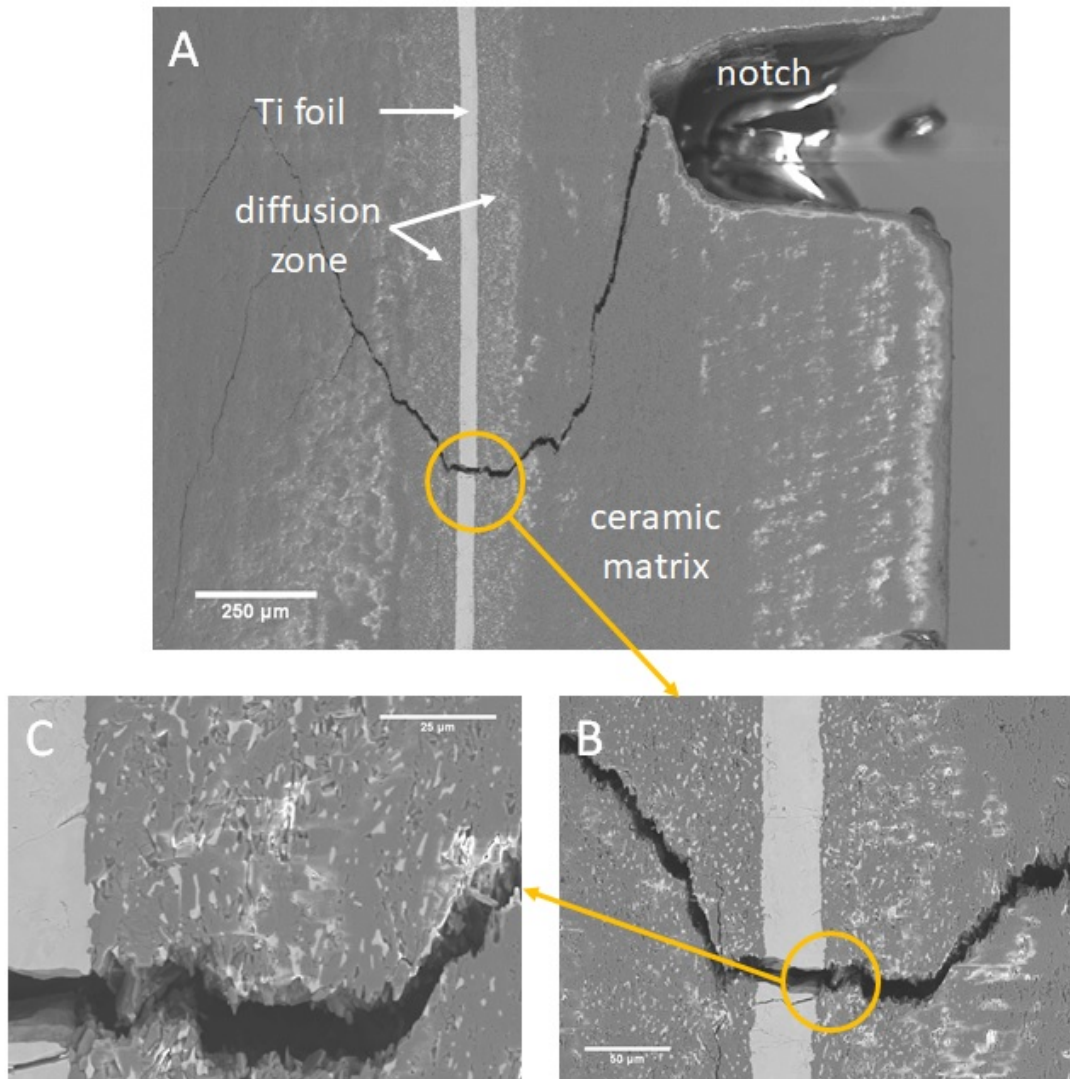


Figure 5.46: SEM pictures of the broken (at 73 N) sample with a layer of titanium foil (without glassy phase) during three point bending *in situ*

5.2.3 Influence of the foil thickness

Due to cracks in titanium foil after cooling ($100\mu\text{m}$ thickness) it was decided to fabricate composites with a lower foil thickness ($20\mu\text{m}$) to see if it could be diffused entirely and with high foil thickness ($500\mu\text{m}$) to check if cracks morphology was dependant on the foil thickness. There were always three metal layers, so volume fraction of titanium varied. Unfortunately, in all cases foil was cracked. For each foil thickness diffusion occurred. In the sample with $20\mu\text{m}$ foil diffusion and layer of metal were present. Results of mechanical testing of those samples are presented below. All samples had three metal layers. First there are curves for specimens with $20\mu\text{m}$ foil (figures 5.47, 5.48 and 5.49). Yellow arrows mark onset of the crack propagation.

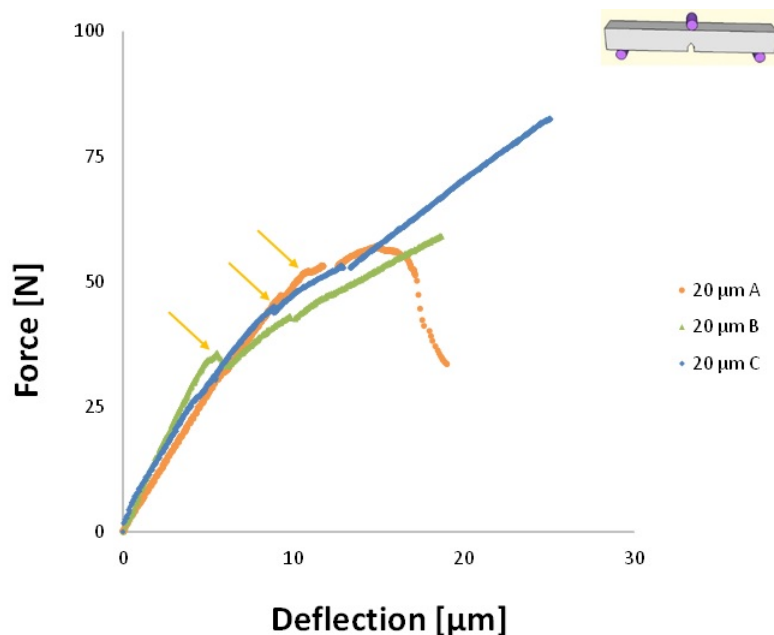


Figure 5.47: Force-Deflection curves of the material with $20\mu\text{m}$ foil. Sintered at 1500°C , heating rate: $100^\circ/\text{min}$, cooling rate: $10^\circ/\text{min}$.

Sample A presents behaviour which differ from samples B and C. While for B and C stress values increase until the rapid failure, A shows drop in stress before breaking. Stress at failure for sample C reaches 250 MPa and it is the highest value among those three specimens.

Difference in mechanical behaviour between the three samples is visible in values of fracture toughness. Although B and C have value at fracture initiation of $2\text{ MPa}\cdot\text{m}^{1/2}$, their fracture toughness increases visibly to almost $8\text{ MPa}\cdot\text{m}^{1/2}$ for B and to almost $13\text{ MPa}\cdot\text{m}^{1/2}$ for C. A starts at $4\text{ MPa}\cdot\text{m}^{1/2}$ but it barely reaches $8\text{ MPa}\cdot\text{m}^{1/2}$. On the other hand R-curves for specimens B and C have unusual form. Their valid fracture toughness might be lower than indicated. In comparison with the reference there is no visible influence of titanium foil on the mechanical performance.

Results for material with foil of $100\mu\text{m}$ are presented in figures 5.50, 5.51 and 5.52, force/deflection, calculated stress/strain and fracture toughness respectively.

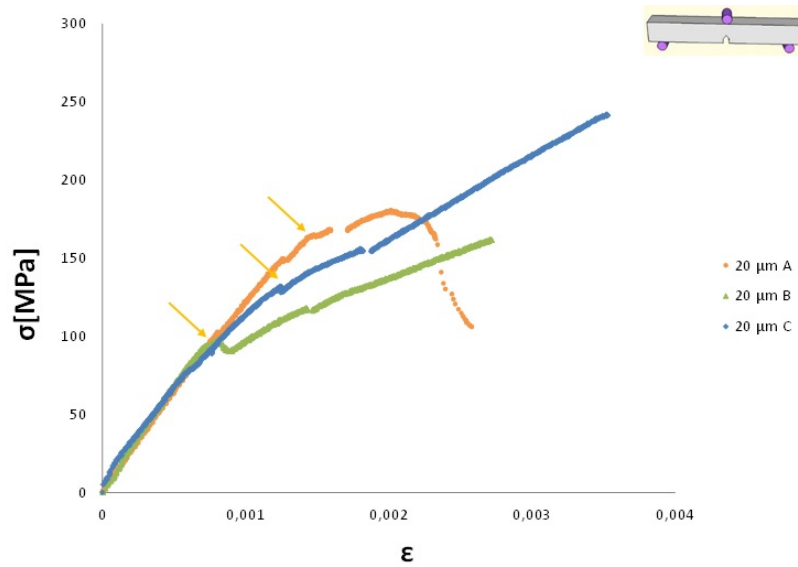


Figure 5.48: Stress-Strain curves of the material with 20µm foil

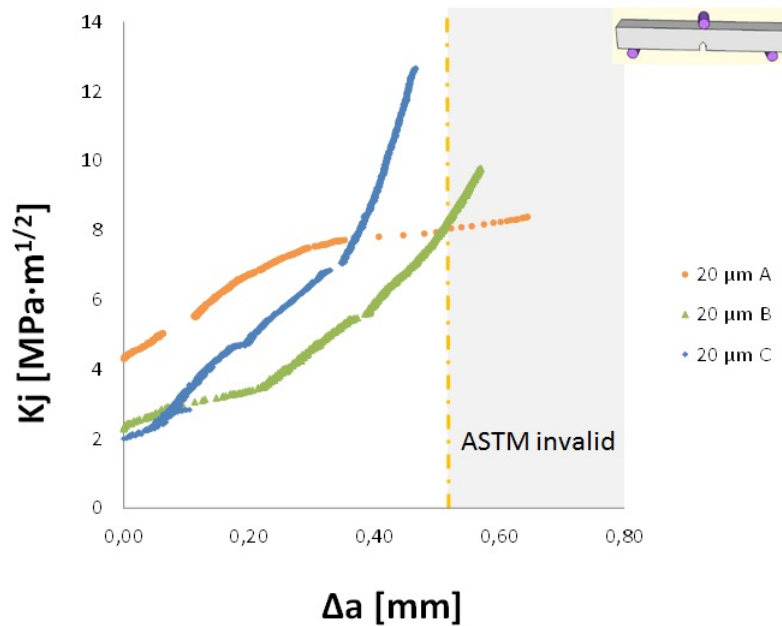
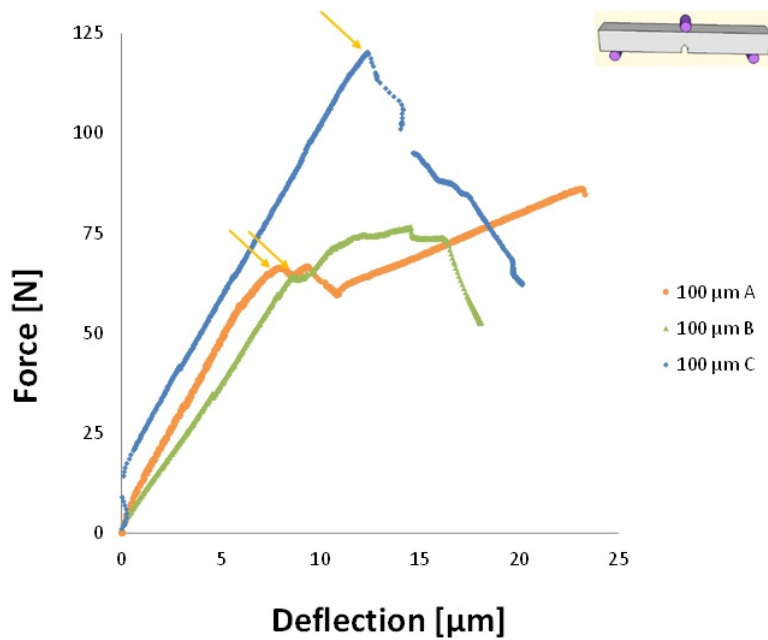
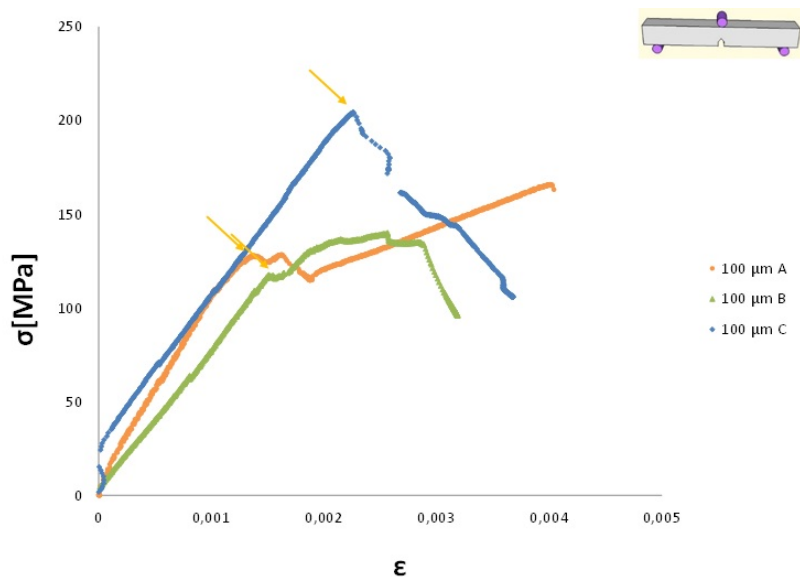


Figure 5.49: R-curves of the material with 20µm foil. For samples B and C an ASTM invalid zone begins earlier, before 0.4 mm crack extension.

Sample A, after a slight drop at stress value during crack propagation, surpasses stress values of 150 MPa before its failure with strain higher than 0.004. Sample B does not reach stress of 150 MPa and its strain only slightly surpasses 0.003. Samples C reaches the highest value of stress at over 200 MPa but afterwards it decreases quickly. Its strain is close to 0.004. It seems probable that crack during its propagation "searches for" a deep crack in the metal foil.

Regarding fracture toughness, for specimen A and B it increased from 3 MPa·m^{1/2}

Figure 5.50: Force-Deflection curves of the material with 100 μm foilFigure 5.51: Stress-Strain curves of the material with 100 μm foil

to 7 $\text{MPa}\cdot\text{m}^{1/2}$ during crack propagation, while for sample C from 5 $\text{MPa}\cdot\text{m}^{1/2}$ to 9 $\text{MPa}\cdot\text{m}^{1/2}$.

Results for material with foil of 500 μm are presented in figures 5.53, 5.54 and 5.55.

Shape of stress-strain curves for all three samples is quite similar: slight decrease of stress after onset of crack propagation, then increase, drop and a small plateau before the failure (no plateau for B). This behaviour was not seen in previous samples. Here, the foil is relatively thick (500 μm). This is why those "jumps" in stress

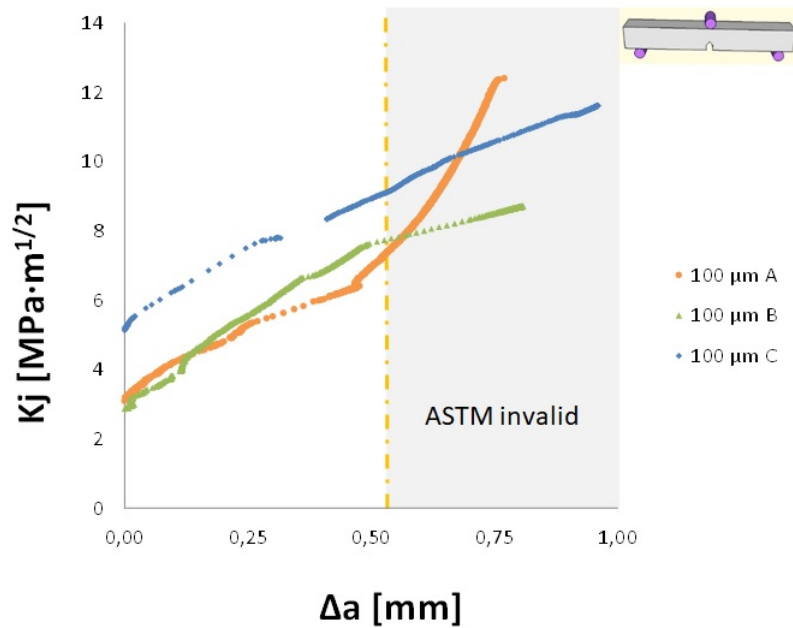


Figure 5.52: R-curves of the material with 100µm foil

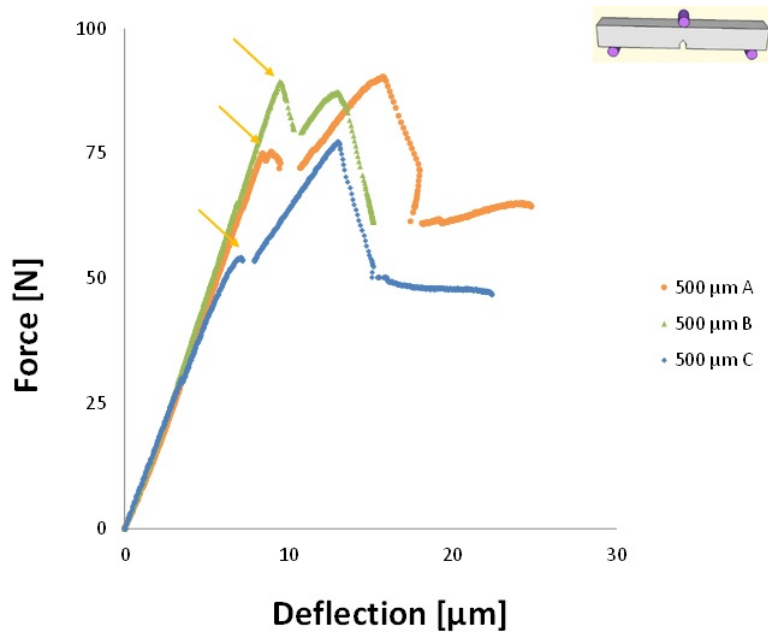
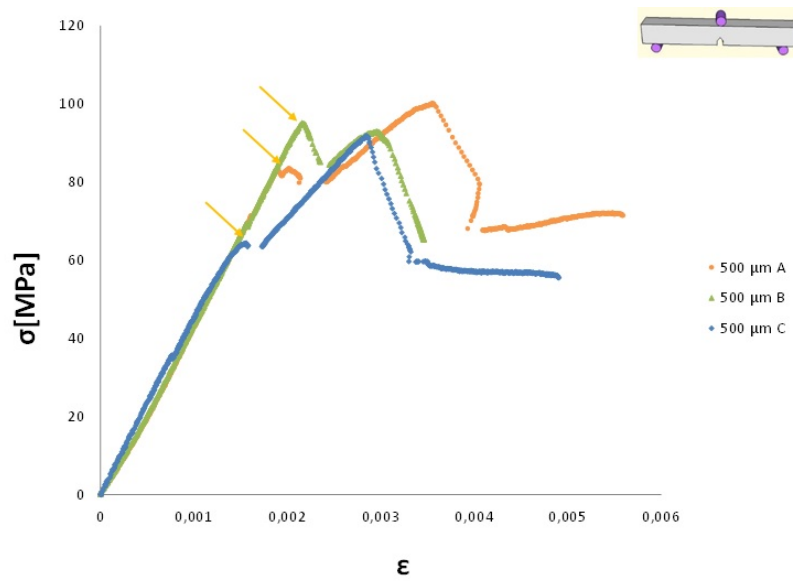
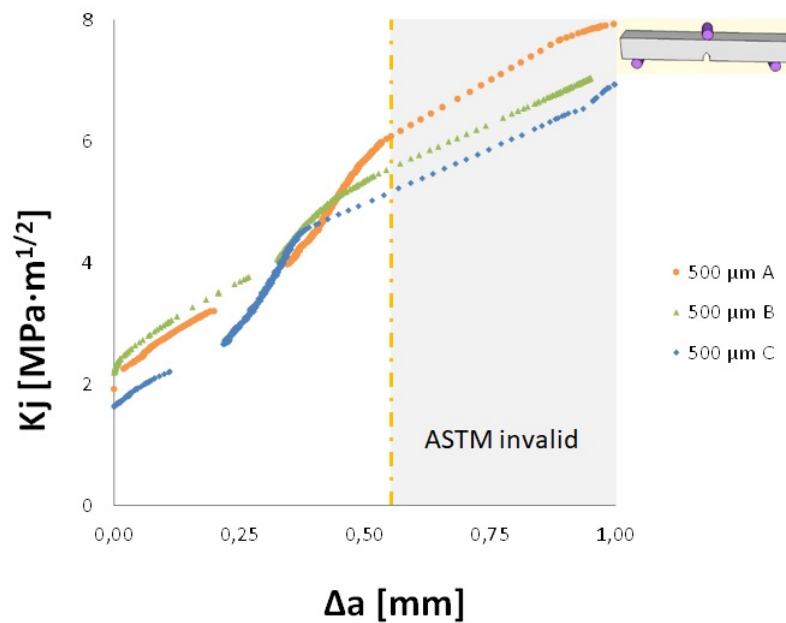


Figure 5.53: Force-Deflection curves of the material with 500µm foil

values are more pronounced and visible. All maximum values are close to 100 MPa but strain at failure differs from slightly over 0.003 to almost 0.006.

Fracture toughness at crack onset is quite low: $2 \text{ MPa}\cdot\text{m}^{1/2}$. At the end of zone of ASTM validity it reaches between 5 and $6 \text{ MPa}\cdot\text{m}^{1/2}$, lower values than those noted for samples with 20 and 100 µm foils.

In the fig. 5.56 stress-strain curves for three foil thickness are compared (one typical curve for each case).

Figure 5.54: Stress-Strain curves of the material with 500 μm foilFigure 5.55: R-curves of the material with 500 μm foil

In elastic regime slope and maximal value of stress decreases with increase of foil thickness. When foil thickness increases, strain at failure increases as well. Depending on the sample, distance between the notch and foil might differ. For each sample notch depth was measured and taken into account during calculations.

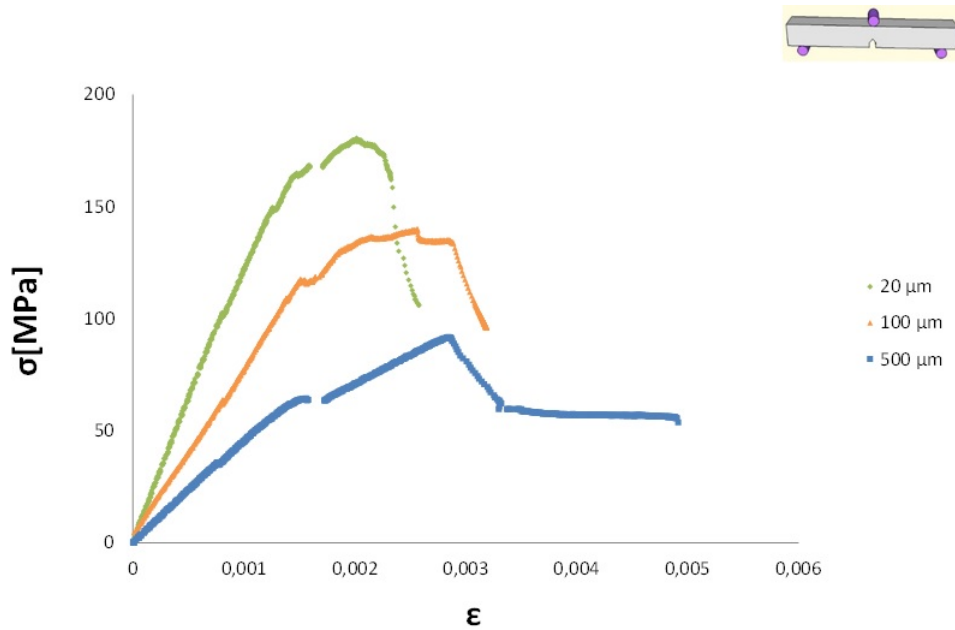


Figure 5.56: Comparison of Stress-Strain curves of materials with different foil thickness

5.2.4 Influence of the foil chemistry

Ti6Al4V

After detailed microstructural analysis (section 1.1.3 of this chapter) samples were tested mechanically. One test did not work due to the experimental problems with the testing set-up, so results of only two tests are presented. Yellow arrows indicate the onset of crack propagation.

Two presented samples are very different. First one (B) reaches its highest stress value of almost 125 MPa even before crack propagation and afterwards it decreases until failure at strain of almost 0.006. For the second one (C) stress continues to increase after the crack began to propagate and its maximum value is around 100 MPa. Its strain at failure is quite high 0.01.

Values of fracture toughness also differ visibly. For specimen B the starting value is close to $4 \text{ MPa}\cdot\text{m}^{1/2}$ and increases to almost $7 \text{ MPa}\cdot\text{m}^{1/2}$. In case of specimen C those values are even lower: 1 and $3 \text{ MPa}\cdot\text{m}^{1/2}$ respectively.

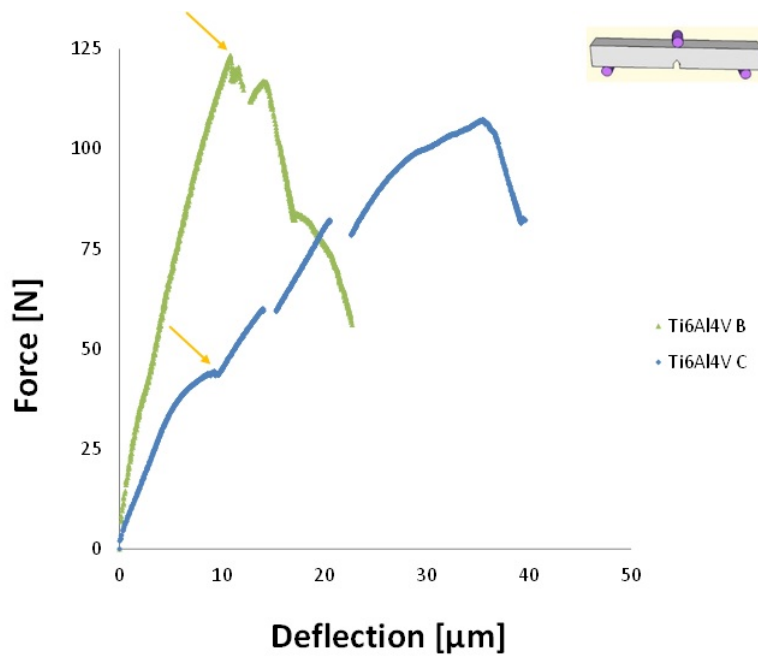


Figure 5.57: Force-Deflection curves of the material with Ti6Al4V foil (around $500\mu\text{m}$ thick)

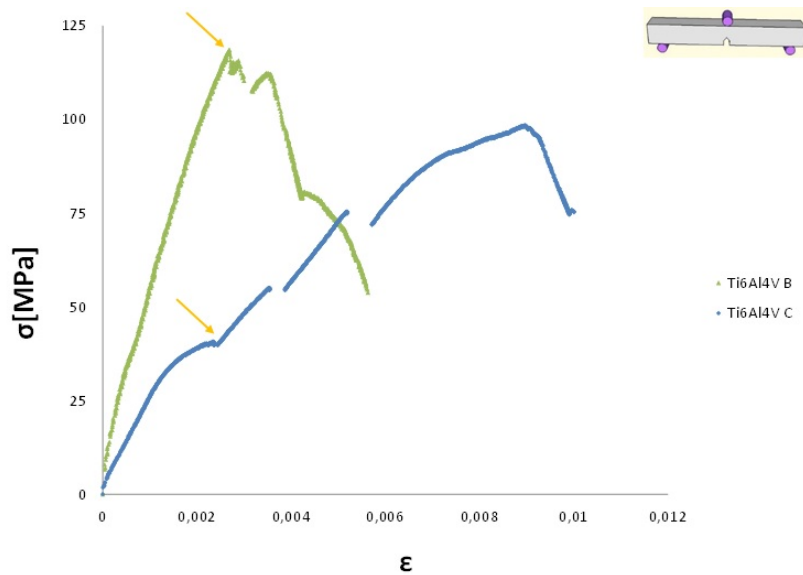


Figure 5.58: Stress-Strain curves of the material with Ti6Al4V foil (around $500\mu\text{m}$ thick)

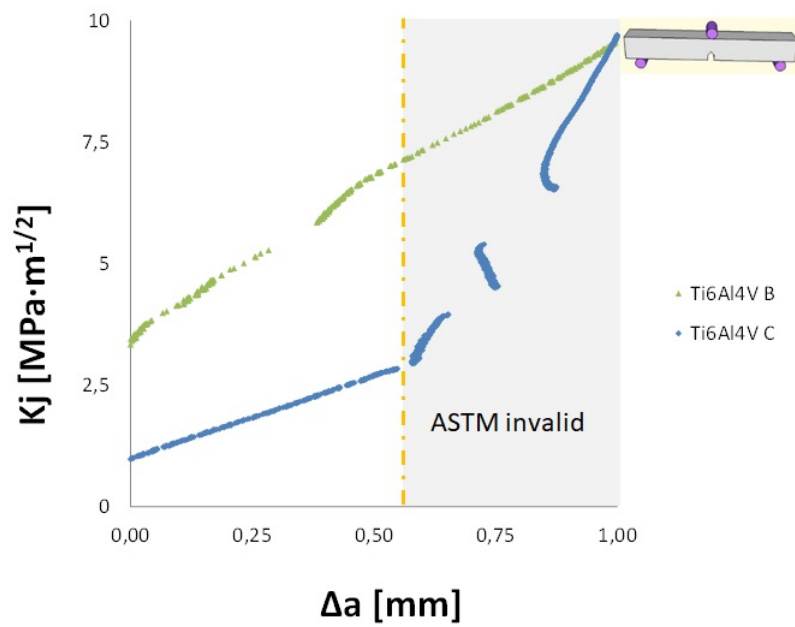


Figure 5.59: R-curves of the material with Ti6Al4V foil (around $500\mu\text{m}$ thick)

Ti(N)

After micro-structural analysis (section 1.1.3 of this chapter) mechanical testing was conducted on the samples with titanium foil coated with thin layer of TiN (total thickness of around $500\ \mu\text{m}$ and thickness of coating $2\text{-}3\ \mu\text{m}$). Results are presented in figures 5.60, 5.61 and 5.62.

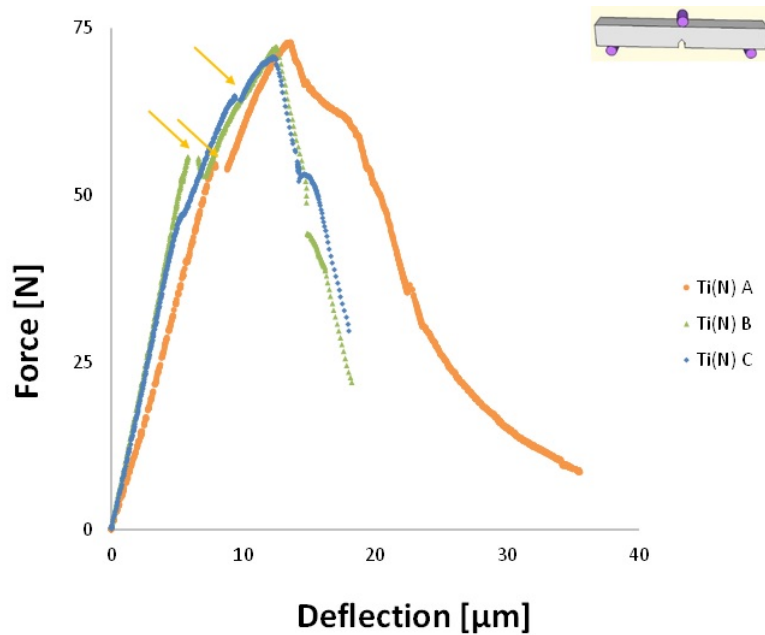


Figure 5.60: Force-Deflection curves of the material with Ti foil with TiN layer (around $500\ \mu\text{m}$ thick)

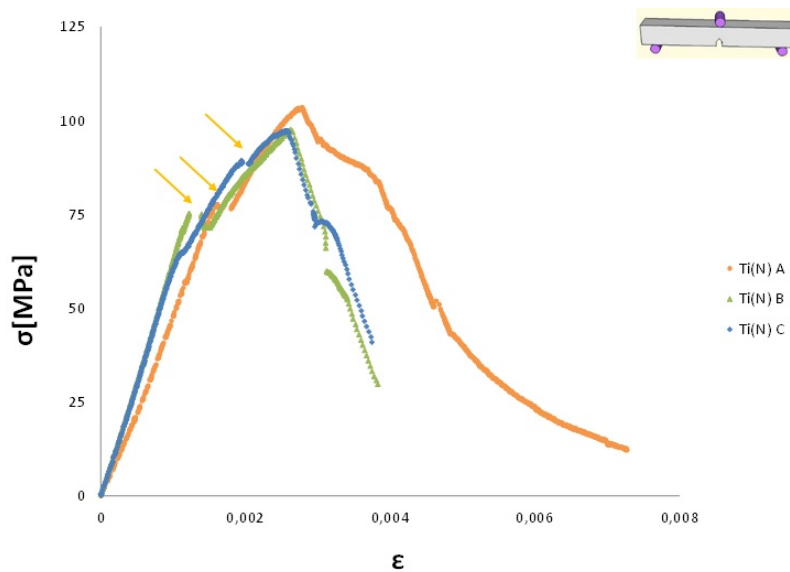


Figure 5.61: Stress-Strain curves of the material with Ti foil with TiN layer (around $500\ \mu\text{m}$ thick)

5.2. MECHANICAL PROPERTIES

Shapes of strain-stress curves resemble each other. After the beginning of crack propagation stress continues to increase only to decrease significantly before failure. Maximum stress values were around 100 MPa. Strain at failure was notably higher for sample A: surpassing 0.007 in comparison to 0.004 of B and C.

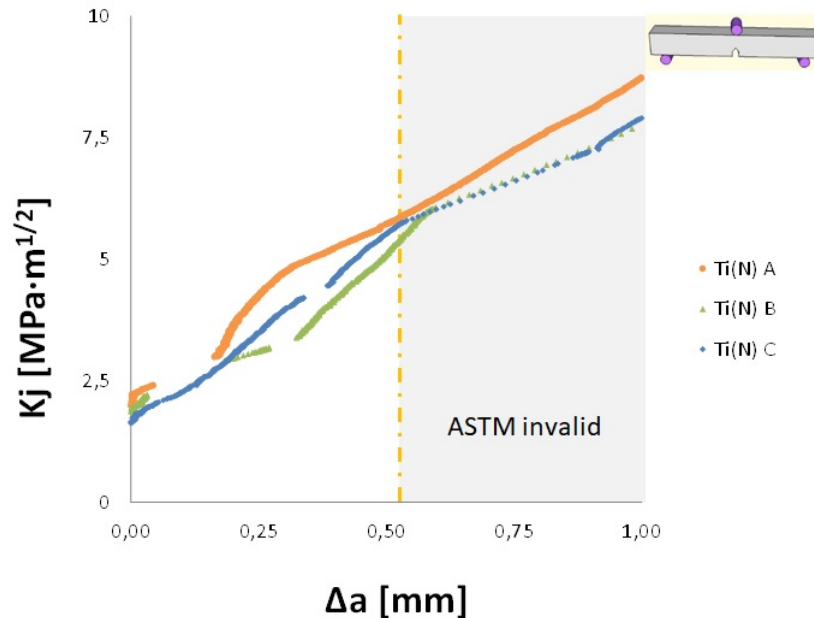


Figure 5.62: R-curves of the material with Ti foil with TiN layer (around 500 μ m thick)

Fracture toughness is almost the same for the three specimens. It begins at 2 MPa·m^{1/2} and increases to almost 6 MPa·m^{1/2}.

Fig. 5.63 shows comparison of stress-strain curves of samples with different foil compositions to reference sample with titanium foil with 500 μ m thickness.

Both compositions showed higher stress and strain values. Sample with Ti6Al4V foil had approximately as many cracks as in samples with pure titanium of various thickness (even each 100 μ m) while in Ti(N) foil crack were less frequent (roughly each 400 μ m). It seems reasonable that to significantly improve mechanical properties of the composite, cracks should be completely eliminated. Diffusion was present as in all previous materials containing metal. Slight improvement might be linked with the fact that Ti6Al4V and TiN have some better properties in comparison with pure titanium.

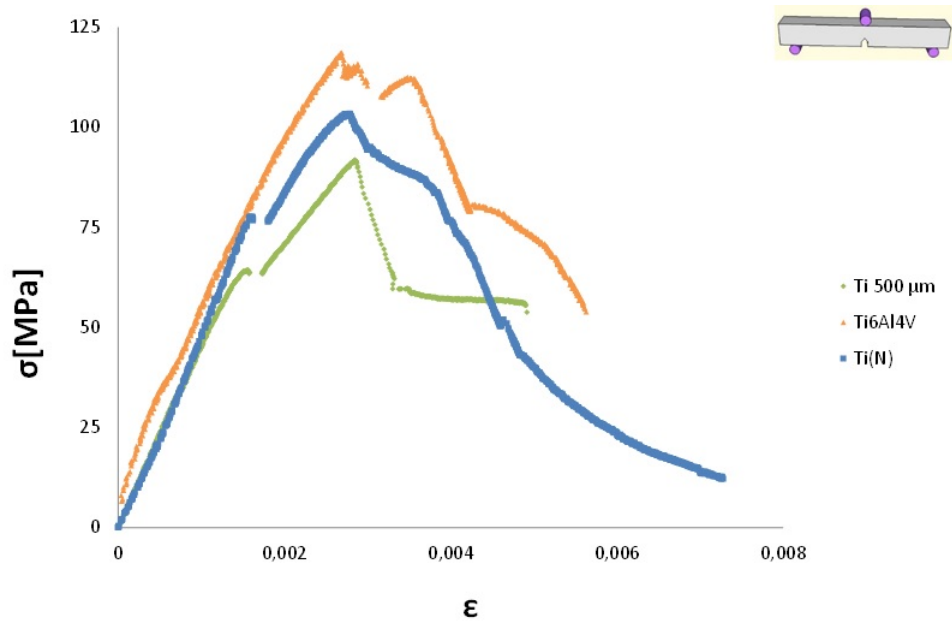


Figure 5.63: Comparison of Stress-Strain curves of materials with different foil chemistry (500 μm thick metal layers)

5.3 General discussion

Certain parts of this chapter were complicated to interpret. A lot of imaging techniques were used to comprehend phenomena discovered during elaboration and explain some microstructure characteristics.

Multiscale structure

When titanium is sintered with alumina in a layered composite at a maximum temperature of 1500 °C, it diffuses into the ceramic matrix, unless holding time at temperature below 1400°C is applied. In this case, almost no diffusion is observed. It is possible that during the 30 minutes of holding time at 1200°C and 1300°C, pores had already been closed before conditions favouring diffusion were reached or that titanium was not liquid. To obtain a material with titanium well-diffused into ceramic matrix it is necessary to reach 1400°C before holding the temperature.

Unfortunately, the metal foil was seriously cracked after cooling due to CTE mismatch between alumina platelets and titanium. Even lowering cooling speed from 100°C/min to 10°C/min to favour stress relaxation did not solve this problem. It is possible that removing the pressure before cooling could help to avoid undesired damage.

As changing cooling speed so significantly could affect crystallography of metal component, EBSD analysis was performed to compare the microstructures obtained for the two cooling conditions (fig. 5.6). The first specimen (cooled 100°C/min) was rich in both titanium phases: hexagonal (α) and body-centred cubic (β). In the outer area of the foil, the concentration of β phase was higher, while in the center,

there was more α phase. In case of second sample (cooled 10°C/min), the hexagonal structure was dominant, with the presence of cubic phase in the middle of the foil. The possible explanation of different proportions of α and β phase in two materials is that during the fast cooling, titanium was not able to reverse its phase change and consequently there was high cubic phase content. During slower cooling, some cubic phase might have been transformed back to hexagonal. Chemical and physical interactions during sintering were also complex.

Titanium was sintered in presence of alumina (platelets and nanoparticles) and liquid phase precursors (silica and calcium carbonate). As titanium reacts easily with oxygen and aluminium (α stabilizers), it is probable that it affected the final microstructure. In both materials, α and β phase were ordered in lamellae. A big difference in microstructure was noticed at the edges of the foil. The second sample (cooled 10°C/min) had lamellae in titanium only in the middle while ordered dual structure of the first sample was present in the entire thickness.

The presence of "brain-shaped" inclusions at the border of the Ti foil was noticed. We initially thought these regions were TiAl intermetallics. However, EDX analysis seemed to indicate that they could be Al_2O_3 . EBSD also indexed those structures as alumina. Moreover, in the Ellingham-Richardson diagram (see fig. 5.64) it is visible that thermodynamically alumina is more stable than titanium oxide (TiO_2) in temperature range we use for sintering.

Understanding interactions between ceramic and metal phase during sintering should allow to explain how alumina penetrated the titanium foil. It is possible that alumina diffused into the molten titanium and re-precipitated upon metal solidification.

By conducting tomography scans with a very high resolution (50nm/pixel) at the ESRF, we hoped to understand the mechanisms of diffusion in those layered composites. By comparing samples prepared in various sintering conditions, we were able to select the "model sample" with very pronounced diffusion and a good quality of the scan: sintered during 30 min at 1500°C. 3D reconstruction allowed us to see that many of the titanium grains were in fact interconnected. It was something we could not determine by SEM due to 2D limitation of this analysis. Possible explanation of the interconnections between grains is that some quantity of the titanium was liquid during the thermal treatment. Even though the maximal programmed temperature was 1500°C and melting point of titanium is the 1670°C, it is probable that the conducting metal heated much faster than non-conducting ceramic. Difference in heating of conductive and non-conductive material are discussed in the part analysing diffusion of titanium and in [24]. The partial melting of metal during FAST would also explain the difference in microstructure between the centre and the edge of the foil. Fig. 5.65 shows the zone of the foil that was probably liquid during sintering because its structure is not lamellar like in the middle.

In the fig. 5.65 lamellae of titanium cubic (in yellow) seem to alternate lamellae of titanium hexagonal (in blue) in a regular manner. This particular morphology is also visible in the fig. 5.66 which shows IPFZ map (Inverse Pole Figure) for both cubic and hexagonal phases (A and B respectively). It is visible that lamellae of hexagonal phase are surrounded by cubic phase within well-defined domains (first domain is

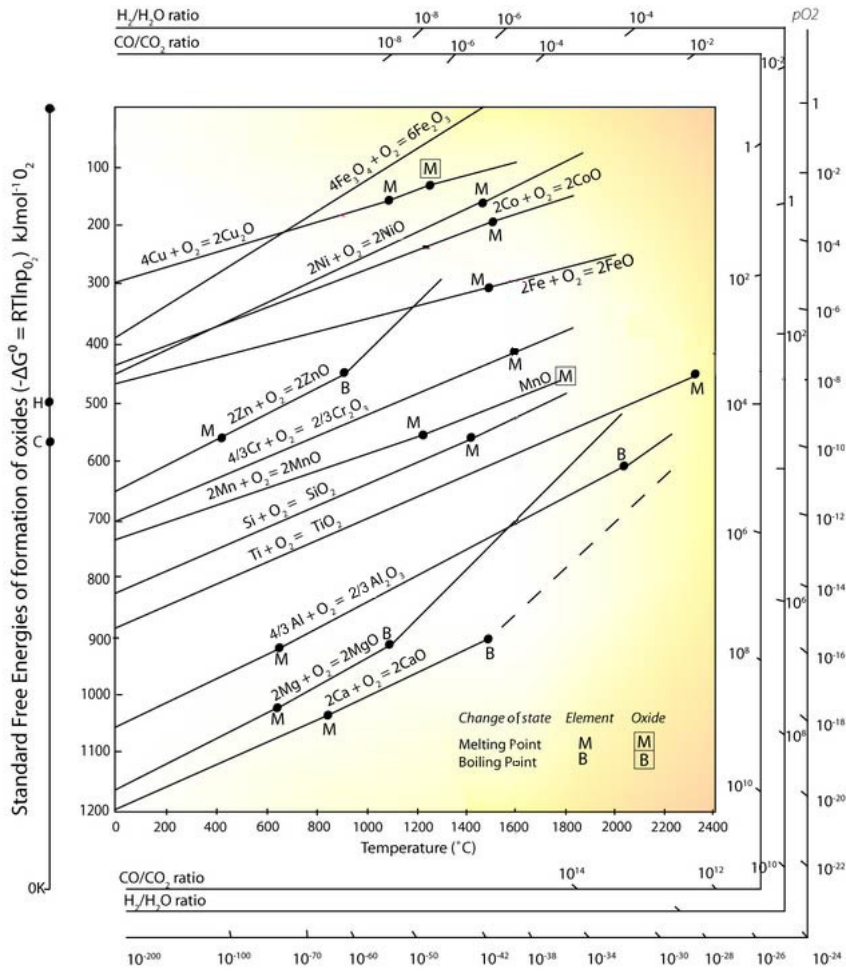


Figure 5.64: Ellingham-Richardson diagram of common oxides (free energy in function of temperature). It shows that thermodynamically alumina is more stable than titanium oxide (TiO_2) in our temperature range.

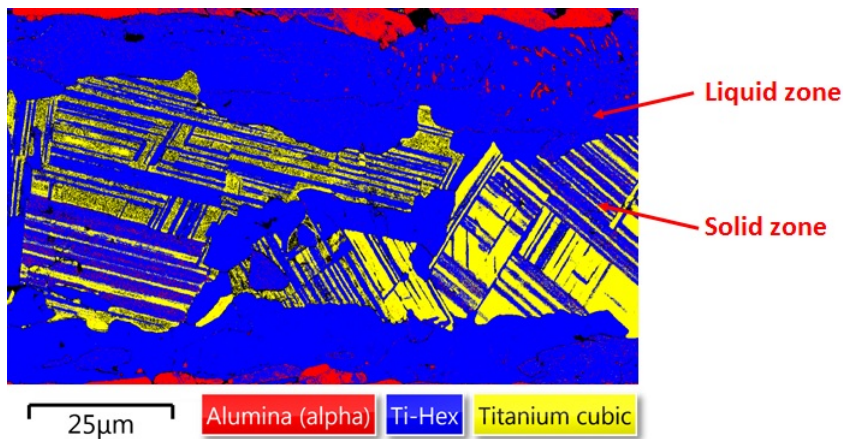


Figure 5.65: Microstructural difference between the zone which was solid and the zone that was probably liquid during sintering

5.3. GENERAL DISCUSSION

contoured in red dashed line in picture A, and the second one in black). Those domains could correspond to parent grains before sintering. This grain morphology is not very common for pure Ti alloys, but commonly observed in the case of TiAl alloys after quenching.

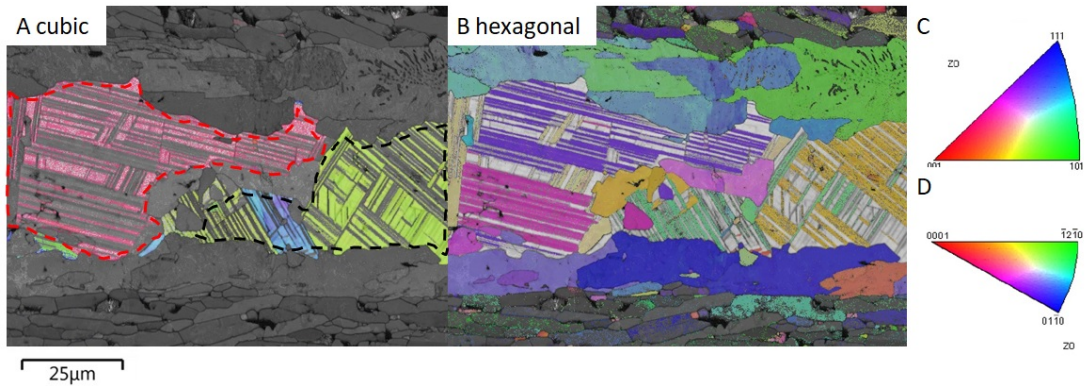


Figure 5.66: IPFZ maps for the titanium foil. A) IPFZ for cubic phase, B) IPFZ for hexagonal phase, C and D) color codes for grain orientations for cubic and hexagonal phase, respectively. Images obtained from EBSD analysis and software Channel 5.

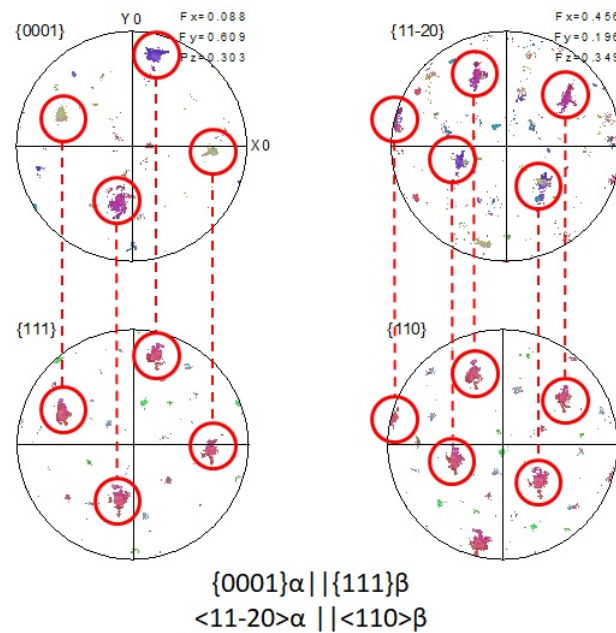


Figure 5.67: Orientation relationships between cubic and hexagonal phase found in the first domain (contoured in a red dashed line in the picture 5.66B)

Fig. 5.67 shows pole figures of both phases present in the first domain. Red circles connected by the dashed line indicate orientation relationship. It allows to conclude that lamellae of cubic and hexagonal phases have in common certain crystallographic orientations. Firstly, we have looked for the Burgers Orientation Relationship: $\{0001\}\alpha \parallel \{011\}\beta$ and $\langle 11-20 \rangle\alpha \parallel \langle 111 \rangle\beta$, which is usually found in

titanium [101], [102]. However the OR that was found is: $\{0001\} \alpha \parallel \{111\} \beta$ and $\langle 11-20 \rangle \alpha \parallel \langle 110 \rangle \beta$, often called Blackburn OR [103]. This result seems to confirm that both phases origin from the same grain. The same analysis was performed on the second domain and same relations were found.

Ti6Al4V

Apart from pure Ti, Ti6Al4V was used to fabricate layered composites. Detailed microstructural and chemical characterisations were conducted as it was proven before that metal/ceramic interactions are complex and can lead to obtaining sophisticated microstructures.

Ceramic inclusions are present in the titanium alloy foil as in case of pure titanium foil. It is not very surprising as the melting point of Ti6Al4V varies between 1604 and 1660°C [104] so it is probable that some part of this alloy was liquid during the sintering and as a consequence, that alumina could be embedded in metal during its solidification. EDX confirmed that those inclusions are composed of oxygen and aluminium.

In the SEM pictures, some differences of grey level within grains were noticed. During chemical analysis it became clear that differences in brightness stems from different ratios of elements present (fig. 5.22). Lighter parts of grains contain almost 40 at% of silicon in comparison to none in the darker parts. Darker parts are however rich in aluminium: 72.5 at% while light ones only around 5.6 at%. It is thus probable that presence of O, Al and Si during the sintering has shifted equilibrium of elements of the alloy and provoked significant heterogeneities.

A linear analysis along the foil, ceramic matrix and diffused grains allowed to examine if some elements diffused gradually (fig. 5.26). Moving away from the foil, the percentage of titanium in grains drops from around 60% in the foil and in the first grain to below 30% in grain 25 μm in the ceramic matrix. On the other hand, it is quite opposite for the aluminium content. In the foil it is almost zero, in the first grain over 20% and in the second close to 30%. It seems that further away from the metal foil, titanium is substituted by aluminium. Evolution of quantity of oxygen is less straightforward. Inside the titanium foil, it varies significantly (between 5 and 45 %), in the first diffused grain it drops to almost 0% only to increase in the second one to over 35%.

Ti(N)

The last layered material analysed was composed of alumina with titanium foil coated with a layer of TiN (2-3 μm thickness). As previously, a detailed microstructure and chemical analysis was applied.

"Brain-like" inclusions in the metal foil were found also in this composite. Some differences in grey level between metal in direct proximity with inclusions and metal further away were noticed. Chemical analysis revealed that material outside of inclusions zone contains 96.4 at% of titanium and 3.4 at% of aluminium in comparison to 83.9 at% of Ti and 15.4 at% between inclusions. Interestingly nitrogen was not

detected. It is possible that part of titanium which melted during sintering dripped outside of nitride layer (TiN melting point is 2950°C [105]). Differences in Ti and Al content seems to confirm that part of titanium was liquid during the sintering and reacted with components of ceramic matrix.

Comparison of spectra of metal and of inclusions further proved that inclusions are most probably Al_2O_3 . In that case it is logical that same structures were found in all types of metallic foil used in this study.

Analogically with Ti6Al4V different metal grain types were found. Closer to the foil they were composed of 56.9 at% of Ti and 43.1 at% Al, while further into the ceramic matrix, the titanium content dropped slightly to 55.9 at%, the aluminium content dropped significantly to 10.3 at% and silicon appeared at ratio of 33.7 %. It seems that titanium diffused further in the ceramic matrix in alumina/titanium composites reacts stronger with glassy phase precursors which are also liquid during the thermal treatment.

Linear chemical analysis was also performed. Two diffused grains were placed quite close to each other and their titanium content was similar (52 and 58 %). On the other hand they differed in terms of aluminium content (14 and 26 % respectively) and oxygen (30 and 0 % respectively). Nitrogen was detected only within the foil and its distribution was heterogeneous. The aluminium content inside the metallic foil increased closer to the interphase. Oxygen was also present in the foil. It is probable that in all types of composites described in this chapter, oxygen in the metallic phase comes from ceramic matrix. Three types of fabricated composites do not differ significantly between each other.

Those results prove that the interactions between elements during thermal treatment in FAST are complex and it will require a lot of additional analysis to understand them.

We managed to fabricate composites with sophisticated multilevel structure in a relatively simple way (preparation of the slurry, uniaxial pressing and FAST). To our knowledge this has not been accomplished so far. Even without freezing step platelets are well-aligned. Thanks to diffusion and probable extrusion of liquid metal through the porous structure due to the applied pressure, metal was incorporated between alumina platelets. There are still possibilities of improvement, limiting cracking of the foil is the crucial one.

Mechanical properties

The ceramic/metal composites were fabricated to obtain material with mechanical properties improved in comparison to nacre-like alumina, especially in terms of fracture toughness. Results from three point bending on notched samples were compared with reference sample made from powder of Bouville's composition and pressed (without freezing under flow step). In figure 5.68 results obtained for samples with different foil thickness for a pure titanium foil were compared and in figure 5.69 results for samples with different foil chemistry are plotted. For each kind of sample one typical result was chosen.

In case of different thickness values, sample with $20\mu\text{m}$ foil had similar maximum stress value but a slightly lower strain at failure. Sample with $100\mu\text{m}$ foil had both values lower than the reference. Sample with $500\mu\text{m}$ foil had higher strain at failure but its maximum stress value was significantly lower.

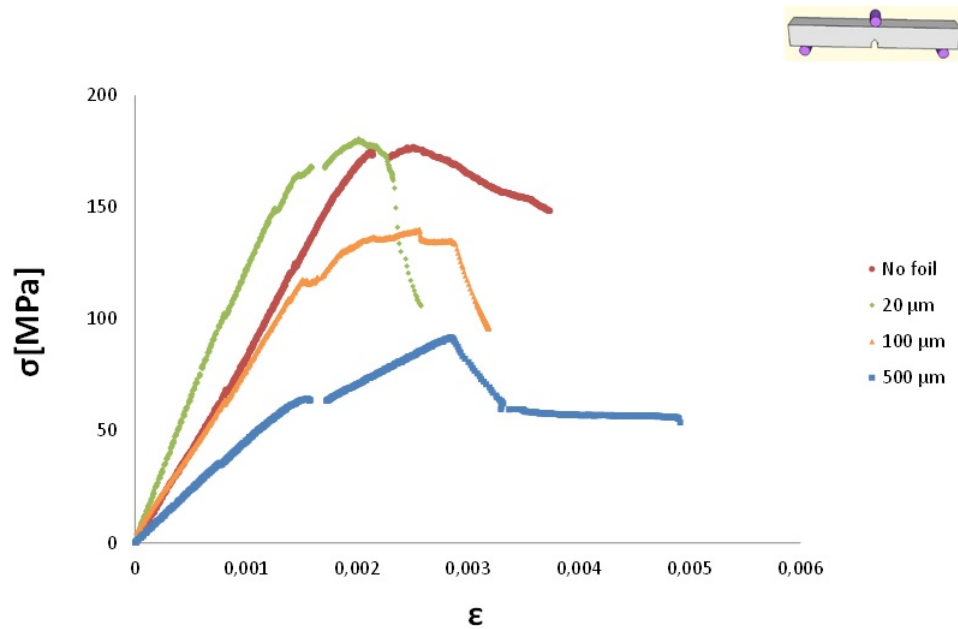


Figure 5.68: Comparison of Stress-Strain curves of materials with different foil thickness with reference material

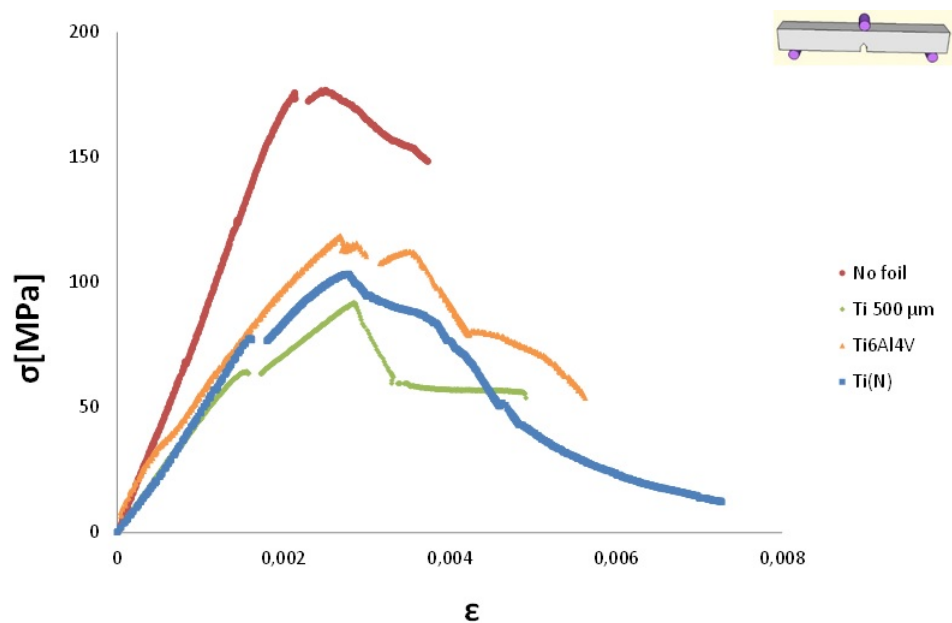


Figure 5.69: Comparison of Stress-Strain curves of materials with different foil chemistry with reference material

5.3. GENERAL DISCUSSION

When comparing material of various foil compositions with the reference ceramic, sample has significantly higher stress at failure than any metal/ceramic multilayer. Composite Ti6Al4V/ Al_2O_3 has high strain at failure but its maximal stress is quite low (probably due to cracks in the metal layer). *In situ* test in a SEM has shown the importance of cracks coming from the mismatch of CTE of both materials.

For the moment, improvement of mechanical properties was not achieved. It is crucial to prevent metal foil cracking to avoid compromising mechanical response. Some possible solutions should be considered. Maybe removing the pressure during sintering, before cooling of the sample could reduce foil cracking. If not, adding some material between titanium and alumina should be considered. It could lower residual stresses coming from the difference in CTE and help preserve Ti. On the other hand surely it would affect diffusion so it could complicate the processing and testing of the material. On another hand, changing ceramic component to the one with higher CTE (like zirconia) could help solve the problem of foil cracking.

General conclusions

The main goal of this work was to improve mechanical properties of nacre-like alumina developed during the PhD of Florian Bouville. One of explored possibilities was modification of the interphase between alumina platelets. Another alternative was to introduce another level to material architecture by developing ceramic/metal layered composites. In this thesis, we also intended to simplify and up-scale material fabrication.

Simplification of material fabrication

Simplification of the material fabrication was essential in order to up-scale it. EBSD maps confirmed the satisfactory alignment of alumina platelets after uniaxial pressing and FAST sintering. It allowed to avoid sophisticated elaboration by freeze-casting. Sintering greater quantities of powder (90 g instead of 2.8 g) required adjustments to the thermal treatment. Considerable grain growth was noticed due to significantly longer sintering cycle (almost 7 hours 30 minutes instead of 30 minutes). To keep satisfactory mechanical properties, grain growth should be limited. It should be studied, if faster heating and/or cooling could be applied.

As freezing under flow is no longer necessary, the rheology of the slurry is less important. Maybe the quantity of organic phase could be limited to shorten burn-out time. On the other hand, it is probable that polymer improves platelets sliding during pressing and their alignment. It should be investigated, if adapting the type and quantity of organic phase could help to keep good alignment and reduce burn-out time.

Modification of the interphase between platelets

Different modifications of the interphase between alumina platelets were tested in order to improve the mechanical properties of the material.

Zirconia was introduced into the materials in two different ways: added directly into the slurry instead of alumina nano-powder or deposited on platelets surface by sol-gel reaction. Samples prepared with sol-gel chemistry exhibited better mechanical properties than those with zirconia simply added to the slurry. It might be caused by difference in homogeneity of the mix of powders. Samples with alumina platelets processed by alkoxide reaction have mechanical properties comparable (similar maximal stress, increased strain at failure) with the reference composition. It is possibly

caused by the presence of residual stresses. It is possible that optimization of sol-gel reaction and the quantity of zirconia could lead to more significant improvement.

Another tested modification was the substitution of the glassy phase and alumina nano-particles by graphene. The mechanical properties were significantly worse than the properties of the reference samples. The slurry with graphene, glassy phase precursors and nano-alumina was too viscous to freeze it under flow. The elimination of the glassy phase precursors while keeping graphene and alumina nano-powder could be a reasonable compromise. However, working with graphene is quite complicated (obtaining good dispersion, different graphene forms and qualities) so we decided not to follow that path due to limited time.

Alkoxide processing of alumina platelets was the most promising approach. Yet, observed improvement of mechanical properties did not seem significant enough. We decided that working on higher architectural level could bring more enhancement of mechanical response of the materials.

Alumina titanium composites

The goal of preparing alumina/titanium composites by uniaxial pressing and FAST sintering was to introduce an additional structural level to the material. This method turned out to be very adequate. It allowed to obtain a material with several desired characteristics: aligned platelets, alternating layers of metal and ceramic and, in addition, some metal diffused into the interphase between alumina platelets. To our knowledge, it is the simplest way to obtain this level of microstructural sophistication in a ceramic/metal composite at different length scales.

Several observations (SEM, EBSD, laboratory and synchrotron tomography) suggested that during sintering some part of metallic foil is liquid and in liquid state metal penetrates porosity in ceramic. Grains of diffused titanium are interconnected and EBSD has shown that foil after sintering has two different crystallographic configurations. Regardless foil thickness (20-500 μm), metal layers in all samples had significant cracks. These cracks are most likely related to the thermal expansion mismatch between metal and ceramic layers. The substitution of pure titanium by alloy Ti6Al4V did not lead to significant change in diffusion mechanism nor did it prevent foil from cracking. Using titanium foil with thin layers of titanium nitride from both sides did not seem to affect diffusion. Titanium diffused into porosity and nitrogen stayed within the foil. Changing cooling speed (from 100°C/min to 10°C/min) was not enough to stop cracking of the metal layer. At the same time it changed significantly the crystallography of titanium.

Mechanical testing *ex situ* and *in situ* shown that the improvement of the mechanical properties of the ceramic/metal composite in respect to purely ceramic material can not be successful without solving the problem of foil cracking first. Although, sometimes crack propagating from the tip of the notch seems to deviate more in search of crack in the foil, it passes easily through the metal layer. To introduce ductility from metal to the composite, the metal part must remain uncracked after processing.

During this thesis we managed to significantly simplify material fabrication and

to increase the size of prepared samples. Thanks to using uniaxial pressing instead of freezing under flow we developed layered alumina/titanium composites. We also proposed processing alumina platelets by sol-gel reaction in order to improve inter-phase properties. It is a considerable progress in the field of architected materials, although additional work is needed to achieve high mechanical properties, especially in terms of resistance to crack initiation and propagation.

Bibliography

- [1] Maximilien E. Launey, Markus J. Buehler, and Robert O. Ritchie. *On the Mechanistic Origins of Toughness in Bone*, volume 40. 2010.
- [2] K J Koester, J W Ager, and R O Ritchie. The true toughness of human cortical bone measured with realistically short cracks. *Nat Mater*, 7(8):672–677, 2008.
- [3] Maximilien E. Launey and Robert O. Ritchie. On the Fracture Toughness of Advanced Materials. *Advanced Materials*, 21(20):2103–2110, 2009.
- [4] Sylvain Deville. Habilitation a Diriger des Recherches, 2013.
- [5] F. Barthelat and H. D. Espinosa. An experimental investigation of deformation and fracture of nacre-mother of pearl. *Experimental Mechanics*, 47(3):311–324, 2007.
- [6] Horacio D Espinosa, Allison L Juster, Felix J Latourte, Owen Y Loh, David Gregoire, and Pablo D Zavattieri. Tablet-level origin of toughening in abalone shells and translation to synthetic composite materials. *Nature Communications*, 2(2):173–179, 2011.
- [7] Maximilien E. Launey, Etienne Munch, Daan H Alsem, Holly B Barth, and Eduardo Saiz. Designing highly toughened hybrid composites through nature-inspired hierarchical complexity. *Acta Materialia*, 57(10):2919–2932, 2009.
- [8] David V. Wilbrink, Marcel Utz, Robert O. Ritchie, and Matthew R. Begley. Scaling of strength and ductility in bioinspired brick and mortar composites. *Applied Physics Letters*, 97(19):193701, 2010.
- [9] Florian Bouville, Eric Maire, Sylvain Meille, Bertrand Van De Moortèle, and Adam J Stevenson. Strong, tough and stiff bioinspired ceramics from brittle constituents. *Nature materials*, 13(5):508–514, 2014.
- [10] Sylvain Deville. Ice templating , freeze casting : Beyond materials processing. (May):1–18, 2013.
- [11] Florian Bouville. *Self-assembly of anisotropic particles driven by ice growth: Mechanisms, applications and bioinspiration*. PhD thesis, 2013.

- [12] Zuhair a. Munir, Dat V. Quach, and Manshi Ohyanagi. Electric Current Activation of Sintering: A Review of the Pulsed Electric Current Sintering Process. *Journal of the American Ceramic Society*, 94(1):1–19, jan 2011.
- [13] D S Perera, M Tokita, and S Moricca. Comparative study of fabrication of Si₃N₄/SiC composites by spark plasma sintering and hot isostatic pressing. *Comparative study of fabrication of Si₃N₄/SiC composites by spark plasma sintering and hot isostatic pressing*, 18:401–404, 1998.
- [14] Gerd Lutjering and James Williams. *Titanium*. Springer, 2003.
- [15] J. C. Williams. *Titanium science and technology*. Plenum Press, 1973.
- [16] E. W. Collings, Gerhard Welsch, and Rodney Boyer. *Materials properties handbook: titanium alloys*. ASM International, 1994.
- [17] S. Meir, S. Kalabukhov, N. Frage, and S. Hayun. Mechanical properties of Al₂O₃/Ti composites fabricated by spark plasma sintering. *Ceramics International*, 41(3):4637–4643, 2015.
- [18] Shmuel Hayun, Shai Meir, Sergey Kalabukhov, Nahum Frage, and Eugene Zaretsky. Phase Constitution and Dynamic Properties of Spark Plasma-Sintered Alumina-Titanium Composites. *Journal of the American Ceramic Society*, 99(2):573–580, 2016.
- [19] Florian Bouville, Etienne Portuguez, Yunfei Chang, Gary L. Messing, Adam J. Stevenson, Eric Maire, Loic Courtois, and Sylvain Deville. Templated Grain Growth in Macroporous Materials. *Journal of the American Ceramic Society*, 97(6):1736–1742, jun 2014.
- [20] M Schehl, R Torrecillas, and L A Diaz. Alumina nanocomposites from powder-alkoxide mixtures. *Acta Materialia*, 50(5):1125–1139, 2002.
- [21] Harshit Porwal, Peter Tatarko, Salvatore Grasso, and Mike J Reece. Graphene reinforced alumina nano-composites. *Carbon*, 4:359–369, 2013.
- [22] Jian Liu, Haixue Yan, and Kyle Jiang. Mechanical properties of graphene platelet-reinforced alumina ceramic composites. *Ceramics International*, 39(6):6215–6221, 2013.
- [23] Acacio Rincón, Rodrigo Moreno, Adriana S.a. Chinelatto, Carlos F. Gutierrez, Emilio Rayón, María Dolores Salvador, and Amparo Borrell. Al₂O₃-3YTZP-Graphene multilayers produced by tape casting and spark plasma sintering. *Journal of the European Ceramic Society*, 34(10):2427–2434, 2014.
- [24] Jan Rathel, Mathias Herrmann, and Wieland Beckert. Temperature distribution for electrically conductive and non-conductive materials during Field Assisted Sintering (FAST). *Journal of the European Ceramic Society*, 29(8):1419–1425, 2009.

- [25] Qiang Chen and Nicola M Pugno. Bio-mimetic mechanisms of natural hierarchical materials: a review. *Journal of the mechanical behavior of biomedical materials*, 19:3–33, mar 2013.
- [26] Sylvain Deville, Eduardo Saiz, and Ravi K Nalla. Freezing as a Path to Build Complex Composites. 311(January):515–518, 2006.
- [27] M.A. Meyers, P.-Y. Chen, A.Y.M. Lin, and Y. Seki. Biological materials: structure and mechanical properties. *Progress in Materials Science*, 53(1), 2008.
- [28] Etienne Munch. Tough, Bio-Inspired Hybrid Materials. *Science*, 322(5907):1516–1520, 2008.
- [29] Matthew R. Begley, Noah R. Philips, Brett G. Compton, David V. Wilbrink, Robert O. Ritchie, and Marcel Utz. Micromechanical models to guide the development of synthetic brick and mortar composites. *Journal of the Mechanics and Physics of Solids*, 60(8):1545–1560, aug 2012.
- [30] Lorenz J. Bonderer, André R. Studart, and Ludwig J. Gauckler. Bioinspired Design and Assembly of Platelet Reinforced Polymer Films. *Science*, 319(5866), 2008.
- [31] Stephen Mann. Molecular Tectonics in Biomineralization and Biomimetic Materials Chemistry. *Nature*, 365:499, 1993.
- [32] Helmut Cölfen and Stephen Mann. Higher-order organization by mesoscale self-assembly and transformation of hybrid nanostructures. *Angewandte Chemie - International Edition*, 42(21):2350–2365, 2003.
- [33] Marc André. Structural Biological Materials: Critical Mechanics-Materials Connections. *Science*, 339(6121), 2013.
- [34] W. J. Clegg, K. Kendall, N. McN. Alford, W. Button, and J. D. Birchall. A simple way to make tough ceramics. *Nature*, 347:455–457, 1990.
- [35] Randall M. Erb, Rafael Libanori, Nuria Rothfuchs, and André R. Studart. Composites Reinforced in Three Dimensions by Using Low Magnetic Fields. *Science*, 335(6065):199–204, 2012.
- [36] M. G. Worster and J. S. Wettlaufer. Natural Convection, Solute Trapping, and Channel Formation during Solidification of Saltwater. *The Journal of Physical Chemistry C Letters*, 101(32):6132–6136, 1997.
- [37] Hiroshi Ishiguro and Boris Rubinsky. Mechanical Interactions between Ice Crystals and Red Blood Cells during Directional Solidification. *Cryobiology*, 31:483–500, 1994.
- [38] Guillaume Gay and M. Aza Azouni. Forced Migration of Nonsoluble and Soluble Metallic Pollutants ahead of a Liquid-Solid Interface during Unidirectional Freezing of Dilute Clayey Suspensions. *Crystal Growth & Design*, 2(2):135–140, 2002.

- [39] J Karlsson. Cryopreservation: freezing and vitrification. *Science*, 296(5568), 2002.
- [40] S. Deville. Freeze-Casting of Porous Ceramics: A Review of Current Achievements and Issues. *Advanced Engineering Materials*, 10(3):155–169, mar 2008.
- [41] Maximilien E Launey, Etienne Munch, Daan Hein Alsem, Eduardo Saiz, Antoni P Tomsia, and Robert O. Ritchie. A novel biomimetic approach to the design of high-performance ceramic-metal composites. *J. R. Soc. Interface*, (October 2009):741–753, 2009.
- [42] Siddhartha Roy and Alexander Wanner. Metal/ceramic composites from freeze-cast ceramic preforms: Domain structure and elastic properties. *Composites Science and Technology*, 68(5):1136–1143, 2008.
- [43] Siddhartha Roy, Benjamin Butz, and Alexander Wanner. Damage evolution and domain-level anisotropy in metal/ceramic composites exhibiting lamellar microstructures. *Acta Materialia*, 58(7):2300–2312, 2010.
- [44] Masao Tokita. Development of Advanced Spark Plasma Sintering (SPS) Systems and its Industrial Applications, in Pulse Electric Current Synthesis and Processing of Materials. In *Ceram. Trans.* John Wiley & Sons, Inc., 2006.
- [45] M Nanko, T Maruyama, and H Tomino. Neck growth on initial stage of pulse current pressure sintering for coarse atomized powder made of cast-iron. *Journal of the Japan Institute of Metals*, 63(7), 1999.
- [46] Mirva Eriksson, Haixue Yan, Mats Nygren, Mike J. Reece, and Zhijian Shen. Low temperature consolidated lead-free ferroelectric niobate ceramics with improved electrical properties. *Journal of Materials Research*, 25(2), 2010.
- [47] S. Le Gallet, L. Campayo, E. Courtois, S. Hoffmann, Yu. Grin, F. Bernard, and F. Bart. Spark plasma sintering of iodine-bearing apatite. *Journal of Nuclear Materials*, 400(3), 2010.
- [48] L. Campayo, S. Le Gallet, Yu. Grin, E. Courtois, F. Bernard, and F. Bart. Spark plasma sintering of lead phosphovanadate $\text{Pb-3(VO}_4\text{)(1).(6)(PO}_4\text{)(0.4)}$. *Journal of the European Ceramic Society*, 29(8), 2009.
- [49] Yan Zhao, Kang-ning Sun, Wei-li Wang, and Yu-xiang Wang. Microstructure and anisotropic mechanical properties of graphene nanoplatelet toughened biphasic calcium phosphate composite. *Ceramics International*, 39(7):7627–7634, 2013.
- [50] YM Kan, PL Wang, T Xu, GJ Zhang, DS Yan, ZJ Shen, and YB Cheng. Spark plasma sintering of bismuth titanate ceramics. *Journal of the American Ceramic Society*, 88(6), 2005.

- [51] C. Drouet, C. Largeot, G. Raimbeaux, C. Estournes, G. Dechambre, C. Combes, and C. Rey. Bioceramics: Spark Plasma Sintering (SPS) of Calcium Phosphates. *Adv. Sci. Technol.*, 49:45–50, 2006.
- [52] SH Risbud, JR Groza, and MJ Kim. Clean grain-boundaries in aluminium nitride ceramics densified without additives by a plasma-activated sintering process. *Philosophical Magazine B-Physics of Condensed Matter Statistical Mechanics Electronic Optical and Magnetic Properties*, 69(3), 1994.
- [53] X. J. Chen, K. A. Khor, S. H. Chan, and L. G. Yu. Overcoming the effect of contaminant in solid oxide fuel cell (SOFC) electrolyte: spark plasma sintering (SPS) of 0.5 weight per cent silica-doped yttria-stabilized zirconia (YSZ). *Materials Science and Engineering*, 374(1-2):64–71, 2004.
- [54] ZJ Shen, H Peng, and M Nygren. Formidable increase in the superplasticity of ceramics in the presence of an electric field. *Advanced Materials*, 15(12), 2003.
- [55] T. Takeuchi, E. Betourne, M. Tabuchi, H. Kageyama, Y. Kobayashi, A. Coats, F. Morrison, D. C. Sinclair, and A. R. West. Dielectric properties of spark-plasma-sintered BaTiO₃. *Journal of Materials Science*, 34(5), 1999.
- [56] M. Yue, J. Zhang, Y. Xiao, G. Wang, and T. Li. New kind of NdFeB magnet prepared by spark plasma sintering. *IEEE TRANSACTIONS ON MAGNETICS*, 39(6), 2003.
- [57] M. Yue, J. X. Zhang, W. Q. Liu, and G. P. Wang. Chemical Stability and Microstructure of Nd-Fe-B Magnet Prepared by Spark Plasma Sintering. *Journal of Magnetism and Magnetic Materials*, 271(2-3), 2004.
- [58] P. Pei, X.P. Song, J. Liu, M. Zhao, and G.L. Chen. Improving hydrogen storage properties of Laves phase related BCC solid solution alloy by SPS preparation method. *International Journal of Hydrogen Energy*, 34(20):8597–8602, oct 2009.
- [59] X. B. Zhao, S. H. Yang, Y. Q. Cao, J. L. Mi, Q. Zhang, and T. J. Zhu. Synthesis of Nanocomposites with Improved Thermoelectric Properties. *Journal of Electronic Materials*, 38(7), 2009.
- [60] J. G. Noudem, M. Prevel, A. Veres, D. Chateigner, and J. Galy. Thermoelectric Ca₃Co₄O₉ ceramics consolidated by spark plasma sintering. *Journal of Electroceramics*, 22(1-3), 2009.
- [61] Koji Amezawa, Yoshito Nishikawab, Yoichi Tomiic And, and Naoichi Yamamoto. Electrical and Mechanical Properties of Sr-Doped LaPO₄ Prepared by Spark Plasma Sintering. *Journal of The Electrochemical Society*, 152(6), 2005.
- [62] Koji Morita, Byung-Nam Kim, Hidehiro Yoshida And, and Keijiro Hiraga. Spark plasma sintering condition optimization for producing transparent MgAl₂O₄ spinel polycrystal. *Journal of the American Ceramic Society*, 92(6), 2009.

- [63] Takekazu Nagae, Masaru Yokota, Masateru Nose, Shogo Tomida, Takashi Kamiya, and Shigeoki Saji. Effects of Pulse Current on an Aluminum Powder Oxide Layer During Pulse Current Pressure Sintering. *Materials Transactions*, 43(6):1390–1397, 2002.
- [64] Airu Wang and Osamu Ohashi. Titanium Mesh/Rod Joined by Pulse Electric Current Sintering: Effect of Heating Rate. *Materials Transactions*, 47(9):2348–2352, 2006.
- [65] R. M. German. *Sintering Theory and Practice*. Solar-Terrestrial Physics, 1996.
- [66] E. A. Olevsky, S. Kandukuri, and L. Froyen. Consolidation Enhancement in Spark Plasma Sintering: Impact of High Heating Rates. *Journal of Applied Physics*, 102, 2007.
- [67] L. A. Stanciu, V. Y. Kodash, and J. R. Groza. Effects of heating rate on densification and grain growth during field-assisted sintering of alpha-Al₂O₃ and MoSi₂ powders. *Metallurgical and Materials Transactions A-Physical Metallurgy and Materials Science*, 32(10), 2001.
- [68] Z. Shen, M. Johnsson, Z. Zhao, and M. Nygren. Spark Plasma Sintering of Alumina. *Journal of the American Ceramic Society*, 85(8):1921–1927, 2002.
- [69] You Zhou, Kiyoshi Hirao, Yukihiko Yamauchi, and Shuzo Kanzaki. Effects of heating rate and particle size on pulse electric current sintering of alumina. *Scripta Materialia*, 48(12):1631–1636, jun 2003.
- [70] U. Anselmi-Tamburini, Z. A. Munir, and J. E. Garay. Preparation of Dense Nanostructured Oxide Ceramics with Fine Crystal Size by High-Pressure Spark Plasma Sintering, 2009.
- [71] A. Zarkades and F. R. Larson. The science, technology and application of titanium. Pergamon, Oxford, 1970.
- [72] Mitsuo Niinomi. Mechanical properties of biomedical titanium alloys. *Materials Science and Engineering: A*, 243(1-2):231–236, 1998.
- [73] Ronald W. Schutz and David E. Thomas. *Corrosion of titanium and titanium alloys*. ASM Handbook, 1987.
- [74] Sylvain Deville, Eric Maire, Guillaume Bernard-Granger, Audrey Lasalle, Agnès Bogner, Catherine Gauthier, Jérôme Leloup, and Christian Guizard. Metastable and unstable cellular solidification of colloidal suspensions. *Nature Materials*, 8(12):966–972, 2009.
- [75] Florian Bouville, Eric Maire, Sylvain Meille, J Adam, and Sylvain Deville. Supplementary information. *Nature materials*, 13(5), 2014.

- [76] T. Lube, M. Manner, and R. Danzer. The Miniaturisation of the 4-Point-Bend Test. *Fatigue & Fracture of Engineering Materials & Structures*, 20(11):1605–1616, 1997.
- [77] ASTM C1421-10. Standard Test Methods for Determination of Fracture Toughness of Advanced Ceramics at Ambient Temperature, 2011.
- [78] ASTM E 1820 - 01. Standard Test Method for Measurement of Fracture Toughness, 2001.
- [79] Bruce Fegley, Paul White, and H. Kent Bowen. Preparation of Zirconia-Alumina Powders by Zirconium Alkoxide Hydrolysis. *Journal of the American Ceramic Society*, 68(2), 1985.
- [80] Nils Claussen and Manfred Ruhle. Design of transformation-toughened ceramics. *Science and Technology of Zirconia*, 3:137, 1980.
- [81] Nils Claussen. Fracture toughness of Al₂O₃ with an unstabilized ZrO₂ dispersed phase. *Journal of the American Ceramic Society*, 59(1-2):49–51, 1976.
- [82] M Ruhle, N.Claussen, and A.H. Heuer. Transformation and Microcrack Toughening as Complementary Processes in ZrO₂-Toughened Al₂O₃. *Journal of the American Ceramic Society*, 69(3):195–197, 1986.
- [83] A.H. DeAza, J. Chevalier, G. Fantozzi, M. Schehl, and R. Torrecillas. Crack growth resistance of alumina, zirconia and zirconia toughened alumina ceramics for joint prostheses. *Biomaterials*, 23(3):937–945, feb 2002.
- [84] P. R. Wallace. The band theory of graphite. *Physical Review*, 71(9):622–634, 1947.
- [85] Wonbong Choi and Jo-won Lee. *Graphene: Synthesis and Applications*. CRC press., 2011.
- [86] A K Geim and K S Novoselov. The rise of graphene. *Nat Mater*, 6(3):183–191, 2007.
- [87] Changgu Lee, Xiaoding Wei, Jeffrey W Kysar, and James Hone. Measurement of the Elastic Properties and Intrinsic Strength of Monolayer Graphene. *Science*, 321(5887):385–388, 2008.
- [88] Alexander A Balandin, Suchismita Ghosh, Wenzhong Bao, Irene Calizo, Desalegne Teweldebrhan, Feng Miao, and Chun Ning Lau. Superior Thermal Conductivity of Single-Layer Graphene. *Nano Letters*, 8(3):902–907, 2008.
- [89] Martin Pumera. Electrochemistry of graphene: new horizons for sensing and energy storage. *The Chemical Record*, 9(4):211–223, 2009.

- [90] Nihar Mohanty and Vikas Berry. Graphene-Based Single-Bacterium Resolution Biodevice and DNA Transistor: Interfacing Graphene Derivatives with Nanoscale and Microscale Biocomponents. *Nano Letters*, 8(12):4469–4476, 2008.
- [91] Junbo Wu, Mukul Agrawal, Héctor A Becerril, Zhenan Bao, Zunfeng Liu, Yongsheng Chen, and Peter Peumans. Organic Light-Emitting Diodes on Solution-Processed Graphene Transparent Electrodes. *ACS Nano*, 4(1):43–48, 2010.
- [92] Meryl D Stoller, Sungjin Park, Yanwu Zhu, Jinho An, and Rodney S Ruoff. Graphene-Based Ultracapacitors. *Nano Letters*, 8(10):3498–3502, 2008.
- [93] Acacio Rincón, Adriana S.a. Chinelatto, and Rodrigo Moreno. Tape casting of alumina/zirconia suspensions containing graphene oxide. *Journal of the European Ceramic Society*, 34(7):1819–1827, 2014.
- [94] A. Centeno, V. G. Rocha, B. Alonso, A. Fernández, C. F. Gutierrez-Gonzalez, R. Torrecillas, and A. Zurutuza. Graphene for tough and electroconductive alumina ceramics. *Journal of the European Ceramic Society*, 33(15-16):3201–3210, 2013.
- [95] Harshit Porwal, Salvatore Grasso, Mahesh Kumar Mani, and Mike J. Reece. In situ reduction of graphene oxide nanoplatelet during spark plasma sintering of a silica matrix composite. *Journal of the European Ceramic Society*, 34(14):3357–3364, 2014.
- [96] Fabian Heinemann, Malte Launspach, and Katharina Gries. Gastropod nacre: Structure, properties and growth - biological, chemical and physical basics. *Biophysical Chemistry*, 153:126–153, 2011.
- [97] Olivier T. Picot, Victoria G. Rocha, Claudio Ferraro, Na Ni, Eleonora D’Elia, Sylvain Meille, Jerome Chevalier, Theo Saunders, Ton Peijs, Mike J. Reece, and Eduardo Saiz. Using graphene networks to build bioinspired self-monitoring ceramics. *Nature Communications*, 8:14425, 2017.
- [98] C. G. Levi, G. J. Abbaschian, and R. Mehrabian. Interface interactions during fabrication of aluminum alloy-alumina fiber composites. *Metallurgical Transactions A*, 9(5):697–711, 1978.
- [99] Alain Leger, N. R. Calderon, Raphael Charvet, Willy Dufour, Claudio Bacciarini, Ludger Weber, and Andreas Mortensen. Capillarity in pressure infiltration: Improvements in characterization of high-temperature systems. *Journal of Materials Science*, 47(24):8419–8430, 2012.
- [100] I. O. Ozer, E. Suvaci, B. Karademir, J. M. Missiaen, C. P. Carry, and D. Bouvard. Anisotropic sintering shrinkage in alumina ceramics containing oriented platelets. *Journal of the American Ceramic Society*, 89(6):1972–1976, 2006.

- [101] W.G. Burgers. On the process of transition of the cubic-body-centered modification into the hexagonal-close-packed modification of zirconium. *Physica*, 1(7-12):561–586, 1934.
- [102] Lionel Germain, Suhash Dey, Michel Humbert, and Nathalie Gey. Determination of parent orientation maps in advanced titanium-based alloys. *Journal of microscopy*, 227(2006):284–291, 2007.
- [103] Yanqing Su, Tong Liu, Xinzhong Li, Ruirun Chen, Hongsheng Ding, Jingjie Guo, and Hengzhi Fu. Lamellar orientation control in directionally solidified TiAl intermetallics. *China Foundry*, 11(4):219–231, 2014.
- [104] Aerospace Specification Metals Inc. consulted on 15/11/2017.
- [105] H O Pierson. *Handbook of Refractory Carbides and Nitrides: Properties, Characteristics, Processing and Apps*. Noyes Publications, 1996.



FOLIO ADMINISTRATIF

THESE DE L'UNIVERSITE DE LYON OPEREE AU SEIN DE L'INSA LYON

NOM : MARCINKOWSKA

DATE de SOUTENANCE : 20/03/2018

Prénoms : Malgorzata Judyta

TITRE : Elaboration and characterization of mechanical properties of ceramic composites with controlled architecture

NATURE : Doctorat

Numéro d'ordre : 2018LYSEI021

Ecole doctorale : ED 34 Matériaux de Lyon

Spécialité : Matériaux

RESUME :

L'objectif de cette thèse était de développer et de caractériser la microstructure et les propriétés mécaniques des céramiques bio-inspirées. L'alumine inspirée par la nacre fabriquée par texturation à la glace (freeze-casting), précédemment développée dans le cadre de la thèse de F. Bouville, a été choisie comme matériau de référence. La simplification et le changement d'échelle du procédé d'élaboration des matériaux ont été étudiés. Le procédé sophistiqué de freeze-casting a été remplacé par le pressage uniaxial à cru. Les mesures de diffraction des électrons rétrodiffusés ont confirmé le bon alignement après frittage des plaquettes d'alumine utilisées pour préparation du matériau. Le cycle de frittage assisté par effet de champs a été adapté à de plus grandes quantités de poudre céramique et d'additifs organiques. La deuxième partie du projet a été consacrée à la modification de l'interphase entre les plaquettes d'alumine, afin d'améliorer les propriétés mécaniques du matériau. Diverses possibilités ont été explorées: ajout de poudre de zircone, dépôt de zircone sur les plaquettes par réaction sol-gel ou substitution de la phase vitreuse par du graphène. Tous les matériaux obtenus ont été caractérisés par flexion quatre points sur des barrettes entaillées. La troisième partie de cette étude a porté sur le développement de composites multicouches métal/céramique, par frittage simultané d'alumine et de titane. L'épaisseur et la composition de la feuille de titane ont été modifiées pour étudier leur influence sur les phénomènes de diffusion lors du frittage. Les composites ont été caractérisés par MEB, EBSD, spectroscopie à rayons X à dispersion d'énergie et tomographie à rayons X au synchrotron.

La fabrication simplifiée des matériaux permet de préparer des échantillons de plus grandes dimensions de céramiques inspirées par la nacre, sans passer par une étape de freeze-casting. Cependant, la croissance des grains doit être limitée pour maintenir de bonnes propriétés mécaniques. La modification de l'interphase entre les plaquettes d'alumine n'a pas amélioré les propriétés mécaniques des matériaux par rapport au matériau de référence. D'autre part, le dépôt de nano-zircone sur la surface des plaquettes semble prometteur et devrait faire l'objet d'études plus poussées. Dans le cas des composites alumine/titane, les composites architecturés multi-échelles ont été fabriqués de manière assez simple. Cependant, il est crucial d'éviter la fissuration des feuilles de métal afin d'améliorer les propriétés mécaniques.

MOTS-CLÉS : Nacre-like alumina, freeze-casting, mechanical testing, metal/ceramic composites

Laboratoire (s) de recherche :

MATEIS – UMR CNRS 5510
INSA de Lyon
25 Avenue Jean Capelle
69621 VILLEURBANNE CEDEX

Directeur de thèse: MEILLE Sylvain (Professeur des Universités), DEVILLE Sylvain (Directeur de Recherche)

Président de jury :

Composition du jury :	ROSSIGNOL Fabrice	(Directeur de Recherche)
	BOUVARD Didier	(Professeur des Universités)
	LE GALLET Sophie	(Maître de Conférences)
	DEZELLUS Olivier	(Maître de Conférences HDR)